Een biomechanische analyse van 'shear wave'-elastografie
toegepast op pediatrische modellen van het hart

A Biomechanical Analysis of Shear Wave Elastography in Pediatric Heart Models

Annette Caenen

Promotor: prof. dr. ir. P. Segers
Proefschrift ingediend tot het behalen van de graad van
Doctor in de ingenieurswetenschappen: biomedische ingenieurstechnieken

UNIVERSITEIT
GENT

Vakgroep Elektronica en Informatiesystemen
Voorzitter: prof. dr. ir. K. De Bosschere
Faculteit Ingenieurswetenschappen en Architectuur
Academiejaar 2017 - 2018

ISBN 978-94-6355-100-7
NUR 954
Wettelijk depot: D/2018/10.500/18

Supervisor:

Prof. dr. ir. Patrick Segers

Research lab:

Institute Biomedical Technology
Biofluid, Tissue and Solid Mechanics for Medical Applications (bioMMeda)
Ghent University
Corneel Heymanslaan 10 - Blok B (entrance 36)
B–9000 Gent
Belgium

Members of the exam committee:

Chairman:	
Prof. dr. Paul Kiekens	Faculty of Engineering and Architecture, UGent
Secretary:	
Prof. dr. ir. Jan Vierendeels	Faculty of Engineering and Architecture, UGent
Reading committee:	
Prof. dr. ir. Jan D'hooge	Faculty of Medicine, KULeuven
Prof. dr. ir. Mathias Kersemans	Faculty of Engineering and Architecture, UGent
Prof. dr. ir. Richard G. P. Lopata	Faculty of Biomedical Technology, Technical University Eindhoven, The Netherlands
Prof. dr. ir. Mark L. Palmeri	Pratt School of Engineering, Duke University, United States of America
Prof. dr. ir. Jan Vierendeels	Faculty of Engineering and Architecture, UGent
Other members:	
Dr. ir. Mathieu Pernot	Langevin Institute, ESPCI, CNRS, France
Prof. dr. ir. Patrick Segers	Faculty of Engineering and Architecture, UGent
Prof. dr. ir. Pascal Verdonck	Faculty of Engineering and Architecture, UGent

This research was funded by a research grant of the Flemish government agency for Innovation and Entrepreneurship (VLAIO/IWT 141010).

It's a dangerous business, Frodo, going out your door.
You step onto the road, and if you don't keep your feet,
there's no knowing where you might be swept off to.

J.R.R. Tolkien

Preface

Doing a PhD is an incredible and exciting opportunity to get in touch with the scientific world. It has been a learning adventure, but also a personal journey. It allowed me to develop my own critical thinking, research one specific area of interest and, just maybe by the end of it all, provide something useful to others. I have to admit that it might be a bit intimidating in the beginning, as you are wondering how a starting PhD student can contribute something to the big world of research. Thankfully, I had some amazing people next to me, who guided and supported me during my PhD-journey, and to whom I want to express my sincere gratitude.

I first want to thank Abigail and Patrick for offering me the opportunity to do a PhD. Even though a different PhD project was initially planned for me, a meeting with physician Luc Mertens completely altered the fate of my PhD-adventure. I am very pleased that I was introduced to the intriguing world of ultrasound and computational biomechanics, with both Abigail and Patrick as my initial promoters. Abigail, thank you for always believing in me, especially during the first year, which was not that easy after an unsuccessful IWT defense and a negative abstract notification for my very first conference. I am very grateful for all the things you learned me, ranging from practicalities - such as writing a successful grant proposal (second time) or making attractive conference presentations - to encouraging my critical thinking after our many scientific discussions. Thank you for introducing me to the ultrasound committee on international conferences, which feels now very familiar. Even though you were not there the last year and a half, the skills developed throughout my initial years as a PhD student were essential for a successful end of the PhD-journey. Patrick, thank you for always looking at the bigger picture of the project, and asking the right questions at the right moment. Your broad scientific knowledge in combination with your enthusiasm really kept me motivated during this project. Thank you for being available and reachable for any question, literally anytime and anywhere!

This PhD project is the result of a fruitful collaboration between our lab and the Langevin Institute in Paris. Therefore, I want to thank Mathieu

Pernot, who always opened his doors to us for performing SWE experiments, as a validation step for our modeling methodology. I also want to express my gratitude to their lab-members Clément and Simon, who helped me tremendously with setting up the experiments or with any problems encountered with the ultrasound machine during our multiple short stays in Paris. In the last year of my PhD, I had the opportunity to collaborate with Duke University in Durham. Therefore, I want to thank Mark Palmeri and Kathryn Nightingale for the very warm welcome during my 5 week research visit. It was a wonderful and instructive experience to participate as a member of their team to lab-meetings and the AIUM meeting. Also, a big thanks to Sam for performing 3D SWE acquisitions on the heart; Pete and Nic for setting up the Verasonics-system and automatically motorizing all probe movements; Maryam for all practical arrangements concerning tissue handling and V for the interesting conversations on cardiac SWE (and the exciting heart transplantation experiment).

I also want to thank the following persons for their specific contributions to my PhD-journey. (Ex)colleagues Sander and Darya, thank you for showing the practicalities of the mechanical testing machine at 'bioMMeda'. Mathias Kersemans from the research group 'Mechanics of Materials and Structures', thank you for performing complementary experiments to mechanically characterize the home-made phantoms. IAESTE-interns Abdullah and José, thank you for helping me with the post-processing of the experimental SWE data. Colleague and office-mate Mathias, thank you for the many interesting and exciting scientific conversations, which provided new insights and ideas into my work. Furthermore, thank you for your expert advice on lay-out (and for making me laugh with your exploding stent simulations). Colleague Charlotte, thank you for introducing me to the youngster working group of the National Committee on Biomedical Engineering. I really enjoyed being part of this organization committee. Colleagues Saskia, Inge and Jurgen, thank you for all the administrative and technical support.

Of course, the PhD-journey was not always easy. There were many hurdles to overcome, such as difficult reviews or working around the limits of the software's capabilities. Thankfully, there were colleagues who were subjected to the same fate, and who became good friends during this PhD-trip. Therefore, I want to thank all current and ex 'bioMMeda' members for the good times and sweet memories in the office, but also outside the office. I will never forget the many fantastic starter parties (but especially the 2013-edition - our edition of course), the cozy coffee breaks with delicious sweets, the fun talks during lunch breaks which were not always work-appropriate and the great after-conference moments such as withstanding the heat in the Tucson-desert (rather running from and to air-conditioned spaces) or

accidentally ordering chicken paws for lunch based on a incomprehensible Taiwanese menu. I also would like to thank the colleagues on the opposite side of the hallway, the colleagues of the 'Medisip'-team, for the great time at the IBiTech. Furthermore, another thank you goes to my colleagues at Duke university for submerging me in the Durhamite habits such as tasting chicken and waffles, participating in story telling events and cheering for the Durham bulls baseball team (and experiencing the steamy eye-flashing bull whenever a home-run is hit).

Ik zou graag dit voorwoord afsluiten met een persoonlijke noot. Op de allereerste plaats wil ik mijn familie bedanken voor hun onvoorwaardelijke steun. Mama en papa, bedankt voor alle mogelijkheden die jullie me hebben geboden. Ik neem het vaak als vanzelfsprekend, maar bedankt om er gewoonweg altijd voor mij te zijn. Ik ben blij dat ik dit moment met jullie kan delen. Mijn zus Stefanie en haar vriend Wesly, bedankt voor alle steun en de nodige ontspanning in de weekends. Verder zou ik graag al mijn vrienden bedanken die de afgelopen vier jaar en een half een luisterend oor zijn geweest, en gezorgd hebben voor de vele gezellige en grappige momenten na het werk. Mijn laatste bedankje gaat naar mijn allerliefste man Bram, die mij ongelofelijk veel gesteund en gemotiveerd heeft tijdens mijn doctoraat. Bedankt voor je begrip als ik een avond doorwerkte of weer op congres/studieverblijf vertrok in het buitenland. Je bent een geweldige man, en ik ben benieuwd naar de volgende avonturen die het leven ons zal brengen!

Annette Caenen
Gent, 7 Maart 2018

Table of contents

Abbreviations and symbols

The following list summarizes the most commonly used abbreviations and symbols in this thesis.

Abbreviations

1D	One-dimensional
2D	Two-dimensional
3D	Three-dimensional
AIUM	American institue of ultrasound in medicine
AR	Aortic valve regurgitation
ARF	Acoustic radiation force
ARFI	Acoustic radiation force imaging
AS	Aortic stenosis
AV	Aortic valve
CSM	Computational solid mechanics
CT	Computer tomography
CUSE	Comb-push ultrasound shear elastography
CWS	Crawling wave sonoelastography
DOF	Depth of field
ED	End-diastole
FEM	Finite element method
FFT	Fast Fourier transform
FWHM	Full-width half maximum
GLM	General linear model
HIFU	High intensity ultrasound
HO	Holzapfel-Ogden
IQ	In-phase quadrature
IVS	Interventricular septum thickness
LDUV	Lamb wave dispersion ultrasound vibrometry
LV	Left ventricle
LVPW	Left ventricle posterior wall thickness
MAC	Modal assurance criterion

mHO	Modified Holzapfel-Ogden
MI	Mechanical index
MRE	Magnetic resonance elastography
MRI	Magnetic resonance imaging
MSE	Mean squared error
OCE	Optical coherence elastography
OCT	Optical coherence tomography
PIHI	Pulse-inversion harmonic imaging
PRF	Pulse repetition frequency
pSWE	Point shear wave elastography
PVA	Polyvinyl alcohol
PWI	Plane wave imaging
QIBA	Quantitative imaging and biomarkers alliance
RANSAC	Random sample consensus
RF	Radiofrequent
RSNA	Radiological society of North America
RV	Right ventricle
SDUV	Shear wave dispersion ultrasound vibrometry
SMURF	Spatially modulated ultrasound radiation force
SNR	Signal-to-noise ratio
SSI	Supersonic shear imaging
SW	Shear wave
SWE	Shear wave elastography
SWEI	Shear wave elasticity imaging
SWS	Shear wave speed
TAST	Time aligned sequential tracking
TE	Transient elastography
TI	Thermal index
TOF	Time-of-flight
ToF	Tetralogy of Fallot
TTP	Time-to-peak
US	Ultrasound
VSD	Ventricular septal defect
VTK	Visualization ToolKit
WFUMB	World federation for ultrasound in medicine and biology

Symbols

α	Attenuation coefficient	[Np/m]
$\ddot{u}$	Acceleration	[m/s^2]
Λ	Wavelength	[m]

λ	Lamé constant	[Pa]
λ_1	Longitudinal elasticity	[Pa]
λ_2	Longitudinal viscosity	[Pa · s]
μ	Shear modulus	[Pa]
μ'	Real part of shear modulus	[Pa]
μ''	Imaginary part of shear modulus	[Pa]
μ_1	Shear elasticity	[Pa]
μ_2	Shear viscosity	[Pa · s]
ν	Coefficient of Poisson	[-]
ω	Angular frequency	[rad/s]
ϕ	Phase angle	[°]
Π	Acoustic interface pressure	[Pa/m²]
π	Pi	[3.14]
Ψ	Eigenvector	[m]
ψ	Strain energy potential	[Pa]
ψ^{dev}	Deviatoric part of strain energy potential	[Pa]
ψ^{vol}	Volumetric part of strain energy potential	[Pa]
ρ	Density	[kg/m³]
σ	Stress	[Pa]
σ_x	Gaussian width of ARF excitation in x-direction	[m]
σ_y	Gaussian width of ARF excitation in y-direction	[m]
σ_z	Gaussian width of ARF excitation in z-direction	[m]
τ	Prony relaxation time	[s]
ε	Strain	[-]
$\widehat{R}_x(1)$	Autocorrelation function of lag one	
$\widehat{T}$	Shear wave arrival time	[s]
$\widehat{v}_z$	Axial velocities	[m/s]
A	Aperture	[m]
a	Isotropic material parameter	[Pa]
a_f	Material parameter in fiber direction	[Pa]
a_n	Material parameter in normal direction	[Pa]
a_s	Material parameter in sheet direction	[Pa]
a_{fs}	Material parameter in fiber and sheet direction	[Pa]
b	Isotropic material parameter	[-]
b	Volume force density	[N/m³]
b_f	Material parameter in fiber direction	[-]
b_n	Material parameter in normal direction	[-]
b_s	Material parameter in sheet direction	[-]
b_{fs}	Material parameter in fiber and sheet direction	[-]
C	General elastic constant	[Pa]
c_ϕ	Phase velocity	[m/s]
c_g	Group velocity	[m/s]

c_L	Longitudinal velocity	[m/s]
c_T	Shear wave velocity	[m/s]
D_F	Width focal zone	[m]
E	Young's elasticity modulus	[Pa]
F	Force	[N]
f	Frequency	[Hz]
f_o	Center frequency	[Hz]
$F_\#$	F-number	[-]
G	Shear modulus	[Pa]
g	Normalized Prony coefficient	[-]
G_o	Initial shear modulus	[Pa]
h	Half-thickness plate	[m]
I	Acoustic intensity	[W/m^2]
I_1	First material invariant	[-]
I_{4f}	Material invariant representing stretch in fiber direction	[-]
I_{4n}	Material invariant representing stretch in normal direction	[-]
I_{4s}	Material invariant representing stretch in sheet direction	[-]
I_{8fs}	Material invariant representing relative shear between fiber and sheet direction	[-]
I_{sppa}	Spatial peak pulse average acoustic intensity	[W/m^2]
I_{spta}	Spatial peak temporal average acoustic intensity	[W/m^2]
J	Elastic volume ratio	[-]
K	Bulk modulus	[Pa]
k	Wave number	[1/m]
k_{im}	Imaginary part of wave number	[1/m]
k_{re}	Real part of wave number	[1/m]
L	Focal length	[m]
L_F	Length focal zone	[m]
n_T	Number of transmit beams	[-]
P	Time-averaged acoustic pressure	[Pa]
p	Acoustic pressure	[Pa]
R	Energetic reflection coefficient	[-]
r	Radial distance	[m]
t	Time	[s]
u	Displacement	[m]
x	Spatial location	[m]
x_o	X-coordinate of ARF focus	[m]
y_o	Y-coordinate of ARF focus	[m]
z_o	Z-coordinate of ARF focus	[m]

Samenvatting

Inleiding

Het systematisch vroegtijdig opsporen van hart- en vaatziekten is essentieel voor de optimale behandeling en opvolging van patiënten enerzijds, en voor een verlaging van de mortaliteit en morbiditeit anderzijds. Dit gaat gepaard met een positieve impact op de maatschappij en economie. De zorg-sector heeft hiervoor verschillende beeldvormingstechnieken ter beschikking, maar deze bieden voornamelijk informatie over de anatomie en structuur van het hart, en niet over belangrijke diagnostische markers, zoals de heersende spanningen of intrinsieke mechanische eigenschappen van het hart. Om deze laatstgenoemde parameters te evalueren is momenteel een invasieve katheterisatie nodig zodat de druk kan gemeten worden in de hartkamer(s). Daarom richt deze doctoraatsthesis zich op het onderzoeken van een relatief nieuwe techniek, gebaseerd op ultrageluid, om myocardiale stijfheid niet invasief te meten. In dit kader zullen we meer bepaald het potentieel van '*shear wave elastography*' (SWE) onderzoeken.

SWE genereert een interne perturbatie in het bestudeerde weefsel en meet vervolgens de voortplanting van deze mechanische golf (de *shear wave*), waarvan de voortplantingssnelheid direct gerelateerd is aan de stijfheid van het weefsel. Uit vorige studies is reeds gebleken dat SWE succesvol stijfheid kan meten in isotrope viscoelastische media zonder geometrische restricties, zoals in borst- of leverweefsel. Echter, om deze techniek toe te passen op niet-lineaire anisotrope viscoelastische media met geometrische restricties, zoals de hartwand, zijn uitgebreide validatie-testen van de techniek nodig. De geometrie en intrinsieke mechanische en structurele karakteristieken van de hartwand kunnen immers zorgen voor complexe golfvoortplantings-fenomenen, zoals dispersie, zodat de post-processing algoritmes aangepast moeten worden. Deze golfvoortplantingsfenomenen zullen anders zijn bij kinderen dan bij volwassenen, vermits de geometrie van hun hart en de dikte van de hartspierwand kleiner is, waardoor de golfpropagatie anders zal geleid worden. Om meer inzicht te verkrijgen en te bieden in de complexe golf fysica geassocieerd met toepassing van SWE op kinderharten, ontwikkelden we *in*

vitro en *ex vivo* gebaseerde computermodellen die toelaten om de complexe relatie tussen geometrie, materiaalkarakteristieken en randvoorwaarden aan de ene kant, en eigenschappen van de golfpropagatie aan de andere kant, uit te klaren.

Deze doctoraatsthesis bestaat uit vier grote delen. Deel I, genaamd '*Shear wave elastography* gebaseerd op ultrageluid', geeft een algemene inleiding over elastografie en over de verschillende technische implementaties van de onderzochte SWE-techniek. Dit deel geeft eveneens een overzicht van de verscheidene post-processing algoritmes die gebruikt zijn in deze doctoraatsthesis om weefsel te karakteriseren, samen met de bijbehorende aannames die gemaakt worden in het algoritme. Tot slot wordt een overzicht gegeven van de verschillende studies die reeds uitgevoerd zijn in het domein van cardiale SWE. Het tweede deel, '*Shear wave elastography* modellering', beschrijft twee modelleringstechnieken voor SWE, gebruikmakend van de eindige elementen (EE) methode: simulaties in het frequentiedomein en in het tijdsdomein. De EE-simulaties in het frequentiedomein zijn gebruikt om inzichten te krijgen in de golfdispersie-karakteristieken zonder het SWE-experiment expliciet te repliceren. De EE-simulaties in het tijdsdomein, daarentegen, bootsen wel het SWE-experiment na zodat deze kunnen aangewend worden om de complexe *shear wave* fysica en bijbehorende materiaalkarakterisering te bestuderen. Deel III, 'Sensitiviteitsanalyse van biomechanische factoren bij SWE op het hart', gebruikt deze EE-simulaties in het tijdsdomein in combinatie met fysische SWE-experimenten om het effect van linker ventriculaire geometrie en myocardiale anisotropie op SWE te onderzoeken. Het laatste deel, 'Sensitiviteitsanalyse van beeldvormingsfactoren bij SWE op het hart', breidt de voorgestelde EE-modelleringstechniek in het tijdsdomein uit door ook de beeldvorming van de *shear wave* propagatie te modelleren. Dit model kan dan gebruikt worden om het belang van beeldvormingsinstellingen op *shear wave* visualisatie en karakterisering te onderzoeken.

Deel I - *Shear wave elastography* gebaseerd op ultrageluid

Hoofdstuk 1 - Elastografie gebaseerd op ultrageluid

Dit hoofdstuk beschrijft de belangrijke rol van ultrageluid binnen het domein van elastografie, en behandelt de twee meest voorkomende klinische applicaties van elastografie, lever- en borstweefsel. Vervolgens wijdt dit hoofdstuk uit over een specifieke implementatie van SWE, nl. SWE waarbij gebruik wordt gemaakt van een akoestische radiatie kracht (ARF). Deze algemene omschrijving omvat verschillende SWE-methodes die een ARF aanwenden om een transversale golf (of *shear wave*) op te wekken in het onderzochte weefsel, en daarna ultrageluid gebruiken om de voortplanting van de *shear*

wave in beeld te brengen. In deze doctoraatsthesis hebben we gefocust op één specifieke vorm van ARF excitatie, nl. impulsieve ARF excitatie. In het algemeen zijn er drie stappen in ARF-gebaseerde SWE: (i) het genereren van een akoestische radiatie kracht, (ii) het in beeld brengen van de transversale golfpropagatie, en (iii) het verwerken van de radiofrequente signalen tot golfkarakteristieken en materiaal eigenschappen. De implementatie van de verschillende stappen in SWE worden in detail uitgelegd zodat de methodiek van de modellen die de SWE-sequentie numeriek repliceren in de delen '*Shear wave elastography* modellering' en 'Sensitiviteitsanalyse van beeldvormingsfactoren bij SWE op het hart' duidelijk zijn. Het hoofdstuk besluit met een korte noot over de veiligheid van SWE bij toepassingen bij de mens, vermits gebruik van een ARF gerelateerd is aan een verhoogd akoestisch vermogen.

Hoofdstuk 2 - Materiaalkarakterisering in *shear wave elastography*

Het verwerken van de SWE geëxciteerde transversale golfpropagatie tot klinisch relevante parameters is één van de belangrijkste stappen in deze SWE-technologie, waarbij echter veel vereenvoudigingen en aannames worden toegepast. Daarom geeft dit hoofdstuk een overzicht van de materiaalkarakteriseringstechnieken die gebruikt worden in SWE en die relevant zijn voor deze doctoraatsthesis. Dit hoofdstuk is onderverdeeld in vier secties. De eerste sectie beschrijft veel voorkomende materiaalmodellen voor weefsel, welke geclassificeerd kunnen worden in eerste orde en hogere orde materiaal modellen. De meest voorkomende aanname in het domein van SWE is dat weefsel vereenvoudigd kan worden tot een lineair elastisch isotroop materiaal. Dit betekent dat slechts twee parameters nodig zijn om het mechanisch gedrag van weefsel te beschrijven, nl. Lamé's eerste en tweede parameter (beter gekend als de schuifmodulus).

De tweede sectie van dit hoofdstuk beschrijft hoe golfkarakteristieken kunnen berekend worden, vertrekkende van de gemeten of gesimuleerde SWE-data. Vooraleer deze verschillende methodes beschreven worden, wordt eerst het fenomeen van dispersie uitgelegd. Dispersie is het gevolg van intrinsieke materiaal eigenschappen zoals viscositeit of een dunwandige geometrie, wat kan leiden tot een frequentie-afhankelijke golfpropagatie snelheid. Dit betekent dat de fase van de golf met een andere snelheid reist dan het centrum van de golf, resulterend in een verschillende fase- en groepssnelheid. In media waar geen dispersie optreedt, daarentegen, zal de fase- en groepssnelheid dezelfde zijn. De golfkarakteristieken van een SWE-acquisitie kunnen geanalyseerd worden in het tijds- en frequentiedomein (gerelateerd aan respectievelijk de groeps- en fasesnelheid). Om golfkarakteristieken te extraheren in het tijdsdomein kunnen de volgende methodes gebruikt worden: algoritme gebaseerd op correlatie, *time-to-peak* verplaatsingsalgoritme, *random sample consensus (RANSAC)* algoritme en radon som trans-

formatie. Golfkarakteristieken kunnen ook geanalyseerd worden in het frequentiedomein, gebruikmakende van *shear wave spectroscopy* algoritme en de *2D fast Fourier transformation* (2D-FFT).

De derde sectie vormt de link tussen de eerste en tweede sectie, nl. de theoretisch relatie tussen het aangenomen materiaalmodel om weefsel te karakteriseren en de golfkarakteristieken afgeleid van een SWE-acquisitie. Deze relatie wordt in deze sectie afgeleid vertrekkende van de algemene golfvergelijkingen voor verschillende weefsel materiaalmodellen (elastisch/viscoelastisch) en geometrische modellen (bulk medium/plaat) die het onderzocht weefsel voorstellen.

De praktische implementatie van materiaalkarakteriseringstechnieken op basis van groeps- en fasesnelheid wordt besproken in de vierde en laatste sectie van dit hoofdstuk. De sectie sluit af met de state-of-the-art technieken in het karakteriseren van materialen in SWE.

Hoofdstuk 3 - *Shear wave elastography* op het hart

Het doel van dit hoofdstuk is om de specifieke uitdagingen gerelateerd aan *shear wave elastography* op het hart te identificeren en om een kort overzicht te geven van wat reeds in dit gebied onderzocht is geweest. Het hoofdstuk start met een beschrijving van het mechanisch gedrag van het hart, waarbij vooral gefocust wordt op de mechanische karakteristieken die golfpropagatie en de daaropvolgende verwerking in SWE zullen beïnvloeden, nl. locatie, geometrie, randvoorwaarden en materiaal eigenschappen.

De uitdagingen gerelateerd aan *shear wave elastography* op het hart zijn zowel van een technische als mechanische aard. De technische uitdagingen hebben vooral betrekking op de locatie van het hart: het orgaan is immers diep gelegen in het menselijk lichaam en omgeven door ribben, wat leidt tot moeilijke *shear wave* excitatie en detectie. De mechanische uitdagingen, daarentegen, zijn een gevolg van de intrinsieke aard van de gegenereerde *shear wave* in de hartwand. De golfpropagatie in de hartwand wordt immers bemoeilijkt door de geometrie, materiaal eigenschappen, belasting en randvoorwaarden die de golfpropagatie in de hartwand beïnvloeden. Dit betekent dat bestaande algoritmes aangepast moeten worden of dat een toevlucht moet genomen worden tot meer geavanceerde materiaalkarakteriseringstechnieken. In deze doctoraatsthesis focussen we op de uitdagingen van het tweede type, nl. die van een mechanische aard.

In de laatste sectie van dit hoofdstuk wordt een overzicht gegeven van de reeds uitgevoerde studies in het kader van *shear wave elastography* op het hart, en hun resultaten en tekortkomingen.

Deel II - *Shear wave elastography* modellering

Hoofdstuk 4 - Modellering van *shear waves* in het tijdsdomein: Een veelzijdig eindig elementenmodel om golffysica te bestuderen

Dit hoofdstuk beschrijft een simulatie omgeving om SWE numeriek na te bootsen, gebruikmakend van de eindige elementenmethode. Dit model kan ingezet worden om de golffysica geïnduceerd door SWE grondig te bestuderen en de nauwkeurigheid van SWE gebaseerde materiaalkarakteriseringstechnieken te beoordelen. Dit model is vooral interessant voor SWE-toepassingen waar complexe golfpropagatie verwacht wordt ten gevolge van geometrie, materiaal eigenschappen of een combinatie van beiden (wat het geval is voor het hart).

Het SWE-model maakt gebruik van de numerieke modellering van ultrageluid en cardiale mechanica, en bestaat uit twee stappen. Eerst dient de grootte en vorm van de ARF berekend worden, gebruikmakend van de simulatie software voor ultrageluid, *Field II*. Deze software laat toe de akoestische drukken gegenereerd door een werkelijke probe te simuleren. De gesimuleerde drukken worden hierna uitgemiddeld in de tijd over het tijdsinterval van ARF applicatie, zodat een temporeel gemiddelde akoestische intensiteit bekomen wordt. De berekende akoestische intensiteit kan dan worden omgerekend naar een ARF, gebruikmakend van de akoestische eigenschappen van het medium. Ten tweede wordt *shear wave* propagatie gesimuleerd door deze ARF toe te passen op het EE-model als een spatiaal variërende volume kracht gedurende een zeker tijdsinterval.

Het computer model wordt in dit hoofdstuk gepresenteerd met toepassing op een relatief eenvoudige set-up, nl. een homogene plaat gemaakt van gelatine-agar, zodat de numerieke instellingen van het model afgesteld kunnen worden op basis van werkelijke SWE-metingen. De uiteindelijke gesimuleerde axiale snelheid golfvormen en groepssnelheden kwamen goed overeen met de meting. Met dit model hebben we eveneens het effect van geometrie en materiaal eigenschappen onderzocht op de gesimuleerde golfkarakteristieken. Dit toonde aan dat de dikte van de plaat vooral de dispersiekarakteristieken beïnvloedt, terwijl viscoelasticiteit de groepssnelheid lichtjes verhoogt waardoor deze nog beter overeenkwam met de gemeten experimentele waarde. Dit hoofdstuk laat zien hoe EE-modellering kan gehanteerd worden om inzichten te krijgen in SWE-mechanica.

Hoofdstuk 5 - Modellering van *shear waves* in het frequentiedomein: Modale analyse om dispersie-karakteristieken te extraheren

Het tweede hoofdstuk van deel II introduceert kort de principes van *shear wave* modellering in het frequentiedomein. Deze modelleringstechniek wordt

voorgesteld in het kader van de verbetering van materiaalkarakterisering op basis van fasesnelheid. Traditioneel wordt een theoretische dispersierelatie (bvb. voor een plaat-geometrie) gefit aan een gemeten frequentie-afhankelijke golfsnelheid om een materiaal parameter te bekomen. Echter, in dit hoofdstuk onderzoeken we of modale analyse kan gebruikt worden als alternatief voor de theoretische dispersie-relatie. Deze methode is immers flexibeler dan het oplossen van theoretische dispersie vergelijkingen, wat vooral interessant is met het oog op weefsels met complexe geometrieën en/of materiaal modellen. Daarbovenop leidt deze methode de dispersie-karakteristieken af op basis van geometrie, materiaal eigenschappen en randvoorwaarden, en is dus kennis van de ARF niet nodig.

We onderzochten het potentieel van deze EE-techniek voor vereenvoudigde elastische modellen, zoals een plaat in vacuüm, een plaat in water en een cilinder in vacuüm. De accuraatheid van deze methode werd beoordeeld door de resulterende dispersierelaties te vergelijken met de theorie en EE-simulaties in het tijdsdomein (na het toepassen van de 2D-FFT op het gesimuleerde snelheidspatroon). Deze vergelijking toonde aan dat de gesimuleerde dispersie karakteristieken zeer goed correspondeerden met de dispersierelaties afgeleid van de theorie en EE-simulaties in het tijdsdomein. Deze verkennende studie toonde goede initiële resultaten, maar meer onderzoek en validatie van deze methode is nog nodig op complexere geometrieën en materiaal modellen.

Deel III - Sensitiviteitsanalyse van biomechanische factoren bij SWE op het hart

Hoofdstuk 6 - Effect van linker ventriculaire geometrie op golffysica en -karakterisering: Experimenten en simulaties

Dit hoofdstuk behandelt de eerste onderzochte biomechanische factor in de sensitiviteitsanalyse van SWE op het hart, nl. *de geometrie van het hart*. Hiervoor werd de SWE-modelleringstechniek, zoals voorgesteld in hoofdstuk 3, toegepast op een generisch model van het linker ventrikel representatief voor kinderen van 10-15 jaar. Dit computermodel werd gevalideerd met SWE-experimenten op een polyvinylalcohol fantoom met dezelfde geometrie. Een viscoelastisch materiaalmodel was aangenomen voor zowel het computermodel als de experimenten.

Meerdere SWE acquisities zijn uitgevoerd op het linker ventrikel fantoom met het *Aixplorer*-systeem, waarbij de ventriculaire zone en hoek van de probe gevarieerd werd. Deze SWE-data werd vervolgens geanalyseerd met twee materiaalkarakteriserginstechnieken, groeps- en fasesnelheidsanalyse. De robuustheid en accuraatheid van deze methodes werd bestudeerd door

de geschatte stijfheid op basis van SWE te vergelijken met de mechanisch gemeten stijfheid. Hieruit bleek dat stijfheid lichtjes overschat werd door de fasesnelheidsanalyse, terwijl er een duidelijke onderschatting was van stijfheid voor de groepssnelheidsanalyse, en dit voor alle acquisities. De performantie van beide methodes was zo goed als onafhankelijk van de geanalyseerde diepte.

Het computationeel model boodt waardevolle inzichten in de fysieke factoren die golfpropagatie in SWE beïnvloeden. Het gaat o. m. om de randvoorwaarden (water), akoestische interface druk, en viscoelasticiteit. Vooral het modelleren van de akoestische interface druk en het omringende water bleken belangrijke factoren om het experimentele golfpropagatie patroon numeriek correct na te bootsen.

Hoofdstuk 7 - Effect van myocardiale anisotropie op golffysica en -karakterisering: Experimenten

Dit en het volgende hoofdstuk onderzoeken de tweede relevante biomechanische factor in de sensitiviteitsanalyse van SWE op het hart, nl. *de anisotrope materiaal eigenschappen van het hart*. Dit onderdeel van het werk is verdeeld over twee hoofdstukken, vermits SWE-experiment en -model niet toegepast zijn op hetzelfde myocardiale weefsel (literatuur gebaseerd materiaal model in de simulaties). Model en experiment zijn niettegenstaande op een analoge manier opgesteld, en verwerkt: beiden beschouwden een opengeknipt linker ventrikel (volgens het interventrikulaire septum), leidende tot een plaat geometrie.

Voorafgaande SWE-studies hebben reeds aangetoond dat *shear wave* propagatie 3D en anisotroop is ten gevolge van de myocardiale vezel oriëntatie, die varieert doorheen de wanddikte. Het doel van onze SWE experimenten was om de performantie van SWE op het hart nog meer te doorgronden door het gecombineerd effect van myocardial anisotropie en mechanische belasting te bestuderen. Hiervoor werden SWE-metingen uitgevoerd op vier varkensharten, gebruik makende van het *Aixplorer*-systeem. Er werden drie verschillende uniaxiale rek toestanden beschouwd: 5%, 10% en 15% (volgens de circumferentiële richting van het ventrikel). Resultaten van deze SWE-acquisities toonden een duidelijke stijging in groeps- en dominante fasesnelheid terwijl de uniaxiale rek toenam. Deze stijging gebeurde voornamelijk voor probe oriëntaties die overeenkwamen met de vezel richting. Ook veranderde de maximale groeps- en dominante fasesnelheid van plaats terwijl de rek toenam, wat duidt op een alignering van de vezels volgens de trekrichting.

Hoofdstuk 8 - Effect van myocardiale anisotropie op golffysica en -karakterisering: Simulaties

Dit hoofdstuk is het numerieke equivalent van vorig hoofdstuk, waarbij een orthotrope materiaal wet werd geïmplementeerd in het computermodel om de interacties tussen myocardiale vezel oriëntatie en mechanische belasting nog verder te onderzoeken. De orthotrope materiaal wet van Holzapfel-Ogden benadert het myocardium als verschillende laagjes waarin de vezel gelegen is, waarbij de vezeloriëntatie varieert doorheen de dikte. Het model werd vervolgens gedeeltelijk gevalideerd door de gesimuleerde groepssnelheidskarakteristieken te vergelijken met deze uit de experimenten van vorig hoofdstuk, voor de drie verschillende uniaxiale rek toestanden.

De multidisciplinaire ontwikkelde simulatie omgeving laat een meer fundamentele studie toe van de factoren die golffysica en bijbehorende groeps- en fasesnelheid bij SWE op het hart beïnvloeden. Het model heeft het voordeel ten opzichte van *ex vivo* of *in vivo* SWE experimenten om direct toegang te geven tot de werkelijke (gemodelleerde) materiaal eigenschappen van het hart en de werkelijke (gemodelleerde) vezel oriëntatie. Dit voordeel werd benut in twee toepassingen. Ten eerste werd het model gehanteerd om de accuraatheid van twee methodes om de vezeloriëntatie te achterhalen op basis van SWE, te bestuderen. Hiervoor werd het resultaat van deze twee methodes vergeleken met de werkelijke vezeloriëntatie in het model. Hieruit bleek dat beide methodes een goede schatting geven van vezeloriëntatie in de centrale regio van de hartwand, maar minder goed presteerden naar de randen van de hartwand toe. Ten tweede werd het model gebruikt om een parameter studie uit te voeren, waarbij de randvoorwaarden (water), vezel oriëntatie en stijfheid volgens vezel, laag en laag-normaal aangepast werden. Bepaalde hartziektes zoals myocardiale fibrose leiden immers tot verandering van myocardiale stijfheid en een stijging van vezel wanorde. Deze verkennende parameter studie toonde aan dat SWE deze veranderingen in myocardiale materiaaleigenschappen en vezeloriëntatie kan detecteren, maar dat de sensitiviteitsanalyse nog verder uitgebreid moet worden voor meer klinisch relevante settings.

Deel IV - Sensitiviteitsanalyse van beeldvormingsfactoren bij SWE op het hart

Hoofdstuk 9 - Effect van *ultrafast* beeldvorming op golffysica en -karakterisering: Experimenten en simulaties

Voorafgaande studies in computermodellen negeerden het effect van beeldvorming op de gevisualiseerde golfpatronen in SWE en de hiervan afgeleide *shear wave* karakteristieken. Het doel van dit hoofdstuk was dan ook om te

beoordelen hoe accuraat SWE is in het visualiseren van de *shear wave* mechanica. Hierbij hebben we gefocust op SWE waarbij gebruik wordt gemaakt van *ultrafast* beeldvorming, een beeldvormingstechniek met een hoge framesnelheid (> 1000 frames per seconde) en een relatief lage beeldresolutie. De resolutie kan verbeterd worden door gebruik te maken van de *compounding*-techniek. We beschouwen daartoe opnieuw het model van hoofdstuk 6, en breiden we dit uit met een extra modelleerstap die de beeldvorming in rekening brengt. Dit wordt gerealiseerd met de simulatie software voor ultrageluid, *Field II*, waarin weefsel wordt voorgesteld door middel van random puntverstrooiers waarop ultrasone golven weerkaatsen. De puntverstrooiers worden dan verplaatst volgens de gesimuleerde verplaatsingen van het EE-model.

Onze multidisciplinaire simulatie omgeving van het linker ventrikel toonde aan dat *ultrafast* beeldvormen de visualisatie van het golfpatroon verandert in het tijdsdomein (breder golffront en lagere magnitude) en het frequentiedomein (gewijzigde en/of afgenomen signaal frequentie-inhoud). Het toepassen van de *compounding* techniek bij beeldvorming leidde zelfs tot andere gevisualiseerde dispersie patronen in model en experiment. Onafhankelijk van het gebruik van de *compounding* techniek, was stijfheidskarakterisering op basis van groepssnelheid variabel en dus minder betrouwbaar, terwijl stijfheidskarakterisering op basis van fasesnelheid meer robuust was.

Conclusies

De conclusies vatten kort de belangrijkste bevindingen van dit werk samen, en kijken naar de toekomstige rol van multidisciplinaire simulaties in *shear wave elastography* op het hart.

Summary

Introduction

Early detection of cardiac disease is essential to reduce its mortality and morbidity, and the associated healthcare expenses for society. Various cardiac imaging modalities (magnetic resonance imaging, computed tomography and ultrasound) are available for the cardiologist, mainly providing information on tissue morphology and structure with high temporal and/or spatial resolution. However, none of these imaging methods is able to directly measure stresses or intrinsic mechanical properties of the heart, which are potential key diagnostic markers to distinguish between normal and abnormal physiology. To quantify cardiac elasticity and contractility in a clinical setting, the gold standard method is still invasive catheterization with direct measurement of pressure (and volume) in the chamber of interest. This dissertation focuses, however, on the non-invasive assessment of myocardial stiffness using a still relatively novel ultrasound-based technique, shear wave elastography (SWE).

SWE applies an internal mechanical perturbation in the tissue of interest and measures the propagation of this disturbance (i.e. the resulting *shear wave propagation*), of which the speed is directly linked to tissue stiffness. In the past, SWE has been shown to be a successful technique for evaluating stiffness in relatively isotropic viscoelastic bulky media, such as liver and breast tissue. However, to expand its applications to the heart, a nonlinear anisotropic viscoelastic bounded media, an extensive validation of the technique is necessary. Indeed, complex wave propagation phenomena might arise, such as wave guiding, dispersion and directionality, hindering application of the post-processing algorithms as developed for bulk media. This might be especially a problem in children, as their cardiac geometry and wall thickness is smaller than for adults, potentially promoting complex shear wave propagation patterns. We therefore developed *in vitro* and *ex vivo* based computer models mimicking cardiac SWE in children, providing a flexible testing environment that allowed to untangle the different confounding factors complicating shear wave physics.

This dissertation is composed of four main parts. Part I, named 'Ultrasound shear wave elastography', gives a more general introduction about elastography, and explains the various technical implementations and features of the SWE-method under investigation. This part also gives an overview of the different post-processing algorithms used for tissue characterization in this thesis, together with the underlying material assumptions. At last, the results of studies performed to date in the field of cardiac SWE are briefly summarized. The second part, 'Shear wave elastography modeling', presents two modeling techniques for SWE using the finite element method (FEM): time and frequency simulations. The frequency domain simulations are used to obtain insights in the wave dispersion characteristics of the considered tissue setting. The FEM simulations in the time domain, on the other hand, aim to mimic the steps of an actual SWE experiment, and are consequently used to analyze shear wave physics and subsequent material characterization. This FEM simulation technique in the time domain is then applied in the third part, 'Biomechanical factors affecting the performance of cardiac shear wave elastography', in combination with physical SWE experiments, to investigate the effect of left ventricular geometry and myocardial anisotropy on SWE. The last part, 'Ultrafast imaging settings affecting the performance of shear wave elastography', expands the current simulation environment by also modeling the imaging technique in conjunction with the biomechanical shear wave propagation. This allowed to assess the effects of imaging on shear wave visualization and characterization.

Part I - Ultrasound shear wave elastography

Chapter 1 - Ultrasound elastography

This chapter situates ultrasound elastography within the general field of elastography, and describes the two most common clinical applications of elastography techniques, i.e. assessment of liver and breast tissue. Then, it continues explaining the subclass of techniques under investigation in this thesis: acoustic radiation force (ARF) driven shear wave elastography. This is a subset of elastography methods using an ARF source to generate shear waves in tissue and ultrasound to track the resulting shear wave propagation. More specifically, this dissertation focuses on impulsive ARF excitation, of which its general principles are explained in this chapter. This technique implies three steps: (i) generating an acoustic radiation force, (ii) recording shear wave motion, and (iii) processing radio-frequent signals into shear wave characteristics and material properties. These steps are explained into detail, as their actual implementation will be mimicked in the multiphysics computer model described in part II and part IV. At the end of this chapter, a concise note about safety considerations is provided, as ARF generation is related to increased acoustic output.

Chapter 2 - Material characterization in shear wave elastography

Translating the acoustically excited shear wave propagation into clinically relevant material characteristics is one of the most important steps in the SWE technology. As many simplifications and implicit assumptions are made in this step, this chapter provides an overview of the SWE-based material characterization techniques relevant for this dissertation. The chapter is subdivided into four sections. The first section describes the common material assumptions made in SWE, which can be categorized into first order and higher order material models. The most commonly made assumption is the simplification of tissue as a linear elastic isotropic material (first order model), characterized by only two elastic parameters, i.e. Lamé's first and second parameter (better known as the *shear modulus*).

The second section in this chapter describes how shear wave characteristics are derived from SWE-data. Important in this matter is whether or not the medium is dispersive. Dispersion causes the propagation speed of the wave to vary in function of frequency, due to intrinsic properties such as viscosity or geometrical constraints. This means that the phase of the waveform propagates with a different speed than the center of the gravity of the pulse, leading to a different phase and group speed. In non-dispersive media, group and phase speed will be the same. Characteristics of ARF-generated shear waves can be extracted in the time and frequency domain (related to group and phase speed respectively). The following methods to extract shear wave features in the time domain are discussed: correlation-based approach, time-to-peak displacement algorithm, random sample consensus (RANSAC) algorithm and radon sum transformation. Shear wave features can also be derived in the frequency domain using the shear wave spectroscopy algorithm or the 2D fast Fourier transformation (2D-FFT).

The third section links the first and second section, i.e. the theoretical relationship between the assumed tissue properties and the derived shear wave characteristics. The general equations of wave motion are presented for various material (elastic/viscoelastic) and geometrical models (unbounded/bounded) of the tissue of interest.

The practical implementation of SWE-based material characterization techniques is presented in the fourth and last section of this chapter. The principles relevant for estimating tissue properties based on group and phase speed are given, and the section concludes with some state-of-the-art techniques in SWE-based material characterization.

Chapter 3 - Cardiac shear wave elastography

The aim of this chapter is to identify the challenges of cardiac SWE and to provide a short overview of studies performed to date in the field of

cardiac SWE. The chapter starts with explaining the structure and mechanical tissue behavior of the heart, focusing on those aspects that affect shear wave propagation and subsequent processing in SWE, i.e. location, geometry, surrounding and material characteristics.

The technical and mechanical challenges to assess myocardial stiffness using transthoracic SWE are pinpointed. The technical challenges relate to the location of the heart, as it is situated deep inside the human chest and encased by ribs, hampering shear wave excitation and detection. This dissertation, however, primarily focused on the mechanical challenges of cardiac SWE, which relate to the intrinsic nature of the generated shear wave in the cardiac wall. Indeed, cardiac geometry, material characteristics, loading and tissue surrounding will all affect shear wave propagation, complicating the processing and interpretation of shear wave results. Alterations to existing algorithms or more advanced material characterization techniques might be needed.

The last section gives an overview of the state-of-the-art in cardiac SWE, summarizing what can be concluded from the available research and formulating some short-comings.

Part II - Shear wave elastography modeling

Chapter 4 - Shear wave modeling in the time domain: A versatile finite element model framework for the study of shear wave physics

The first chapter of part II introduces the computational methodology that was developed to study shear wave physics in the time domain and to asses the accuracy of subsequent shear wave characterization. This is especially relevant for settings where complex shear wave propagation phenomena are expected (as in the cardiac wall).

The SWE simulation environment encompasses the numerical modeling of ultrasound and cardiac mechanics, and is composed of two steps. First, the magnitude and shape of the ARF is calculated by mimicking ultrasound propagation as emitted by an actual transducer in the ultrasound simulation software *Field II*. The simulated acoustic pressures are then temporally averaged over the ARF push duration, leading to a time-averaged acoustic intensity which can be used to derive the ARF. Second, shear wave propagation is computed by applying this ARF as a spatially varying body force on the finite element model for the ARF push duration.

The initial results of the computer model were obtained in a relatively basic set-up, a homogeneous slab of gelatin-agar material, allowing the validation of the numerical settings using physical SWE measurements. The

simulated tissue velocity waveforms and derived group shear wave propagation speed matched well with the measurements. Further, the impact of geometrical and material parameters on shear wave propagation characteristics was studied. As expected, phantom thickness was a determining factor of dispersion. Adding viscoelasticity to the model increased the estimated wave speed (leading to an even better match with the experimentally determined value). This chapter demonstrates the power of FE-modeling and how it can be used to gain insights into SWE mechanics.

Chapter 5 - Shear wave modeling in the frequency domain: Modal analysis for the extraction of dispersion characteristics

The second chapter of part II briefly introduces the principles of shear wave modeling in the frequency domain. Traditionally, phase speed based material characterization fits a theoretical relationship to the measured frequency-dependent wave velocity to estimate the tissue stiffness. In this chapter, we investigate whether modal analysis can be used as alternative to derive the ground truth shear wave dispersion characteristics. This is especially relevant in tissue settings with complex geometries and/or advanced material models, as there are no theoretical dispersion equations available. Furthermore, this method derives dispersion characteristics solely based on geometry, material characteristics and boundary conditions, and does not require any ARF calculation.

The potential of numerical modal analysis in providing a dispersion relationship was investigated for simplified elastic tissue settings, i.e. a plate in vacuum, a plate in water and a cylinder in vacuum. The accuracy of this method was assessed by comparing the resulting dispersion relationships to the theory and FE-simulations in the time domain (derived after application of 2D-FFT on the simulated axial velocity pattern). We found an excellent agreement between the retrieved dispersion characteristics and the dispersion relationships obtained from theory and FE-simulations in the time domain. This initial feasibility study showed thus promising results for improving SWE-based material characterization, however, further research and validation for more complex tissue settings is still mandatory.

Part III - Biomechanical factors affecting the performance of cardiac shear wave elastography

Chapter 6 - Effect of left ventricular geometry on shear wave physics and characterization: Experiments and simulations

This chapter addressed the impact of *cardiac geometry* on SWE of the heart. The modeling methodology proposed in chapter 4, was used on a generic

model of a left ventricle, representative for a 10-15 year old patient. Besides computer model simulations, actual SWE experiments were performed on a polyvinylalcohol replicate of the same geometry.

The accuracy of different shear modulus estimation techniques, i.e. group and phase velocity analysis, was assessed by performing various SWE acquisitions with the *Aixplorer*-system on different ventricular zones using varying probe orientations. Additionally, the phantom's material stiffness was obtained via mechanical tests. Comparing the results of SWE experiments and mechanical tests, we found a slight stiffness overestimation for phase speed analysis and a clear stiffness underestimation for the group velocity analysis for all acquisitions. Both methods showed a limited variation in stiffness estimates dependent on the selected shear wave path across depth.

The computational model further provided valuable 3D insights in the factors influencing calculated shear wave patterns, especially the surroundings (water), acoustic interface force, and viscoelasticity. Especially, including tissue surroundings and acoustic interface force in the model was found to be crucial to mimic the experimental shear wave pattern and corresponding shear stiffness.

Chapter 7 - Effect of myocardial anisotropy on shear wave physics and characterization: *Ex vivo* experiments

This and the next chapter investigate the influence of *cardiac anisotropy* on SWE of the heart by using experiments and simulations respectively. This work was divided into two chapters, as complete mechanical characterization of the actual porcine cardiac tissue was not possible, leading to the implementation of a literature-based material model in the simulations, though in a similar set-up. Both experiment and model considered a slab of left ventricular tissue, obtained by cutting the ventricle along the interventricular septum and unfolding it into a planar geometry.

Previous studies demonstrated a 3D anisotropic shear wave propagation pattern in cardiac SWE due to the intrinsic myocardial fiber architecture, which varied throughout tissue thickness. The aim of these SWE experiments was to further investigate the performance of cardiac SWE by studying the effect of uniaxial stretching on anisotropic shear wave propagation and characterization. Therefore, we performed SWE-experiments on four *ex vivo* porcine hearts, using the *Aixplorer*-system. Three different uniaxial stretch ratios were considered: 5%, 10% and 15% (along the circumferential direction of the ventricle). Results showed a clear increase in group and dominant phase speed with stretching, especially along the direction of the fiber. Additionally, the maximal group and dominant phase speed value spatially shifted with stretching, indicating an alignment of the fibers to the stretch direction.

Chapter 8 - Effect of myocardial anisotropy on shear wave physics and characterization: *Ex vivo* simulations

The content of this chapter complements chapter 7, and presents a SWE modeling environment incorporating an orthotropic material law to further explore the interactions between myocardial fiber architecture and cardiac loading during SWE. The orthotropic material law of Holzapfel-Ogden considers the myocardium as stacked sheets in which the fibers are located with an orientation that varies over thickness. The realism of the numerical framework was assessed by comparing the resulting group speed features for various uniaxial stretch states to those obtained from the experiments in chapter 7.

The numerical framework has the advantage over *ex vivo* or *in vivo* cardiac experiments to provide direct access to the true cardiac material properties and the ground truth fiber orientation. This advantage was exploited in two applications. First, the accuracy of two previously reported SWE-based fiber extraction methods was assessed by comparing their resulting fiber orientation to the ground truth fiber orientation in the model. Both methods performed equally well for the center of the cardiac slab, whereas they performed considerably less towards the edges of the sample. Second, the model was used to perform a parameter study by including tissue surrounding in the model (water), varying fiber orientation to model a.o. a transverse isotropic material, and fiber/sheet stiffness to mimic the fibrotic myocardium. Results demonstrated that imposed changes in myocardial characteristics and fiber orientation are reflected in altered shear wave features, but further research is necessary for more clinically relevant settings to assess the effective accuracy and sensitivity of SWE to diagnose pathological myocardial stiffening.

Part IV - Ultrafast imaging settings affecting the performance of shear wave elastography

Chapter 9 - Effect of ultrafast imaging on shear wave visualization and characterization: Experiments and simulations

Previous simulation studies addressed in this dissertation ignored the effect of imaging on visualized shear wave patterns and subsequent derived shear wave features. Therefore, the objective of this chapter was to assess the capability of SWE imaging in accurately visualizing the underlying shear wave mechanics. We hereby focused on a SWE technique that uses ultrafast imaging to visualize the shear wave propagation, which is known for its high frame rate (> 1000 frames per second) and relatively low image resolution. The image resolution is then typically improved by applying compounding in combination with ultrafast imaging.

As *in vitro* or *in vivo* SWE experiments do not provide access to the true shear wave mechanics behind the SWE image, we make use of the multiphysics model developed in chapter 4, expanded with an extra modeling step, representing the imaging of the biomechanical shear wave propagation. This is realized in the ultrasound simulation software *Field II*, where tissue is modeled as a collection of random point scatterers on which the ultrasound waves reflect. The scatterers are then displaced according to the simulated displacements of the FE-model.

The results revealed that plane wave imaging alters the visualization of the shear wave pattern in the time (broadened front and negatively biased velocity estimates) and frequency domain (shifted and/or decreased signal frequency content). Furthermore, coherent plane wave compounding (effective frame rate of 2.3 kHz) altered the visual appearance of shear wave dispersion in both the computer model and physical experiments. This mainly affected stiffness characterization based on group speed, whereas phase velocity analysis provided a more accurate and robust stiffness estimate independent of the use of compounding.

Conclusion

Here, we recapitulate the major findings and achievements of this dissertation, and glance beyond the horizon for (multiphysics modeling in) cardiac shear wave elastography.

Introduction

Clinical rationale

Pediatric heart disease can manifest in several ways, ranging from a congenital heart defect to a cardiac condition developed during childhood. Congenital heart diseases can be simple in nature, such as a ventricular septal defect (VSD), or quite complex, such as tetralogy of Fallot (ToF), comprising three other defects next to a VSD - pulmonary valve stenosis, an overriding aorta and right ventricular hypertrophy. On the other hand, one of the most common acquired heart diseases in children is Kawasaki disease - a systemic vasculitis affecting the coronary arteries [1]. The etiology of cardiac disease in children is thus very different than that in adults, where the most common type of heart disease is coronary artery disease [2]–[4]. Furthermore, the pathophysiological process in children is complicated by morphology, growth and loading conditions [5]. Due to these difficulties, limited literature is available about the exact pathophysiology and management of pediatric heart diseases, whereas heart failure in adults has been the subject of extensive research and generation of evidence-based guidelines [4], [6]. For this project, we are particularly interested in a sub-group of pediatric heart patients, i.e. children suffering from congenital or acquired aortic valve dysfunction and pulmonary regurgitation after repaired ToF, disorders implicating complex ventricular remodeling and development of myocardial fibrosis due to valve insufficiency.

To gain a better understanding of the complex disease processes in children due to malfunctioning valves and to guide treatment and patient follow-up, reliable techniques are required to assess cardiac function in systole (contraction) and diastole (relaxation). It is particularly important to evaluate diastolic function, as impaired diastolic function often precedes systolic dysfunction and is consequently believed to be a more sensitive indicator of cardiovascular pathology [7]. For adults, diastolic function can be assessed by invasively registering pressure-volume loops (gold standard technique) [8] or by non-invasively evaluating several functional parameters such as mitral inflow velocity via echocardiography [9] or magnetic resonance imaging (MRI). However, these techniques cannot simply be extrapolated to

children as the first technique requests cardiac catheterization which is not routinely done in children (nor in adults) and the second uses adult-specific guidelines that are not applicable to children because of the too large range of normal values in children [10]. Moreover, these indices do not directly depict the primary mechanism of diastolic function, i.e. the relaxation of the heart muscle tissue leading to a sufficient reduction of myocardial stiffness [11]. Therefore, there is a need for a technique that is able to assess diastolic function in children in order to (i) gain fundamental understanding of the disease process, which might be significantly different than in adults, but also to (ii) assist in early detection of myocardial damage and in optimal timing of valve replacement surgeries to preserve ventricular function in children.

Shear wave elastography

For this purpose, the potential of the ultrasound-based technique, *Shear Wave Elastography (SWE)*, in evaluating myocardial stiffness and thus cardiac function was explored. SWE has shown promising results in quantitatively measuring tissue stiffness, and has the same advantages as other ultrasound-based methods, i.e. it is radiation-free, non-invasive, relatively low cost and widely available. This technique generates a mechanical vibration inside the tissue by applying a focused ultrasonic high-energy beam with a conventional ultrasound transducer. Then, the propagation of the internal mechanical perturbation, or the so-called *shear wave propagation*, is imaged. The propagation characteristics of these shear waves (e.g. their propagation speed c_T) can be directly linked to the mechanical properties of the medium (e.g. density ρ, shear modulus μ), in which the most commonly used relationship in the field of SWE is the following:

$$\mu = \rho c_T^2 \tag{1}$$

One has, however, to be careful with the inherent assumptions that come with this equation, i.e. conditions of homogeneity, isotropy, linearity, elasticity and bulk medium.

SWE has been successfully applied to various organs, amongst which breast tissue for diagnosing breast cancer [12] and liver tissue for staging liver fibrosis [13]. To extend the range of SWE-applications to the heart, adjustments are needed in:

1. *Technical settings to generate and detect shear waves*, as the heart is a fast-moving and deeply located organ, encased by ribs; whereas breast or liver tissue are relatively easy accessible organs to generate and image

shear waves. Furthermore, these challenges are different for children than for adults as the imaging depth is shallower and the chest wall is thinner.

2. *Mechanical settings for post-processing the acquired shear wave data*, as the shear wave physics in the thin, anisotropic cardiac wall will be different than that for large, relatively homogeneous, isotropic tissues such as the liver and the breast. Additionally, the thinner cardiac wall in children compared to adults might pose extra challenges.

This PhD project focuses on the *mechanical* challenges related to cardiac SWE. Commercial SWE systems have mainly focused on large or bulk media, and thus, extensive validation of the SWE-technique in the myocardial setting is necessary. Indeed, SWE-excited shear waves in the myocardium will get reflected by the cardiac boundaries and are thus confined to propagate within the cardiac wall, also known as the *guided wave effects*. Furthermore, the myocardium has anisotropic material properties, possibly creating an *orientation-dependent* shear wave propagation and characterization. Hence, the combination of thin geometry and layered anisotropic material properties of the myocardium induces complex 3D guided wave propagation, which hinders application of the 2D imaging set-ups and signal processing algorithms developed for bulk tissues in the pediatric cardiac setting. Furthermore, the relationship between wave propagation speed and tissue stiffness as depicted in equation (1) is no longer valid, even though most current commercially available SWE systems implement this equation [14].

Research objectives

The objective of this PhD project frames within the broader research for investigating the feasibility of SWE in measuring myocardial stiffness in children. As previous *in vivo* and *ex vivo* animal studies of cardiac SWE [15], [16] have demonstrated the complexity in shear wave propagation patterns and subsequent material characterization that rises with application of SWE to the cardiac wall, it is necessary to first gain a fundamental understanding of the ongoing shear wave physics in the cardiac setting. Therefore, we implemented and optimized a computational testing environment replicating actual SWE that allows to unfold the intricate relationship between wave propagation characteristics and cardiac mechanical properties, in combination with *in vitro* and *ex vivo* studies. More specifically, the objective of this dissertation can be subdivided into three different sub-goals:

Goal 1 - Implementing, optimizing and validating a multiphysics simulation environment representing virtual SWE, by integrating the domain of numerical modeling of ultrasonic imaging together with that of structural mechanics.

Goal 2 - Investigating the biomechanical factors affecting shear wave propagation and characterization through simulations and experiments: left ventricular geometry and anisotropic material properties.

Goal 3 - Investigating the effect of ultrasound imaging on shear wave visualization and subsequent characterization through simulations and experiments.

To accomplish above-mentioned goals, this PhD project makes use of the numerical expertise available at the bioMMeda-lab, where *in silico* tools for the development and validation of ultrasound applications have been established in the past, e.g. for blood flow imaging in [17]. This project expands these developed numerical tools at bioMMeda to the field of shear wave elastography. Additionally, a collaboration was set-up with the Langevin Institute at the Ecole Supérieure de Physique et de Chimie Industrielles (EPSCI) in Paris (dr. ir. Mathieu Pernot), in order to get access to the SWE technology, together with its image and signal processing algorithms. This collaboration allowed us to perform experiments for validation of our numerical models.

Structure

This dissertation is divided into four major parts. The first part, *Ultrasound shear wave elastography*, gives some practical background on the shear wave elastography technique. This starts with a broad overview of all elastography techniques available, and then focuses on the elastography technique under study in this dissertation. Its technical implementation and the commonly used material characterization algorithms are briefly described and explained. Subsequently, this part ends with describing the challenges related to cardiac shear wave elastography, and summarizing the latest studies and developments in this field.

The second part, *Shear wave elastography modeling*, focuses on the available shear wave modeling techniques by using the finite element method (FEM). More specifically, this part describes extensively the implementation of shear wave modeling in the time domain and applies this methodology to a simple plate geometry, concurrent with actual SWE-experiments on a

gelatin-agar replicate. These experiments allowed validation of this modeling technique for bounded media, representing an extension of currently reported modeling applications. Next to FEM modeling in the time domain, this part also shortly introduces shear wave modeling in the frequency domain using FEM and provides proof of principle of this method for simple geometries and material models.

Biomechanical factors affecting the performance of shear wave elastography (part III) analyzes the complex shear wave physics of SWE in the cardiac setting more into depth, by separately analyzing the effect of cardiac geometry (together with tissue surrounding) and anisotropic material properties on SWE. Both biomechanical factors are investigated using a combination of experiments with the numerical methodology in the time domain, as proposed in the second part.

Part IV, *Ultrafast imaging settings affecting the performance of shear wave elastography*, extends the modeling methodology of part II by simulating the ultrafast imaging sequence in combination with the biomechanics of the shear wave propagation (using FEM). This allowed to study the effect of ultrafast imaging settings on shear wave visualization and characterization for SWE in general.

This dissertation concludes with a summary of the major findings of previous parts, and looks into the future perspectives of cardiac SWE.

List of publications

First author proceedings and peer-reviewed papers

- A. Caenen, M. Pernot, M. Peirlinck, L. Mertens, A. Swillens and P. Segers, 'An in silico framework to analyze the anisotropic shear wave mechanics in cardiac shear wave elastography', accepted for publication in the journal *Physics in Medicine & Biology*.

- A. Caenen, A. Thabit, M. Pernot, D. A. Shcherbakova, L. Mertens, A. Swillens and P. Segers, 'The effect of stretching on transmural shear wave anisotropy in cardiac shear wave elastography', in *IEEE International Ultrasonics Symposium (IUS) 2017*, IEEE TUFFC.

- A. Caenen, M. Pernot, I. Kinn Ekroll, D. Shcherbakova, L. Mertens, A. Swillens and P. Segers, 'Effect of ultrafast imaging on shear wave visualization and characterization: An experimental and computational study in a pediatric ventricular model', *Applied Sciences*, vol. 7, no. 8, 2017.

- A. Caenen, M. Pernot, D. A. Shcherbakova, L. Mertens, M. Kersemans, P. Segers and A. Swillens, 'Investigating shear wave physics in a generic pediatric left ventricular model via in vitro experiments and finite element simulations', *IEEE Trans Ultrason Ferroelectr Freq Control*, vol. 64, no. 2, pp. 349–361, 2017.
- A. Caenen, P. Segers and A. Swillens, 'Finite element simulations to support the measurement and analysis of shear wave dispersion', in *IEEE International Ultrasonics Symposium (IUS) 2016*, IEEE, pp. 1–4.
- A. Caenen, M. Pernot, C. Papadacci, D. Shcherbakova, L. Mertens, P. Segers and A. Swillens, 'Myocardial stiffness assessment in pediatric cardiology using shear wave imaging', in *IEEE International Ultrasonics Symposium (IUS) 2015*, IEEE, pp. 1–4.
- A. Caenen, D. Shcherbakova, B. Verhegghe, C. Papadacci, M. Pernot, P. Segers and A. Swillens, 'A versatile and experimentally validated finite element model to assess the accuracy of shear wave elastography in a bounded viscoelastic medium', *IEEE Trans Ultrason Ferroelectr Freq Control*, vol. 62, no. 3, pp. 439–450, 2015.

Co-author proceedings and peer-reviewed papers

- D. A. Shcherbakova, N. Debusschere, A. Caenen, F. Iannaccone, M. Pernot, A. Swillens and P. Segers, 'A finite element model to study the effect of tissue anisotropy on ex vivo arterial shear wave elastography measurements', *Phys Med Biol*, vol. 62, no. 13, pp. 5245–5275, 2017.
- D. Shcherbakova, A. Caenen, A. Swillens, P. Segers, S. Chatelin, C. Papadacci and M. Pernot, 'Experimental study on the effect of the cylindrical vessel geometry on arterial shear wave elastography', in *IEEE International Ultrasonics Symposium (IUS) 2015*, IEEE, pp. 1–4.
- D. A. Shcherbakova, C. Papadacci, A. Swillens, A. Caenen, S. De Bock, V. Saey, K. Chiers, M. Tanter, S. E. Greenwald, M. Pernot and P. Segers, 'Supersonic shear wave imaging to assess arterial nonlinear behavior and anisotropy: Proof of principle via ex vivo testing of the horse aorta', *Advances in Mechanical Engineering*, vol. 6, pp. 1–12, 2014.
- D. Shcherbakova, A. Swillens, A. Caenen, S. De Bock, P. Segers, C. Papadacci, M. Tanter, M. Pernot, V. Saey and K. Chiers, 'Supersonic shear wave imaging to assess arterial anisotropy: Ex-vivo testing of the horse aorta', in *IEEE International Ultrasonics Symposium (IUS) 2013*, IEEE, pp. 1545–1548.

I

Ultrasound shear wave elastography

Chapters

Chapter 1

Ultrasound elastography

This chapter first provides a general introduction into elastography, with a concise overview of available elastography techniques and how these can be classified. Elastography is applied in combination with three (medical) imaging methods: ultrasound, magnetic resonance imaging and optical techniques. The first section concludes with applications of elastography that are currently used in the clinic. The second section discusses different implementations of acoustic radiation force driven shear wave elastography, a type of shear wave elastography based on ultrasound. This section is followed by an introduction into the general principles of the impulsive version of this type of elastography, which is the technique under investigation in this thesis. Lastly, a concise note about safety considerations is provided.

1.1 Elastography: a short overview

In biophysics, elastography is the general field of elasticity imaging, which groups all techniques visualizing tissue elasticity in order to improve diagnosis, as changes in tissue stiffness are known to be correlated with pathological changes [28]. It refers to the old technique of palpation, where clinicians qualitatively sense tissue stiffness from differences in required hand pressure to displace any type of tissue in a similar matter. This principle is the foundation of elastography: the imaging method employs a mechanical excitation to displace the tissue and then subsequently monitors the resulting movement in the tissue. The first known elastography technique was ultrasound-based

and developed in the late 1980s to early 1990s to provide additional information next to conventional ultrasound imaging [29]. One of its earliest clinical applications was the prostate gland [30]. The success of this technique led to the development of elastography in other imaging fields, such as magnetic resonance imaging and optical coherence tomography. We will give a short overview of existing elastography techniques, but for a more complete review of elastography techniques, the reader is referred to Gao et al [31] and Ophir et al [28].

This section first describes the classification of elastography techniques in general. Then, commercially available elastography systems are mentioned together with their clinically validated applications.

1.1.1 Classification of elastography

All elastography techniques essentially employ three steps: (i) exciting the tissue of interest, (ii) measuring the induced movement inside the tissue and (iii) deriving the mechanical parameters based on the measured tissue response [31]–[35]. Elastography methods can be categorized based on the implementation of each of these steps [36], of which a concise overview is given in table 1.1. These three key features of elastography will be shortly described below.

Table 1.1: Classification of elastography.

Elastography		
Type of excitation	*Imaging method*	*Mechanical parameter estimation*
- Temporal characteristics	- Ultrasound	- Qualitative
- Quasi-static	- Magnetic resonance imaging	- Quantitative
- Dynamic	- Optical techniques	
- Spatial characteristics		
- Internal		
- External		

1.1.1.1 Type of excitation

The applied mechanical stress can be characterized based on its temporal and spatial characteristics [35], [36]. This first feature subdivides the elasticity imaging techniques into two main categories: *(quasi-)static* and *dynamic* elastography. Static methods apply a constant stress to compress the tissue. An excitation method can be considered quasi-static when the generated displacements are small and slow compared to the measurement time (e.g. only one observation before and after application of the stimulus) [35]. On the contrary, dynamic elastography methods use a time-varying force to excite the tissue of interest. This can be either a short transient mechanical force (also called *transient* elastography) or an oscillatory force at a fixed frequency (also called *harmonic* elastography) [34].

The type of excitation may also be classified based on its external or internal nature. External approaches employ a stress, or a compression force, on the skin to deform the tissue beneath. This is often realized by simple mechanical means, such as pressing and holding a plate/ultrasound transducer on the skin (static elastography) or vibrating the skin using a vibratory device (dynamic elastography). On the other hand, internal excitation methods apply the excitation internally and thus directly on the tissue of interest. These internal excitations can be further subdivided into two groups: natural motion and forced motion. Natural internal sources of motion are for example respiration or cardiac pulsations (also called *organic* elastography) [37]–[40]. A forced internal motion is possible by exciting the tissue of interest through a remote palpation (also called *remote* or *acoustic radiation force* elastography) [41]. This type of excitation method uses a focused high-intensity ultrasound beam generated by a conventional ultrasound transducer, to produce an acoustic radiation force (ARF) that locally deforms the tissue [42], [43]. The major advantage of the internal excitation methods compared to the external excitation methods is that the excitation energy is directly deposited in the tissue of interest. Indeed, external excitation methods are challenged in their ability to couple enough energy through the skin and subcutaneous fat to generate adequate tissue displacements within organs, especially in obese subjects [44].

A classification based on the above described categories can be seen in table 1.2 for some relevant elastography techniques. Notice that all natural internal stress stimuli such as cardiac contractions and pulsatile blood flow are categorized under quasi-static excitations [35], [45], [46].

Table 1.2: Elastography classification based on type of excitation (this table does not represent a complete overview of all available elastography techniques).

	(Quasi-)static	**Dynamic**	
		Impulsive	*Harmonic*
Internal			
Natural	Intravascular Ultrasound based Strain Imaging [47], Cardiac Strain Imaging [48]		
Forced	Kinetic Acoustic Vitreoretinal Examination (KAVE) [51], Thermal Elastic Optical Doppler Tomography [53]	Acoustic Radiation Force Impulse Imaging (ARFI) [49], Shear Wave Elasticity Imaging (SWEI) [43], Supersonic Shear Imaging (SSI) [54], Acoustomotive Optical Coherence Elastography (AM-OCE) [55]	Harmonic Motion Imaging (HMI) [50], Shear wave Dispersion Ultrasound Vibrometry (SDUV) [52]
External	Strain Elastography [32]	Vibration-controlled Transient Elastography (VCTE - such as Fibroscan) [57]	Dynamic Magnetic Resonance Elastography (MRE) [56], Sonoelasticity imaging [58]

1.1.1.2 Imaging modality

The second step in elasticity imaging is to measure the tissue response, in which the main measurement methods are ultrasonography, magnetic resonance imaging (MRI) and optical techniques (see table 1.1). Ultrasound (US) has been widely used for elasticity imaging and is generally more accessible and less expensive than the other imaging technologies. Tissue motion can be derived from the recorded radiofrequency (RF) signals by various methods, in which the most commonly used approaches are based on time or phase shift estimation between the pre- and post-compression RF signals [35] (see section 1.2.2.4 for more information). The primary limitations of the ultrasound-based method are the requirement of an acoustic window to get the US signal into the tissue, 1D assessment of tissue displacement (only along the direction of the US beam), and limited measurement depth because of attenuation and scattering of the US beam [59].

Next to ultrasonography, MRI is the second main method used for measuring tissue motion in elasticity imaging. While a number of (quasi-)static and dynamic Magnetic Resonance Elastography (MRE) techniques have been developed, the most common form of MRE is dynamic MRE, i.e. MRI in combination with an external vibrator. The basic principle underlying this technique is to encode information about tissue motion into the phase of the MRI images, a method also called phase-contrast MRI. This is done by applying a motion-encoding gradient at the same frequency as the harmonic excitation signal, leading to a phase contribution in the MR image which is directly proportional to the displacement of the vibrating tissue (see figure 1.1). Typically two such images are collected with opposite polarity of the motion-encoding gradients and the difference of these two images depicts the phase-difference image, eliminating all non-motion-related phase artifacts of the individual phase images. By switching the motion-encoding gradient on at different time points of the motion signal (i.e. changing time offset θ in figure 1.1), the propagating waves inside the tissue can be measured [36], [57], [60].

Compared to ultrasound, MRE has the advantage that it is not restricted by the presence of gas or bone, and it is sensitive to motion in 3D. However, ultrasonic estimation of soft tissue displacement is generally more accurate and precise, relatively fast, more easily accessible and less costly than MRE [61].

Optical methods have also emerged to detect the tissue response after excitation, but are less developed than US and MRI techniques. These methods have a superior spatial resolution, sensitivity and contrast compared to US and MRI (see table 1.3), allowing to image mechanical properties at a different spatial scale than US/MRI, i.e. the intermediate level in between cell and

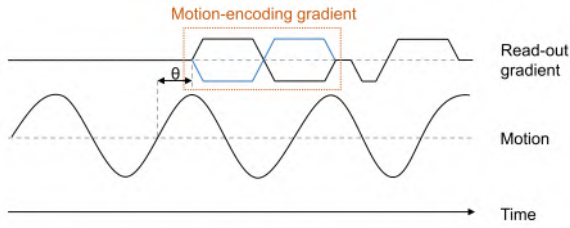

Figure 1.1: Example of Motion-Encoding gradients applied in Magnetic Resonance Elastography (MRE). Black and blue lines indicate the motion-encoding gradient with opposed polarities used in subsequent MRE acquisitions (adapted from [35]).

organ level. This provides new information about the physiological state of particular tissue pathologies, contributing to improvement of understanding, diagnosis and treatment of disease. Several optical elastography methods have emerged throughout the years of which two techniques, optical coherence tomography (OCT) and Brillouin microscopy, have recently shown particular promise for medical applications [62]. OCT elastography, also termed optical coherence elastography (OCE), and Brillouin microscopy measure different frequency ranges of mechanical properties: <10 Hz for static OCE, 50-500 Hz for harmonic OCE, >1 kHz for transient OCE and >1 GHz for Brillouin microscopy. The OCE methods for measuring tissue displacement are similar to speckle-tracking and phase shift imaging techniques in US elastography, but use light waves instead of ultrasound to measure the tissue motion [63]. On the other hand, the Brillouin microcopy method uses the physical phenomenon of *Brillouin scattering*, i.e. the inelastic scattering of light by GHz-frequency acoustic waves (phonons) intrinsic to a material, to describe the tissue response. This microscope has a high-numerical-aperture imaging lens, leading to very high spatial resolution as shown in table 1.3 and thus making it suitable for applications in cell mechanics and ophthalmology [62]. The limitations of optical methods are similar as the ultrasonic techniques, i.e. measurements are only possible through an appropriate optical window, recorded tissue displacements are limited to 1D, and significant depth restrictions because of high optical scattering and attenuation properties of tissues [59].

1.1.1.3 Mechanical parameter estimation

The third step in elastography is to estimate the mechanical tissue properties from the acquired data (see table 1.1). The result can be a single value or an image, also called an *elastogram*, depending on the applied method. There are different manners to display various mechanical attributes of the tissues of interest, which can be classified into two distinct groups [49], [64]. The first group of methods depicts mechanical attributes based on a direct

Table 1.3: Performance metrics of Magnetic Resonance Elastography, Ultrasound Elastography and Optical Elastography techniques (adapted from [35]).

	Resolution	**Imaging Depth**	**Signal-to-noise ratio**	**Scan time**
Magnetic resonance elastography	1-3 mm	Whole body	5-14 dB	2-20 min (3D)
Ultrasound elastography	0.1-0.5 mm	4-5 cm	8-12 dB	4-30 µs
Optical coherence elastography	15-100 µm	0.5-3.0 mm	10-25 dB	20-100 µs
Brillouin microscopy	0.5-5 µm	0.1-3.0 mm	10-30 dB	2-5 min

estimation of parameter(s) from experimental observations, which provides qualitative information about tissue stiffness. These imaged parameters can be longitudinal or shear strains, estimated from pre- and post-compression data. An example is shown in the left panel of figure 1.2. Here, tissue strain is a surrogate parameter for actual tissue stiffness: low strains correspond to high stiffness and high strains to low stiffness.

For the second group, the imaged mechanical attributes are based on an indirect estimation of parameter(s) obtained through reconstructions relating the directly estimated experimental data to the underlying tissue properties. This group of elasticity methods allows to display quantitative information about mechanical tissue behavior such as the shear modulus or Young's modulus (see right panel of figure 1.2 for an example elasticity map). Earlier approaches of these methods utilized inversion of the wave equilibrium equation, i.e. the Helmholtz equation, to estimate the tissue elastic modulus based on the obtained strain/displacement image by assuming a homogeneous, linear, isotropic, elastic material law for soft tissue [35]. However, this inverse modeling approach was challenged by the amplified noise due to differentiation of the measured displacement data for the Helmholtz equation. Therefore, nowadays, most research groups have moved to utilization of *time-of-flight* (TOF) wave speed estimation methods to determine the wave speed of the internally excited waves, which is representative for tissue stiffness. Especially shear waves are interesting to study as their shear wave speed depends on the shear modulus, of which its range of variation is several orders of magnitude larger than that of the bulk modulus (determinant of longitudinal wave speed), and thus allowing easier differentiation between the imaged types of tissue [43]. This will be further explained in section 1.2 of this chapter.

Quantitative elasticity methods require assumptions about the tissue model and boundary conditions in order to calculate tissue elasticity, whereas qualitative methods use no assumptions but only direct measurements. In general, soft tissues are mechanically anisotropic, non-homogeneous, viscoelastic and non-linear. Therefore, it is important to define the strain or stress ranges of interest and the type of imaged tissue to verify the validity

of the isotropic, homogeneous and elastic tissue approximation. On the other hand, several studies [65]–[67] have shown that these other mechanical characteristics could provide additional diagnostic value to an elastogram.

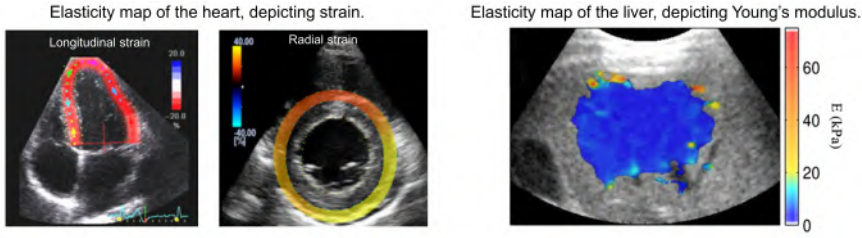

Figure 1.2: Left panel: example of a qualitative elasticity image (adapted from [68]). Right panel: example of a quantitative elasticity map (adapted from [13]).

1.1.2 Clinical applications

Knowledge about the biomechanical tissue properties provides additional and clinically relevant information to support diagnosis for clinicians in many pathologies. However, several steps are required to take this new imaging method from bench to bedside, including system development, feasibility testing, primary limited trials and multi-center trials before commercialization and integration in the daily clinical routine [69]. Currently, only MRE and a few methods from US elastography are commercially available. Most other elastography modalities are still in pilot studies or clinical trials, but it is to be expected that additional commercial products will become available in the near future [69].

Clinically available MRE uses a commercial MRI scanner (usage of GE and Philips 1.5T MRI scanners has been reported for MRE [70]), in combination with an external actuator inducing harmonic shear waves (external dynamic excitation method; table 1.2). For US elastography, several vendors have implemented an elastography function in their ultrasound machine providing additional diagnostic information about tissue stiffness for the clinician. These ultrasonic technologies can be classified based on their measured physical quantity as shown in table 1.4, i.e. strain imaging (qualitative) and shear wave imaging (quantitative). Strain imaging can be further subdivided into Strain Elastography (SE) and Acoustic Radiation Force Impulse (ARFI) strain imaging, where the difference is in the manner of excitation: SE uses manual compression with the US probe or internal physiologic motion, whereas ARFI generates an ARF with a conventional US transducer to displace the tissue. For shear wave imaging, three methods are commercially available (see table 1.4): (i) Point Shear Wave Elastography (pSWE), (ii) 2D Shear Wave Elastography (2D-SWE) and (iii) 1D Transient Elastography (TE).

The main difference between pSWE/2D-SWE and TE is again the manner of excitation: both pSWE and SWE utilize an ARF to excite tissue, while TE uses a mechanical vibrating device which is integrated in the Fibroscan™ probe together with the US transducer. pSWE and 2D-SWE differ in their manner of stiffness measurement: pSWE provides an average stiffness value from a localized region of tissue and 2D-SWE generates a 2D image of stiffness over a larger region of tissue [71].

The main applications of current commercially available elastography techniques are abdominal (more specifically liver) and breast imaging. There is encouraging data that elastography can be applied to many other organs (thyroid [72], prostate [73], heart [68], etc.), but further research with unbiased large scale studies is still required. Also, technique standardization to allow comparison of values between studies and development of new solutions for current technical limitations and biologic/physiologic confounders need to be pursued [71]. The elastography applications for liver and breast tissue will be described concisely below.

Table 1.4: Overview of clinically available US elastography techniques from different vendors (based on [74], [75]).

Type	Subtype	Elastography function	Vendor
Strain imaging	Strain Elastography	Elaxto™	Esaote
		Real-time tissue elastography™	Hitachi, Aloka
		Elastography	GE, Philips, Toshiba, Zonare
		Elastoscan™	Samsung, BK ultrasound, Carestream
		eSieTouch™	Siemens
	Acoustic Radiation Force Impulse (ARFI) strain imaging	Virtual Touch™ (VTI/ARFI)	Siemens
Shear Wave Imaging	Point Shear Wave Elastography (pSWE/ARFI quantificaiton)	Virtual Touch™ Quantification (VTQ/ARFI)	Siemens
		ElastPQ™	Philips
		QelaXto™	Esaote
		S-Shearwave	Samsung
	2D Shear Wave Elastography (SWE)	Shear Wave Elastography	Supersonic Imagine, Philips
		Virtual Touch™ Quantification (VTQ/ARFI)	Toshiba, GE, Siemens
	1D Transient Elastograpy (TE)	Fibroscan™	Echosens

1.1.2.1 Liver

The most validated application of elastography is the evaluation of diffuse liver disease. It allows non-invasive detection and staging of liver fibrosis as well as monitoring liver treatment response in patients with chronic liver disease.

The progression of liver disease is scored between F0 and F4 according to the METAVIR histopathologic grading system, where F0 corresponds to normal liver and F4 to liver cirrhosis [71]. It provides a non-invasive and rapid alternative for the gold standard method, i.e. liver biopsy, which is limited in its accuracy, is invasive and relatively expensive [76]. Several elastography techniques have been developed for assessing liver stiffness, of which the most commonly used and validated are: TE, MRE, strain elastography, pSWE and 2D-SWE [46], [71], [76].

For the ultrasound elastography techniques, the level of evidence that the technique improves diagnosis is high for TE, moderate for pSWE and still low for 2D-SWE and strain elastography. Some methods have been used for more than ten years while others have been introduced more recently, resulting in a large variability in the number of published manuscripts on the different techniques [74]. Additionally, results of SWE-based and strain imaging techniques vary a lot between manufacturers. Currently, efforts are done to standardize these measurements across different imaging systems to obtain a biomarker for staging liver fibrosis (e.g. the Radiological Society of North America (RSNA) Quantitative Imaging and Biomarkers Alliance (QIBA) Ultrasound Shear Wave Speed committee). Recent guidelines of the World Federation for Ultrasound in Medicine and Biology (WFUMB) only recommends its use in distinguishing significant ($F \geq 2$) or advanced fibrosis ($F \geq 3$) from non-significant fibrosis ($F \leq 1$) due to limitations in differentiating between individual fibrosis stages. Similar guidelines are given by the Society of Radiologists in Ultrasound Consensus Conference Statement [71].

MRE has proven to be superior to ultrasound elastography in the early stages of suspected liver fibrosis and in patients who have medical conditions that preclude the use of sonographic elastography (e.g. obesity) [77]. Additionally, it images a larger proportion of the liver, hereby reducing sampling variability for longitudinal monitoring. However, MRE requires more post-processing and offline analysis and its availability is often limited outside the academic centers [46].

1.1.2.2 Breast

Another common application of elastography are breast examinations to distinguish cancerous lesions from benign ones. Elastography has been introduced as complimentary modality for improving lesion characterization next to mammography and ultrasonography, as both modalities had their limitations: mammography often yields false-negative results in dense breasts, whereas US has a poor specificity in characterization [78]. Both methods utilize the Breast Imaging Reporting and Data System (BIRADS) that sorts

the results from images into categories numbered 0 to 6, from benign to malignant (with 0 corresponding to incomplete analysis). Various types of elastography have been studied to contribute to the improvement of breast cancer diagnosis, of which strain imaging and shear wave elastography are the most extensively studied [71], [75].

Studies have shown a comparable diagnostic performance of US elastography to that of conventional US. A combination of US elastography and conventional US had the best sensitivity and accuracy and the lowest false-negative rate [76]. Therefore, qualitative US elasticity measurements (soft, intermediate, or hard) of breast lesions have been incorporated in the second edition of the BI-RADS US lexicon [71]. However, there is still much work to be done to further support the current clinical applications of breast US elastography, such as: (i) comparative study between strain imaging and shear wave elastography, (ii) determination of appropriate cut-off values of strain or shear wave velocity in different US elastography systems, and (iii) assessment of diagnostic performance of the technique in lesions of different sizes and at different breast tissue depths.

1.2 Acoustic radiation force driven shear wave elastography

This PhD thesis focuses on ARF driven SWE, which is a subset of elastography methods using an ARF source to induce shear wave propagation in tissue and ultrasound to track the generated shear motion. It provides a quantitative indication of tissue stiffness based on shear wave speed. An ARF-based excitation can be generated by any conventional US transducer, having the advantage of easy integration into daily clinical practice as no additional or specific equipment is needed. This section first gives a short overview of different ARF driven SWE-techniques, then explains the general principles of the subtype of ARF driven SWE under investigation in this project, followed by safety considerations.

1.2.1 Implementations of acoustic radiation force driven shear wave elastography

ARF based SWE was originally introduced by Sarvazyan et al. [43] in 1998, termed as *Shear Wave Elasticity Imaging (SWEI)*. Since then, it has been implemented in several laboratories in different forms. We will describe some variants of SWEI below, as shown in figure 1.3, based on the implementation of shear wave excitation and tracking. Shear waves can be generated by a harmonic or impulsive ARF (< 1 ms) [49]. For impulsive ARF excitation, there are four different implementations depicted in figure 1.3 [79]:

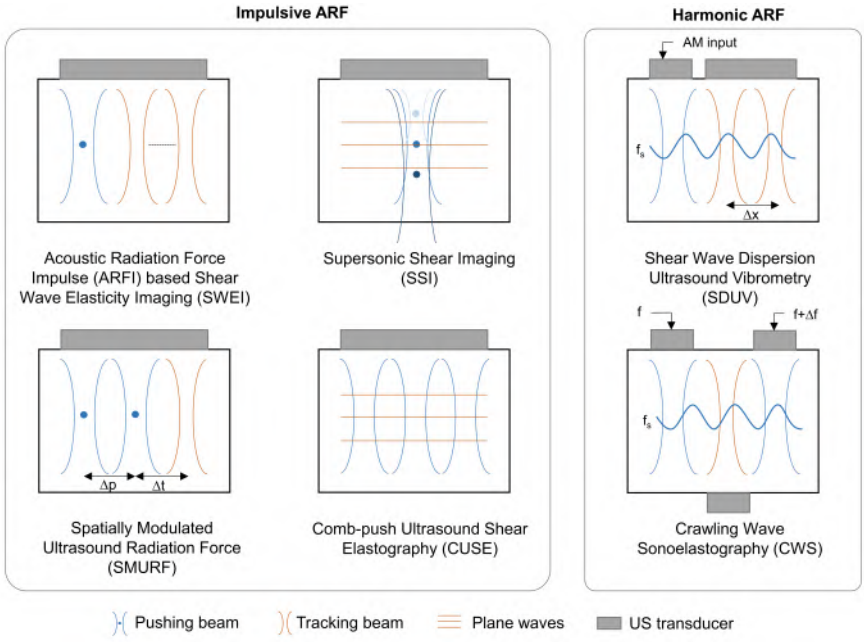

Figure 1.3: Overview of some ARF based shear wave techniques for impulsive and harmonic excitation (based on [79], [80]).

1. Acoustic Radiation Force Impulse (ARFI) based SWEI: the ARF is generated by application of one pushing beam with a short duration (~ 100 µs), and the resulting displacements are imaged with the same transducer outside the region of excitation. Basically, focused US beams are used to track shear wave motion. The shear wave speed is estimated with conventional TOF-methods, and can be used to derive tissue stiffness under certain assumptions. This technique was developed by Nightingale et al. [81] at Duke University (Durham, NC, United States).

2. Supersonic Shear Imaging (SSI): multiple impulsive ARF excitations, focused at different depths, are utilized such that the spherical generated waves of each push will interfere like a Mach cone. The source propagates faster than the generated shear wave and creates a quasi-planar wave front in the imaging plane (cylindrical-like wave front) [34], [54], explaining the 'supersonic' part in the name. These displacements are then imaged using plane waves instead of focused US beams, allowing real time and high frame rate imaging. Shear wave speed (and underlying tissue stiffness) are derived in a similar way as for ARFI based SWEI. Advantage of the supersonic push is the increased tissue displacement: displacements up to 100 µm in phantoms and 40

μm in vivo have been reported [54], compared to the in vivo reported displacements of 10-20 μm for a single push [49]. This technique was developed by Bercoff et al [54] at Institut Langevin (Paris, France).

3. Spatially Modulated Ultrasound Radiation Force (SMURF): impulsive ARF excitations are applied at separate locations simultaneously to induce shear waves of a specific wavelength. The shear wave displacement is monitored at a single location. By measuring the frequency of the shear wave and knowing its wavelength, its speed can be estimated. Advantages of SMURF are the reduction of error due to tracking displacement at a single location which cancels out speckle bias (i.e. difference between the precise position of a tracking beam and its prescribed location due to stationary speckle noise) and the ability to form quantitative stiffness images with high spatial resolution by increasing spatial frequency. This technique was developed by McAleavey et al [82] at University of Rochester (Rochester, NY, United States).

4. Comb-push Ultrasound Shear Elastography (CUSE): the comb-push technique is used to create a complex shear wave field with shear waves propagating through all imaging pixels including the push beam area. After the comb-push transmission, the US system switches to plane wave imaging modes to record the resulting tissue motion. A directional filter is applied to the tissue displacement data to remove destructive shear wave interferences and allow shear wave speed estimation by using conventional TOF methods. The advantages of this technique are that elasticity information is available from the full field of view (including push beam region) from one imaging sequence and that the SNR in all regions is similar as the shear wave will not attenuate that much. This technique was developed by Song et al [83] at Mayo Clinic (Rochester, MN, United States).

The following methods use a harmonic ARF excitation (see figure 1.3):

1. Shear Wave Dispersion Ultrasound Vibrometry (SDUV): a continuous amplitude-modulated ARF excitation is applied to the tissue, resulting in a monochromatic shear wave of a single frequency instead of broadband shear waves as with SWEI or SSI. The shear wave motion is tracked by diagnostic imaging pulses outside the region of excitation. The shear wave speed can be estimated by comparing the shear wave's phase at different locations, as the frequency is known. This technique can also characterize viscoelastic behavior in tissue by estimating shear wave speeds over a range of different excitation frequencies. This technique was developed by Chen et al [84] at Mayo Clinic (Rochester, MN, United States).

2. Crawling Wave Sonoelastography (CWS): harmonic ARF excitations are applied at two different locations at slightly different frequencies to induce shear waves traveling in opposite directions. These produce an interference pattern which slowly moves between the two excitation sources, termed *crawling waves*. The speed of the slow crawling waves can be estimated by using conventional Doppler techniques. This technique can also be used to assess viscoelastic properties of the investigated tissue by repeating measurements at different vibration frequencies. This technique was developed by Parker et al [85] at the University of Rochester (Rochester, NY, United States).

1.2.2 General principles of impulsive acoustic radiation force driven shear wave elastography

In this PhD thesis, we focused on techniques generating shear waves by using impulsive ARF at one lateral location. This concerns the initial implementation of ARFI based SWEI and SSI as mentioned in previous section. Throughout this work, we will refer to *impulsive ARF driven SWE* or just *SWE* to point to these techniques. This section explains the general principles of impulsive ARF driven SWE, in which a basic overview of the different steps is given in the first subsection, with each step further explained in detail in the subsequent subsections.

1.2.2.1 Different steps: push - image - process

ARF driven SWE consists of three essential steps (figure 1.4): (i) pushing mode – deforming the tissue of interest, (ii) imaging mode – measuring the resulting tissue displacement mode with ultrasound and (iii) post-processing – estimating stiffness based on the displacement magnitude of the tissue.

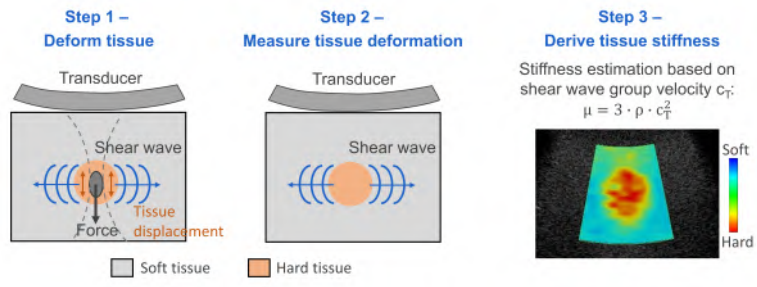

Figure 1.4: Basic steps in impulsive ARF driven SWE (elastogram adapted from *Toshiba Medical*[*]).

[*] Toshiba Medical - https://medical.toshiba.com/products/ultrasound/aplio-platinum/technology.php

In the first step, the tissue is deformed by sending out high-intensity pulses focused at one specific tissue depth from a conventional ultrasound transducer (see figure 1.4). The resulting body force or ARF is mainly oriented in the direction perpendicular to the transducer surface, causing a tissue displacement primarily in this direction. The resulting tissue deformation will be measured in the second step by switching the transducer into imaging mode: low-intensity acoustic pressure pulses are sent out to image the tissue displacement. The excited tissue displacements are first situated very locally around the pushing focus, but then start propagating away from the focus in all directions. Depending on the geometry of the focal zone, propagation path of the displacements will be spherical, cylindrical or even conical (see section 1.2.2.2). The particle displacements which are propagating in the directions parallel to the transducer surface, correspond to *shear* or transverse wave motion, as shown in figure 1.5.

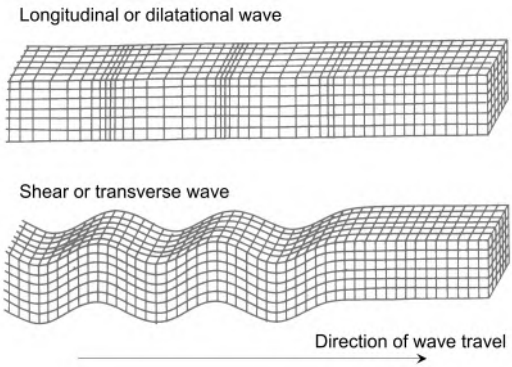

Figure 1.5: Particle displacements are oriented in the same direction as the direction of wave travel in longitudinal waves, whereas particle displacement orientation is perpendicular to the direction of wave travel in shear waves (adapted from *Astronomy and Astrophysics*[†]).

The third step in SWE techniques is to derive tissue stiffness (see figure 1.4). This is realized in a quantitative way based on the wave propagation speed of the shear wave: the higher the shear wave speed, the stiffer the imaged medium. In large and relatively uniform media, assumed to be purely elastic with density ρ, there is an exact link between shear wave propagation speed c_T and shear modulus μ:

$$\mu = \rho c_T^2 \tag{1.1}$$

[†]Astronomy and Astrophysics - http://www.astro.uwo.ca/ jlandstr/planets/webfigs/earth/images/waves.gif

Typical shear moduli values for various types of tissue are given in figure 1.6, in comparison with their bulk moduli. This figure shows a larger range in shear moduli than bulk moduli for different tissues. The bulk modulus determines mostly the dilatational wave speed, demonstrating directly the benefit of studying shear waves instead of longitudinal waves: the range in shear wave propagation speed is much larger than in longitudinal wave speed, allowing easier differentiation between the imaged types of tissues and thus increasing the technique's sensitivity. Furthermore, the shear wave propagation speed (order of a few m/s) is much lower than the longitudinal wave velocity (order of a few 1000 m/s – average propagation speed for sound in body tissue is 1540 m/s), requiring a smaller field of view and/or a lower frame rate to image wave propagation. Note that both the shear wave and compression wave speeds are frequency and temperature dependent [86].

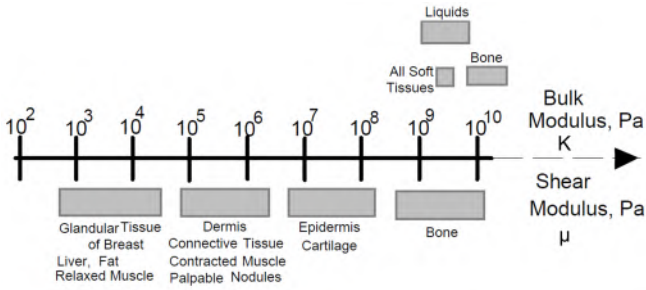

Figure 1.6: Order of magnitude of shear modulus vs. bulk modulus for various types of tissue (adapted from [86]).

1.2.2.2 Generating an acoustic radiation force

An acoustic radiation force is a universal phenomenon associated with the propagation of all acoustic waves in soft tissue. Its appearance is related to the momentum transfer from wave to medium, caused by the absorption (predominantly) and scattering processes in soft tissues, leading to changes in the acoustic energy density. This momentum transfer results in the application of a body force in the direction of the dilatational wave propagation (i.e. the direction perpendicular to the transducer surface or axial direction), evoking particle displacements in the same direction. To derive a formula for the ARF, tissues can be modeled as viscous fluids at ultrasonic frequencies, as they do not support shear stresses at these frequencies. Based on this linear viscous fluid model, one can account for the appreciable loss of energy from the propagating wave to find the following expression for the ARF under

plane wave assumptions [80], [81], [87] (with vector symbols indicated in **bold**):

$$\boldsymbol{B}(x, y, z) = \frac{2\alpha \boldsymbol{I}(x, y, z)}{c_L} \tag{1.2}$$

with $\boldsymbol{B}(x, y, z)$ the acoustic radiation force, α the attenuation coefficient, c_L the longitudinal wave speed and $\boldsymbol{I}(x, y, z)$ the time-averaged intensity. The force $\boldsymbol{B}$ has the same orientation as the acoustic intensity $\boldsymbol{I}$, corresponding to the direction of wave propagation, i.e. Poynting vector. This vector is oriented purely axial for locations within ±10% of the focal depth. For shallower locations closer to the transducer, this vector points toward the focal point, whereas for other locations further from the transducer, it points away from the focal point [88]. This is demonstrated in figure 1.7.

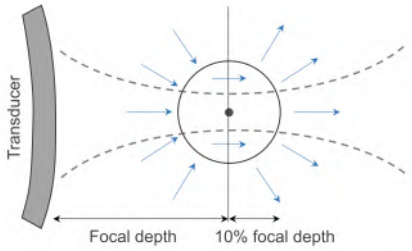

Figure 1.7: Orientation of acoustic radiation force with respect to focal depth (dimensions are not to scale).

The spatial distribution of the magnitude of the ARF is similar as the one of the time-averaged acoustic intensity, which can be derived based on the time-averaged acoustic pressure P:

$$I(x, y, z) = \frac{P^2(x, y, z)}{\rho c_L} \tag{1.3}$$

The spatial distribution of the time-averaged acoustic pressures $P(x, y, z)$ is on its turn dependent on the focusing process, which is a combination of natural diffraction focusing and geometric focusing. The latter type of focusing is induced by using a lens with curved aperture or by applying electronic delays between the different piezoelectric elements of the array [17]. The process of focusing is also called *beamforming*, which is one of the most important factors in determining image quality. A relevant parameter in determining the beam shape of the ARF is the F-number $F_\#$. This dimensionless parameter expresses the ratio of the focal length L, the distance between

the focal point and transducer tip, to the aperture A, the active zone of the transducer that transmits acoustic pressures (see figure 1.8):

$$F_{\#} = \frac{L}{A} \tag{1.4}$$

This parameter together with wavelength $\Lambda = c_L/f_o$ (with f_o corresponding to the frequency of the emitted ultrasound beam) determines the size of the focal zone with width D_F and length L_F, as indicated in figure 1.8.

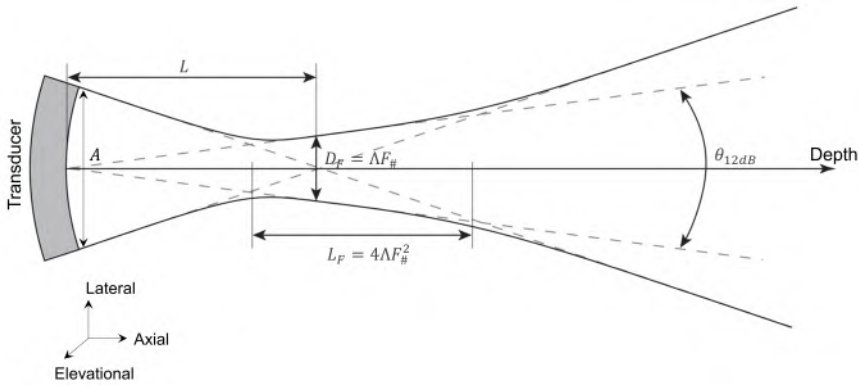

Figure 1.8: Important parameters of a focused transducer (adapted from [17]).

Depending on the length of the focal zone, the excited wave can be rather cylindrical (line source) than spherical (point source), as shown in figure 1.9. The wave can also propagate in a cone-shaped fashion, as is the case for SSI.

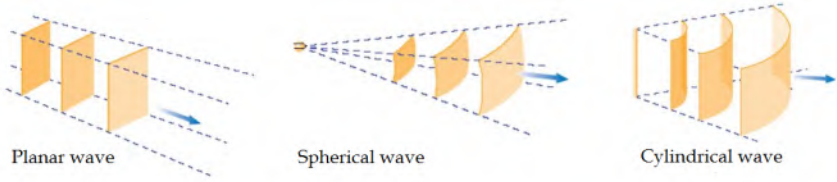

Figure 1.9: Type of wave propagation is dependent on the geometry of the source: planar vs. spherical vs. cylindrical wave propagation (adapted from [89]).

Now, to generate displacements of the order of microns due to the ARF, equation (1.2) shows that an increased acoustic intensity and/or increased attenuation is necessary. However, increasing attenuation should be nuanced, as indeed a higher attenuation increases the momentum transfer from wave to medium, but it also decreases the acoustic intensity. Furthermore, attenuation is dependent on depth and frequency, indicating that the optimal frequency used to generate an ARF is application-specific [80]. Two examples of ARF

distribution in media with different acoustic attenuation coefficients can be seen in figure 1.10. The distribution on the left hand side of figure 1.10 shows a typical ARF pattern: a peak in the force field near the focal point. However, for higher frequencies and/or highly attenuating materials, the force field is more uniformly distributed throughout the geometric shadow of the aperture, as can be seen on the right hand side of figure 1.10. The optimal frequency to generate an ARF is thus dictated by the tradeoff between attenuation losses in the near field and the focal gain [88].

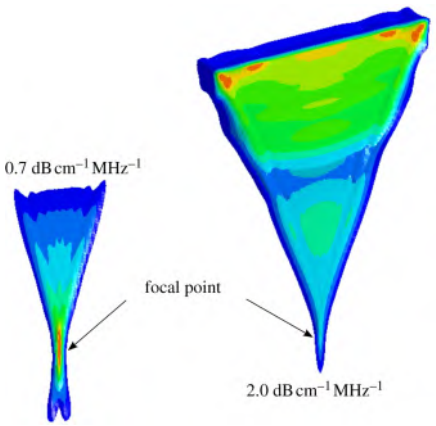

Figure 1.10: Isocontours of acoustic radiation force distribution from a focused linear array in media with two different attenuation coefficients (0.7 and 2.0 dB/MHz/cm). Red indicates peak radiation force magnitudes (adapted from [88]).

To increase the ARF-generated displacements to tens of microns, one will generally increase the acoustic intensity by utilizing longer and/or higher power acoustic pulses. Additionally, to further maximize the acoustic output of the transducer, no apodization or amplitude-weighting is applied, indicating that sidelobes are still present in the transmit beam. In general, the pushing frequency will be in the lower end of the transducer bandwidth, and the transmit voltage will be at the upper end of the system capability. The pushing pulses are similar to those used for Power Doppler imaging, but much longer in duration (factor of 20 difference) [49]. The total magnitude of the radiation force will be in the order of mN, leading to shear strain energy in the order of mJ [49]. ARF generation can be achieved with any type of transducer, either diagnostic or High Intensity Focused Ultrasound (HIFU) transducers, either linear or phased array probes.

1.2.2.3 Recording shear wave motion

Depending on the lateral location of the push, shear waves will generally start to propagate from the transducer's center towards the edges of the

transducer, spanning a distance of 2.5 cm when assuming a transducer width of 5 cm. Their speed generally varies between 0.3-10 m/s for soft tissue [90]. Considering a median shear wave velocity of 5 m/s, the shear wave has travelled outside the field of view of the transducer within 5 ms. If 10 frames are desired to record the shear wave motion, a frame rate of at least 2000 Hz is needed to properly visualize the shear wave propagation in the time domain. For a shear wave analysis in the frequency domain, an even higher frame rate might be necessary, depending on the frequency content of the shear wave. There are two imaging modalities widely used to record this shear wave motion at the desired frame rate: conventional focused ultrasound imaging and ultrafast ultrasound imaging (also called *plane wave* or *flash imaging*). The principle of both modalities is shown on the left hand side of figure 1.11, together with an illustration of their performance in rendering a regular B-mode. Conventional focused ultrasound imaging sequentially insonifies the medium by using focused pulses that allow the reconstruction of one image line, resulting in a good image quality. Many ultrasonic beams are thus needed to produce one single image, explaining the lower frame rate. Ultrafast imaging excites all piezoelectric elements of the transducer at once, generating an unfocused ultrasonic beam (also called *plane wave*). This leads to a higher frame rate and a lower image quality, as can be seen from figure 1.11. We will now discuss the imaging sequence of both modalities more in detail with respect to monitoring shear wave propagation.

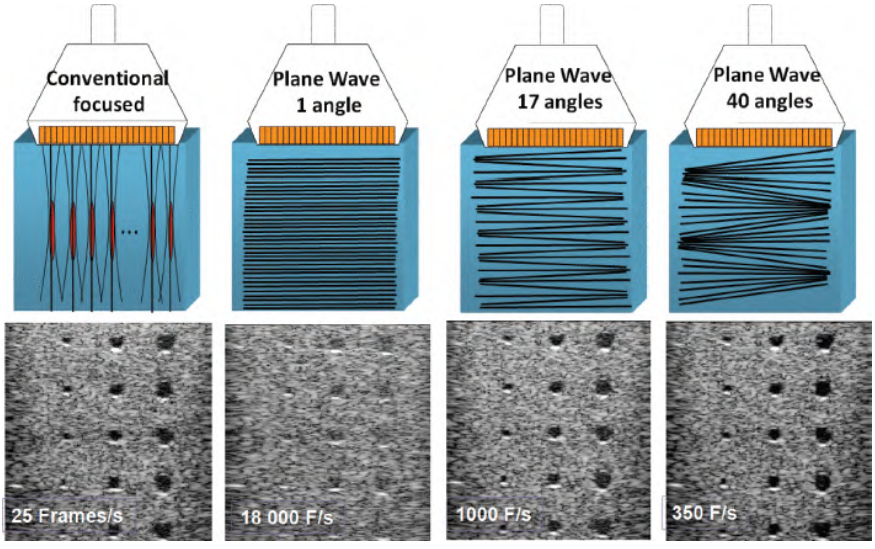

Figure 1.11: Comparison of conventional focused and ultrafast ultrasound imaging sequences with and without compounding for a 4 cm deep region of interest (adapted from [91]).

The initial implementation of conventional focused ultrasound imaging in SWE consisted of a reference track A-line (i.e. US A-mode) before the push, followed by the pushing pulse (usually situated at the center of the transducer), and repeated tracking A-lines in the same location as the reference after the push [92]. This is schematically shown in figure 1.12. The amount of repeated tracking pulses is chosen based on the duration that shear wave propagation needs to be recorded. This sequence of reference pulse, push pulse and tracking pulses is then repeated, in which the location of the reference pulse and tracking pulses alters, but the location of the pushing pulse remains the same, to create a full image of the propagating shear wave (see figure 1.12). Assuming the maximal allowable pulse repetition frequency (PRF) in between pulses, the PRF is limited by the time the pulse needs to travel to a certain imaging depth and the time the echo needs to travel back to the transducer. Thus, the PRF is then only dependent on imaging depth and dilatational speed of sound: $PRF = c_L/2/d = 1540/2/0.04 = 19250Hz$ for an imaging depth d of 4 cm. If we further assume a push pulse duration of 250 µs and 40 tracking pulses, the acquisition time of one sequence of reference pulse, push pulse and tracking pulses is at least 2.4 ms. If this is repeated for 128 lateral locations, the total scan acquisition takes at least 307.2 ms for recreating a full image. The resulting frame rate to create a full image is thus $40/(307.2ms) = 130.2Hz$, whereas the shear wave is imaged at a frame rate of the PRF, i.e. 19250 Hz. The long acquisition time might be disadvantageous when applying SWE to fast moving organs.

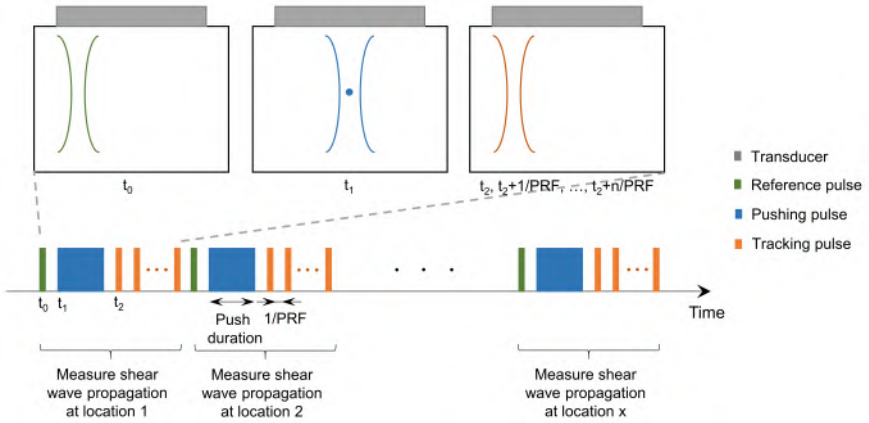

Figure 1.12: Example of imaging sequence when using focused ultrasound to image shear wave propagation for x locations and n time frames.

The above-mentioned imaging scheme requires multiple cycles of push-and-detect shear wave acquisitions, indicating a longer acquisition time and a higher risk at tissue heating due to the repetition of the high-intensity

pushing pulses (more information about safety considerations is given in section 1.2.3). Both issues can be dealt with by making use of *parallel receive beamforming*, which is nowadays available on many ultrasound scanners [79], [93], [94]. This technique allows beamforming of multiple imaging lines at a time with a single pulse-echo cycle, reducing the total acquisition time and the amount of push-and-detect cycles. For example, if a 4:1 parallel receive is implemented, this means that the effective PRF in our above-mentioned example is the same (19250 Hz), but the total acquisition time is reduced from 307.2 ms to 76.8 ms and the amount of push-and-detect shear wave acquisitions is now 32 instead of 128 (both reduced by a factor 4).

Another option to reduce the acquisition time and the risk at of tissue heating, is to cut the number of imaging lines. This requires either an increase of spacing between the imaging lines if the same width of the field of view is desired or shrinking the width of the field of view if the spacing of the imaging lines needs to be maintained. For example, reducing our field of view with a factor 2 (64 lines instead of 128 image lines) in combination with the before-mentioned 4:1 parallel receive beamforming technique leads to a reduction in the total acquisition time (38.4 ms instead of 76.8 ms) and in the number of push-and-detect cycles (16 instead of 32), while the effective PRF is maintained.

A third option to further reduce both features is to make use of a kind of *beam interleaving*, splitting the transducers up into several zones, in which for every push-and-detect sequence, the shear wave is tracked sequentially for one specific zone. This would further decrease the total acquisition time and the risk at tissue heating, but it also alters the effective PRF. An example of this tracking sequence is schematically shown in figure 1.13. Retaking our numerical example from above, for 128 imaging lines, 4:1 beamforming, imaging depth of 4 cm and 8 transducer zones (thus 8 push-and-detect cycles), the effective PRF is 4812.5, which is still sufficiently high for shear wave tracking. The total acquisition lasts 19.2 ms. It should be noted that within one zone of tracking pulses, the starting point of the first pulse differs from that of the second pulse, which should be taken into account while calculating the shear wave speed. This can be done by using an upsampling-based approach such as Time Aligned Sequential Tracking (TAST) [95], which interpolates the tracked shear wave motion for the missing time points.

In general, the effective shear wave tracking PRF or PRF_e of one push-and-detect shear wave acquisition (or zone) is given by [96]:

$$PRF_e = \frac{PRF}{N/(pZ)} \tag{1.5}$$

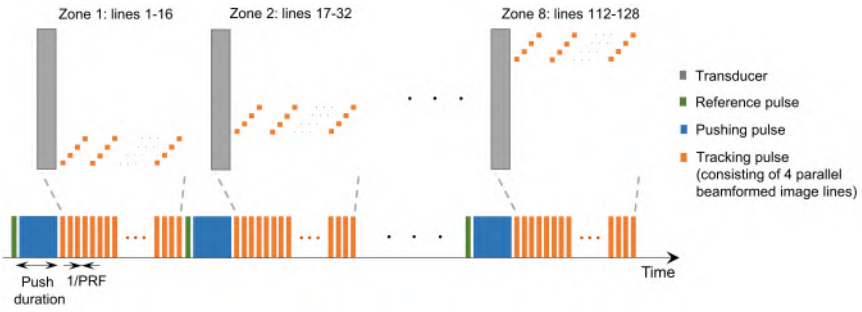

Figure 1.13: Example of tracking sequence incorporating parallel beamforming (4 imaging lines) and a multi-zone detection scheme (8 zones with each 4 pulses or 16 imaging lines). After every zone of tracking, the reference and pushing pulse needs to be repeated.

with PRF the original pulse-repetition frequency, N the number of imaging lines, p the number of imaging lines that can be parallel beamformed and Z the number of zones (or number of push-and-detect shear wave acquisitions). It should be noted that the performance of the beamformer depends on the type of beamformer implemented in the US scanner. Conventional scanners typically use hardware beamformers, which only allow beamforming of a certain number of channels at a time and are only capable of imaging in a line-by-line scanning fashion. This is typically a *delay-and-sum* beamformer in combination with *dynamic receive focusing* (varying the focal point on receive). Since the end of the 2000s, new powerful graphical processing units (GPUs) have reached a satisfactory level of performance to speed up processing algorithms. Additionally, the introduction of fast numerical links (PCI express technology) allowed transfer of huge volume of data to the GPUs. The combination of both technological innovations led to a shift in the US beamforming process from hardware to software, enabling full parallelization of ultrasound image computation [97]. This type of beamforming is called *software based* or *pixel oriented*. For these systems, there are no limitations anymore in the amount of image lines that can be parallel beamformed with a single pulse-echo insonification, indicating that the effective PRF approaches the original PRF. Although such platforms provide better support for shear wave elastography, it should be kept in mind that the majority of current clinical US systems do not have this software beamforming capability [96]. Therefore, efforts (e.g. TAST method [95]) have been done for shear wave tracking to provide a feasible way for translating 2D SWE technique from laboratory to clinical scanners.

Software based beamforming was introduced together with *plane wave imaging* or *ultrafast US imaging*, which is an alternative to focused US imaging in recording the ARF-generated shear wave propagation. This was the

first technique that allowed very high frame rate and real time imaging of the propagating shear wave. The complete SWE sequence then consists of a reference plane wave, a pushing pulse and tracking plane waves, as schematically illustrated in figure 1.14 [54]. The effective PRF is equal to the original PRF, and this sequence needs to be executed only once. Thus, retaking our previously mentioned numerical example, this means that the effective PRF and actual frame rate will be equal to 19250 Hz for an imaging depth of 4 cm, and the total acquisition lasts for 2.4 ms instead of the 307.2 ms as initially mentioned.

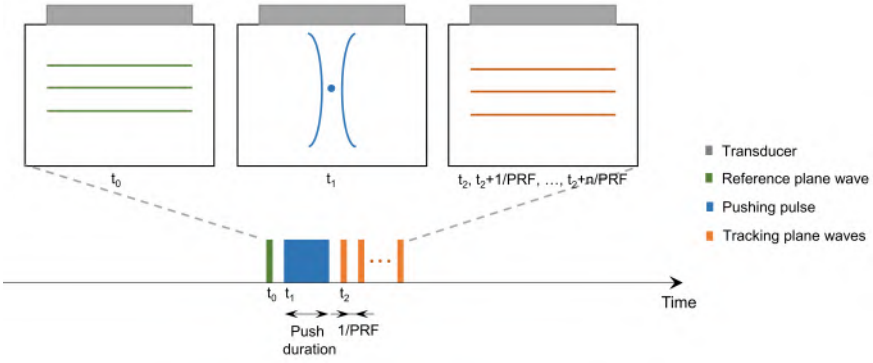

Figure 1.14: Example of imaging sequence when using plane waves to image shear wave propagation for n time frames.

These ultrafast frame rates with single plane wave imaging came at the cost of reduced image contrast and resolution compared to the conventional transmissions. However, this limitation can be overcome by introducing *coherent plane wave compounding* [98], [99], a technique that sends out multiple tilted and non-tilted plane waves into the medium and coherently sums the backscattered echoes to compute the full image, or compounded image. The principle of such a sequence is shown in figure 1.15 for the emission of 3 angulated plane waves.

Coherent compounding drastically improved the quality of the image as can be seen in figure 1.11. This figure clearly shows that when more tilted plane waves are sent out, the image quality gets better, but it reduces the frame rate with a factor equal to the amount of used plane wave angles. The concept of high frame rate imaging and coherent compounding has also been employed with *diverging waves* [100], which allows a larger field of view than plane waves (see figure 1.16). Diverging waves are generated by exciting all piezoelectric elements in the transducer with a certain time delay with respect to the center of the aperture. This way, the focus of the transmitted wave is situated behind the transducer surface (negative focus). Diverging waves

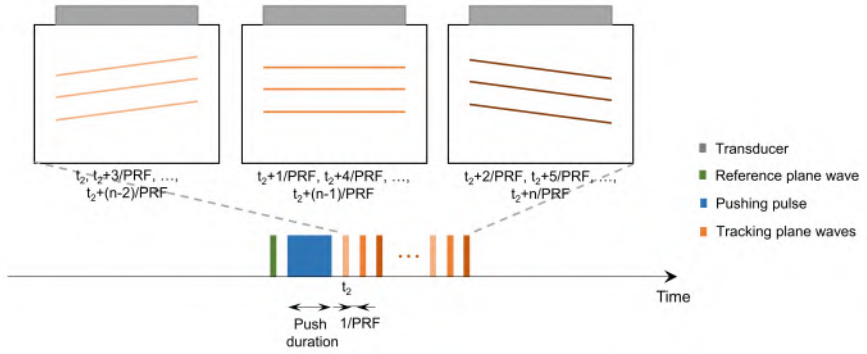

Figure 1.15: Example of plane wave sequence with compounding for n time frames of single plane wave images (n/3 time frames of compounded plane wave images).

are of particular interest in cardiac applications to create a small aperture in combination with a large field of view [100], [101].

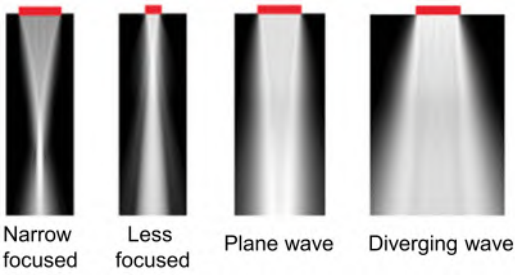

Figure 1.16: Different types of ultrasound transmit beams (adapted from [101]).

Depending on the specifications of the scanner (i.e. implementation of software based beamforming), focused or plane wave imaging are typically used to track shear wave propagation. Focused ultrasound imaging is conventionally utilized when high quality data is desired and a smaller field of view needs to be covered. Plane wave imaging is preferred when real time imaging and high frame rates are favored and a large field of view is needed [102]. More recently, other ultrasound-based shear wave tracking techniques have been developed to resolve the issue of noise contaminated US signals (potentially caused by clutter, phase aberration and US reverberation), especially for challenging settings such as the heart in a closed-chest setting. More information about some of these shear wave tracking techniques is given in section 3.2.1.

1.2.2.4 From RF signals to shear wave characteristics and material properties

Post-processing of the radio-frequent (RF) or complex demodulated IQ signals consists of three steps: (i) tissue motion estimation, (ii) data filtering

and (iii) shear wave speed estimation. Each of these steps will be described below, and is mainly adapted from [102]. The first step in data post-processing is estimating tissue displacement or velocity. All available tissue motion estimators can be broadly characterized into two categories:

1. *Correlation-based approaches* that operate on RF-data: cross-correlation techniques (see figure 1.17) look for the similarity between small segments of the pre- and post-deformation signals to assess the change in arrival time between these echoes, resulting in an estimate of tissue displacement [64]. This can be done in 1D, 2D or 3D. The 2D and 3D cross-correlation methods make use of the image's speckle pattern, generated by the interference pattern of echoes from a dense distribution of scatterers. Tracking this speckle pattern with appropriate pattern matching techniques leads to an evaluation of the tissue response, as illustrated in the right panel of figure 1.17 [17]. These algorithms are significantly more computationally intensive than phase-shift algorithms, so these are less readily used in real-time applications.

2. *Phase shift algorithms* that operate on IQ-data: commonly used phase shift estimation methods, also called *Doppler methods*, are the algorithms developed by Kasai et al. [103] and Loupas et al. [104]. Kasai's algorithm, also known as the *1D autocorrelation technique*, determines the displacement between a reference and displaced signal by measuring the average phase shift with respect to the central frequency of the transducer. Loupas' algorithm is a *2D autocorrelator*, which also uses information from within the axial range next to that from the depth samples [105], [106]. The difference between both algorithms is that the Kasai algorithm assumes a constant carrier frequency, while the Loupas algorithm calculates the mean Doppler frequency and the mean RF frequency at each axial position. It has been shown that the Loupas algorihm yields more accurate displacement estimates than the Kasai algorithm [103].

Two kinds of reference schemes are possible in both algorithms: *fixed* or *progressive referencing*. For fixed referencing, the signal trace before the pushing pulse is typically used as the reference signal, such that comparison of each tracked signal after the pushing pulse with the reference signal leads to calculation of the absolute displacement at each step. In a progressive reference scheme, each tracked signal is compared with the tracked signal at the previous time step so that a differential average displacement is calculated. Based on this differential displacement, the axial velocity signal is

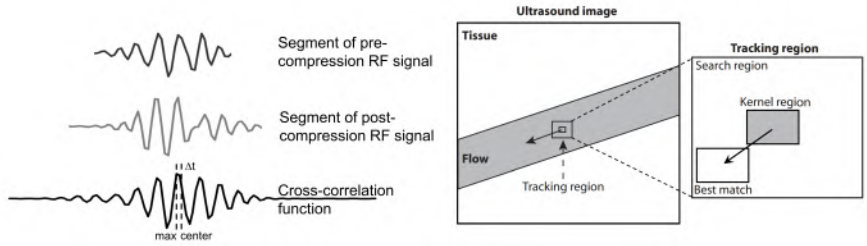

Figure 1.17: Left panel: illustration of 1D cross correlation. Right panel: principle of speckle tracking (adapted from [17]).

easily derived. If needed, the tissue displacement signal can be calculated by accumulating the differential displacements.

The second step in data post-processing is filtering the obtained tissue motions. First, the recorded frames right after the push are not considered, as these contain high spatial variations and unrealistic amplitudes due to reverberation of the push. These are usually removed or interpolated from the other data points if a fixed reference scheme is used. Second, a low pass filter is generally applied to reduce the high-frequency jitter due to signal decorrelation, finite window lengths and noise. The cut-off frequency of this filter has to be selected carefully to not reject any shear wave energy by the filter. Deng et al [102] recommends a cut-off frequency of 1500 Hz for displacement data collected with a linear array probe with center frequency of 5.2 MHz and bandwidth of 4-7 MHz. Third, motion and directional filters can be used to reduce background motion arising from transducer movement and/or biological motion and waves reflected from the boundaries.

The third step in data post-processing is estimating group shear wave speed. Both tissue displacement and velocity data can be used to estimated shear wave velocity. Usually, particle velocity data are favored because they are less susceptible to wave shape changes introduced by the reflections at the boundaries and background motion. However, the velocity peak occurs earlier in time than the displacement peak, making the former more difficult to detect properly in the presence of reverberation frames or in the case of a stiff material. An example of resulting axial particle velocities depicting shear wave propagation in an elastic bulk phantom is shown in the left panels of figure 1.18. Typically, time-of-flight (TOF) methods are used to estimate group shear wave speed, which characterize the shear wave position in function of time. One of the most commonly used TOF-methods is linear regression: it fits a linear curve to the tracked shear wave position in time at a specific depth of the shear wave path. The slope of this fitted curve corresponds to the group shear wave velocity (see right panel of figure 1.18). This method

can be implemented in various ways, and will be discussed more in detail in chapter 2 together with other TOF-methods.

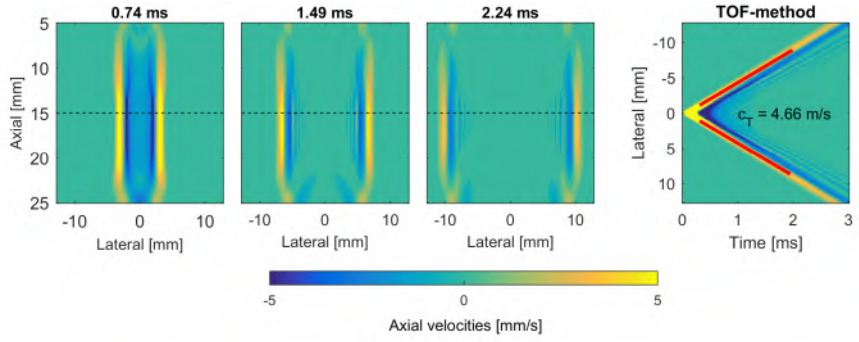

Figure 1.18: Example of shear wave propagation (left three panels) and characterization (right panel) in an elastic phantom with Young's modulus of 68 kPa and a thickness of 20 mm. TOF-method is applied on the temporal wave pattern obtained at an axial depth of 15 mm, indicated with the black dotted line.

The procedure can be applied for the left and right shear wave (when focusing push US pulse around the center of the transducer) and repeated for multiple depths. These values might be averaged when considering a large homogeneous elastic phantom, e.g. Deng et al [102] proposes averaging over the axial depth of field defined by $8F_{\#}^2\lambda$ around the focal depth of the push beam. Bias in shear wave speed estimation might arise when (i) the lateral focus of the pushing pulse does not correspond with the inherent elevational focus of the transducer or (ii) the lateral window for the TOF-methods starts within the near field of the shear wave source.

1.2.3 Safety considerations

As ARF driven SWE comes with an increased acoustic output power, it is essential to confine the acoustic output to limit the risk on bio-effects such as tissue heating or cavitation phenomena. These limits are expressed in appropriate safety parameters, usually in terms of:

1. *Acoustic power*: several parameters describe the acoustic power of an ultrasound system such as acoustic pressure, total power, spatial peak temporal average intensity (I_{spta}) or spatial peak pulse average intensity (I_{sppa}). These acoustic output parameters are typically measured in water and then *"derated"* to account for tissue attenuation (standard 0.3 dB/MHz/cm).

2. *Safety indices*: two commonly used indices are the mechanical index (MI) and the thermal index (TI). Both indices are usually provided

on the screen of the ultrasound system, where the MI provides information about the likelihood and magnitude of non-thermal effects (such as cavitation phenomena) and the TI gives information about the potential for tissue heating. Both are defined as follows:

$$MI = \frac{p_r}{\sqrt{f_o}} \cdot 1 \frac{\sqrt{Hz}}{Pa} \tag{1.6}$$

$$TI = \frac{W}{W_{deg}} \tag{1.7}$$

with p_r the peak rarefaction pressure, f_o the center frequency of the pulse, W_{deg} the acoustic power required to achieve an increase in temperature of $1°C$ at some position within the exposed tissue and W the acoustic power being used under otherwise identical conditions of scanning and target tissue.

Guidelines have been published by various international organizations such as the International Electrotechnical Commission (IEC) and the World Federation for Ultrasound in Medicine and biology (WFUMB) but also by national organizations such as the Food and Drug Administration (FDA) in the USA or the Royal College of Obstetricians and Gynaecologists in Europe [80], [107], [108]. Whilst the FDA guidelines have no legal force outside the USA, they have had, and continue to have, an important effect on the control of acoustic exposure throughout the world. This is partly because the ultrasound industry is dominated by four or five international companies, most with manufacturing facilities in the USA [107]. In all predefined tracks and applications, the FDA defined levels for the derated global maximum acoustic output [109]:

1. Derated $I_{spta} \leq 720 mW/cm^2$
2. $MI \leq 1.9$ or derated $I_{sppa} \leq 190 W/cm^2$
3. $TI \leq 6.0$ (explanation is needed if the TI exceeds this value)

Note that an MI of 1.9 can result in a derated I_{sppa} much larger than 190 W/cm^2, setting no effective limit on I_{sppa} [110]. Next to these limits, the FDA and IEC also restrains the temperature rise in tissue to be maximally 6°C [49]. Despite these predefined limits, it should be kept in mind that all diagnostic information should be obtained at an acoustic output that is As Low As Reasonably Achievable (ALARA-principle).

Typical acoustic output values reported for ARFI [49], [90] and SSI [54] are summarized in table 1.5. It should be noted that these parameters are dependent on transmit frequency and pulse duration. Even though the temperature rise is not reported in [54] for SSI, it is expected that SSI will have a similar or a slightly increased temperature rise as one single push-and-detect sequence in ARFI imaging (< 0.2 °C). ARFI-based SWEI will have similar temperature rises as ARFI, as the only difference is an off-axis tracking instead of an on-axis tracking. A complete sequence of conventional real-time 2D ARFI imaging (without any parallel beamforming) can have a significant impact on tissue heating: finite element models have shown that the temperature increase can reach up to 4.5 °C with an ARFI frame rate of just 3 Hz, 50 image lines, and an acoustic absorption of 0.5 dB/cm/MHz [108]. However, this is a worst case scenario, and implementing new tracking methods such as parallel tracking/beamforming will reduce tissue heating [93]. ARFI (even with conventional tracking methods) and SSI are thus achievable within the standard diagnostic limits set by the FDA regarding I_{spta}, MI or I_{sppa}, and thermal increase [111].

It should be noted that the FDA guidelines are outdated as they were developed based on the output and efficacy of US systems produced before 1976 and are not based on specific scientific knowledge regarding bio-effects resulting from US. Therefore, the American Institute of Ultrasound in Medicine (AIUM) established a subcommittee to review bio-effects literature and publish new recommendations regarding the use of transiently increased output in non-fetal and non-contrast agent US imaging, in particular focusing on increased MI [80], [111].

Table 1.5: Acoustic output values reported for ARFI and SSI (based on [49], [54], [90]). For all reported intensities an attenuation factor of 0.3 dB/cm/MHz was assumed, except for I_{sppa} reported for ARFI a factor of 0.5 dB/cm/MHz was used.

Parameter	**ARFI [49], [90]**	**SSI [54]**
Frequency	2-7 MHz	4.3 MHz
Focal depth	not reported	40 mm
Intensity I_{sppa}	$1400 - 3000 W/cm^2$	$190 W/cm^2$
Intensity I_{spta}	$700 mW/cm^2$	$62 mW/cm^2$
MI	1.5-3.0	0.96
Push duration	$100 - 500 \mu s$	$100 \mu s$ (5 pushes)
Temperature rise	$0.02 - 0.2 °C$	not reported

Chapter 2

Material characterization in shear wave elastography

This chapter gives an overview of the different material characterization techniques commonly used in shear wave elastography (SWE), more specifically SWE using an acoustic radiation force (ARF) to excite shear waves. Tissue characteristics can be described using mathematical material models, which are discussed in the first section of this chapter. Before tissue properties can be linked to any shear wave characteristic, it is necessary to derive relevant shear wave features from the SWE acquisition with techniques described in the second section. Then, the third section (section 2.3) provides the theoretical link between the tissue material assumptions (section 2.1) and the shear wave characteristics (section 2.2). The last section (section 2.4) describes the practical implementation of the different material characterization techniques by linking all previous three sections, and it also gives an overview of the commonly reported quantities in previous SWE-studies.

2.1 Tissue material assumptions in shear wave elastography

In general, tissues are essentially anisotropic, viscoelastic and non-linear. Their behavior changes through time and is dependent on moisture. Furthermore, tissues are metabolically active when alive, exhibiting certain mechanical properties, which will alter during aging and after death [28]. Hence, it is very difficult to describe this kind of material behavior in closed-form mathematical expressions, and therefore, many assumptions are made in

the field of elasticity imaging to simplify the analysis and interpretation of elasticity images [112]. The most commonly assumption in shear wave elastography is linear elasticity, described in the first subsection. This is the model implemented in commercial elastography systems, when a value of tissue stiffness is displayed. The second subsection defines higher order material models, that take into account more advanced material characteristics of tissues. This section mainly focuses on viscoelastic material models, as these are widely used next to elastic material models in SWE.

2.1.1 First order material model

If the tissue loading is applied short enough such that the viscous nature of the material can be ignored, the tissue can be assumed to behave elastically. This means that it follows the generalized law of Hooke, which linearly relates the nine stress components σ_{ij} $(i, j = 1, 2, 3)$ to the infinitesimal nine strain components ε_{mn} $(m, n = 1, 2, 3)$ through the tensor of elastic moduli $\mathbf{C}$:

$$\sigma_{ij} = C_{ijmn}\varepsilon_{mn} \tag{2.1}$$

This equation indicates that the tissue's elastic behavior is described by a tensor C_{ijmn} $(i, j, m, n = 1, 2, 3)$ of 81 stiffness constants. The number of constants is often further reduced, as it is a very challenging process to obtain all stiffness constants. Usually, by carefully choosing the scale or size of the tissue samples that are being studied, it is often possible to approximate tissue as a *linear elastic isotropic* material under *small deformation* assumptions such that only two parameters are needed to describe the tissue response to mechanical loads. These two parameters are the Lamé constants: λ, Lamé's first parameter, and μ, Lamé's second parameter, better known as the *shear modulus* [28]. Equation (2.1) is then reduced to the following constitutive law [113]:

$$\sigma_{ij} = \lambda\varepsilon_{kk}\delta_{ij} + 2\mu\varepsilon_{ij} \tag{2.2}$$

where ε_{kk} indicates the trace of ε and δ_{ij} is the Kronecker delta. Lamé constants can be converted into two other elastic constants that can be directly measured, i.e. the Young's modulus E and Poisson's ratio ν. The relationship between the Lamé constants, λ and μ, and the elastic moduli pair, E and ν, is thus:

$$\lambda = \frac{E\nu}{(1+\nu)(1-2\nu)} \tag{2.3}$$

$$\mu = \frac{E}{2(1+\nu)} \tag{2.4}$$

As soft tissues contain both solid and fluid components, their mechanical properties fall somewhere between those of both materials. Many soft tissue are nearly incompressible, i.e. Possion's ratio varies between 0.49000 to 0.4999, making them mechanically similar to fluids [114]. Note that equation (2.4) reduces to the simple relationship $\mu = E/3$ when $\nu = 0.5$. Typical mechanical characteristics for different soft tissues are given in table 2.1.

Table 2.1: Typical mechanical characteristics for different soft tissues with increasing E-modulus (adapted from [90], [115]).

Type of tissue	Young's modulus (kPa)	Shear modulus (kPa)	Shear wave speed (m/s)	Bulk modulus (GPa)	Dilatational wave speed (m/s)
Fat	~1	~0.3	~0.5	2-2.5	1490-1540
Healthy liver	1-12	0.3-4	0.5-2.0	2-2.5	1490-1540
Skeletal muscle	3-30	1-10	1-3.2	2-2.5	1490-1540
Prostate	6-45	2-15	1.4-3.9	2-2.5	1490-1540
Myocardium	20-150	6.7-50	2.6-7.1	2-2.5	1490-1540
Fibrotic liver	30-300	10-100	3.2-10	2-2.5	1490-1540

2.1.2 Higher order material models

The stress-strain relationship for most tissues is non-linear. Different factors contribute to this non-linearity, but this section will mainly focus on the factor viscoelasticity. Viscoelastic behavior combines the behaviors of both viscous fluid and elastic solid, meaning that the stress-strain response will be a function of rate of excitation. Generally, the faster a viscoelastic material is excited, the stiffer it will seem [90]. Tissue stiffness is thus dependent on the excitation frequency. A viscoelastic material in general has a complex shear modulus $\mu(\omega)$ (or complex Young's modulus), in which the real part $\mu'(\omega)$ represents the storage modulus and the imaginary part $\mu"(\omega)$ represents the loss modulus:

$$\mu(\omega) = \mu'(\omega) + i\mu"(\omega) \tag{2.5}$$

Many models have been proposed relating stress and strain based on the linear theory of viscoelasticity, as described by Voigt, Maxwell and Kelvin [31]. Their models of viscoelasticity are shown in figure 2.9, where the springs represent the elastic component and the dashpots represent the viscous component.

The most commonly used model in the field of SWE is the Kelvin/Voigt model (see figure 2.9), where the Lamè parameters become complex values and dependent on angular frequency ω:

$$\lambda = \lambda_1 + i\omega\lambda_2 \tag{2.6}$$

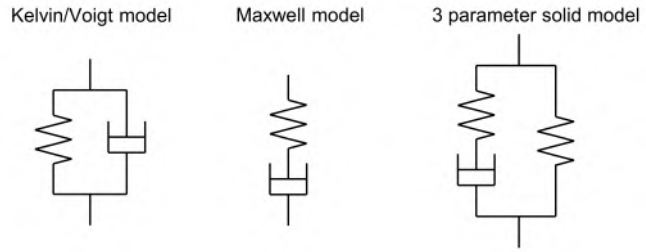

Figure 2.1: Typical models for modeling viscoelasticity: Kelvin/Voigt, Maxwell and 3-parameter solid.

$$\mu = \mu_1 + i\omega\mu_2 \tag{2.7}$$

with λ_1 and μ_1 representing the longitudinal and shear elasticity and λ_2 and μ_2 the longitudinal and shear viscosity. This simple model of viscoelasticity gives an acceptable approximation to creep behavior but does not account for relaxation (stresses remain constant at constant strain). Modeling tissue as a viscoelastic material is a more accurate and realistic representation of actual tissue and it provides an additional parameter, i.e. viscosity, which might be of additional diagnostic value for detection and characterization of malignant lesions next to elasticity [116].

Another advanced material model that has been used for modeling tissue in the domain of shear wave elastography is a transverse isotropic material model, that takes into account the material orientation. This has been applied to the skeletal muscle without considering viscoelasticity in [117]. Later, this material model has been extended in [118] to include viscoelasticity characterized with a Voigt model. The researchers verified the applicability of this material model by an *ex vivo* SWE-experiment in combination with finite element simulations on porcine skeletal muscle. For more details, we refer to [117], [118].

2.2 Shear wave characteristics derived from shear wave elastography data

This section gives an overview of the different methods commonly used to extract the shear wave characteristics in the time domain (see section 2.2.2) and frequency domain (see section 2.2.3). Both shear wave characteristics relate to group and phase speed, respectively. Therefore, the concepts of group and phase speed will first be briefly revised in section 2.2.1.

2.2.1 Concepts of group and phase speed

A wave's velocity can be characterized in two ways: the group velocity and the phase velocity. The group velocity is the speed with which the center of the gravity of the pulse propagates, whereas the phase velocity is the speed with which any given phase of the waveform propagates. For non-attenuating media, group speed and phase speed are equal. However, in attenuating media, the propagation speed will be frequency-dependent, leading to a difference in phase and group velocity, a phenomenon also called *dispersion*. In a strongly dispersive medium, the effect of speed dispersion can even cause the waveform to become distorted [86]. This effect is illustrated in figure 2.2, which clearly shows dispersion for the lower two panels (speed of envelope differs from speed of waveform). Nevertheless, only the lower panel demonstrates a distorted waveform, as the pulse is stretched at $x = 20mm$ compared to the original width of the pulse at $x = 10mm$.

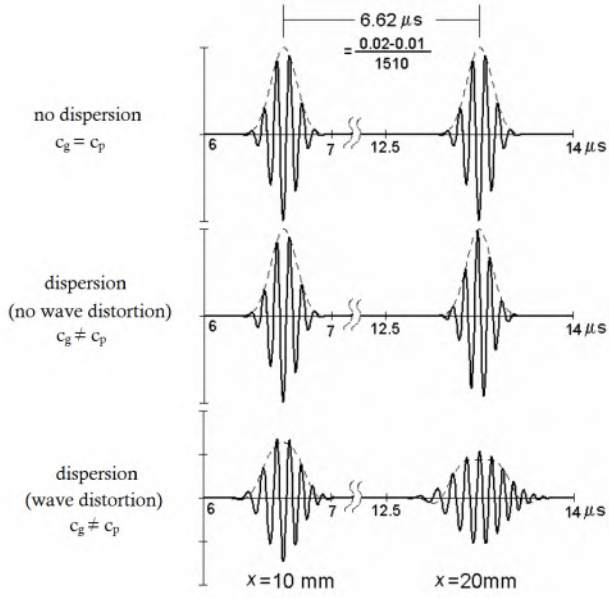

Figure 2.2: Effect of dispersion: all panels show a propagated wave (with envelope) from $x = 10mm$ to $x = 20mm$, where the upper panel depicts no wave dispersion and the other two panels do depict dispersion. The middle panel does not show a distorted wave shape at $x = 20mm$, whereas the lower panel depicts a distorted waveshape. This is caused by the non-linear variation of wave number in function of frequency (adapted and adjusted from [86]).

Both speeds are easily defined by considering a harmonic wave $\phi(x,t) = \phi_o cos(\omega t - kx)$ propagating in the x-direction in time t with wavenumber k, amplitude ϕ_o and angular frequency ω. After a distance of Δx and a time

interval of Δt, the wave will have the same phase if $\omega t - kx = \omega(t + \Delta t) - k(x + \Delta x)$ or $\Delta x/\Delta t = \omega/k$. Thus, phase speed c_ϕ is defined as

$$c_\phi = \frac{\omega}{k} \tag{2.8}$$

The group speed c_g, or speed with which the center of gravity of the pulse propagates is then defined as (with ω_c the center angular frequency):

$$c_g = \frac{1}{\left[\frac{dk}{d\omega}\right]_{\omega=\omega_c}} \tag{2.9}$$

Note that dispersion can be caused by intrinsic properties or by geometrical constraints, called *material dispersion* and *geometric dispersion*, respectively. For material dispersion, dispersion is always related to absorption of wave energy, which can be caused by different mechanisms such as thermal conductance, chemical or viscous effects. The main cause of acoustic wave absorption for homogeneous solids are viscous effects [86]. Material anisotropy will also play a role in dispersion, as it can guide wave packets in a certain direction, leading to separation of wave fronts. Additionally, viscosity might be direction-dependent, resulting in different attenuation mechanisms depending on the directionality of the shear wave (as for example shown in the Achilles tendon [119]). For geometric dispersion, the wave continuously interacts with the boundaries of the medium, leading to reflections that interfere to form guided wave packets. These different wave modes propagate then along the structure at different velocities.

2.2.2 Shear wave characteristics in the time domain

Initially, inversion of the theoretical wave equation was used to estimate shear wave speed from axial displacement/velocity data. However, the presence of jitter in the tissue motion estimates led to unreliable second derivatives in space and time for the wave equation, resulting in variable shear wave speed estimates [88], [116]. Therefore, different methods were developed to reconstruct shear wave speed, the so-called *time-of-flight (TOF) methods*, which characterize shear wave position as a function of time. We will shortly describe the basic principles of the initial implementation of the following TOF-methods: correlation-based algorithm, time-to-peak (TTP) displacement algorithm, random sample consensus (RANSAC) algorithm and radon sum transformation below. Note that TOF-based methods employ a priori assumptions, including local homogeneity, negligible dispersion (no wave distortion), and a known direction of propagation, such that the arrival time at adjacent positions can be used to determine the shear wave speed [88]. When these assumptions are true, the calculated wave speed corresponds with the shear wave group velocity.

2.2.2.1 *Correlation-based approach*

The TOF-method proposed by McLauglin and Renzi [120] consists of two sub-algorithms. First, the arrival time front needs to be found from the shear wave displacement data. This is realized by applying a cross-correlation procedure between the time traces of the displacement signals of two different spatial locations (principle is demonstrated in the left panel of figure 1.17). Second, the Eikonal equation, relating arrival times $\widehat{T}$ to shear wave speed c_T, is used to estimate the shear wave speed by approaching $|\nabla \widehat{T}|$ with the first order distance method for $\Delta t \to 0$:

$$\begin{aligned} &|\nabla \widehat{T}| c_T = 1 \\ &\quad c_T \approx \frac{1}{\Delta t} \inf \left\{ |x - \widehat{x}| : \widehat{x} \text{ satisfies } \widehat{T}(\widehat{x}) = \widehat{T}(x) + \Delta t \right\} \end{aligned} \tag{2.10}$$

with inf representing the mathematical infimum or the greatest lower bound. This method can give inaccurate results when physiological motion, low signal-to-noise ratio (SNR) or spatial tissue inhomogeneities are present [94]. Additionally, the mathematical complexity rules out real-time applications [121]. Accuracy of the shear wave speed estimates can be improved by applying a higher order distance method [120].

2.2.2.2 *Time-to-peak displacement algorithm*

The TTP algorithm has been proposed by Palmeri et al [44] and estimates shear wave position by quantifying the time needed to reach the peak displacement at several lateral positions. These calculations are repeated over a certain range of axial positions over the *depth of field (DOF)* of the focused radiation force excitation. An example of the TTP procedure is shown in figure 2.3. The left panel shows the shear wave shape for different lateral positions. For each lateral position, the TTP value is determined and plotted in function of the lateral position, as illustrated in the right panel of figure 2.3. Linear regressions are performed on this graph, of which the inverse slope represents the shear wave speed.

This TOF-method as well can give inaccurate results when physiological motion, low SNR or spatial tissue inhomogeneities are present. These problems can potentially lead to gross outlier data leading to less reliable shear wave speed reconstructions. Efforts have been done to improve the accuracy of the shear wave speed estimate by averaging the shear wave speed estimates over multiple spatial locations, employing goodness-of-fit criteria to remove unreliable linear regression results (based on e.g. R^2-value or 95% confidence interval) or iteratively removing data with the largest residual after least squares fitting [94].

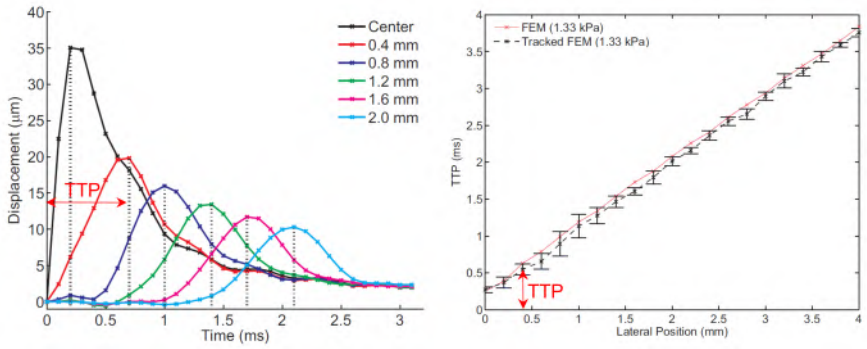

Figure 2.3: Principle of Time-to-peak displacement algorithm: left panel depicts wave shapes for different lateral positions and right panel plots TTP in function of lateral position (adapted from [44]).

2.2.2.3 *RANSAC algorithm*

Wang et al [122] introduced a more robust TOF-method, by applying a widely used iterative fitting algorithm, random sample consensus (RANSAC), to the TTP-data extracted over a 2D region of interest from the SWE acquisition. This algorithm is capable of interpreting data containing a significant number of outliers. The steps of the algorithm are the following:

1. Select randomly a minimal set of data points required to calculate the shear wave speed.
2. Enlarge this data-set including other data that give a shear wave speed consistent with the initial estimate.
3. Repeat above procedure for different data-sets.
4. Select the shear wave speed estimate with the largest number of consistent data points.

The main advantage of this method is its robustness to outliers, but it has the disadvantage that a large number of trial solutions are required. Additionally, the algorithm critically depends on the threshold parameter used to distinguish between inlier and outlier data [94].

2.2.2.4 *Radon sum transformation*

Another robust method that has been proposed is the radon sum transformation by Rouze et al [94]. The radon sum represents a metric that characterizes wave motion along a certain shear wave trajectory, as for

example the total particle displacement or velocity. The space of shear wave trajectories consists of random linear shear wave paths from a starting point (x_{start}, t_{start}) to an ending position (x_{end}, t_{end}), with wave speed $c = (x_{end} - x_{start})/(t_{end} - t_{start})$. For each trajectory, the radon sum is calculated by summing e.g. the displacement data along the trajectory (see right panel of figure 2.4). The optimal shear wave trajectory is then given by the peak radon sum (identifying the shear wave trajectory with the largest shear wave displacement), and the corresponding wave speed is the sought-after shear wave speed. This procedure is illustrated in figure 2.4, where the left panel shows an axial displacement shear wave pattern in space and time and the right panel depicts the corresponding radon sum. The optimal shear wave trajectory is indicated in white in both panels.

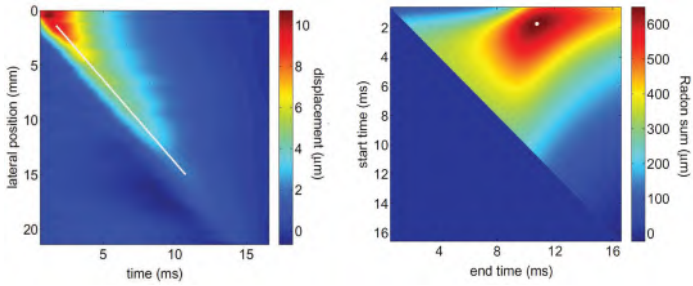

Figure 2.4: Principle of radon sum transformation. Left panel represents displacement data in position and time with white line indicating the optimal shear wave trajectory. Right panel shows radon sum data in position and time with white dot corresponding to the optimal shear wave path (adapted from [94]).

This algorithm is robust to outlier data, as is the RANSAC method, but it is superior to the RANSAC method in computational time. Additionally, it does not rely on determination of adjustable parameters such as the inclusion threshold in the RANSAC method or acceptance criteria in the lateral TTP method [94]. This makes real-time feedback during data acquisition possible. However, the performance of the method in heterogeneous media still needs to be investigated as increased jitter in the shear wave speed estimations is expected due to application of the method on smaller spatial sub-domains.

2.2.3 Shear wave characteristics in the frequency domain

Before describing the methods to analyze the shear wave frequency characteristics, it is essential to note that the wave number k can be complex valued, as the shear wave can be attenuated by different mechanisms: (i) geometrical diffraction, (ii) material absorption, and (iii) energy leakage into the surrounding media. This is represented as

$$k = k_{re} + ik_{im} = \frac{\omega}{c_\phi} + i\alpha \tag{2.11}$$

which is directly linked to phase speed c_ϕ and attenuation coefficient α. The imaginary wave number has the following physical interpretation [123]

$k_{im} < 0$: waves grow exponentially with distance;

$k_{im} = 0$: waves propagate without any damping;

$k_{im} > 0$: waves decay exponentially with distance.

Waves with increasing amplitude have not been physically observed and are thus not considered. The imaginary part of the wave number will thus either be zero or positive (so-called *evanescent waves*) for ARF-generated shear waves. This section describes two techniques to estimate phase speed c_ϕ and attenuation coefficient α (or real and imaginary part of the wave number) from SWE acquisitions, namely shear wave spectroscopy [124] and 2D Fast Fourier Transformation [125]. Both methods analyze the shear wave frequency characteristics based on a selected shear wave propagation path. The methods in this section are described from the point of view of unbounded media, i.e. the propagation path is considered perpendicular to the symmetry axis of the ARF within its depth of field and thus perpendicular to the axis of the tracking beams (see also section 1.2.2.4 in chapter 1). It should be noted that this procedure can be easily extended to bounded media, where the shear wave path will follow the geometrical boundary of the tissue of interest due to wave guiding. The selected path will be quasi-perpendicular to the symmetry axis of the ARF (and axis of the tracking beams) for locations near the pushing zone, but this assumption is not automatically valid for locations further away. This means that the tracking beams might not pick up the total magnitude of the vector representing shear wave particle motion. If this is true, the described methods below allow only a correct estimation of phase speed, but not of attenuation (additional correction factor is necessary).

2.2.3.1 Shear wave spectroscopy algorithm

The concept of shear wave spectroscopy was introduced by Deffieux et al [124] in 2009. It derives the shear wave phase velocity based on the phase gradient of the 1D Fourier transform of the SWE-measured tissue motion data (particle velocity $v(t)$ or displacement $u(t)$ of which their Fourier transforms $\mathcal{F}\{v(t)\}$ and $\mathcal{F}\{u(t)\}$ are related through $\mathcal{F}\{v(t)\} = i\omega\mathcal{F}\{u(t)\}$). When assuming cylindrical waves excited by a harmonic infinite line source, the axial displacement at a large distance from the pushing line is written as [124]

$$u_z(x,t) \approx \frac{i}{4}\sqrt{\frac{2}{\pi k x}}\, e^{-i(k_{re}x-\omega t+\frac{\pi}{4})}\, e^{-k_{im}x}. \tag{2.12}$$

A large distance from the pushing line is defined as $kr >> 1$, where r is the radial distance between analyzed location and source [126]. For waves

propagating in the direction of increasing x, the phase $\phi(x, \omega)$ is thus the following [124]:

$$\phi(x, \omega) = -k_{re}x \tag{2.13}$$

indicating that the phase $\phi(x, \omega)$ of the propagating wave is linearly dependent on wave propagation direction x with the real part of the wave number, i.e. k_{re}, as slope. This means that the real part of the wave number can be estimated from a linear fit of the phase function $\phi(x, \omega)$ along x. Consecutively, phase speed can be calculated by applying equation (2.8).

The practical implementation of this method is illustrated in figure 2.5, which essentially contains four steps. First, a shear wave path is selected and phase information of the waveform is extracted for different lateral locations via the Fourier transform. Second, this phase information is replotted such that the relationship between phase and lateral location for each frequency is known. Third, a linear fitting procedure is performed on the location-phase data, of which the slope represents the real part of the wave number (see equation (2.13)). Fourth, the phase velocity can then be finally derived from wave number and frequency using equation (2.8).

Next to the phase speed, the attenuation coefficient can be determined from the decay of the wave amplitude, caused by multiple factors such as viscous absorption and diffraction. Based on the theory of cylindrical wave approximation, the attenuation coefficient can be derived from equation (2.12). The relationship between amplitude $A_c(x)$ and distance x is thus given by [127]

$$A_c(x) = \frac{1}{4}\sqrt{\frac{2}{\pi k}}x^{-0.5}e^{-\alpha x} \tag{2.14}$$

By taking the natural logarithm on both sides of equation (2.14), we get the following relationship

$$ln(A_c(x)) = ln(A_{co}) - \alpha x - \frac{1}{2}ln(x) \tag{2.15}$$

with $A_{co} = \frac{1}{4}\sqrt{\frac{2}{\pi k}}$. This amplitude equation of a cylindrical wave demonstrates the presence of an extra term compared to that of a plane wave, namely term $\frac{1}{2}ln(x)$. This term represents the effect of diffraction due to the line excitation source (instead of a planar excitation). Practically, equation (2.15) comes down to (i) plotting the logarithmic maximal wave amplitude in function of lateral space x for a specific shear wave trajectory, (ii) taking term

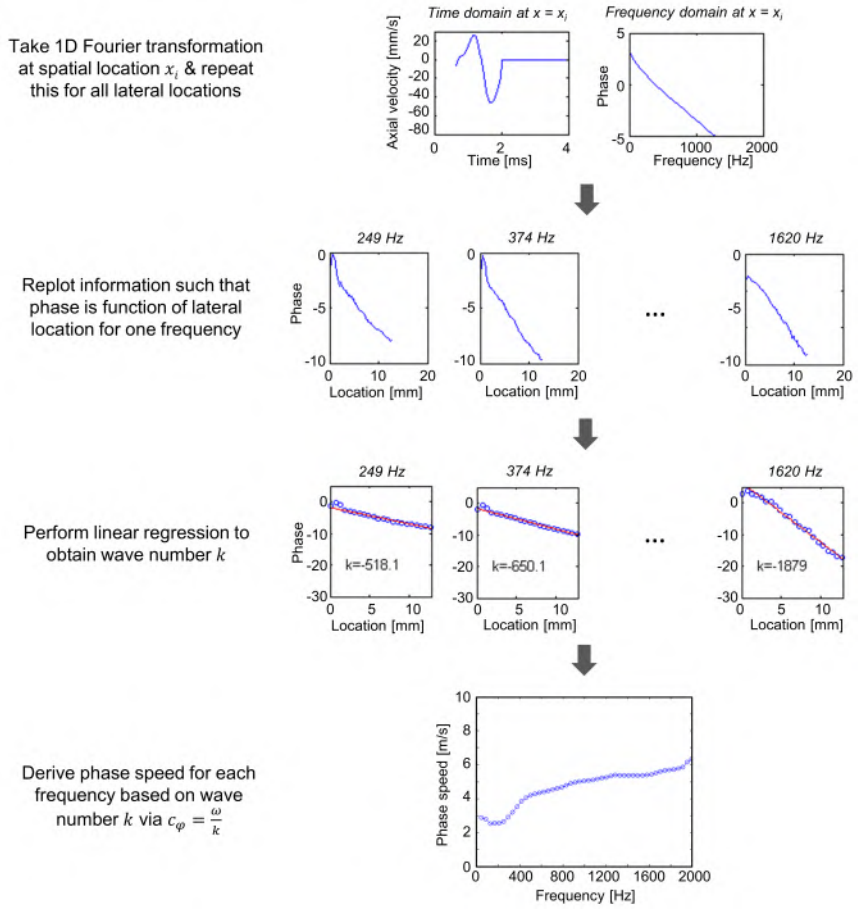

Figure 2.5: Principle of phase speed spectroscopy in deriving phase speed (based on [124]).

$\frac{1}{2}ln(x)$ into account in this plot and (iii) performing a linear regression fit on the resulting plot depicting amplitude data in function of space. The slope of this fit then corresponds to attenuation coefficient α. An example of estimating the attenuation coefficient for a plane wave (transient elastography or TE acquisition) and cylindrical wave (supersonic shear imaging or SSI acquistion) is shown in figure 2.6. This figure demonstrates the importance of the diffraction term in equation (2.15): the estimated attenuation coefficient for the cylindrical wave only corresponds with the value obtained from the TE-acquisition when the diffraction correction is taken into account, otherwise attenuation is overestimated.

Note that it is important to estimate the attenuation coefficient in a region where the cylindrical wave assumption is valid, corresponding to the focal region of the pushing line [127].

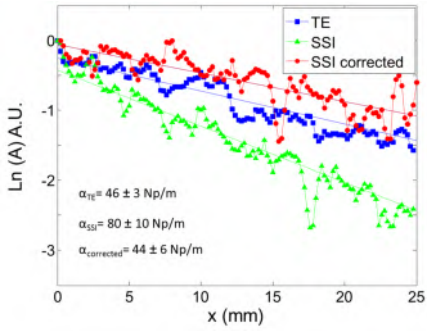

Figure 2.6: Principle of estimating attenuation coefficient based on amplitude decay in function of lateral distance x (adapted from [127]). The effect of discarding the diffraction term is also investigated. AU refers to arbitrary units; Np to Nepers corresponding to ~8.686 dB.

2.2.3.2 2D Fast Fourier transformation

Another way to obtain the dispersive characteristics of the shear wave speed is by taking a 2D Fast Fourier Transformation (2D-FFT) of the axial tissue motion [125]. After one specific shear wave path is selected, a 2D tissue velocity matrix depicting shear wave motion should be obtained, where the rows and columns represent lateral position and time, respectively. Taking the 2D-FFT of this matrix transforms the velocities in the time-space domain to Fourier energies in the frequency-wave number domain. Phase velocity can then be derived by applying equation (2.8). The dispersion curves are obtained by finding for each frequency the phase velocity at which the Fourier transform amplitude is maximal. This procedure is illustrated in figure 2.7.

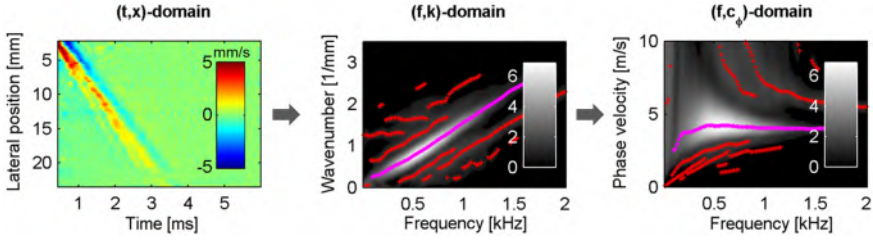

Figure 2.7: Principle of estimating phase velocity based on 2D-FFT: take the 2D-FFT of an axial velocity matrix of a selected shear wave trajectory and track the maximal energies for each frequency. When tracking these high energy points for each frequency in this figure, the pink dots represent the phase velocity or wave number with maximal energy and the red dots indicate velocities or wave numbers with high energy.

It should be noted that the 2D-FFT analysis is sensitive to the finite spatial and temporal range of the axial velocity shear wave pattern, which might introduce biases in the extracted dispersion characteristics [128].

Nenadic et al [129] showed that the attenuation coefficient can also be derived based on the 2D-FFT of the axial velocity signal, an approach that is called *Attenuation Measuring Ultrasound Shearwave Elastography* or *AMUSE*. When assuming plane wave propagation, the attenuation coefficient is the following

$$\alpha = \frac{\pi}{\sqrt{3}} FWHM \tag{2.16}$$

with $FWHM$ corresponding to the full-width half maximum of the 2D FFT signal at one specific frequency. It can be proven that equation (2.16) is also valid when the US elastography method used measures particle velocities instead of particle displacements [130]. However, ARF-excitation generates cylindrical waves rather than plane waves, indicating that above equation is not valid for ARF-excited shear waves. Indeed, Nenadic et al proposed to weight the shear wave signal by a factor $\sqrt{x}$ to compensate for this difference in wave type. However, it is unsure whether this $\sqrt{x}$ weighting factor would apply for shear wave motion near the source or for shear wave motion generated by an asymmetric excitation source (which is a more realistic representation of the ARF) [131]. The actual attenuation coefficient of a cylindrical source is the following [131]

$$\alpha = \frac{\pi}{\sqrt{15}} FWHM \tag{2.17}$$

The procedure for determining the attenuation coefficient based on 2D-FFT can thus be done simultaneously with estimating phase speed based on 2D-FFT. Instead of looking at the maximal Fourier energy content, we now investigate the FWHM of the Fourier signal at a specific frequency, as illustrated in figure 2.8. This procedure needs to be repeated for all frequencies.

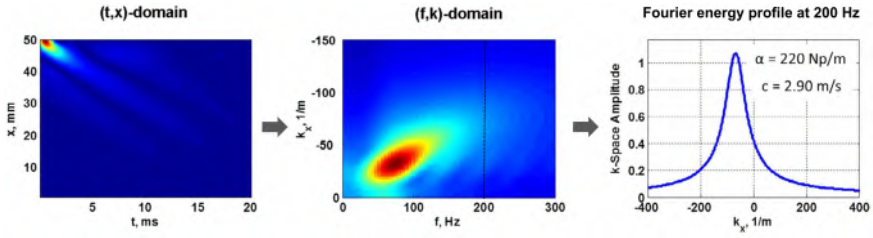

Figure 2.8: Principle of estimating attenuation coefficient based on 2D-FFT: take the 2D-FFT of an axial velocity matrix of a selected shear wave trajectory and study the FWHM of the Fourier signal at each frequency (adapted from [130]).

2.3 Physics of shear wave propagation: relationship between tissue and shear wave characteristics

This section presents the theoretical link between the tissue characteristics described in section 2.1 and the shear wave characteristics discussed in section 2.2. Depending on the material and geometrical characteristics of the tissue of interest, different mathematical relationships can be derived. This section gives the wave equations of wave propagation in unbounded elastic and viscoelastic media (see section 2.3.2), followed by the wave equations for bounded elastic and viscoelastic media (see section 2.3.3). In the latter subsection, the effect of the surrounding (vacuum vs. fluid) on wave propagation is also studied. The wave physics in unbounded and bounded media is governed by the same set of equilibrium equation, as described in the first subsection (section 2.3.1). A more complete overview of the theoretical background on wave motion can be found in [86], [123].

2.3.1 General equations of wave motion

Wave propagation is governed by the general equations of motion, which are denoted in a Cartesian tensor notation as follows:

$$\sigma_{ij,j} + \rho f_i = \rho \ddot{u}_i \tag{2.18}$$

with σ_{ij} representing stress, ρ density, f_i external forces and u_i displacement ($i, j = 1, 2, 3$). Written out in full, equation (2.18) represents the following three equations:

$$\begin{aligned}
\frac{\partial \sigma_{11}}{\partial x_1} + \frac{\partial \sigma_{21}}{\partial x_2} + \frac{\partial \sigma_{31}}{\partial x_3} + \rho f_1 &= \rho \frac{\partial^2 u_1}{\partial t^2}, \\
\frac{\partial \sigma_{12}}{\partial x_1} + \frac{\partial \sigma_{22}}{\partial x_2} + \frac{\partial \sigma_{32}}{\partial x_3} + \rho f_2 &= \rho \frac{\partial^2 u_2}{\partial t^2}, \\
\frac{\partial \sigma_{13}}{\partial x_1} + \frac{\partial \sigma_{23}}{\partial x_2} + \frac{\partial \sigma_{33}}{\partial x_3} + \rho f_3 &= \rho \frac{\partial^2 u_3}{\partial t^2}
\end{aligned} \tag{2.19}$$

These equations describe any kind of wave propagation, including shear wave propagation excited by an ARF. If no boundary conditions are considered, the equations represent *bulk wave propagation* (see section 2.3.2), otherwise they describe *guided wave propagation* (see section 2.3.3).

2.3.2 Wave motion in unbounded media

This subsection describes the theoretical relationships of wave motion in unbounded media, first for an elastic tissue response, followed by the assumption of a viscoelastic material model.

2.3.2.1 *Wave motion in unbounded elastic media*

Equation (2.18) can be rewritten by eliminating the stress and strain factors based on considering equation (2.2) together with the strain-displacement equations $\varepsilon_{ij} = \frac{1}{2}(u_{i,j} + u_{j,i})$. When neglecting body forces, the following transformed equations of motions are obtained ($i, j = 1, 2, 3$):

$$(\lambda + \mu)u_{j,ij} + \mu u_{i,jj} = \rho \ddot{u}_i \tag{2.20}$$

Equation (2.20) represents the following three equations:

$$\begin{aligned}
(\lambda + \mu)\frac{\partial}{\partial x_1}\left(\frac{\partial u_1}{\partial x_1} + \frac{\partial u_2}{\partial x_2} + \frac{\partial u_3}{\partial x_3}\right) + \mu\left(\frac{\partial^2}{\partial x_1^2} + \frac{\partial^2}{\partial x_2^2} + \frac{\partial^2}{\partial x_3^2}\right)u_1 &= \rho\frac{\partial^2 u_1}{\partial t^2} \\
(\lambda + \mu)\frac{\partial}{\partial x_2}\left(\frac{\partial u_1}{\partial x_1} + \frac{\partial u_2}{\partial x_2} + \frac{\partial u_3}{\partial x_3}\right) + \mu\left(\frac{\partial^2}{\partial x_1^2} + \frac{\partial^2}{\partial x_2^2} + \frac{\partial^2}{\partial x_3^2}\right)u_2 &= \rho\frac{\partial^2 u_2}{\partial t^2} \\
(\lambda + \mu)\frac{\partial}{\partial x_3}\left(\frac{\partial u_1}{\partial x_1} + \frac{\partial u_2}{\partial x_2} + \frac{\partial u_3}{\partial x_3}\right) + \mu\left(\frac{\partial^2}{\partial x_1^2} + \frac{\partial^2}{\partial x_2^2} + \frac{\partial^2}{\partial x_3^2}\right)u_3 &= \rho\frac{\partial^2 u_3}{\partial t^2}
\end{aligned} \tag{2.21}$$

When using the vector notation (vector symbols are indicated in **bold**) and introducing the nabla operator $\nabla = \left(\frac{\partial}{\partial x_1}, \frac{\partial}{\partial x_2}, \frac{\partial}{\partial x_3}\right)$, equation (2.21) is transformed into:

$$\mu\nabla^2\boldsymbol{u} + (\lambda + \mu)\nabla(\nabla \cdot \boldsymbol{u}) = \rho\ddot{\boldsymbol{u}} \tag{2.22}$$

These equations thus describe any kind of wave propagation in a homogeneous isotropic linear elastic material, regardless of the considered geometry. In an unbounded medium, this relationship can be further simplified by using Helmholtz decomposition, i.e. decompose the displacement vector field as a pair of potentials: a vector potential $\boldsymbol{\psi}$, which has zero divergence ($\nabla \cdot \boldsymbol{\psi} = 0$), and a scalar potential ϕ, which has zero curl ($\nabla \times \phi = 0$).

$$\boldsymbol{u} = \nabla\phi + \nabla \times \boldsymbol{\psi} \tag{2.23}$$

Substituting equation (2.23) in equation (2.20) gives the following:

$$\nabla\left((\lambda + 2\mu)\nabla^2\phi - \rho\frac{\delta^2\phi}{\delta t^2}\right) + \nabla \times \left(\mu\nabla^2\boldsymbol{\psi} - \rho\frac{\delta^2\boldsymbol{\psi}}{\delta t^2}\right) = 0 \tag{2.24}$$

Above equation is only satisfied if both terms vanish. This leads to the following two equations

$$\nabla^2\phi = \frac{\rho}{\lambda + 2\mu}\frac{\delta^2\phi}{\delta t^2} = \frac{1}{c_L^2}\frac{\delta^2\phi}{\delta t^2} \tag{2.25}$$

$$\nabla^2\boldsymbol{\psi} = \frac{\rho}{\mu}\frac{\delta^2\boldsymbol{\psi}}{\delta t^2} = \frac{1}{c_T^2}\frac{\delta^2\boldsymbol{\psi}}{\delta t^2} \tag{2.26}$$

describing *longitudinal* or *compressive* and *shear* or *transverse* waves, respectively. These equations also give directly the formula for shear wave propagation speed c_T and longitudinal wave speed c_L:

$$c_L^2 = \frac{\lambda + 2\mu}{\rho} \tag{2.27}$$

$$c_T^2 = \frac{\mu}{\rho} \tag{2.28}$$

Equation (2.28) corresponds with equation (1.1), which denotes the typical equation used in the field of shear wave elastography, but one has to be aware with the assumptions behind this equation (i.e. homogeneity, isotropy, linearity, elasticity and bulk medium).

2.3.2.2 Wave motion in unbounded viscoelastic media

The equation of wave propagation (equation (2.18)) in a viscoelastic material (Kelvin/Voigt-model: equation (2.6) and equation (2.7)) can be solved in a similar way as shown in section 2.3.2.1: the displacement vector is again split into an irrotational and incompressible component, leading to the equations for longitudinal and transverse waves, respectively (see [86], [123] for more information). We will from now on focus only on shear waves, as these are mainly excited by ARF driven SWE. The resulting propagation speed and attenuation for shear waves is given by:

$$c_T = \sqrt{\frac{2\left(\mu_1^2 + \omega^2\mu_2^2\right)}{\rho\left(\mu_1 + \sqrt{\mu_1^2 + \omega^2\mu_2^2}\right)}} \tag{2.29}$$

$$\alpha_T = \sqrt{\frac{\rho\omega^2\left(\sqrt{\mu_1^2 + \omega^2\mu_2^2} - \mu^2\right)}{2\left(\mu_1^2 + \omega^2\mu_2^2\right)}} \tag{2.30}$$

The speed of the wave is now no longer only dependent on the material characteristics as in equation (2.28), but also on the excited frequencies in

the wave. Example of this frequency-dependent relationship of shear wave speed and attenuation in a tissue-like medium are given in figure 2.9 and figure 2.10. In these figures, frequencies from 0 to 2000 Hz are considered as these represent a realistic excited frequency range during a SWE acquisition. Figure 2.9 shows that phase speed increases for higher frequencies, when compared to their elastic bulk speed. Attenuation is also higher for higher frequencies. When stiffness increases, the phase speed and attenuation curves shift upwards.

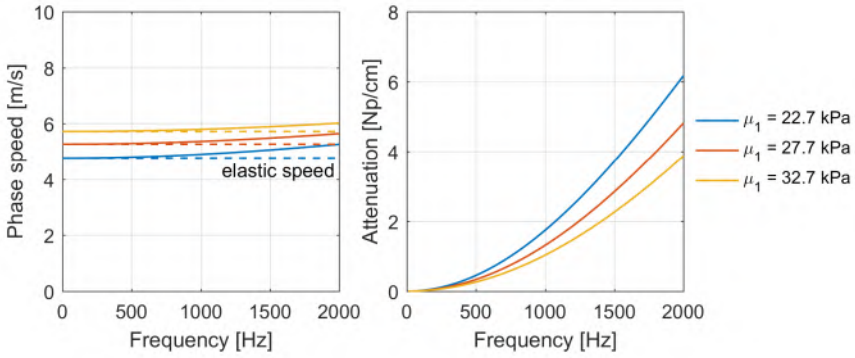

Figure 2.9: Variation of shear wave speed and attenuation for a viscoelastic bulk medium when stiffness alters (ρ =1000 kg/m^3 and μ_2 = 1 Pas). Dotted lines represent bulk speed in elastic medium.

Figure 2.10 shows the effect of increasing viscosity on phase speed and attenuation. For low frequencies, this effect is minimal, but for higher frequencies, both phase speed and attenuation increase. Thus, in general, the phase velocity offset reflects the stiffness of the material at very low frequency whereas the slope gives information about viscosity [124].

2.3.3 Wave motion in bounded media

Guided waves are waves that compulsorily require boundaries to maintain propagation, such as waves in a rod, plate, tube or plate-like laminates. These boundaries cause multiple reflections, mode conversions and interferences of longitudinal and shear waves, creating a wave guide character of sound propagation within the boundaries of the considered medium. Well-known wave modes that have been discovered (and named after their discoverer) are *Rayleigh* waves for surfaces; *Love* and *Lamb* waves for plates; and *Stoneley* waves at interfaces.

This section focuses on Lamb wave propagation (especially the antisymmetric modes), as ARF-excited shear wave propagation in bounded tissues such as the arteries [14], [125], [132] and the myocardium [38], [133], [134]

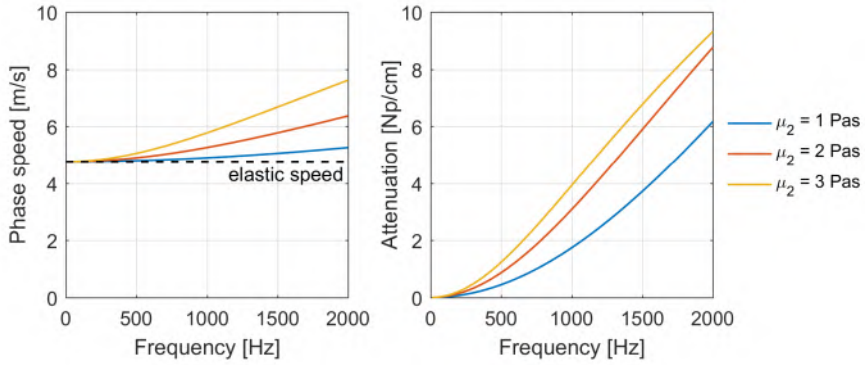

Figure 2.10: Variation of shear wave speed and attenuation for a viscoelastic bulk medium when viscosity alters (ρ = 1000 kg/m^3 and μ_1 =22.7 kPa). Dotted lines represent bulk speed in elastic medium.

are often approximated as antisymmetric Lamb wave propagation. Their particle motion is in the same plane as that contains the wave propagation direction and the plate normal. Two sets of Lamb wave modes are illustrated in figure 2.11: symmetric and antisymmetric modes. Symmetric modes are symmetric in displacement with respect to the mid-plane of the plate and are denoted as S_i, with i the order of the mode. Antisymmetric modes displace antisymmetrically with respect to the mid-plane of the plate and are denoted as A_i. Sound perturbations within a wave guide can thus be represented as a superposition of these resonant guided wave modes (so-called *eigen-modes*).

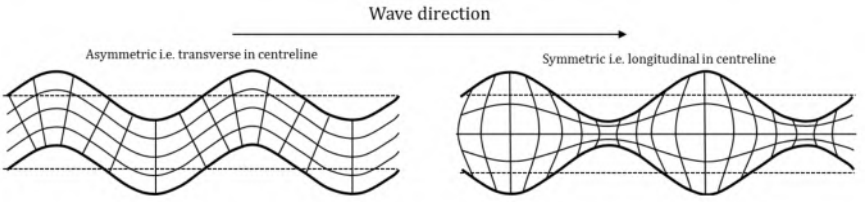

Figure 2.11: Diagrammatic representation of symmetric and antisymmetric Lamb wave modes (adapted from [135]).

This subsection first describes wave motion in bounded elastic media in vacuum, followed by the relationship between wave and tissue characteristics in fluid-loaded bounded elastic and viscoelastic media.

2.3.3.1 Wave motion in bounded elastic media in vacuum

Lamb waves in elastic media obey the same equilibrium equations as shear and longitudinal wave modes in unbounded elastic media (i.e. equation (2.25)

and equation (2.26)). As Lamb waves act in a plane, these equations can be reduced to 2D by assuming the plane strain conditions. When considering a plate with thickness $2h$ as displayed in figure 2.12, the equations of motion are reduced to:

$$\frac{\delta^2\phi}{\delta x_1^2} + \frac{\delta^2\phi}{\delta x_3^2} = \frac{1}{c_L^2}\frac{\delta^2\phi}{\delta t^2} \tag{2.31}$$

$$\frac{\delta^2\psi}{\delta x_1^2} + \frac{\delta^2\psi}{\delta x_3^2} = \frac{1}{c_T^2}\frac{\delta^2\psi}{\delta t^2} \tag{2.32}$$

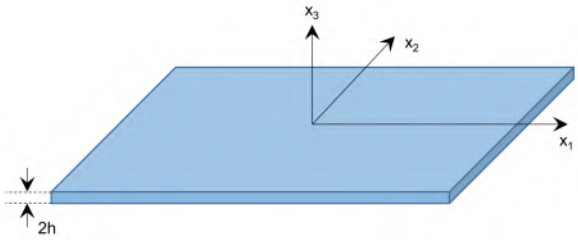

Figure 2.12: Schematic geometry of the plate for deriving Lamb wave equations.

These equations together with appropriate boundary conditions, representing the structural geometry and surrounding, can be solved by assuming sinusoidal solutions for this problem. This is a widely used approach in physical acoustics and corresponds to a classical eigenvalue problem. For a free plate problem, the plate is situated in vacuum and the boundary conditions at the edges are

$$\sigma_{31} = \sigma_{33} = 0 \text{ at } x_3 = \pm h \tag{2.33}$$

Assuming now sinusoidal solutions for the problem defined by equation (2.31) and equation (2.32), together with before-mentioned boundary conditions, this leads to the following dispersion equations:

$$\frac{tan(qh)}{tan(ph)} = -\left[\frac{4k^2pq}{(q^2-k^2)^2}\right]^{\pm 1} \tag{2.34}$$

with $p^2 = \frac{\omega^2}{c_L^2} - k^2$, $q^2 = \frac{\omega^2}{c_T^2} - k^2$, angular speed ω and wave number k. The exponent +1 describes the symmetric modes, whereas the exponent −1 represents the antisymmetric modes. Equation (2.34) gives the link between angular speed ω and wave number k, or frequency f and phase speed c_ϕ.

If we retake our numerical example from section 2.3.2.2, the resulting dispersion curves for an elastic plate with the same material properties are illustrated in figure 2.13. It is immediately clear that multiple symmetric and antisymmetric modes are present in the considered window of figure 2.13. Actually, an infinite number of wave modes characterize the considered problem, whereas only two modes exist for the bulk wave problem, i.e. longitudinal and shear wave mode. There are only two Lamb wave modes present at low frequencies, called A_0- and S_0-mode, and all subsequent modes at higher frequencies have a cut-off frequency in the low frequency range. These are called A_j- and S_j-mode with $j = 1, 2, \ldots, n$ with $n \in \mathbb{Z}$ when cut-off frequency increases. During an ARF-excitation of a SWE-acquisition, it has been reported that mainly antisymmetric modes will be excited, more specifically the A_0-mode [125], due to the geometry and orientation of the ARF volume force with respect to the tissue of interest. Therefore, in the following sections, we will focus on the antisymmetric dispersion curves.

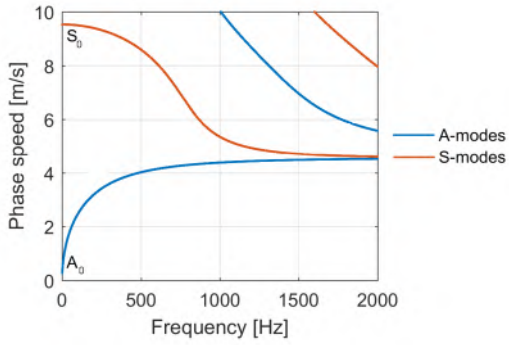

Figure 2.13: Dispersion equations for an elastic plate in vacuum (ρ =1000 kg/m^3 and μ_1 =22.7 kPa).

It should be noted that equation (2.34) has no analytical solutions, and thus numerical techniques (such as bisection, secant, and inverse quadratic interpolation methods, available in the *Matlab*-function *fzero*) are needed to solve this non-linear equation.

2.3.3.2 *Wave motion in fluid-loaded bounded elastic media*

For a fluid-loaded plate, continuity of the displacement and stresses at the boundaries should be ensured, leading to the following boundary conditions

$$\begin{aligned} \sigma_{33}^{fluid} &= \sigma_{33}^{solid}, \\ \sigma_{31}^{solid} &= 0, \text{ and} \\ u_3^{fluid} &= u_3^{solid} \text{ at } x_3 = \pm h. \end{aligned} \tag{2.35}$$

Considering equation (2.31) and equation (2.32) together with these boundary conditions, results in a dispersion equation with an extra term compared to equation (2.34). This term represents the damping or energy loss due to radiation of energy of the guided wave into the surrounding medium (now called a *leaky Lamb wave*) [125]. The antisymmetric Lamb wave dispersion equation is the following [38], [136]:

$$4k^2\eta\beta cosh(\eta h)sinh(\beta h) - (2k^2 - k_T^2)^2 sinh(\eta h)cosh(\beta h) = \frac{\rho_f \eta k_T^2}{\rho \eta_f} cosh(\eta h)cosh(\beta h) \tag{2.36}$$

with ρ_f the density of the fluid, k the Lamb wave number of the solid, $k_j = \omega/c_j$ the compressional and shear wave number of the solid for $j = L$ and $j = T$ respectively, $\beta = \sqrt{k^2 - k_T^2}$, $\eta = \sqrt{k^2 - k_L^2}$, $\eta_f = \sqrt{k^2 - k_f^2}$ and k_f is the compressional wave number of the fluid. This equation can be simplified by assuming the following for guided waves generated with ARF driven SWE in tissues: (i) $k_f \approx k_L$, as fluids (blood) have a similar compressional wave numbers as the studied solid (tissue) for the considered application, (ii) $\eta_f \approx \eta = \sqrt{k^2 - k_L^2} \approx k$ as the Lamb wave number (k) is on the same order of magnitude as the shear wave number (k_T) and the compressional wave number (k_L) is much smaller than the shear wave number (k_T) and (iii) $\rho_f \approx \rho$, since blood has a similar density as tissue. This reduces equation (2.36) to [38], [136]

$$4k^3\beta cosh(kh)sinh(\beta h) - (k_T^2 - 2k^2)^2 sinh(kh)cosh(\beta h) = k_T^4 cosh(kh)cosh(\beta h) \tag{2.37}$$

We will reconsider the numerical example of previous section, but now the plate is surrounded with water (ρ_f = 1000 kg/m^3). For ARF driven SWE, the phase velocity of the plate wave will be much lower than the compressional wave speed of the fluid, as is also presumed in the second above-mentioned asumption, indicating that no energy will leak into the surrounding [123]. Therefore, figure 2.14 shows the resulting dispersion curves by assuming a real wave number (thus no attenuation). Nevertheless, dispersion characteristics are altered by the presence of the water compared to those in vacuum, as is noticeable from the extra term present in equation (2.36) compared to equation (2.34) which is demonstrated in figure 2.14.

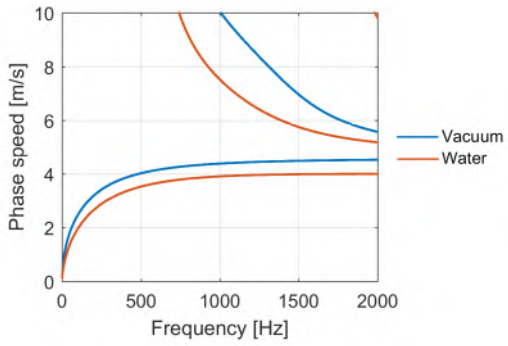

Figure 2.14: Antisymmetric dispersion equations of an elastic plate in water vs. an elastic plate in vacuum (ρ_f =1000 kg/m^3, ρ =1000 kg/m^3 and μ_1 =22.7 kPa).

2.3.3.3 Wave motion in fluid-loaded bounded viscoelastic media

Lamb wave propagation in a viscoelastic plate is governed by the same simplified equations (i.e. equation (2.37)) as for an elastic fluid-loaded plate. However, the Lamé elastic parameters now become complex values as mentioned in equation (2.6) and equation (2.7), according to the Kelvin/Voigt model. This means that both wave numbers k and k_T also become complex values (see section 2.2.3). Retaking our numerical example, resulting dispersion characteristics are illustrated in figure 2.15. This figure shows mainly an effect of viscosity at higher frequencies, leading to increased phase speed and attenuation compared to a fluid-loaded elastic plate. Note that the attenuation in this case could be caused by a combination of energy absorption due to viscosity and energy leaking into the surrounding. However, the latter effect is non-existent for ARF driven SWE in tissue as the longitudinal wave speed of body fluids is much higher than the lamb wave speeds of tissue.

To solve this non-linear problem defined in equation (2.37) in the complex domain, we used the Levenberg-Marquard-Fletcher method, as implemented in *LMFnlsq.m* [137] in *Matlab*. Another option to solve these equations is using the commercial software *'Disperse'*, developed by Brian Pavlakovi and Mike Lowe at Imperial College [138].

2.4 Practical implementation: reporting shear wave or material characteristics

When studying elastography literature, one can observe that different shear wave quantities are reported for various ARF driven SWE based techniques and distinct tissues of interest. Therefore, this section gives an overview of the reported parameters and quantities in SWE together with their assumptions.

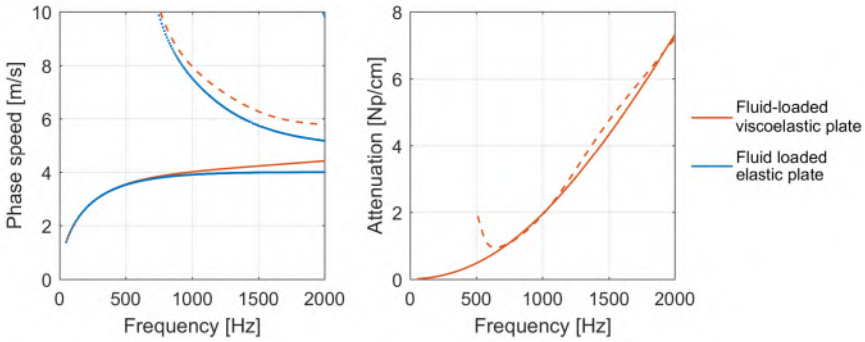

Figure 2.15: Antisymmetric dispersion equations of a viscoelastic plate in water vs. an elastic plate in water (ρ_f =1000 kg/m^3, ρ =1000 kg/m^3, μ_1 =22.7 kPa and μ_2 =1 Pas). Orange full line indicates A_0-mode, orange dotted line indicates A_1-mode. A1-mode has a cut-off frequency at around 500 Hz, explaining, the course of the attenuation curve.

Additionally, this section discusses more in detail the practical implementation of the methodology to obtain the desired SWE quantity. This section thus links all above three sections.

The first subsection discusses group speed analysis, which is usually applied when assuming a first order tissue model in combination with an unbounded tissue geometry. The second subsection explains phase speed analysis, typically used for higher order tissue models and/or bounded tissue geometries. The goal of this section is not to present a complete overview of all available material characterization techniques in ARF driven SWE (see a.o. [139] for a more general overview), but to give a short introduction to some methods relevant for this thesis. Finally, the last subsection provides some future research perspectives for SWE-based material characterization techniques.

Note that both types of analyzes can be applied when assuming any tissue model or geometry, but one has to be cautious with the assumptions accompanied with these methods e.g. applying group speed analysis on an unbounded viscoelastic medium characterizes the averaged behavior of the shear wave. Additionally, both types of analysis assume a known direction of wave travel. This poses no problems for isotropic media, as we can assume the following: (i) a perpendicular shear wave trajectory with respect to the axis of the ARF and tracking beams for unbounded media (within the depth of field of the ARF), and (ii) a propagation path following the geometric boundary of the tissue of interest for bounded media. The situation might get more complex for anisotropic media when no information is known about the orientation of the fiber structure with respect to the tracking beams, as the

shear wave is guided along the fiber. Solutions and insights to this problem have been proposed in [117], [140].

2.4.1 Group speed analysis

Group speed analysis examines the shear wave characteristics in the time domain, using one of the algorithms mentioned in section 2.2.2. This is the kind of processing usually implemented in commercially available ultrasound systems. The reported parameter is typically group speed [m/s], shear modulus [Pa] or Young's modulus [Pa]. One has to be aware that when a shear or Young's modulus is reported, equation (2.28) (with equation (2.4) in case of Young's modulus) is used to derive tissue stiffness, assuming the conditions of a homogeneous isotropic linear elastic unbounded medium. A shear wave speed or stiffness estimate can be obtained per shear wave trajectory, or per sub-domain (by reducing the length of the shear wave trajectory considered for the TOF-estimate) or in the limit per pixel, allowing to create a 2D stiffness image [44].

Biological tissues are in general anisotropic, viscoelastic and non-linear, which has the following influence on the derived shear wave quantity [90]:

Anisotropy: orientation-dependent shear wave speed or elastic moduli;

Viscoelasticity: rate-dependent shear wave speed or elastic moduli;

Non-linearity: strain-dependent shear wave speed or elastic moduli.

If material or geometrical dispersion is present, and the wave shape is not completely distorted (see figure 2.2), the group velocity can be calculated. It then represents an average of the phase velocities over the frequency content of the shear wave [102]. However, this measured group velocity in a dispersive material depends on the excited frequency content of the shear wave (function of the ARF excitation beamwidth and duration, the material stiffness/viscosity, and shear attenuation [141], [142]). Therefore, it is crucial to report the exact conditions in which the group velocity measurement is made or to report the frequency information of the generated shear wave next to the group speed. This way of reporting is then complete and appropriate to interpret and compare the results between different studies [143]. Note that the frequency-dependency of the group velocity in dispersive media is also one of the causes of the variability between shear wave speed measurements across different ultrasound devices in viscoelastic media (as mentioned in section 1.1.2.1).

2.4.2 Phase speed analysis

Phase speed analysis studies the shear wave characteristics in the frequency domain (see section 2.2.3). The reported quantities are typically phase speed [m/s] (and attenuation [Np/m] or [dB/m]) or tissue stiffness [Pa] (and viscosity [Pas]). When reporting tissue stiffness, there are two main approaches to

estimate these parameters: approaches that assume a rheological model and approaches that do not assume a rheological model. Traditionally, model-based approaches used solely the measured frequency-dependent relationship of phase speed to estimate material parameters, hereby assuming a fixed relationship between phase velocity and attenuation coefficient [130]. This largely stems from the inability to make stable and reproducible measurements of shear wave attenuation. Only recently, model-free approaches [127], [130], [144] have been introduced to estimate material parameters of an unbounded viscoelastic medium based on both measured phase velocity and attenuation. The principles of both approaches are shortly described below.

1. **Model-based approaches** - these methods first use the shear wave spectroscopy algorithm or the 2D FFT method to derive the relationship between phase speed and frequency. A recent (2015) study on the liver [142] has shown poor success in extracting frequency information with phase spectroscopy due to phase aberration and acoustic attenuation. The authors of this study concluded that the 2D FFT method is more robust in deriving frequency characteristics of the shear wave in human liver data. The success rate of the 2D FFT method in this study was only 72.6% due to insufficient SNR in the SWE acquisitions. This indicates one of the biggest challenges in performing a phase speed analysis: recording SWE data with sufficient SNR.

   After the measured dispersion characteristics are obtained, the model-based approaches assume a rheological material model to estimate tissue stiffness based on the acquired shear wave data. This can be a single (elastic), dual (viscoelastic) or multi-parameter material model, for which a theoretical relationship between phase speed and frequency is known (see section 2.3). Typically, the material parameters are estimated by looking for the theoretical dispersion relationship between phase speed and frequency that best resembles the measured dispersion characteristics of the main excited mode. This is typically done by performing a least squares fitting procedure or applying the Radon sum approach to look for the most plausible dispersion trajectory in the measured 2D FFT spectrum. For unbounded viscoelastic media, the dispersion relationship can also be represented by a linear model [142] instead of the Kelvin/Voigt model in equation (2.29)

$$c_\phi = c_0 + \frac{dc}{df} f \tag{2.38}$$

   with c_0 the intercept at zero frequency and $\frac{dc}{df}$ the dispersion slope, which simplifies the material model fitting and leads to more robust parameter estimations compared to equation (2.29).

2. **Model-free approaches** - these methods require measurement of wave velocity and attenuation at a given frequency using no rheological model (section 2.2.3.1 and section 2.2.3.2), where again the 2D FFT method represents a more robust way to obtain phase velocity and attenuation coefficient [130].

   From these measurements, the complex modulus $\mu(\omega)$ of an unbounded viscoelastic medium (equation (2.5)) can be estimated as follows [130]

$$\mu(\omega) = \mu'(\omega) + i\mu"(\omega) = \rho \left(\frac{\omega}{\frac{\omega}{c_\phi} + i\alpha} \right)^2 \tag{2.39}$$

   where $\mu'(\omega)$ and $\mu"(\omega)$ are the storage and loss shear moduli. This method thus assumes a linear, homogeneous, isotropic and viscoelastic medium, but no particular rheological model to estimate the tissue material properties. For a bounded viscoelastic medium, equation (2.39) can also be applied for ARF driven SWE, as the leakage of wave energy into the fluid is nihil, and thus wave attenuation is caused solely by energy absorption due to viscosity.

Phase speed and attenuation coefficient estimates are typically region-based, as a certain lateral extent of wave propagation is necessary for analysis in the Fourier domain. As for group velocities, phase speed values are orientation- and strain-dependent when applied to anisotropic and nonlinear tissue.

2.4.3 State-of-the-art in material characterization techniques

The most general SWE-derived quantities are thus the quantities obtained from model-free approaches, such as group speed, phase speed (and attenuation coefficient) and complex shear modulus. Nevertheless, still a lot of research has been performed or is still ongoing to further improve tissue characterization in SWE. Investigators have looked into more advanced material characterization such as imaging transverse isotropic properties of muscle [117], but also into manners to characterize tissue material properties different from the classical approaches mentioned in section 2.4.1 and section 2.4.2. We will describe some of these new material characterization approaches below, which have been primarily focused on unbounded viscoelastic media.

Rouze et al [145] introduced in 2016 a material characterization method that characterizes shear stiffness μ_1 and viscosity μ_2 solely based on group velocity analysis. The proposed method determines the group speed based

on the axial displacement data v_{disp} and the axial velocity data v_{vel}, and uses the difference $v_{vel} - v_{disp}$ as a measure for the material viscosity. Material characteristics can then be derived via analytically determined lookup tables using a model-based approach (Kelvin/Voigt model) for shear stiffness μ_1 and viscosity μ_2 in function of mean group velocity and the difference between both group velocities, as shown in figure 2.16. The main advantage of this method is that it avoids the Fourier decomposition of the shear wave signal, which can be noisy, especially on in vivo shear wave data.

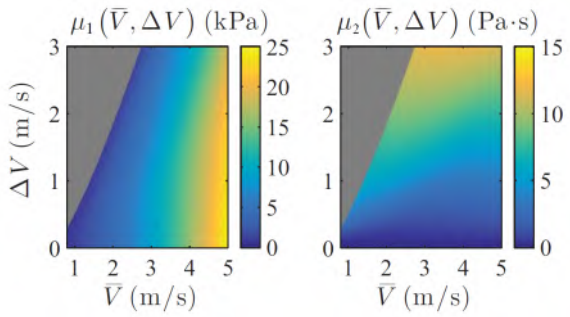

Figure 2.16: Lookup table for shear stiffness μ_1 and viscosity μ_2 in function of $\overline{V} = (v_{disp} + v_{vel})/2$ and $\Delta V = v_{vel} - v_{disp}$ (adapted from [145]).

Van Sloun et al [116] proposed in 2017 to consider the viscoelastic material as a dynamic linear system, of which the impulse response can be locally identified by input-output analysis of shear wave time-displacement signals at two different lateral locations. A local model-based estimator of the impulse response is derived from the Navier-Stokes equation (assuming Kelvin/Voigt model), which is then fitted to the experimental data in a least squares fashion. This principle of this method is illustrated in figure 2.17. This method is able to generate stiffness and viscosity estimates in a pixel-based point-to-point fashion.

Next to this, a lot of research and effort has been put into developing SWE simulation platforms that are useful for a better understanding of the ongoing shear wave physics, but also for developing and validating new material characterization techniques in SWE. These simulations are typically realized by using an analytical approach based on Green's formalism [54], [65], [146], [147] or the Finite Element Method (FEM) [148], [149].

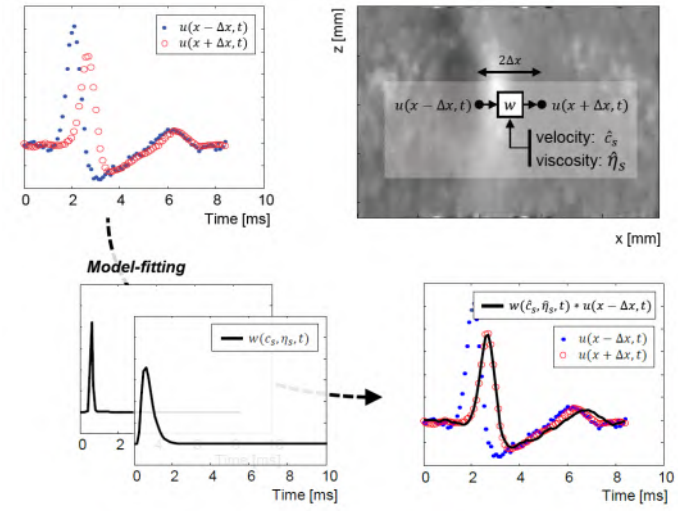

Figure 2.17: Principle of method proposed by van Sloun et al [116]. Illustration of how the impulse response w is estimated from the time-displacement curves at two lateral locations $x - \Delta x$ and $x + \Delta x$ (adapted from [116]).

Chapter 3

Cardiac shear wave elastography

Shear wave elastography (SWE) of the heart can be realized in different manners by using intracardiac [150], trans-esophageal [151] or conventional transducers [152]. Intracardiac and trans-esophageal SWE acquisitions bring the probe closer to the organ of interest (requiring less deep image acquisitions) and eliminate all field of view limiting factors such as ribs. However, these applications require small transducers with sufficient power to generate an acoustic radiation force (ARF) [153]. Furthermore, both methods are at discomfort of the patient, especially intracardiac SWE as it is (minimally) invasive. In this PhD thesis, we focused on transthoracic SWE with conventional ultrasound (US) transducers.

Before discussing the barriers to overcome in the field of cardiac SWE, a short general description of the mechanical behavior of the heart is provided in section 3.1. This section focuses on relevant cardiac features influencing shear wave propagation and subsequent processing in SWE, i.e. cardiac location, geometry, surrounding and material characteristics. Based on these features, the technical and mechanical challenges related to cardiac SWE are identified in section 3.2. The last section (section 3.3) then gives an overview of the state-of-the-art in cardiac SWE and pinpoints the remaining questions.

3.1 Mechanical tissue behavior of the heart

The heart is a specialized muscle that contracts regularly and continuously to pump blood, containing oxygen, nutrients, wastes and many other substances,

to the body and lungs. In order to fulfill this function, it has a specific morphological and structural design of which the features affecting the SWE acquisition are enlightened in this section. The first subsection focuses on the location and the morphology of the heart, whereas the second subsection describes the different layers and its constituents of the cardiac wall more in detail. The mechanical response of the cardiac wall is shortly discussed in the third subsection. The last subsection describes the effect of pathology on the heart's geometry, structure and material properties. Most of this section is inspired on the textbook on *Anatomy & Physiology* by Marieb and Hoehn [154].

3.1.1 Location and morphology of the heart

The heart is enclosed in the medial cavity of the thorax (so-called *mediastinum*) and it extends obliquely for 12 to 14 cm from the second rib to the fifth intercostal space (see left panel of figure 3.1). It rests on the diaphragm and is situated anterior to the vertebral column and posterior to the sternum. The heart is laterally surrounded with the right and left lung, which partially cover the heart, as shown in the right panel of figure 3.1. Approximately two-thirds of the heart's mass lies to the left of the midsternal line.

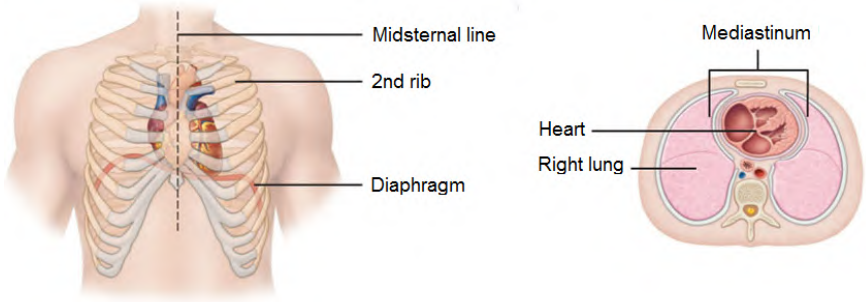

Figure 3.1: Location of the heart in longitudinal view (left panel) and cross-sectional view (right panel); adapted from [154].

The heart has four chambers: two superior *atria* and two inferior *ventricles*, as can be seen in figure 3.2. The heart is divided longitudinally by an internal partition, which is called the *interatrial septum* where it separates the atria, and the *interventricular septum* where it separates the ventricles.

The atria are the receiving chambers for the blood returning to the heart from the circulation. They are thin-walled chambers as they need to contract minimally to pump blood to the ventricles below them. For this thesis, we are mainly interested in the ventricles, which are the discharging chambers of the heart. They are the actual pump of the heart, meaning that their walls are much more massive than those of the atria. Furthermore, the ventricles are

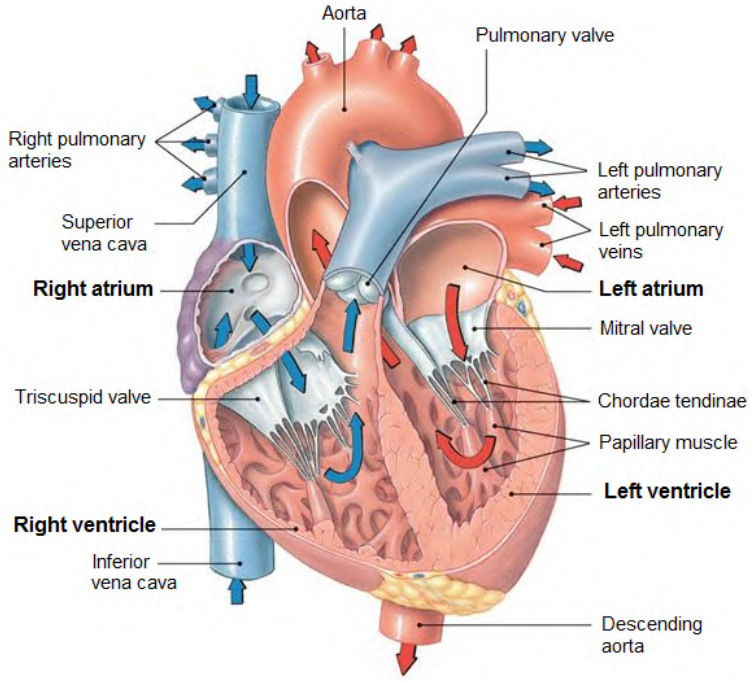

Figure 3.2: Gross anatomy of the heart in a frontal section (adapted from [154]).

also larger in size than the atria. Left and right ventricle are anatomically very different structures, partly because of their difference in functionality. The left ventricle (LV) needs to pump blood into the systemic circuit, which is a long and high-pressure pathway. Therefore, it has a thicker wall (three-times as thick as the right ventricle) and its cavity has a circular shape (see left panel of figure 3.3). The right ventricle (RV) on the other hand, pumps blood to the pulmonary circuit, which is a short low-pressure circulation. Therefore, it is much thinner than the LV. The RV is crescent shaped and it wraps around the LV (see left panel of figure 3.3). Consequently, the LV can generate much more pressure than the RV and is a far more powerful pump.

The heart's morphology changes as it contracts (*systole*) and relaxes (*diastole*), an alternating process in which it forces blood out of its chambers, and then refills its chambers with blood. This causes pressure changes in the chambers of the heart, controlling the blood flow in the heart. The geometry of the ventricular chambers changes considerably during this process, as visualized in the right panel of figure 3.3. Relaxation causes a more spheroid shape of the heart, i.e. increase in circumference and decrease in base-to-apex length, and a decrease in cardiac wall thickness.

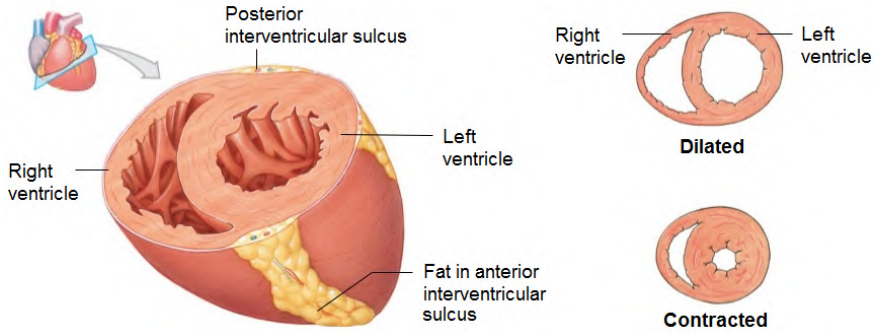

Figure 3.3: The morphology of the heart (left panel) and the morphological changes of the heart during contraction (right panel); adapted from [154].

Reported changes in left and right ventricular wall thickness during the cardiac cycle are given in table 3.1. The left-ventricular wall increases 62.5% in thickness compared to its end-diastolic state, whereas the right ventricular wall increases 70.0% in thickness. Guidelines for echocardiographic assessment of left and right ventricular dimensions report reference ranges of 0.6-1.0 cm for the septal and posterior left ventricular wall thickness at end-diastole [155]; and 4-5 mm for the right ventricular wall thickness at end-diastole [156]. Thicknesses higher than 1.5 cm for the left ventricle and 0.5 cm for the right ventricle are considered abnormal (*hypertrophy*).

Table 3.1: Overview of reported left and right ventricular wall thickness in healthy adults in diastole and systole [157], [158].

Wall thickness	End-diastole	End-systole
Left ventricle (n=10) [157]	0.8 ± 0.2 cm	1.3 ± 0.2 cm
Right ventricle (n=19) [158]	3.0 ± 0.92 mm	5.1 ± 1.64 mm

For children, the trends in left ventricular wall thickness at end-diastole is depicted in figure 3.4 in function of body weight (n=587 children, aged from birth to 18 years). The averaged interventricular septum thickness varied between 2.8 and 10.0 mm for the depicted body weights, whereas values between 3.3 and 10.8 mm were reported for the left ventricular posterior wall thickness.

3.1.2 Structure of the cardiac wall and its surroundings

The heart is enclosed in a double-walled sac, called the *pericardium* (see figure 3.5). The outer layer of this sac is the *fibrous pericardium*, which is a dense connective tissue layer protecting and anchoring the heart and preventing overfilling of the heart. Under this fibrous pericardium is the *serous pericardium* which is a thin, two-layer serous membrane: a *parietal*

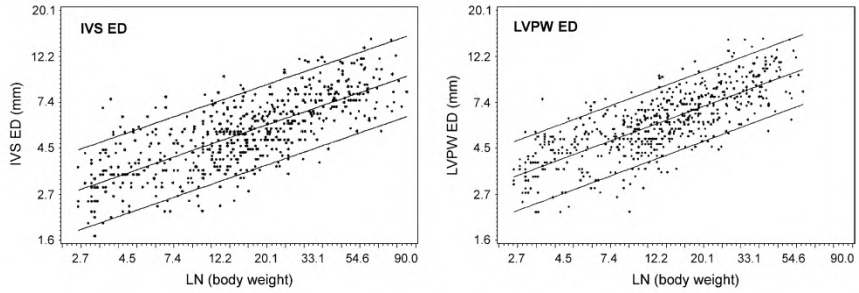

Figure 3.4: Monograms of interventricular septum thickness (IVS) and left ventricle posterior wall thickness (LVPW) at end-diastole (ED) (adapted from [159]).

layer, which lines the internal surface of the fibrous pericardium, and a *visceral layer*, which lines the external heart surface. The visceral layer is also called *epicardium*, which is an integral part of the heart wall. In between the parietal and visceral layer of the pericardium is a *pericardial cavity*, containing a film of serous fluid (*pericardial fluid*). This fluid lubricates the heart during contractions and movements of the lungs and diaphragm.

The cardiac wall is composed of three layers: the *epicardium*, the *myocardium*, and the *endocardium*; as illustrated in figure 3.5. The first layer, the epicardium, is actually the visceral layer of the serous pericardium, as mentioned above. The second layer, the myocardium, is composed of mainly cardiac muscle and forms the bulk of the heart. The cardiac muscle cells are anchored in a connective tissue network, mainly consisting of collagen and elastin fibers, the so-called *fibrous skeleton* of the heart. It reinforces the myocardium internally, anchors the cardiac muscle fibers and limits the direct spread of action potentials across the heart. The third layer or endocardium, is a sheet of endothelium together with a thin connective tissue layer, which lines the inner myocardial surface. The internal walls of the ventricular

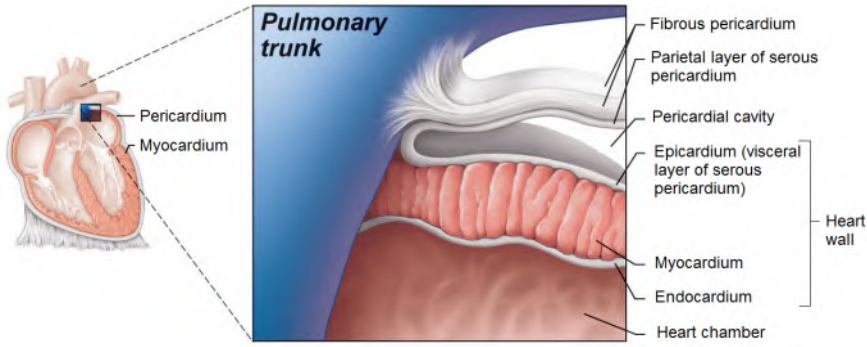

Figure 3.5: The pericardial layers and layers of the heart wall (adapted from [154]).

chamber are marked with irregular ridges of the muscle, called *trabeculae carneae*.

The cardiac muscle fibers in the myocardium are organized in different layers, with each layer a specific fiber orientation. Consequently, the muscle fiber orientations change with position through the wall, as is demonstrated in figure 3.6 for the left ventricle. The predominant muscle fiber orientation rotates from -50° to -70° in the sub-epicardial region to nearly 0° in the mid-wall region to +50° to +70° in the sub-endocardial region with respect to the circumferential direction of the left ventricle [160]. However, the myocardial muscle fibers are in general not parallel to the ventricular walls, meaning that they have a transverse angle component next to their helix angle component. This transverse angle component varies between +9° to +34° on average for the left ventricle [161], which is relatively small compared to the helix angle component, and therefore it is often assumed that the cardiac fibers are relatively parallel to the myocardium.

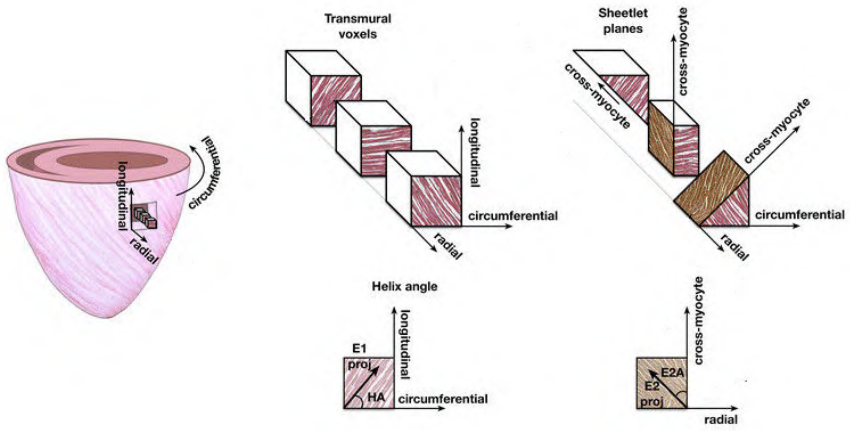

Figure 3.6: Anisotropy of the left ventricle: illustration of the 3D transmural variation of the myocardial fiber orientation (adapted from [162]).

3.1.3 Mechanical response of the passive myocardium

Passive myocardial tissue is an orthotropic material having three mutually orthogonal planes with distinct material response, as depicted in figure 3.7. This figure shows the mechanical results of simple shear tests on a cubic specimen of pig left ventricular myocardium, which are very distinct in the three planes fiber-sheet (fs), fiber-normal (fn) and sheet-normal (sn), hence demonstrating the orthotropy of the material. Furthermore, these results clearly exhibit a nonlinear response and the effect of viscoelasticity is demonstrated by the hysteresis curve between loading and unloading.

Additionally, these mechanical tests revealed that the ventricular myocardium is most resistant to shear deformations that extend the myocyte axis (f) in the fs and fn planes [160].

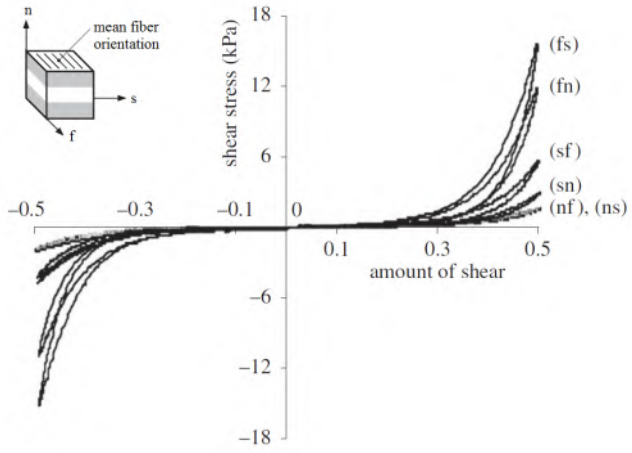

Figure 3.7: Mechanical response of the heart: shear stress versus amount of shear for simple shear tests on a cube (~ 3 × 3 × 3 mm) of pig left ventricular myocardium. The (ij) shear refers to shear in the j direction in the ij plane, where $i \neq j \in f, s, n$ (adapted from [160]).

It should be noted that uniaxial shear testing do not suffice to fully characterize the material behavior of the myocardium. For example, biplanar tensile tests in combination with triaxial shear tests allow a more complete characterization of the heart's mechanical response [163].

3.1.4 Pathological changes of the heart

Cardiac disease can alter the mechanical properties, structure and geometry of the heart. For this PhD project, we focused on two cardiac pathologies in pediatric patients involving ventricular remodeling as a consequence of valve insufficiency, namely pulmonary valve regurgitation after repaired tetralogy of Fallot and aortic valve stenosis/insufficiency. The next part of this subsection will shortly describe the pathological changes related to these two disease processes.

Tetralogy of Fallot (ToF) is one of the most common cyanotic congenital heart diseases and it accounts for 7-10% of all congenital cardiac malformations [164]. Current management of the disease involves complete neonatal repair at the age of 3 to 11 months [165], [166]. This greatly improves the prognosis of ToF-patients, however one of the most common complications is pulmonary regurgitation or leaking of the pulmonary valve, located between the pulmonary artery and the right ventricle, as indicated in figure 3.2. This

contributes to progressive right ventricle (RV) dilation and hypertrophy in response to volume overload (see figure 3.8). This can lead to ventricular dysfunction, arrhythmia and sudden cardiac death [167]. Additionally, RV fibrosis is also present in patients with repaired ToF [168], which has recently been associated with RV diastolic dysfunction [169].

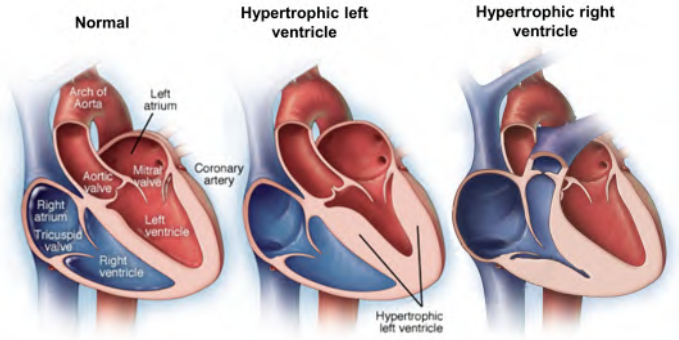

Figure 3.8: Geometrical alterations of the left and right ventricle due to hypertrophy (adapted from *Mayo Clinic*[*]).

On the other hand, aortic (valve) stenosis (AS) and insufficiency are both diseases of the aortic valve, located between the aorta and the left ventricle. AS prevents the valve from completely opening and therefore obstructs the blood flow, whereas aortic insufficiency or regurgitation (AR) indicates leakage of the valve. For children, both pathologies might be congenital or acquired. Aortic valve diseases cause chronic pressure and volume loading on the left ventricle (LV) wall in order to maintain the required cardiac output, leading to LV concentric hypertrophy (see figure 3.8), myocardial fibrosis and possibly diastolic dysfunction [170]. Additionally, it is reported that the developed fibrosis might not be uniformly distributed across the cardiac wall [171].

Both cardiac diseases thus generally lead to cardiac wall thickening, concurring with a change in myo-architecture (alteration in number of fibers and/or fiber orientation) [172], in combination with the development of myocardial fibrosis (interstitial or replacement fibrosis). These alterations occur non-uniform across the heart and various forms of the mentioned heart conditions are possible. It is crucial to detect these changes of the heart before the heart is irreversible damaged.

3.2 Current status and challenges of cardiac shear wave elastography

Myocardial stiffness assessment with transthoracic SWE faces many challenges, ranging from a technical to a mechanical nature. The technical chal-

[*]Mayo Clinic - https://www.mayoclinic.org/

lenges relate to adequate excitation and robust detection of the shear wave motion due the location of the heart, as it is situated deep inside the human body and surrounded by ribs which restricts the viewing angles. Furthermore, these challenges are different for children than for adults as imaging depth is shallower (scanning depth of 7.5-15 cm and 5-10 cm for conventional cardiac transducers for adults and children respectively) and the chest wall is thinner, requiring the use of higher frequency ultrasound. Additionally, it is a fast deforming organ evoking difficulties with properly locating the cardiac wall for ARF generation. On the other hand, the mechanical challenges of cardiac SWE are related to the intrinsic nature of the generated shear wave, which is different in the cardiac wall than in bulky viscoelastic media such as liver and breast tissue. Furthermore, the generated shear wave might be mechanically more complex in children than in adults due to children's thinner cardiac wall. Therefore, tissue characterization algorithms as used in bulk tissue applications need to be applied carefully to intrinsically different structures, as alterations to these existing algorithms or more advanced material characterization techniques might be needed. Both kinds of challenges in transthoracic SWE are described in the following two sections below. This PhD thesis primarily focuses on the biomechanical challenges.

3.2.1 Technical challenges

A SWE image of deep tissues such as the heart, liver or kidney has a low image quality due to distortion of the transmitted pulses caused by (i) phase aberration as a result of spatial variations in ultrasound propagation velocity in tissue, destroying the focusing of the US beam and increasing the level of the side lobes of the transmit beam, (ii) reverberations of sound between two strong parallel reflectors, (iii) clutter noise as a result of contributions of signals of stationary structures and (iv) bias and jitter, representing the effects of noise, bandwidth, stationary echoes, kernel size, down sampling, interpolation and quadrature demodulation on the accuracy of time delay estimation [106]. Additionally, shear wave motion is weak due to significant attenuation of the ARF, what makes it difficult to accurately detect tissue motion [96]. Over the years, several efforts have been made to address these issues [96]:

1. Improve shear wave generation by using a supersonic push [54] or comb-push [83].

2. Develop more robust shear wave motion calculation techniques, e.g. the Loupas 2D autocorrelator has proven to perform as well as the gold standard (normalized cross-correlation), and it requires less computational time [106].

3. Investigate better and more robust methods for measuring shear wave speed: different algorithms have been proposed such as the lateral time to peak displacement algorithm [44], the radon sum transformation[94] and the RANSAC algorithm (see section 2.2.2).

4. Increase the signal-to-noise ratio (SNR) of the ultrasound signal by applying imaging techniques such as plane wave compounding [98] or Pulse-Inversion Harmonic Imaging (PIHI) [152] (see below).

Closed-chest cardiac elasticity imaging remained largely an unfulfilled goal for SWE until the introduction of PIHI in 2013. Harmonic imaging uses the non-linear propagation of a low-frequency transmitted US wave to improve image quality. The basic principle of harmonic generation due to sound wave propagation in tissue is as follows: longitudinal wave propagation consists of zones of compression and rarefaction, leading to regions with increased and decreased density respectively. Now, the speed at which a wave propagates throughout a medium depends partly on the medium's density: waves travel faster in denser media. Consequently, sound waves in the compressed regions of the tissue (positive pressure) travel faster, whereas sound waves in the expanded regions of the tissue (negative pressure) travel slower [173], as shown in figure 3.9. This leads to a distorted wave shape

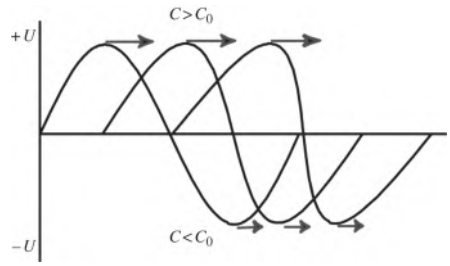

Figure 3.9: Harmonic generation: during wave propagation, the higher pressure portion of the wave travels faster owing to the higher density of the medium and the lower pressure travels slower, leading to wave distortion and harmonic generation (adapted from [173]).

and generation of harmonics at multiples of the fundamental frequency of the transmitted ultrasound beam. These non-linear effects increase with the amplitude of the pressure in the acoustic pulse, and with the propagation distance of the sound wave (related to acoustic properties of medium). Harmonic imaging thus uses reflections from sound waves at harmonics of the transmitted frequency to reconstruct an image, whereas standard imaging only uses reflections around the transmitted frequency (also called fundamental frequency). Harmonic images tend to have less noise and higher

image resolution than fundamental images as the harmonic content of the echo is mainly contained in the central portion of the US beam (higher energy sound waves will generate a greater amount of harmonic than low energy waves) removing information from signals outside the center of the US beam and improving the lateral resolution. However, its application is only suited for certain imaging environments where the tissue of interest is situated deep enough to allow a significant amount of harmonic generation.

The harmonic components in the echo signals have a much lower energy content than the fundamental component, leading to the development of a pulse-inversion technique to increase the SNR of the harmonics. Therefore, in pulse-inversion harmonic imaging, two US pulses are transmitted sequentially with the phase of the second pulse inverted, and the corresponding receive signals are summed to cancel linear and odd harmonic components and to double the even harmonic components [152], as shown in figure 3.10. This technique has the additional advantage to cancel any harmonic content generated by the electronics.

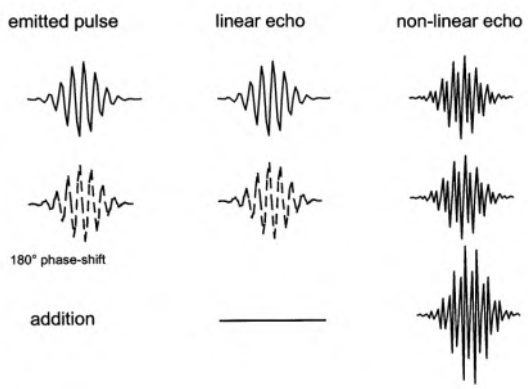

Figure 3.10: Principle of pulse-inversion harmonic imaging: the phase shift of the emitted pulses is preserved in the linear echoes, leading to signal extinction when the two received signals are added. The non-linear scattering properties of structures do not preserve the phase shift in their echoes, resulting in the harmonic signature of the structure when adding both echoes (adapted from [174]).

An accuracy study of PIHI in cardiac SWE on an *ex vivo* closed-chest pig [152] showed that PIHI could consistently track shear wave motion and provided robust shear wave speed estimates while the fundamental sequence completely failed (see figure 3.11). This study also demonstrated the feasibility of performing transthoracic SWE with PIHI *in vivo*, even though cardiac SWE failed in one subject (out of seven), the subject with the highest BMI, indicating that obesity still remains an issue with the proposed method.

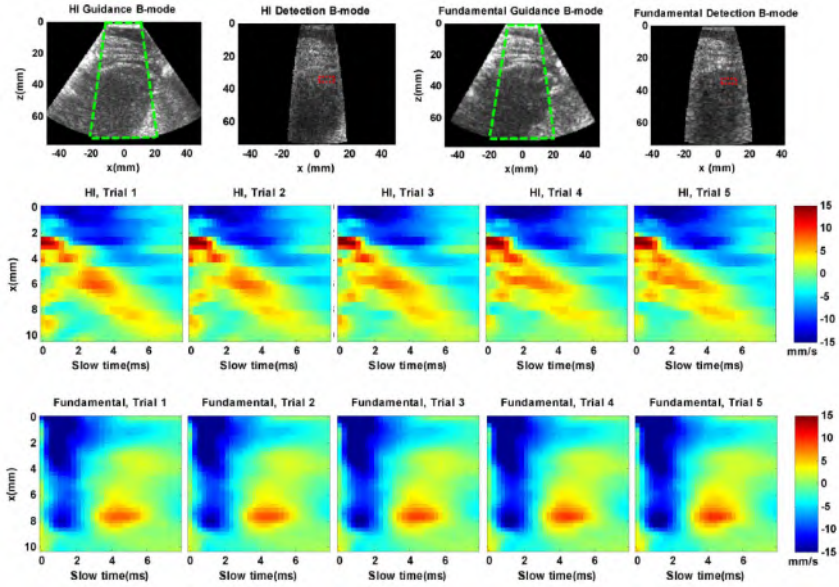

Figure 3.11: Comparing the shear wave signals of fundamental imaging and harmonic imaging (HI) in the left ventricular wall of an *ex vivo* close-chest pig at a fixed location for five trials (adapted from [152]).

In 2015, the PIHI-technique was implemented on a pediatric probe, together with time-aligned sequential tracking (TAST, see section 1.2.2.3 in chapter 1) [175], [176]. These initial feasibility studies demonstrated that the success rate of cardiac SWE among younger children increased when using a pediatric transducer. Furthermore, PIHI shear wave detection substantially improved the shear wave signal quality as compared to shear wave detection using fundamental imaging.

Recently (2016), another technique has been proposed to facilitate closed-chest cardiac SWE, which combines pulse-inversion harmonic imaging using diverging waves with coherent compounding [177]. The investigators of this study [177] showed that the combination of both techniques can further increase the SNR of the SWE signal and reduce clutter and aberration noise.

3.2.2 Mechanical challenges

The biomechanical challenges relate to the fact that the ARF-generated shear wave characteristics in the myocardium will not only depend on tissue stiffness, but also on tissue geometry and organization, tissue surroundings, more advanced material properties and mechanical loading. This leads to difficulties in post-processing the shear wave characteristics to specific material characteristics. We will now discuss several of these relevant factors individually, together with its impact on the temporal shear wave pattern. For each

factor, we will also describe the efforts yet done in cardiac SWE to take this factor into account.

3.2.2.1 Impact of geometry and surrounding on shear wave propagation

The wavelengths of the ARF-generated shear wave (typically 10-50 mm) are in general larger or of the same order as the dimensions of the thickness of the tissue of interest (reference range for left ventricular free wall thickness is 6-10 mm in adults and 3-10 mm in children, see section 3.1.2) [38], [133], [134], [178]. This means that the shear wave will no longer be a true shear wave as in a homogeneous infinite medium, but it will become a complex guided wave, especially in children. The reflections from the boundaries confine the mechanical energy within the wall and create multiple propagation paths for the guided wave [125]. This causes each frequency component in the guided wave to travel with a different phase velocity (so-called geometrical dispersion; see section 2.2.1) [123]. Additionally, the ventricular bending of the cardiac wall might also affect shear wave propagation. Examples of how geometrical dispersion affects the ARF-generated shear wave pattern in the lateral space and time domain are shown in figure 3.12 for tubular geometries. The temporal shear wave pattern can look distorted such that it is difficult to obtain an accurate time-of-flight (TOF) estimate of stiffness (see left panel of figure 3.12). However, dispersion does not necessarily mean a visually distorted temporal shear wave pattern (see right panel of figure 3.12), as was yet demonstrated in section 2.2.1. The presence of dispersion can be checked by investigating the frequency content of the generated shear wave characteristics and examine whether phase velocity changes in function of frequency (see section 2.2.3). As the resulting shear wave characteristics depend on the excited frequencies (determined by medium characteristics in combination with ARF-settings) and the settings of the imaging acquisition [141], the most complete way to characterize shear wave characteristics is to report the shear wave's frequency information next to the TOF-estimate [143].

In previous cardiac SWE studies [38], [133], [134], the LV free wall myocardium has been approximated as a plate loaded with fluids on both sides, as blood and pericardial fluid are situated on either side. This means that wave energy can leak to the surrounding media and the amount of energy leakage depends on both the material properties of the medium of interest and the surrounding medium and is a function of frequency. Generally spoken, leakage will not arise in ARF driven SWE applications as the phase velocity of the guided wave is lower than the bulk velocity of the surrounded material [123].

3.2.2.2 Impact of viscoelasticity and anisotropy on shear wave propagation

The passive myocardium is inherently viscoelastic and orthotropic, which also influence the temporal shear wave pattern characteristics:

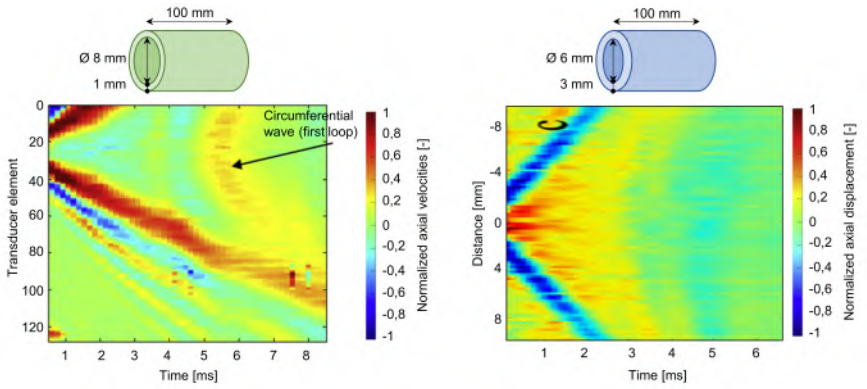

Figure 3.12: Example of temporal shear wave patterns in low-viscous plate-like geometries: agar tube immersed in water (left panel – adapted from [125]) and PVA tube immersed in water (right panel – adapted from [132]). The circumferential wave represents the wave traveling in the circumferential direction of the tube.

1. Viscoelasticity: viscoelastic tissue behavior leads to absorption of wave energy of the ARF-generated shear wave, contributing to a frequency-dependent phase velocity (so-called material dispersion [40]; see section 2.2.1). Next to a frequency-dependent phase velocity, viscoelastic media also reveal a frequency-dependent attenuation. An example of the effect of viscoelasticity on the temporal shear wave pattern in viscoelastic bulk media such as the liver is shown in figure 3.13, which demonstrates a gradual broadening of the shear wave during propagation, putting the dispersion effects in evidence [96]. Viscosity thus acts as a low-pass filter attenuating the wave amplitude and cutting off the high frequencies contained in the sharp edge of the elastic response [65]. It has been reported that shear waves in soft tissues only propagate at low frequencies between 1 and 1000 Hz [125].

   In 2005, Kanai et al [38] studied the viscoelastic behavior of the cardiac wall after wave generation due to aortic valve (AV) closure by assuming a Lamb wave model in a viscoelastic medium. This was the first time that viscoelasticity of the myocardium was non-invasively determined. Later, Urban et al [134] investigated the cardiac dynamics of the viscoelastic properties of the myocardium measured by performing Lamb wave dispersion ultrasound vibrometry (LDUV, similar to SDUV as explained in section 1.2.1 in chapter 1) in open-chest pigs and using a similar Lamb wave model as Kanai.

2. Anisotropy: cardiac tissue is composed of a connective tissue network anchoring the cardiac muscle cells, or fibers, which vary in orientation

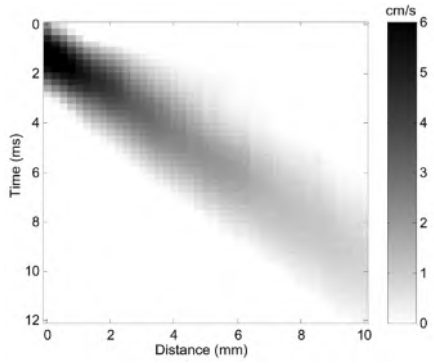

Figure 3.13: Example of temporal shear wave pattern in *in vivo* human liver (adapted from [124]).

transmurally [160] (see section 3.1.2). It is known from physics that shear waves propagate faster along the fiber direction than across the fiber [149], leading to anisotropy in shear wave propagation. This effect is illustrated in figure 3.15 for an *in vivo* upper-arm muscle (assumed to be a transverse isotropic material): a higher propagation speed is obtained for the longitudinal direction than for the transversal direction. The investigators also noted in this study that more shear wave dispersion was observed across than along the muscle fibers [179].

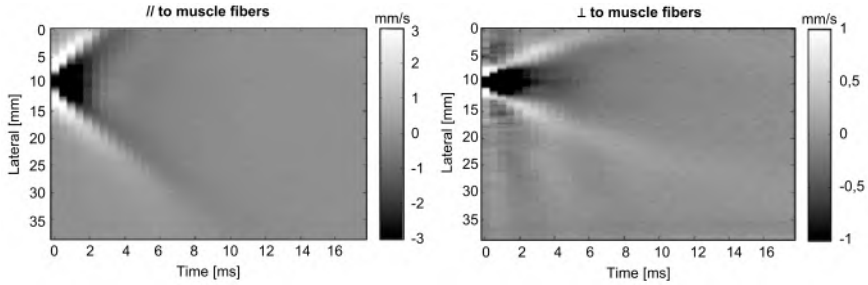

Figure 3.14: Example of the temporal shear wave pattern in longitudinal and transverse direction in the *in vivo* upper-arm muscle (adapted from [179]).

The spatial dependence of shear wave speed in the heart was first studied by Bouchard et al [150] on 18 different spatial locations during ARFI-based SWEI measurements on an open-chest dog heart. This effect has been further investigated by Couade et al [15] using the SSI-technique while rotating the probe from the heart's short axis to long axis in steps of 10°. For every SSI-acquisition, shear wave results were averaged over 2 mm depth, resulting in a shear wave speed that is dependent on acquisition angle and tissue depth.

3.2.2.3 *Impact of cardiac dynamics on shear wave propagation*

The heart is an actively contracting organ, in which the cardiac wall stiffens during systole due to the active contraction of the myocardial fibers. In diastole, the myocardium can be regarded as a passive material and thus has a lower stiffness [15]. The variation of the temporal shear wave pattern during one complete cardiac cycle is shown in figure 3.15. This has been studied by Couade et al [15] during open-heart surgery on sheep and by Pernot et al [16] on Langendorff-perfused rat hearts.

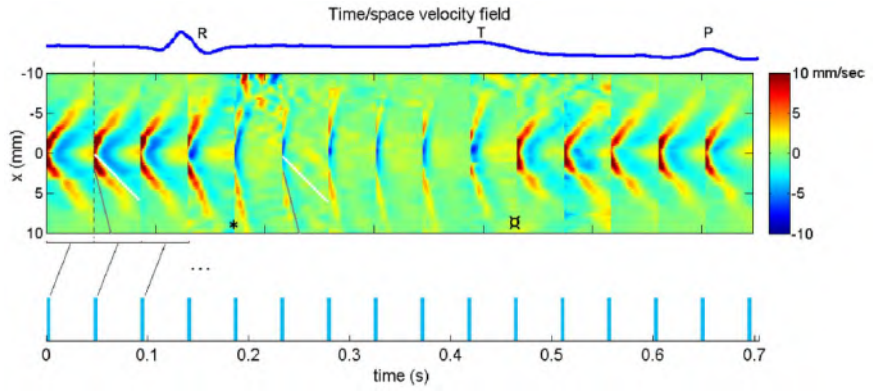

Figure 3.15: Variation of temporal shear wave pattern during one heart cycle, obtained during open-heart surgery of a sheep (adapted from [15]).

3.3 State-of-the-art in cardiac shear wave elastography and remaining questions

Any cardiac SWE acquisition has to deal with all difficulties introduced by the factors of geometry, tissue surroundings, material characteristics and loading, as mentioned in section 3.2.2. Cardiac shear wave physics is therefore complex as it is the result of the interplay of various factors, of which each's contribution to the shear wave characteristics is difficult to untangle. This also means that the term 'shear wave' is no longer valid for the ARF-generated intrinsic wave in the myocardium, however, in this manuscript, we continued calling the generated wave a 'shear wave' as its intrinsic nature is so complex that there is no longer a correct definition for the generated wave.

As mentioned above, several studies investigated the effect of above-mentioned factors on cardiac shear wave propagation, with an overview given in table 3.2 (with relevant details about the used sample, technique, reported quantity, material characterization algorithm and factors taken into account in the used algorithm for each study). As can be observed from this table, there is some variability in all reported study characteristics. First,

used specimens are *in vivo* or *ex vivo* hearts, indicating that geometry, tissue surrounding and material characteristics will simultaneously affect shear wave propagation and characterization (mechanical loading is also important when considering *in vivo* hearts). Second, the type of used techniques determines the excited frequency contents of the generated shear wave: monochromatic shear waves for SDUV (repetition is necessary), 1-1000 Hz for ARF based SWE methods [125] and 15-150 Hz for the natural shear wave generated by aortic valve closure [180]. Third, the reported SWE quantity can be a shear wave characteristic or a mechanical feature such as elasticity and viscosity. Fourth, the outcome depends on the used material characterization algorithm, which may be a group or phase speed analysis (where the phase speed analysis was based on a Lamb wave model of a fluid-loaded viscoelastic plate). Fifth, the factors taken into account in the material estimation technique did not completely correspond to the actual factors that play a role. It is unsure whether more advanced material characterization is necessary or if a qualitative measure of myocardial stiffness is sufficient. Additionally, it is questioned which are the optimal parameter(s) to report.

These studies thus only provided partial solutions and answers to the posed biomechanical challenges, as (i) the effect of individual factors on shear wave characterization is not investigated and (ii) a true validation study with mechanical parameter estimation is missing, except for the effect of myocardial fiber orientation on shear wave characterization (validated with histology in [149]).

Table 3.2: Overview of recent experimental cardiac SWE studies with AV: aortic vale, SWEI: Shear Wave Elasticity Imaging, SDUV: Shear wave Dispersion Ultrasound Vibrometry and SSI: Supersonic Shear imaging.

Study	Specimen	Technique	Reported quantity	Material characterization algorithm	Factors taken into account in algorithm
Kanai [38] (2005)	Human hearts *in vivo*	Wave due to AV closure	Elasticity, viscosity	Lamb wave model in fluid-loaded Voigt medium	Geometry, fluid, surrounding, loading and viscoelasticity
Bouchard [150] (2009)	Open-chest canine heart *in vivo*	ARF based SWEI	Group speed	TOF-method	Loading
Nenadic [133] (2011)	Porcine myocardium *ex vivo* embedded in gelatin	SDUV	Elasticity, viscosity	Lamb wave model in fluid-loaded Voigt medium	Geometry, fluid, surrounding and viscoelasticity
Pernot [16] (2011)	Langendorff-perfused rat hearts *ex vivo*	SSI	Elasticity	TOF-method	Loading
Couade [15] (2011)	Open-chest sheep heart *in vivo*	SSI	Elasticity, group speed	TOF-method	Loading and anisotropy
Lee [149] (2012)	Porcine heart *ex vivo* and open-chest sheep heart *in vivo*	SSI	Group speed	TOF-method	Loading and anisotropy
Urban [134] (2013)	Open-chest pig heart *in vivo*	SDUV	Elasticity, viscosity	Lamb wave model in fluid-loaded Voigt medium	Geometry, fluid, surrounding, loading and viscoelasticity
Vejdani-Jahromi [181], [182] (2015 & 2017)	Langendorff-perfused rabbit hearts *ex vivo*	SSI	Elasticity	Radon sum transformation	Loading
Urban [183] (2016)	Porcine heart *ex vivo*	ARF based SWEI	Group speed	TOF-method	Anisotropy
Pernot [184] (2016)	Open-chest sheep heart *in vivo*	SSI	Elasticity	Not defined	Loading

II

Shear wave elastography modeling

Chapters

Chapter 4

Shear wave modeling in the time domain

A versatile finite element model framework for the study of shear wave physics

This chapter introduces a shear wave simulation environment based on the Finite Element Method (FEM), that allows an in-depth study of the occurring shear wave physics together with an accuracy analysis of subsequent shear wave characterization by mimicking actual shear wave propagation in the time domain. This is especially relevant for settings where complex shear wave physics are expected due to geometry, advanced material characteristics or a combination of both (as in the cardiac setting). The modeling methodology is applied on a simple plate geometry with viscoelastic properties, for illustration. Furthermore, the resulting shear wave physics and characterization of this model are immediately validated with actual SWE experiments on a gelatin-agar plate phantom with the same geometry, illustrating the similarity between SWE-experiment and model. Next to validating the modeling approach with SWE experiments, this chapter also demonstrates the accuracy of the FEM in modeling shear waves by simulating Lamb wave propagation and comparing the results to the theoretical solution (see section 2.3 in chapter 2). The chapter concludes with a sensitivity study, demonstrating the capabilities of this powerful simulation tool.

This chapter is based on the IEEE-TUFFC paper *"A Versatile and Experimentally Validated Finite Element Model to Assess the Accuracy of Shear*

Wave Elastography in a Bounded Viscoelastic medium", vol. 62, no. 3, pp. 439-450, March 2015 [23]. The results have been updated and re-processed by employing more realistic acoustic parameters and the ultrasound simulation software *Field II* [185], [186] instead of *Focus* (Michigan State University, East Lansing). Furthermore, open-source post-processing code from Duke University was applied to the simulated and measured data to obtain the resulting shear wave speed.

4.1 Introduction

Over the past two decades, a broad range of elastography techniques has emerged in the field of medical ultrasound (US) due to the high clinical relevance of soft tissue characterization. In fact, the mechanical properties of soft tissues may contain important diagnostic information on tissue stiffness and structure, both potential markers of pathological tissue anomalies, such as tumor growth or myocardial fibrosis. In this work, we focused on elastography techniques generating an internal tissue perturbation by applying an appropriate 'acoustic radiation force' (ARF) [43], [81], [187]. The manner of ARF excitation can be impulsive (<1 ms), harmonic or steady state [49]. We will focus in this chapter on impulsive ARF excitation of localized tissue displacements, causing shear waves (SW's) to propagate in the tissue that can be monitored in real time using parallel beamforming on receive (>1000 frames per second) [93], [99], [188]. The propagation characteristics of these shear waves, such as the propagation speed, can be directly linked to the mechanical properties of the medium. Dependent on excitation and acquisition scheme of the SW's, one can distinguish different techniques within this category of shear wave elastography (SWE) such as Supersonic Shear wave Imaging (SSI) [54] and Shear Wave Elasticity Imaging (SWEI) [43], [49] (see section 1.2 in chapter 1 for a more complete overview).

SWE has proven to be successful for direct stiffness quantification in bulky media such as the breast (cancer diagnosis) [189], [190] and the liver (fibrosis staging) [13], [44], [112], [191], as also shown in section 1.1.2 in chapter 1. The use of SWE for arterial stiffness characterization (cardiovascular risk assessment) [125] or corneal elasticity measurement (glaucoma diagnosis) [192] has also been recently reported but the performance and accuracy of SWE in such complex configurations remain to be investigated. In particular, the geometrical constraints of these thin-walled configurations may complicate the ARF-induced shear wave propagation. When the axial thickness of the tissue under investigation is smaller than the wavelength, i.e. a 'bounded medium', the wave propagation pattern is altered through reflections and mode conversions at the tissue boundaries, evoking guided wave effects and wave dispersion [193]. Furthermore, the intricate material

properties (typically non-linear, viscoelastic and anisotropic) may induce complex 3D wave propagation paths (out of the imaging plane) in a dispersive regime, as elaborated in section 3.2 of chapter 3. Hence, both geometrical and material characteristics of the investigated tissue may distort the shear waveform, potentially resulting in a frequency-dependent propagation speed and ultimately complicating the link between SW speed and tissue stiffness.

To unfold this intricate relationship between wave propagation characteristics and tissue mechanical properties, a testing environment is needed, which allows complete analysis of wave propagation phenomena with full flexibility at the level of the tissue's configuration, its material properties and the acoustic radiation force. A computer modeling environment is most suited for this purpose, which is realized through a 3D finite-element method (FEM) in the commercial software *Abaqus*, allowing numerical computation of ultrasonic SW propagation in soft tissue. The acoustic radiation force imposed on the modeled tissue is obtained from the US simulation software package *Field II*, which allows simulation of the acoustic pressure field as emitted by a realistic ultrasound probe. The combination of the two modeling approaches represent the pushing sequence of an actual SWE experiment (see figure 4.1). This does not take the imaging sequence into account, as we will now primarily focus on the biomechanics of the shear wave propagation. However, the imaging sequence will be incorporated in the modeling methodology in chapter 9, when our focus shift to studying the effect of imaging on shear wave visualization and characterization.

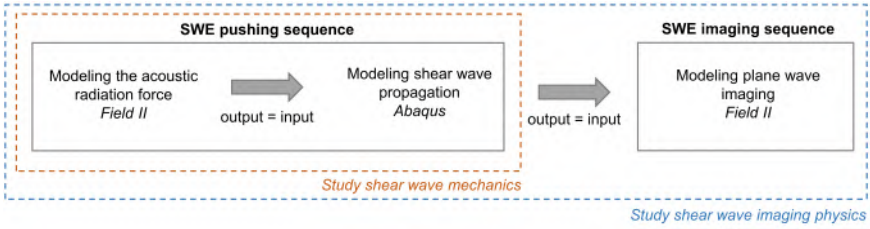

Figure 4.1: Different steps in SWE modeling, together with its analogy in actual SWE experiments. Numerically mimicking the SWE pushing sequence allows to study the biomechanics of the shear wave propagation. If another modeling layer, representing the SWE imaging sequence, is added to the current model, the modeling approach is able to also investigate the imaging physics.

This modeling strategy has previously been demonstrated for ARFI in bulky media [149], [194] (see also discussion). In this work, the methodology was adjusted and tested for SWE in viscoelastic bounded media, i.e. a 3D rectangular slab representative of a home-made gelatin-agar phantom, on which we performed real SWE-measurements to serve as a reference for our

numerical wave propagation results. The material parameters of this phantom were characterized via a uniaxial mechanical test bench with a twofold aim: (i) to use as input for the material model in the FEM-computations and (ii) to compare the Young's modulus from the SWE-measurements to the one from the mechanical testing. As such, this chapter presents an *in vitro* based numerical model for studying SW propagation phenomena, with its numerical settings validated and optimized according to SW characteristics from actual measurements. Furthermore, by adapting the material parameters and the thickness of the simulated phantom, we aim to gain more insight in the complex relationship between geometrical configuration and tissue mechanics on the one hand and SW propagation characteristics on the other hand.

4.2 Materials and methods

To establish a flexible testing ground for SW imaging techniques, we present an *in vitro* based computational model of SW propagation developed in *Abaqus/Explicit* (Abaqus Inc., Providence, RI, USA), a well-spread and accepted tool within the community of finite element modeling. In section 4.2.1, the following modeling steps will be subsequently discussed: (i) phantom construction, (ii) material characterization, (iii) imposed ARF and (iv) wave propagation. In section 4.2.2, we describe how we assess the realism of the proposed modeling approach, i.e. by analyzing SW propagation characteristics such as propagation speed and shear waveform from both the numerical model and experimental data. In the last section (section 4.2.3), we present a brief parameter study varying the tissue's geometrical and material parameters in order to demonstrate their influence on SW speed, shear waveform and dispersion curve.

4.2.1 *In vitro* based numerical model

4.2.1.1 Phantom

In vitro - We created a gelatin-agar phantom using the following ingredients: 8 wt% of gelatin powder, 3 wt% of agar-agar powder, 1 wt% of SiO_2-particles to enhance ultrasonic scattering ('Silica gel 60 (15-40 μm)', Merck, Darmstadt, Germany) and 88 wt% of distilled water. The exact formula and procedure can be found in Hansen et al [195]. The dimensions of the resulting phantom were measured at opposite ends with 0.1 mm precision, resulting in the following averaged dimensions: 107.20 mm in elevational, 56.80 mm in lateral and 4.35 mm in axial direction (orientation of coordinate system is visualized in figure 4.2). For the SWE-experiment, the phantom was completely submerged in water and fixed at its elevational ends.

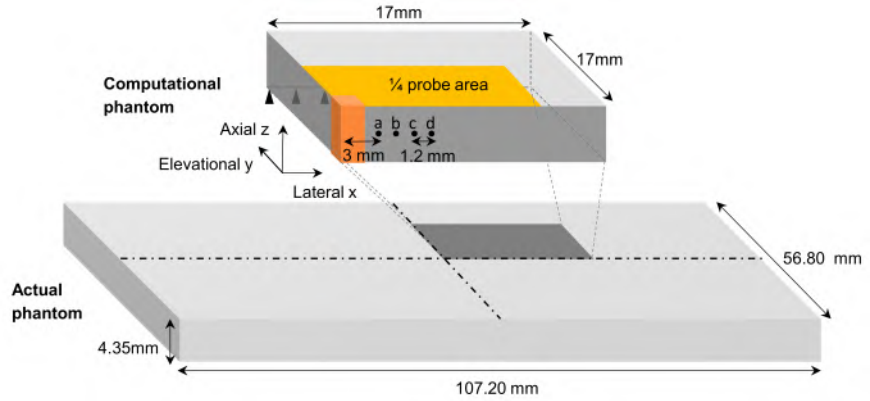

Figure 4.2: 3D-scheme of FE-model (dimensions not to scale). Dark grey planes represent symmetry planes, while other planes are free surfaces. The phantom is fixed at its elevational end in the axial direction.

Numerical - To reduce computational time, only a quarter of the *in vitro* phantom was modeled by incorporating two symmetry planes, indicated in dark gray in figure 4.2 (at x = 0 mm and y = 0 mm). For the same reason, we reduced the size of the phantom in the lateral and elevational direction to 17 mm. Note that this size still ensures that the shear wave can travel throughout the phantom without reflecting at its ends, at least within the observation time of our experiment (4 ms, see further). As was the case in the experiment, the phantom was fixed along its elevational ends in the axial direction (see figure 4.2). The other planes are considered free surfaces.

The phantom was modeled with 3D solid brick elements with reduced integration (C3D8R). A mesh size of 70 elements per wavelength Λ in the lateral direction, 39 elements per Λ in the elevation direction and 40 elements per Λ in the axial direction was applied for the phantom. The chosen mesh size exceeded the 10-15 elements per wavelength criterion suggested in literature [196], in order to allow accurate application of the ARF to the numerical model but also to avoid numerical oscillations and dispersion [197]. The asymmetry in mesh size is the result of a trade-off between reducing computational time and accurately applying the spatial varying ARF. This gives a total of 1 325 184 elements for the complete phantom.

4.2.1.2 Material properties

In vitro - The material characteristics of the phantom were derived by conducting uniaxial mechanical tests on a uni-axial tensile testing machine (Instron 5944, Norwood, MA, USA), where the phantom was clamped between two grips at its ends in the elevational direction. One clamp stayed fixed, while the other stretched the phantom at a strain rate of 1%/s until a value of

5% strain was reached. The Young's modulus was then determined by fitting a linear trendline through the obtained strain-stress data in a least square fashion using *Matlab R2013a* (The MathWorks Inc., Natick, MA, USA).

Numerical - In the default numerical model, a linear elastic material model was implemented, characterized by its Young's modulus E, the coefficient of Poisson v and its density ρ. Since the phantom mainly consists of water, v of 0.49999 and ρ of 1000 kg/m^3 were assumed. The applied E-modulus was determined as 68.10 kPa based on previously described mechanical testing, during which no material non-linearity was observed (see *in vitro* part of section 4.2.1.2).

4.2.1.3 Acoustic radiation force

In vitro - An acoustic radiation force was generated with the Aixplorer system (SuperSonic Imagine, Aix-en-Provence, France) in the middle of the phantom, by using a linear array probe with a bandwidth of 4-15 MHz and the following settings: 8 MHz sinusoidal pulse of 250 µs, an F-number of 2 (corresponding to an aperture of 15 mm) and an excitation voltage of 50 V. The axial and elevational focus were set at 30 mm and no apodization was applied.

Numerical - Our proposed FE modeling strategy relies on imposing the ARF on the phantom as a volume force B with i components, as described in [194] according to (see also equation (1.2) in chapter 1):

$$B_i = \frac{2\alpha I_i}{c_L} \tag{4.1}$$

with I_i the temporally averaged acoustic intensity in direction $i (i = 1, 2, 3)$, α the attenuation coefficient and c_L the longitudinal speed of sound. The temporally averaged acoustic intensity I can be derived from the acoustic pressure field p, using the following equation (see also equation (1.3) in chapter 1):

$$I = \frac{P^2}{\rho c_L} = \frac{\frac{1}{T}\int_0^T p^2 dt}{\rho c_L} \tag{4.2}$$

with P the time-averaged acoustic pressure and T the duration of the excitation. The orientation of the intensity vector I is given by the wave-propagation Poynting vector [198], which represents the directional energy flux density (see also section 1.2.2.2 for further details). This vector points in the axial direction for locations within 10% of the focal position from the focus. For locations closer to the transducer, the vector is oriented toward

the focal point and thus has a lateral, axial and elevational component. The same is true for locations further away from the transducer (below the ARF focus), but then the vector is directed away from the focal point toward the considered location [198].

The acoustic pressure field was calculated in the ultrasound simulation software *Field II* [185], [186], that takes into account both the technical characteristics of the used US acquisition and the material properties of the phantom. The modeled pressure field was the result of applying the pushing settings of the experiment (see *in vitro* part of section 4.2.1.3) in *Field II*. The phantom material was mimicked by assuming the elastic material characteristics mentioned in table 4.1 for model I. The attenuation coefficient α for the phantom was taken to be 0.4 $dBcm^{-1}MHz^{-1}$ [199], and the longitudinal sound speed was assumed to be 1540 m/s (conventional speed of sound in tissues). The resulting temporally averaged acoustic intensities were normalized and scaled to an intensity of 1500 W/cm^2 [49].

The next step was to apply this 3D spatially varying body force in the load integration points for all elements under the area of the probe, as indicated in figure 4.2 by the yellow area. For this purpose, 2D Gaussian functions $\widetilde{B}$ were fitted to the simulated ARF B at every axial depth in *Matlab R2013a*, according to the formula (see the left panel of figure 4.3):

$$\widetilde{B} = B_{max} e^{-\frac{(x-x_0)^2}{2\sigma_x^2} - \frac{(y-y_0)^2}{2\sigma_y^2}} \tag{4.3}$$

with maximal amplitude B_{max}, Gaussian peak location x_0 and y_0, and spread in lateral and elevational direction, σ_x and σ_y respectively. The resulting fit is depicted in the right panel of figure 4.3, in comparison with the original *Field II*-data. The magnitude of the resulting body force has dropped significantly at the border of the loaded region (yellow in left panel of figure 4.2), ensuring a smooth transition between the loaded and unloaded region. The body force was imposed for the total pulse duration of 250 µs (corresponding to the settings mentioned the *in vitro* part of section 4.2.1.3) in a smoothed step manner, in order to minimize high-frequency excitations.

4.2.1.4 Wave propagation

In vitro - The propagation of the shear waves was imaged using plane wave imaging with image compounding (3 angles), resulting in an effective frame rate of 8.5 kHz. These plane wave imaging pulses consisted of 2 cycles at 8 MHz, using 128 probe elements of the linear array probe.

Numerical - The shear wave propagation problem is described by the following dynamic equation of motion for a system with mass matrix $\boldsymbol{M}$,

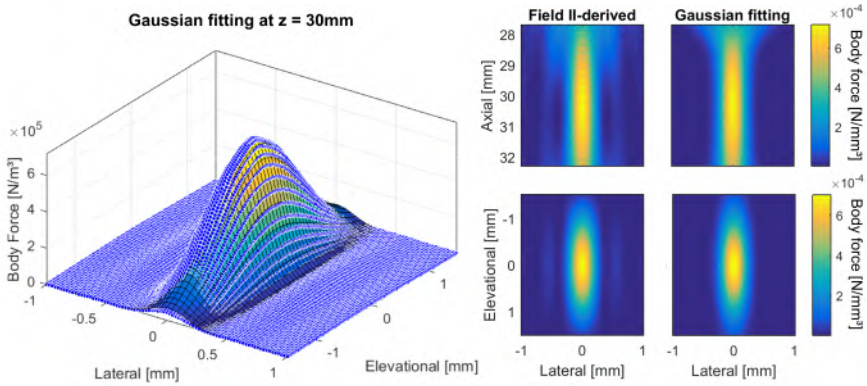

Figure 4.3: Procedure of Gaussian fitting: left panel demonstrates the Gaussian fit at an axial depth of 30 mm, and right panel compares the total resulting body force from the Gaussian fit to that of *Field II*. The upper right panels depict the cross-section at the lateral-axial plane (elevation y = 0 mm), and the lower right panels represent the cross-section at the lateral-elevational plane (axial z = 0 mm) within a lateral range of 2 mm and an elevational range of 3 mm (corresponding to the orange zone indicated in figure 4.2).

damping matrix $\boldsymbol{C}$ and stiffness matrix $\boldsymbol{K}$ [200] (see also equation (2.18) in chapter 1):

$$\boldsymbol{M}\ddot{U}(t) + \boldsymbol{C}\dot{U}(t) + \boldsymbol{K}U(t) = P(t) \tag{4.4}$$

when the system is excited with a given external load P(t). The term U(t) represents the displacement vector. These equations are numerically solved for each element and time increment via an explicit direct integration scheme (*Abaqus/Explicit*), since this method is computationally the most efficient for a high-speed dynamic problem, such as a wave propagation analysis. However, this method is only conditionally stable, meaning that the time increment size is restricted by the highest natural frequency present in the entire model. This translates into the minimum time required for a dilatational wave to propagate across the smallest element in the model. While our simulations required many time increments to be solved (typical increment size in our simulation is in the order of 60 ns), the chosen method was still far more computationally efficient than the implicit direct integration schemes (*Abaqus/Standard*), since no iterations and inverse matrices calculations were required per time increment. The chosen explicit integration scheme contained numerical damping in the form of two parameters, linear and quadratic bulk viscosity, in order to improve the modeling of high-speed dynamic events. These parameters retained their default value (0.06 for linear and 1.2 for quadratic bulk viscosity), as variation of these parameters had no

significant effect. Since hexahedral elements with reduced integration were used in this model, default hourglass-control was applied in order to ensure that zero-energy modes (caused by the reduced integration) were properly controlled.

4.2.2 Validating the FEM-model with SWE-experiment

The numerical model is validated by analyzing the simulated SW propagation in two ways:

1. The computed tissue velocities are compared at different lateral locations to the measured ones. For the measurements, the axial tissue velocities were provided by the Aixplorer system after applying an autocorrelation algorithm [103] to the acquired IQ-data (with a frame rate of 8.5 kHz). The obtained velocities were then averaged over 0.58 mm in axial depth, and artificially up-sampled in slow-time with a factor 10. However, the first images weren't usable due to the reverberation of the push which temporarily blinded the probe, resulting in a dead time of 0.53 ms during which no useful information could be extracted. For the simulations, the presented axial velocity data were obtained after filtering with a low-pass filter (type Butterworth) with a cut-off frequency of 2000 Hz, as justified by the maximum SW frequency content present in the measurements.

2. The shear wave speed (SWS) from experiment and simulation are compared. The SWS is extracted from the axial velocity data by using a lateral time-to-peak algorithm [44]. This method first identifies the maximal axial velocities at a particular depth throughout time using quadratic sub-sample estimation (open-source code from Duke University) and then tracks these velocities through a regression algorithm. For the simulations, the SWS was determined by analyzing this velocity map at focal depth. However, for the experiment, the inherent measurement variability required to average the estimated SWS at 15 different axial depths (every 0.19 mm).

Additionally, the proposed strategy also allowed validation of the SWE-technique by comparing its outcome to the stiffness modulus obtained from the mechanical experiments. Assuming the ideal case of an unbounded elastic material without any dispersion, the Young's modulus E can be derived from the experimental shear wave speed c_T by using following equations (see also equation (1.1) in chapter 1):

$$E \approx 3\mu \tag{4.5}$$

$$\mu = \rho c_T^2 \tag{4.6}$$

with density ρ and shear modulus μ.

4.2.3 Parameter study

The phantom's material characteristics and geometry were altered to investigate their influence on SW propagation. For the material characteristics, the effect of including viscoelasticity and increasing Young's modulus (×10) were considered, whereas for geometry, the thickness was changed from 4.35 mm to 20 mm.

The viscoelastic component was included by using a generalized Maxwell model in *Abaqus* through a Prony series expansion of the shear modulus G versus time t with n_G terms, as follows [149], [201]:

$$G(t) = G_0 \left[1 - \sum_{i=1}^{n_G} g_i \left(1 - e^{-\frac{t}{\tau_i}} \right) \right] \tag{4.7}$$

where G_0 is the initial value of the shear modulus, coefficients g_i are the ratio of the considered and initial shear modulus and τ_i are the material time constants. The unknown parameters g_i and τ_i were determined by fitting the model in a least-squares manner to the relaxation measurement data, in which the phantom was uniaxial stretched at 5% strain during 300 s (for specifications of the mechanical testing system, see section 4.2.1.2). A Prony model with two terms gave a root-mean-square error of 0.14% for the fitting and thus already realistically represented the relaxation of the material. A summary of all studied models can be found in table 4.1.

Table 4.1: Summary of the changed parameters in the different models. Model I represents the viscoelastic model (according to Prony), model II investigates the influence of an elevated E-modulus (× 10) and model III examines the effect of increased thickness (× 4.5).

Parameter	Model I	Model II	Model III
Thickness [mm]	4.35	4.35	20
Young's modulus E [kPa]	68.10	681.02	68.10
Normalized Prony coefficient g_1 [-]	0.0262		
Relaxation time τ_1 [s]	$132 \cdot 10^{-6}$		
Normalized Prony coefficient g_2 [-]	0.0632		
Relaxation time τ_2 [s]	74.410		

The sensitivity of the SW physics to geometry and material characteristics of the model will be assessed by comparing axial velocity maps, SWS (see section 4.2.2) and dispersion curves from the different considered models to the

default numerical model and experiment. The dispersion curves are derived for both simulations and experiment based on the 2D-Fourier transformation method described by Couade et al [125]. Therefore, we considered the velocity waveforms at lateral locations between 4 and 14 mm, averaged over 1 mm axial depth. Application of the 2D-Fourier transform to these velocity data in the slow time - lateral space domain resulted in Fourier-amplitude data in the frequency - wave number domain. The wave number k can then be converted into phase speed c_ϕ through $c_\phi = \omega/k$. Finally, the dispersion curves are obtained by finding the phase velocity with maximum energy content for each frequency.

4.3 Results

4.3.1 Comparison simulation versus experiment

First, we compared the experimental data to the results of the numerical model by visualizing the spatial distribution of the axial tissue velocities in the imaging plane at three different time points, as shown in figure 4.4. The three upper panels show the experimental data at time points 0.77 ms, 1.00 ms and 1.35 ms; the lower panels display the numerical data at the same time points. Most obvious are the nearly planar shear wave fronts (yellow stripes), propagating to the borders of the phantom and representing zones of larger, negative velocities. These correspond to downward tissue movement (away from the probe) induced by the pushing beam. After this downward velocity zone has passed, positive velocities (towards the probe) are detected, representing the upward relaxation movement of the phantom (dark blue).

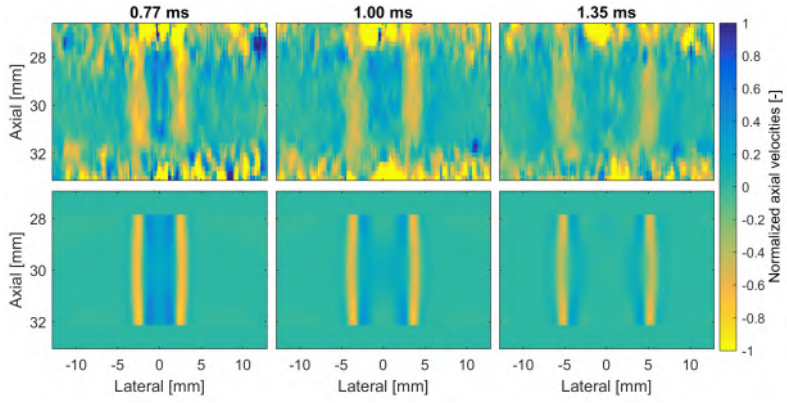

Figure 4.4: Normalized axial velocity pattern in the imaging plane for different time frames in the experiment (upper panel) and default numerical model (lower panel). Maximal peak velocity in simulation is 11.64 mm/s.

From these numerical and experimental velocity data, we extracted the axial tissue velocity versus time at 4 different lateral locations (see figure 4.5), as indicated in figure 4.2. In general, the wave shape in the simulation is very similar to that of the measurement. Also, little dispersion is visible in both cases, since the waveform doesn't change markedly for the different lateral locations. In particular, the downward axial velocity peak (away from the probe) is relatively well captured by the simulations (max. 28.0% deviation at the lateral position of 6.6 mm). Also, the attenuation of this downward peak along its propagation path is very similar in the simulation as in the experiment (decrease of 48.4% in magnitude from lateral location 3.0 mm to 6.6 mm for the simulation vs. 35.2% for the experiment). However, the positive velocity peaks (towards the probe) are less well represented by the simulation. The first positive velocity peak seen in the experiment, before the downward velocity peak, is hardly visible in the simulation (e.g. magnitude of 0.04 in simulation vs. 0.2 in experiment for lateral location 6.6 mm). On the other hand, the simulations show a distinct positive velocity peak, after the downward peak has passed, which is only weakly present in the experiment at the two locations closest to the focus. As such, the phantom relaxes more quickly in the simulation than in the experiment.

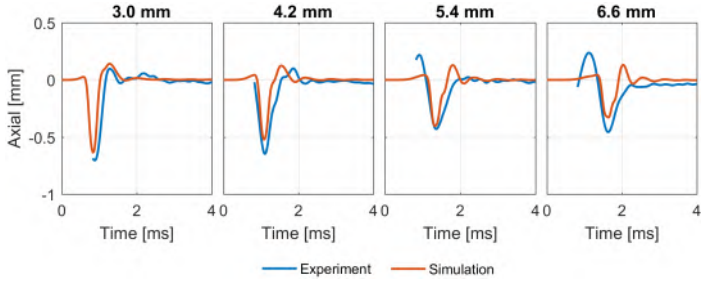

Figure 4.5: Comparison of the measured and simulated normalized axial velocity versus time at four different lateral locations 3.0 mm, 4.2 mm, 5.4 mm and 6.6 mm at focal depth (see figure 4.2 for indication of plotted spatial locations). Simulated and experimental velocities are normalized with respect to the maximal absolute axial velocity acquired in first time frame after the experimental dead time. Minimal axial velocity in the simulation was 11.64 mm/s at the lateral location of 3.0 mm. The negative velocity peak matched well with the experiment, whereas the positive velocity peaks are less well represented by the simulation.

By tracking the maximal values in a 2D axial velocity map (lateral-time domain, cfr. methods section), the resulting shear wave speed was determined for the default numerical model (figure 4.6 – left) and the experiment (figure 4.6 – right). This resulted in 4.42 m/s for the simulation and an averaged 4.63 m/s in the experiment (with standard deviation 0.07 m/s, representing the SWS variation throughout the thickness of the phantom). The obtained

shear wave speeds led to an E-modulus of 58.61 kPa for the simulation and 64.31 kPa for the experiment, according to equation (4.6) and equation (4.5). Both values underestimate the value derived from the uniaxial mechanical test (68.10 kPa), deviating respectively 13.9% and 5.6%.

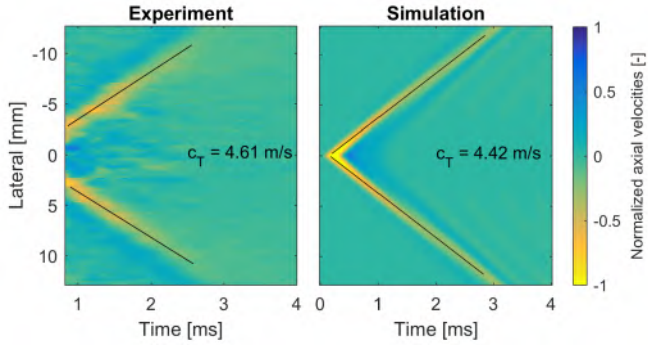

Figure 4.6: Axial velocity maps at focal depth with estimated shear wave speed in simulation vs. measurement. The black line indicates the linear regression fit with as slope the mentioned shear wave speed. Axial velocities are normalized with respect to the maximal absolute axial velocity of the default model at focal depth.

4.3.2 Sensitivity study of material characteristics and geometry

First, the influence of viscoelasticity, E-modulus and thickness on the wave propagation characteristics was investigated. Propagation speeds were analyzed via tissue velocity maps in the lateral-time domain, as illustrated in figure 4.7. The left panel of figure 4.7 depicts the resulting axial velocity map when including viscoelasticity in the material model, showing a similar pattern as in the default model (see figure 4.7). However, for the viscoelastic model, the magnitude of the tracked negative velocities is lower compared to the default model (maximal axial velocities are 4.5% lower at focal depth) and the wave travels faster (a SWS of 4.61 m/s vs. 4.42 m/s in an elastic material). The influence of increasing the E-modulus on the velocities is displayed in the middle panel of figure 4.7. A first observation is that the maximal magnitude of the negative velocities is 79.2% lower in case of a stiffer material. Secondly, the wave has a higher propagation speed (13.42 m/s) than the less stiff default model (4.42 m/s). For the thicker phantom, the resulting time-lateral axial velocity map at focal depth is illustrated in the right panel of figure 4.7. The obtained SWS of 4.70 m/s is somewhat higher than in the thinner default phantom (4.42 m/s). However, the downward velocities are on average 1.9% lower than in the original model, whereas the maximum of the relaxation velocities is 44.2% higher. This indicates that the thicker phantom returns more quickly to its original position than the thinner phantom.

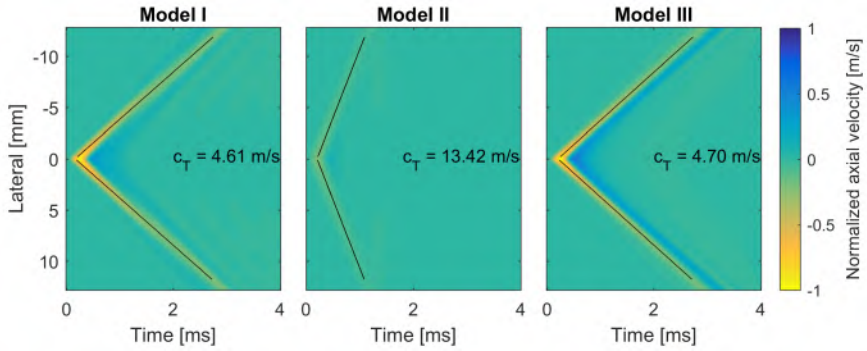

Figure 4.7: Axial tissue velocity maps at focal depth with estimated shear wave speed for models with viscoelasticity (model I) , an increased E-modulus (model II) and an increased thickness (model III).

To further demonstrate the different dynamic behavior of the thick phantom compared to the default configuration, figure 4.8 illustrates the displacement patterns at respective time points 0.51 ms, 1.01 ms and 1.52 ms, both in the lateral-axial and lateral-elevational plane. For the thick phantom (model III), we again observe a nearly planar shear wave front, with highest displacements visible around the ARF focus at time 0.51 ms, though diminishing towards the top and bottom of the phantom. After the wave has passed and the phantom relaxes, the highest displacements are to be found towards the edges of the phantom (indicated by the black arrows on figure 4.8). For time points closer to the moment of the push (250 µs), the displacement pattern corresponds to the shape of the ARF (figure 4.3), cfr. upper panel in figure 4.8.

Finally, the effect of geometry and material characteristics on SW propagation was quantified by analyzing the dispersion curves of the different simulated setups, displayed in figure 4.9. This figure shows the dispersion characteristics for the low-frequency range between 0 and 1500 Hz, as the signal-to-noise ratio decreases for increasing propagation distance in the high-frequency limit of the shear wave spectrum, due to attenuation and diffraction [124]. For the dispersion curve of the default model (red curve), the phase speed varied between 0.23 m/s and 4.58 m/s and reached the plateau value of 4.50 m/s at around 1000 Hz, corresponding to a wavelength of 4.5 mm. This wavelength almost matches the thickness of the phantom, indicating that for frequencies below 1000 Hz the observed dispersion can be explained on geometrical grounds (too large shear wavelengths compared to phantom thickness). Furthermore, for the thick phantom, the plateau value (4.80 m/s) of the dispersion curve was reached at an even lower frequency of about 500 Hz (corresponding wavelength of 9.6 mm). Including viscoelasticity in the model shifted the dispersion curve upwards (yellow), especially

in the low frequency region (0-250 Hz). For the experimental dispersion curve, the phase speed varied between 2.16 m/s and 5.15 m/s in the mentioned frequency range.

4.4 Discussion

4.4.1 FEM-modeling for shear wave physics

In this study, we proposed an *in vitro* validated numerical model capable of simulating shear wave propagation in bounded media as induced by an impulsive acoustic radiation force. This model allowed us to better understand the intricate relationship between shear wave physics and tissue characteristics, as for instance arising in the clinically relevant but challenging setting of

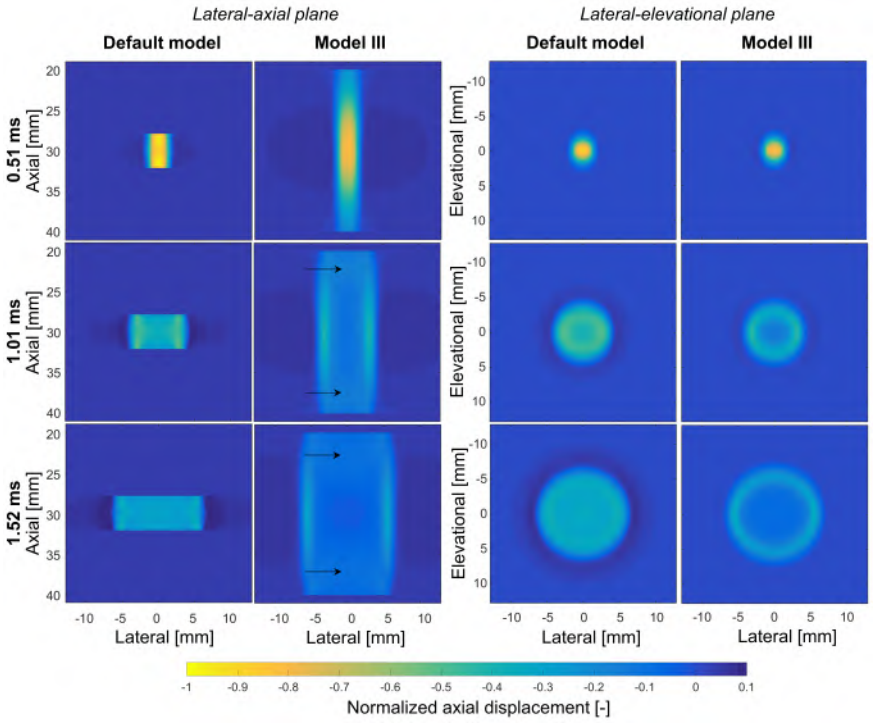

Figure 4.8: Normalized axial displacement pattern in the imaging plane (left panels) and in the lateral-elevational plane at focal depth (right panels) for different time frames for the default and thick phantom model (model III). Maximal simulated axial displacement was 4.23 µm and 4.08 µm respectively (when considering all time frames). Black arrows indicate region of maximal displacements after SW has passed for the thick phantom. Circular displacement patterns are visible in the lateral-elevational plane, however quick relaxation takes place after the shear wave has passed.

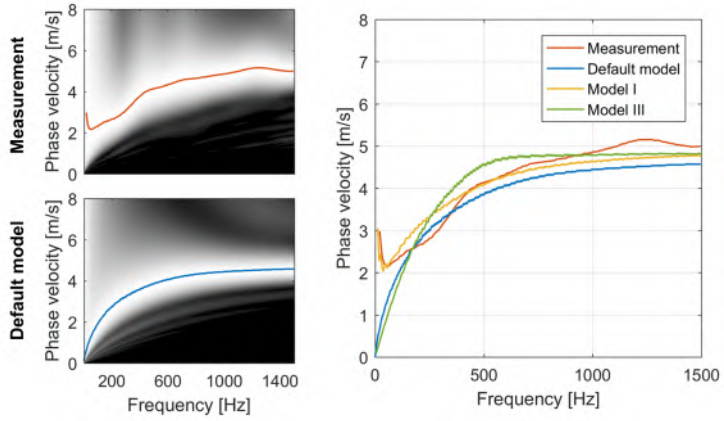

Figure 4.9: Normalized Fourier transform amplitude for experiment and default model (left) and dispersion curves for experiment and default, viscoelastic and thick phantom model (right).

shear wave elastography in bounded viscoelastic media (e.g. the cardiac wall). However, before diving into highly challenging configurations, both from an anatomical and tissue mechanical point of view, a sound modeling strategy [149], [194] should be established. Therefore, we chose a FEM approach, presented in a relatively basic setup, i.e. a homogeneous slab of gelatin-agar material (thickness in the order of the dominant shear wavelength), ensuring little involvement of complicating wave phenomena (e.g. dispersion). In fact, while both experimental and simulated data indicated the presence of dispersion in the lower frequency range (see figure 4.9), the Fourier transform of the measured tissue velocity waveform showed us that frequencies around 830Hz were mainly excited, indicating that little dispersion was present (horizontal part of dispersion curve in figure 4.9). As such, this strategy allowed us to tune, optimize and thoroughly validate the numerical settings of the FE model to actual SWE-measurements, as well as to assess the accuracy and realism of all involved simulation steps, of which the complexity cannot be underestimated. Hence, this work can be considered a first important step in establishing the reliability of modeling SWE physics in viscoelastic bounded media by using FEM (*Abaqus* software), before advancing to more complex anatomical configurations and tissue properties.

Bercoff et al. [54], [65] were the first to theoretically study SSI-induced shear wave propagation in unbounded viscous and viscoelastic media, based on a Green's function formalism. However, including complex geometries (e.g. patient-specific configurations) in such a theoretical model is less straightforward compared to our more flexible numerical approach. Recently, numerical strategies similar to ours were presented by Palmeri et al [194]

and Lee et al [149], both based on ARFI (Acoustic Radiation Force Imaging) performed on significantly larger gelatin-based phantoms with a thickness of respectively 25 and 95 mm, hence rather representative of unbounded media. Furthermore, our material model was more extensively characterized based on uniaxial mechanical tests compared to the work of Palmeri, who did not include viscoelasticity, and Lee, who did not perform independent material testing as ground truth for their computer model. When appropriate, we will discuss our obtained results in the context of their respective investigations (see section 4.4.2 below).

4.4.2 Comparison FEM-model and SWE-experiment

Our results showed that the SWE-experiment was in general well represented by the numerical model, based on both the tissue velocity waveforms and the propagation speed. However, when comparing FEM and experimental results, one should keep in mind that the autocorrelation algorithm used to obtain the SWE tissue velocities is inherently encumbered with a bias and variance, not included in the current modeling approach. We plan to investigate this in the near future by expanding our modeling approach, using the FE results to propagate point scatterers (representing the tissue) in the US simulation software *Field II*, which allows to flexibly model the ultrasonic image acquisition process.

The downward peak in the axial velocity waves, the one tracked when estimating the propagation speed, was well captured by the simulation and matched the experiment both in magnitude and shape. However, the positive velocity peaks were less well reproduced by the simulation. The first positive velocity peak, representing the upward movement of the phantom ahead of the push as a result of conservation of mass principles [149], was less distinctly present as in the measurement. Further, the second positive velocity peak signified an upward movement of the phantom after the push and thus characterized the relaxation behavior of the phantom. This peak attenuated more slowly in the simulation than in the measurement, indicating that the computational phantom relaxed back more quickly to its original position. This was also reported by Palmeri [194] though their phantom's relaxation behavior was even quicker due to the fixation of the phantom at its bottom end (free in our case). The difference in relaxation behavior between our experiment and simulation might be contributed to the fixation of the model at its elevational end (y = 17 mm), closer to the pushing region than in the experiment to reduce computational time. While we considered it important to analyze the full SW shape to assess the accuracy of the proposed numerical model and its potential for more advanced applications, it should be noted that current SWE strategies only rely on tracking the downward velocity peak which is well represented in the simulation.

Besides the axial velocity wave shapes, the estimated SWS of the elastic numerical model deviated only 4.5% from the measured 4.63 m/s, similar to the reported deviations by Palmeri et al [194], ranging from 3.6% to 8.3% dependent on the elastic modulus of their phantom. Finally, the dispersion curve of the default numerical model in figure 4.9 followed a highly similar trend as the dispersion curve derived from the experiment.

4.4.3 Accuracy FEM model

Although the comparison between the SWE-experiment and the FEM results was convincing (see figure 4.4, figure 4.5 and figure 4.6), one has to be aware of the assumptions and limitations of our numerical approach, as they might affect the outcome and its interpretation. First, the numerical model assumes vacuum conditions while actually the phantom was surrounded with water in our experiment. Second, the fact that the ARF was imposed as a time-averaged body force is an approximation of the real set-up, where the emitted acoustic pressure travels through the water into the phantom. As the time it takes the longitudinal ultrasound waves to travel through the phantom thickness (a few µs) can be considered negligible compared to the duration of the imposed ARF (250 µs), the ARF was modeled as a time-averaged body force affecting the whole phantom simultaneously for the applied time period of 250 µs. However, it might be relevant to dynamically impose the evoked ARF by directly modeling in *Abaqus* the propagation of the US beams towards the phantom and the occurring wave interactions (reflections, mode conversions, etc.) at the water-phantom interfaces as it might induce a significant surface force, potentially affecting SW propagation. Another disadvantage of applying the ARF as an time-averaged force for 250 µs is the excitation of high frequencies (though a smoothed step was used), requiring a Butterworth-filter with cut-off frequency of 2000 Hz to get rid of the oscillations in the results. This filtering operation could be avoided by applying material damping (Rayleigh model) for the higher frequencies (damping factor of 15.92 µs to get 5% damping at 1000 Hz), resulting in a quasi-match with the original simulation data after filtering (data not shown). However, this increased the computational time drastically from 1h to 604h (calculations are executed with 8 CPUs, 1.6 GHz processor and 15.6 GB RAM memory). Besides the effect of material damping, we also examined the influence of numerical damping, though changing the linear and quadratic bulk viscosity minimally affected the outcome (data not shown). Third, the viscoelastic material model was characterized based on a relaxation test with a duration of 300 s, which is too long to accurately capture the relaxation behavior on a ms-scale. However, adding viscoelasticity using the experimentally derived material constants did improve the match with the measurement, suggesting that the obtained Prony model is a good initial estimate of the actual relaxation behavior. And

lastly, we should also point at the assumptions made to calculate the ARF according to equation (4.1) and equation (4.2). The parameters attenuation coefficient, pressure magnitudes and Poisson's ratio (speed of sound) are not fully known and are thus subject to inaccuracies. Even though these values are not completely known, the resulting ARF induces displacements that correspond very well to those previously reported for SWE (max. 40 µm in vivo [54]).

Finally, to verify the correctness of our numerical setup, we simulated the propagation of Lamb waves in a 2D plate in vacuum, where a known analytical solution is at hand. More specifically, only the A0-mode was considered since this is the main mode excited by SWE in the arteries [125]. The frequency of this A0-wave was taken to be the dominant frequency present in the experiment, i.e. 830 Hz. The A0-wave was excited in the model by applying the theoretical displacement profile at the left edge. The simulated displacement pattern corresponded well to theory, as displayed in the left panel of figure 4.10. The right panel illustrates two normalized (w.r.t. maximum displacement of excitation) displacement profiles across the plate thickness at 2 different lateral locations (indicated by 1 and 2 in left panel of figure 4.10), with a maximal normalized displacement difference of 0.06 between the two curves.

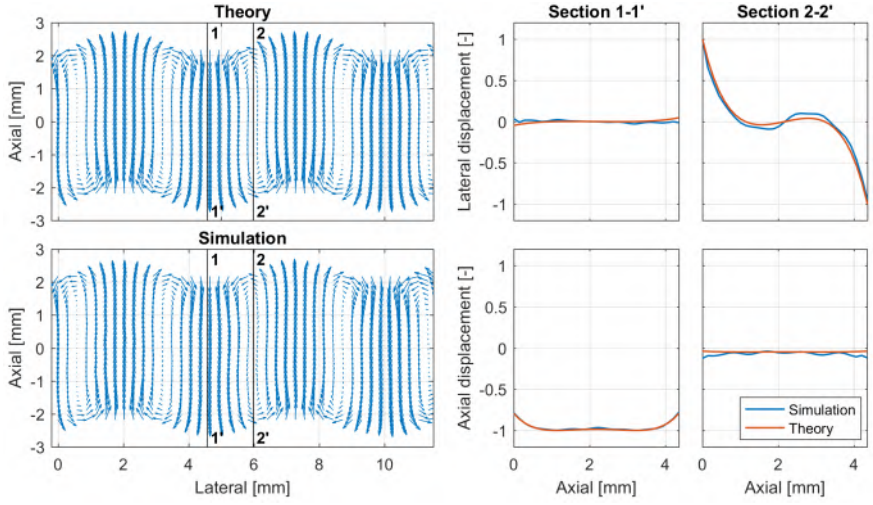

Figure 4.10: A0 Lamb wave pattern in simulation vs. analytical solution at time point 2.70 ms and two normalized (w.r.t. maximum displacement of excitation) displacement profiles over the thickness at two different lateral locations (x = 4.6 mm & x = 6.0 mm) at time point 2.70 ms.

4.4.4 Effect of phantom thickness and material properties

4.4.4.1 Effect of phantom material parameters

An increased E-modulus (× 10) led to an augmented wave speed of about a factor three higher than in the original model, as expected from equation (4.5) and equation (4.6). This resulted in a SWE-based estimated stiffness of 540.29 kPa, which is lower than the implemented material stiffness of 681.02 kPa. The deviation between estimated SWE-based and true stiffness for the material with increased E-modulus was thus larger than for the original material. This was to be expected since the square dependence between SWS and E-modulus in equation (4.5) and equation (4.6) indicate the error will increase for higher deviations in SWS. On the other hand, including viscoelasticity in the material model attenuated the wave front, as also proven by Bercoff et al. [65], and augmented the SW group speed to 4.61 m/s, as the phase speed likewise increased according to the dispersion curves displayed in figure 4.9. Furthermore, these dispersion curves demonstrated the effect of material properties on dispersion. The derived SWS better corresponded to the measured one, as illustrated in figure 4.7. The SWS-derived E-modulus (63.76 kPa) also better agreed to the mechanically determined one (68.10 kPa).

Besides the elastic behavior, Palmeri [194] also demonstrated the effect of the Poisson coefficient ν (compressibility) on their simulation results, i.e. a difference of 20% in peak displacement at the focus when varying ν between 0.499 and 0.4999. We also examined this effect on SW propagation characteristics but no significant influence was retrieved when changing the accuracy of Poisson's coefficient.

4.4.4.2 Effect of phantom thickness

Increasing the thickness of the numerical phantom accelerated the return of the phantom to its original position. The additional material of the phantom thus acted as a support and advanced the relaxation process of the phantom. Also, the maximal displacement induced by SWE (4.08 μm) was in the same order of magnitude as reported by Bercoff et al [54]. Furthermore, the increased thickness also slightly augmented the SWS with 6.3% (4.70 m/s). This value in fact corresponded better to the SWS (4.76 m/s) as derived from the E-modulus (68.10 kPa) of the mechanical tests via equation (4.5) and equation (4.6) since the simulated situation is closer to the idealized conditions of an unbounded elastic medium assumed by these equations. Concerning the dispersion curves, an increased thickness led to a lower frequency range (0-500 Hz instead of 0-1000 Hz) where dispersion occurs (see figure 4.9), demonstrating the effect of geometrical properties on dispersion.

4.4.5 Comparison SWE-experiment and mechanical testing

The performed mechanical experiments also allowed to validate the SWE-technique by comparing their obtained E-moduli. The Young's modulus of the SWE experiment (64.31 kPa) deviated 5.6% from the value derived from the mechanical test (68.10 kPa). This slight discrepancy might be attributed to the time difference of 8h between experiment and mechanical testing, during which the phantom could lose water and thus become stiffer [202]. Other potential error sources were identified as the inherent measurement variability in the SWS estimation procedure, the use of equation (4.5) and equation (4.6) for bounded media (even though little dispersion was present), the assumption of a density of 1000 kg/m^3 and the effect of the surrounding temperature on the phantom stiffness as discussed by de Korte et al [202]. Palmeri et al [194] also compared the E-modulus from their mechanical tests and ARFI-experiments for phantoms with stiffness values ranging from 4 to 23 kPa, but reported deviations ranging from a 22.4% underestimation to a 7.5% overestimation.

4.5 Conclusion

We presented an *in vitro* validated FEM approach to study SW propagation in bounded media, offering flexibility at the level of studied tissue configuration, material characterization and applied US probe design. This numerical approach was demonstrated in a homogeneous gelatin-agar phantom, and allowed us to vary material and geometrical parameters of the investigated tissue, in order to study how these interact with shear wave propagation characteristics and the stiffness-linked propagation speed. Our next step is to elaborate the current model to the more challenging conditions of SWE in healthy and diseased myocardium for the purpose of cardiovascular risk assessment, requiring to model their anisotropic, layered material properties, the guided wave-phenomenon due to the thin cardiac wall and the effects of shear wave leakage to the surrounding tissue.

Chapter 5

Shear wave modeling in the frequency domain

Modal analysis for the extraction of dispersion characteristics

Next to modeling shear wave propagation in the time domain, it is also possible to mimic shear wave elastography (SWE) numerically in the frequency domain. Again, the finite element method (FEM) is used for this purpose. This chapter is mainly written from the point of view to use these frequency FEM simulations to derive the shear wave's dispersion characteristics as an alternative for theoretically solving the equations of motion or applying a 2D fast Fourier transform (FFT) on the simulated axial velocity/displacement data extracted from temporal FEM simulations. This allows to characterize the system's dispersive wave charateristics solely based on the structure's geometry, material properties and its boundary conditions, without considering the applied loading. Nevertheless, shear wave modeling in the frequency domain can also be used to study the shear wave physics and characterization more into depth, as is elaborated in the discussion (see section 5.3.4) and as recently (2017) published by Maksuti et al [128]. Note that this chapter only presents an initial study of frequency FEM simulations for simple tissue geometries and material models, which mainly contributed to the understanding of guided wave modes and the meaning of dispersion curves in general, and thus should be further investigated in the future for more complex geometries and material characteristics.

This chapter is based on the IEEE-proceeding of the International Ultrasound Symposium 2016, entitled *"Finite element simulations to support the measurement and analysis of shear wave dispersion"* [21].

5.1 Introduction

Commercially-available SWE-systems quantitatively measure tissue stiffness by determining the group shear wave speed. This approach is valid when no dispersion (i.e. variation of velocity with frequency) occurs. However, shear wave dispersion might arise in tissues, due to a confined geometry (such as arteries) or the tissue's viscosity. Therefore, material characterization through phase speed analysis of the shear wave represents a more generally applicable approach and might be more accurate. This requires analysis of the dispersive shear wave characteristics in the frequency domain, which can be realized by taking the 2D FFT of the excited tissue velocities in the time domain. Tissue stiffness is then derived by fitting a theoretical dispersion relationship between phase speed and frequency to the measured one. However, these theoretical equations can only be solved numerically, even for simple plate- or cylinder-problems, and consequently, it will be even more challenging to dispose of a theoretical curve for complex tissue geometries and properties.

Therefore, we explored an alternative and more flexible way to provide a fitting ground truth for the measured dispersion characteristics. As previously proposed in the field of non-destructive testing [203], modal analysis through the FEM allows to derive dispersion curves solely based on simulated geometry, material properties and boundary conditions. Furthermore, the FEEM methodology permits to more easily incorporate advanced material models and complex geometries than the commonly used theoretical framework.

In this work, we will investigate the accuracy and performance of modal analysis based dispersion curve extraction for simplified tissue settings. This is realized by comparing the resulting dispersion curves to the ones obtained from theory, a method with established value within the field of SWE. As theoretical dispersion curves are only available for simplified settings, this initial study will focus on plates and cylinders. Additionally, the dispersion characteristics of virtual SWE acquisitions (FEM-simulations in the time domain [23], [149], [194]) on similar tissue settings will be examined and matched to those of the frequency FEM simulations.

5.2 Materials and methods

5.2.1 Tissue configurations

The performance of deriving dispersion characteristics from frequency FEM simulations was examined by considering three models with different geo-

metries and boundary conditions: a plate in vacuum, a plate in water and a cylinder in vacuum (see upper panels of figure 5.1). The plate has a thickness t_1 of 4.35 mm, and is assumed to be infinite in the two other directions. The infinitely long cylinder has a lumen radius r of 3 mm and a thickness t_2 of 0.6 mm (representative for a carotid artery). The tissue-mimicking material model was considered to be elastic, with a density ρ of 1000 kg/m^3, Young's modulus E of 68.1 kPa, bulk modulus K of 2.37 GPa and Poisson coefficient ν of 0.49999. Water was modeled with the same density and a bulk modulus K_f of 2.2 GPa.

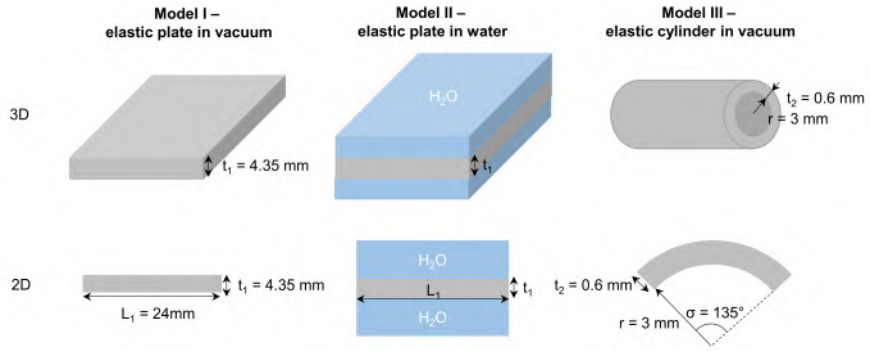

Figure 5.1: 2D and 3D geometry of the three considered models: a plate in vacuum, a plate in water and a cylinder in vacuum (dimensions are not to scale).

5.2.2 Dispersion curve extraction through modal analysis

5.2.2.1 Eigenmode and -frequency calculation

The natural frequencies and corresponding modes of a system are found by solving the dynamic equilibrium equations with mass-matrix $\boldsymbol{M}$ and stiffness-matrix $\boldsymbol{K}$ without damping or external loads. This is essentially an undamped free vibration:

$$\boldsymbol{M}\ddot{\boldsymbol{U}}(t) + \boldsymbol{K}\boldsymbol{U}(t) = 0 \tag{5.1}$$

with $\boldsymbol{U}(t)$ the displacement as a function of time. If we assume a solution in the form of $\boldsymbol{U}(t) = \boldsymbol{\Psi} cos(\omega t - \theta)$, we get the following transformed equations:

$$\boldsymbol{K}\boldsymbol{\Psi} - \omega^2 \boldsymbol{M}\boldsymbol{\Psi} = 0 \tag{5.2}$$

which is an eigenvalue problem with eigenvalue ω^2. A non-trivial solution for $\boldsymbol{\Psi}$ is only possible if its determinant is equal to zero. The resulting polynomial in ω^2 leads to null points ω_j^2 (or eigenfrequencies $f_j = \frac{\omega_j}{2\pi}$) with corresponding eigenvector Ψ_j. These modal parameters will be derived by using a

natural frequency extraction procedure in the FEM software *Abaqus* (Abaqus Inc., Providence, US), which is a linear perturbation step in *Abaqus/Standard*. The default eigenvalue extraction method with the most general capabilities is applied, i.e. the lanczos solver with traditional architecture [204]. Structural-acoustic coupling is included in this eigensolver.

As the investigated configurations are periodic, we only considered a 2D periodic element of the two geometries in the FEM-model, (i) a plate-element with length L_1 of 24 mm and (ii) a circular segment with an opening angle σ of 135° or length $L_2 = r\sigma$, and we kinematically coupled the displacements at their ends [203]. We are interested in eigenfrequencies up to 2 kHz, as this low-frequency range represents the eigenmodes generally excited by an ARF in a SWE-acquisition [125]. This led to a mesh size of 0.1 mm in both directions in order to accurately model the smallest wavelength. The water is modeled with acoustic elements, which represent an elastic medium with purely hydrostatic stresses (no shear stress) and with pressure proportional to volumetric strain [20]. The acoustic mesh size is the same as the plate-model close to the plate, and coarser (×20) far away from the plate (100 mm). The acoustic pressures in the acoustic medium were coupled to the mechanical displacements in the tissue-mimicking phantom using a tie-constraint. The other boundaries of the acoustic domain are modeled as infinite by using radiation boundary conditions, which absorb the incident wave energy.

5.2.2.2 Mode identification

As our main focus is to use this technique for material characterization in SWE, we will only identify antisymmetric modes, which are generally excited in SWE due to the orientation of the acoustic radiation force [125]. These modes can be identified through visual inspection or by comparing the simulated displacements ϕ_i to that of a simple sine, describing the antisymmetric movement ψ_j with wavelength $\lambda_j = \frac{L}{j}$, as is done in the 'Modal Assurance Criterion' (MAC) [203]:

$$MAC_{ij} = \frac{\left|\phi_i^T \psi_j\right|^2}{\left(\phi_i^T \phi_i\right)\left(\psi_j^T \psi_j\right)} \tag{5.3}$$

The modes correspond well when the MAC-value approaches 1. An example of a MAC-matrix for the plate in vacuum is shown in the right panel of figure 5.2, where the rows i represent the simulated modes below 2 kHz (i.e. 156 modes) and the columns j represent 10 sinusoidal modes with decreasing wavelength. The left panel of figure 5.2 demonstrates some of the simulated antisymmetric modes below 2 kHz, grouped according to wavelength λ_j. The MAC-matrix thus allows easier identification of wavelength λ_j, which

is necessary to calculate phase velocity, as the maximal MAC-value for an antisymmetric mode j with wavelength $\lambda_j = \frac{L}{j}$ (column of MAC-matrix) gives one or multiple sought-after simulated modes and corresponding eigenfrequencies (row of MAC-matrix).

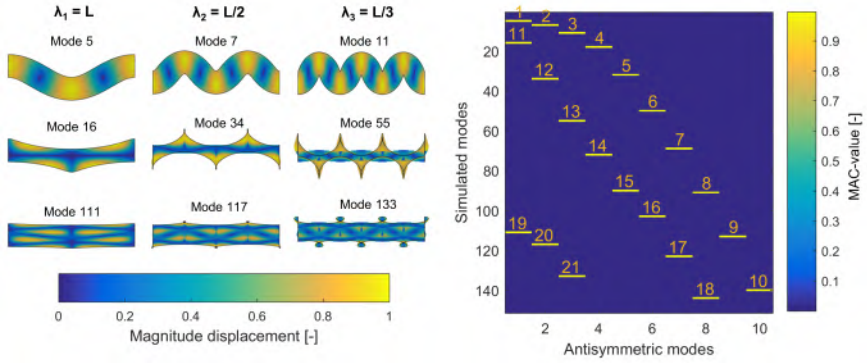

Figure 5.2: Example of some antisymmetric simulated modes for a plate in vacuum (left panel) and an illustration of the corresponding Modal Assurance Criterion (MAC) matrix between the 156 simulated modes below 2 kHz and the 10 sinusoidal modes with wavelength λ_j (right panel).

The eigenfrequency f_j of the MAC-identified simulated antisymmetric modes together with its wavelength λ_j thus allow to calculate its phase velocity as $c_\phi = \lambda_j f_j$. This is repeated for all MAC-identified simulated modes in the considered range (i.e. 21 modes, see left panel of figure 5.3), and the resulting dispersion characteristics are illustrated in the right panel of figure 5.3. This figure clearly shows three different characteristic modes with varying wavelengths, as also expected from the eigenmode visualization in the left panel of figure 5.2: $(f_j, c_{\phi,j})$ with $j = 1, \ldots, 10$, representing the so-called A_0-mode of the plate in vacuum (see also section 2.3.3.1 in chapter 2); $(f_j, c_{\phi,j})$ with $j = 11, \ldots, 18$, representing the A_1-mode; and $(f_j, c_{\phi,j})$ with $j = 19, \ldots, 21$, representing the A_2-mode.

5.2.3 Performance study of modal analysis based dispersion curve extraction

The performance and accuracy of modal analysis based dispersion curve extraction is studied by comparing the resulting dispersion characteristics to the ones obtained from theory and the temporal finite element simulations. Both procedures will be shortly described below.

5.2.3.1 Theory

In general, bulk and guided wave motion can be described by the same set of equilibrium equations: the equation of motion, the continuity equation and

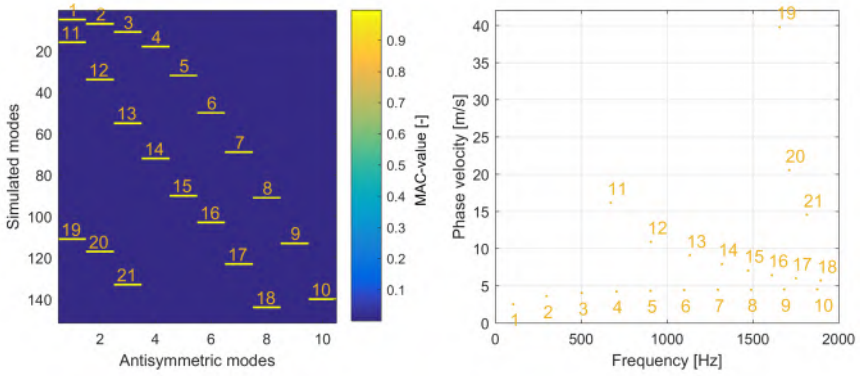

Figure 5.3: Numbering of the simulated modes identified by the MAC-criterion (left panel) and their corresponding dispersion characteristics in the frequency-phase velocity domain (right panel).

the equation of state (as discussed in chapter 2). However, the guided wave problem must satisfy some physical boundary conditions, such as displacement and stress continuity at the solid-liquid interface, in case of surrounding water, or traction-free boundaries, in case of vacuum. For a more complete overview and understanding of these theoretical wave propagation equations, we refer to chapter 2.

As explained in section 2.3.3.1 of chapter 2, the resulting dispersion equation for antisymmetric Lamb waves in an elastic plate in vacuum with thickness $2h$ is the following (see also equation (2.34)) [123]:

$$\frac{tan(qh)}{tan(ph)} = -\frac{(q^2 - k^2)^2}{4k^2pq} \tag{5.4}$$

with relationships $p^2 = k_L^2 - k^2$ and $q^2 = k_T^2 - k^2$; wave numbers $k_T = \frac{2\pi f}{c_T}$, $k_L = \frac{2\pi f}{c_L}$, and $k = \frac{2\pi f}{c_\phi}$; and longitudinal and shear wave speeds c_L and c_T respectively. These equations need to be solved for frequency-phase speed pairs (f, c_ϕ), while shear and longitudinal wave speed are derived from the material model described in section 5.2.1 as follows:

$$\begin{aligned} c_T &\approx \sqrt{\frac{E}{3\rho}} \\ c_L &\approx \sqrt{\frac{K}{\rho}} \end{aligned} \tag{5.5}$$

For the elastic cylinder in vacuum, the dispersion characteristics of the circumferential modes were derived based on [123]:

$$\|D_{mn}\| = 0 \text{ (n,m=1,...,4)} \tag{5.6}$$

in which the terms of the matrix **D** are the following:

$$\begin{aligned}
D_{11} &= \left[J_{M-2}\left(\frac{\varepsilon}{\chi}\right) + J_{M+2}\left(\frac{\varepsilon}{\chi}\right) - 2\left(\chi^2 - 1\right) J_M\left(\frac{\varepsilon}{\chi}\right)\right]\chi^{-2} \\
D_{12} &= i\left[J_{M-2}(\varepsilon) - J_{M+2}(\varepsilon)\right] \\
D_{13} &= \left[Y_{M-2}\left(\frac{\varepsilon}{\chi}\right) + Y_{M+2}\left(\frac{\varepsilon}{\chi}\right) - 2\left(\chi^2 - 1\right) Y_M\left(\frac{\varepsilon}{\chi}\right)\right]\chi^{-2} \\
D_{14} &= i\left[Y_{M-2}(\varepsilon) - Y_{M+2}(\varepsilon)\right] \\
D_{21} &= i\left[J_{M-2}\left(\frac{\varepsilon}{\chi}\right) - J_{M+2}\left(\frac{\varepsilon}{\chi}\right)\right]\chi^{-2} \\
D_{22} &= -\left[J_{M-2}(\varepsilon) + J_{M+2}(\varepsilon)\right] \\
D_{23} &= i\left[Y_{M-2}\left(\frac{\varepsilon}{\chi}\right) - Y_{M+2}\left(\frac{\varepsilon}{\chi}\right)\right]\chi^{-2} \\
D_{24} &= -\left[Y_{M-2}(\varepsilon) + Y_{M+2}(\varepsilon)\right] \\
D_{31} &= \left[J_{M-2}\left(\frac{\gamma\varepsilon}{\chi}\right) - J_{M+2}\left(\frac{\gamma\varepsilon}{\chi}\right) - 2\left(\chi^2 - 1\right) J_M\left(\frac{\gamma\varepsilon}{\chi}\right)\right]\gamma^2\chi^{-2} \\
D_{32} &= i\left[J_{M-2}(\gamma\varepsilon) - J_{M+2}(\gamma\varepsilon)\right]\gamma^2 \\
D_{33} &= \left[Y_{M-2}\left(\frac{\gamma\varepsilon}{\chi}\right) + Y_{M+2}\left(\frac{\gamma\varepsilon}{\chi}\right) - 2\left(\chi^2 - 1\right) Y_M\left(\frac{\gamma\varepsilon}{\chi}\right)\right]\gamma^2\chi^{-2} \\
D_{34} &= i\left[Y_{M-2}(\gamma\varepsilon) - Y_{M+2}(\gamma\varepsilon)\right]\gamma^2 \\
D_{41} &= i\left[J_{M-2}\left(\frac{\gamma\varepsilon}{\chi}\right) - J_{M+2}\left(\frac{\gamma\varepsilon}{\chi}\right)\right]\gamma^2\chi^{-2} \\
D_{42} &= -\left[J_{M-2}(\gamma\varepsilon) - J_{M+2}(\gamma\varepsilon)\right]\gamma^2 \\
D_{43} &= i\left[Y_{M-2}\left(\frac{\gamma\varepsilon}{\chi}\right) - Y_{M+2}\left(\frac{\gamma\varepsilon}{\chi}\right)\right]\gamma^2\chi^{-2} \\
D_{44} &= -\left[Y_{M-2}(\gamma\varepsilon) - Y_{M+2}(\gamma\varepsilon)\right]\gamma^2
\end{aligned} \tag{5.7}$$

with $M = \frac{kt_2}{1-\gamma}$, $\varepsilon = \frac{\omega h}{c_T(1-\gamma)}$ and $\gamma = \frac{r}{r+t_2}$. The functions J_i and Y_i represents Bessel functions of the first and second kind respectively, with order i. The

linear phase velocity c_ϕ of the circumferential wave for a given radius r can be derived from the angular phase velocity $\alpha = \frac{\omega}{k(r+t_2)}$ as follows [123]:

$$c_\phi = r\alpha = \frac{\omega}{k}\frac{r}{r+t_2} \tag{5.8}$$

For the elastic plate in water, the boundary conditions of the wave equilibrium equations need to be adapted to assure continuity for the displacements and stresses at the solid-liquid boundaries, leading to the following antisymmetric Lamb wave dispersion characteristics for a plate with thickness $2h$ (see also equation (2.37)) [123], [136]:

$$\begin{aligned} 4k^3\beta cosh(kh)sinh(\beta h) - (k_T^2 - 2k^2)^2 sinh(kh)cosh(\beta h) \\ = k_T^4 cosh(kh)cosh(\beta h) \end{aligned} \tag{5.9}$$

with $\beta = \sqrt{k^2 - k_T^2}$. More information about the derivation of this equation together with its assumptions can be found in section 2.3.3.2 of chapter 2.

All dispersion equations, i.e. equation (5.4), equation (5.9) and equation (5.6), are numerically solved using the rootfinder function *fzero* of *Matlab R2013a* (The MathWorks Inc., Natick, MA, USA).

5.2.3.2 Temporal finite element simulations

Next to the 2D FE simulations in the frequency domain (see section 5.2.2), we also performed temporal 3D FE simulations in *Abaqus* to mimic an actual SWE measurement, through which we model the shear wave propagation in time [23], [149], [194], as explained in chapter 4 (see figure 5.4). In brief, shear waves are excited by applying a temporally and spatially varying body force, derived from acoustic pressures simulated in *Field II* [185], [186] by mimicking an actual SWE probe (center frequency of 8 MHz, push duration of 250 μs, an F-number of 2 and the axial focal depth corresponded to the transducer's elevational focus i.e. 15 mm). The resulting ARF is shown in the left panel of figure 5.4. This simulation framework has been elaborately described for the plate-model in vacuum in our previous work [23] (see also chapter 4), and these findings are now extended to the plate-model in water and cylinder-model in vacuum.

For the 3D plate-model, quarter-symmetry is applied, and the lateral and elevational extent of the structural domain is restricted to 17 mm (larger than half of the lateral range of a linear probe with 128 elements and a pitch of 0.2 mm, leading to a total lateral range of 25.6 mm). A mesh sensitivity study resulted in 1 325 184 hexahedral brick elements. Chapter 4 provides

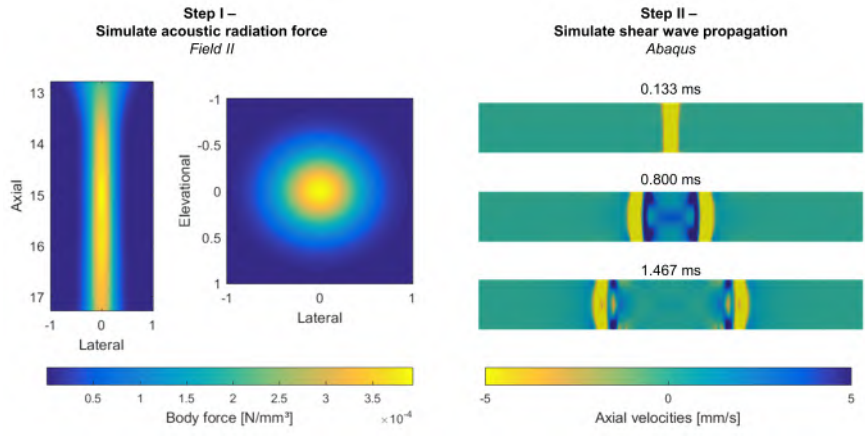

Figure 5.4: Procedure of simulating shear wave propagation in the time domain with the Finite Element Method (FEM): (i) simulate the acoustic radiation force (ARF) in the ultrasound simulation software *Field II* (left panel demonstrates the ARF in the imaging plane and in the focal lateral-elevational plane) and (ii) simulate the shear wave propagation in the FEM-software *Abaqus* (right panel illustrates simulated shear wave propagation in the imaging plane).

more details about the numerical geometry and set-up. If the plate-model is considered in water, the water is modeled as an upper and lower acoustic layer with respect to the plate, having the same FEM geometry as the plate-model. The acoustic domain is modeled with 3D acoustic brick elements (100 920 elements in total). One surface of the acoustic domain is coupled to the structural domain using a tie-constraint, whereas the other acoustic boundaries are modeled as infinite. For the 3D cylinder-model, half-symmetry is applied along the lateral direction and a lateral extent of 17 mm is considered. A mesh sensitivity study resulted in a total of 443 904 elements.

Shear wave propagation was simulated using the explicit dynamics of *Abaqus* for 3.6 ms (more than the time needed for a shear wave to travel to the lateral end of the structural domain). Axial velocities were extracted from the simulation (radial velocities for the cylinder-model), and consequently, dispersion curves are derived by taking the 2D Fast Fourier Transform (FFT) of the axial/radial velocities in the temporal and spatial domain (t, x) at mid-wall. This transforms them into Fourier energies in the frequency and wavenumber domain (f, k) (see also section 2.2.3.2 in chapter 2). The phase speed c_ϕ can then be derived by using the relationship $c_\phi = 2\pi f/k$. Finally, the dispersion curves are obtained by looking for the local maxima in energies for each frequency.

5.3 Results and discussion

5.3.1 Comparison of dispersion characteristics

The dispersion curves, obtained from theory, temporal and frequency FE simulations, are depicted in figure 5.5 for all three tissue settings. The modal analysis based dispersion curve ('Frequency FE' in figure 5.5) agrees well with the ones from theory and virtual SWE measurements ('Time FE' in figure 5.5). This is also visible in the mean squared error (MSE) values, mentioned in table 5.1, in which the maximal MSE is $5.08 \cdot 10^{-3}$ in comparison with theory, and $1.42 \cdot 10^{-1}$ with respect to the FE simulations in the time domain (higher MSE-value due to mis-match of dispersion curves at low frequencies).

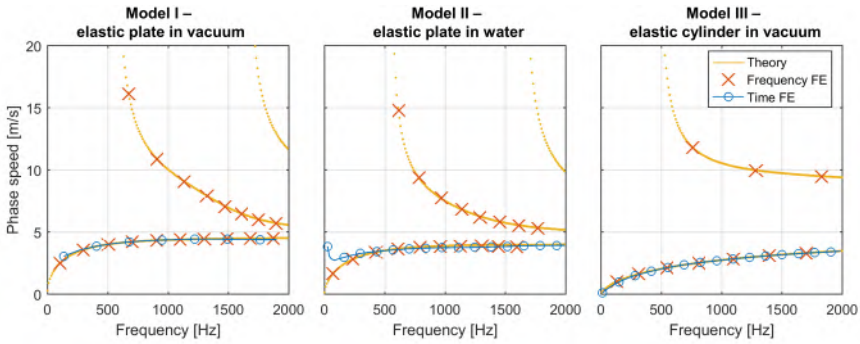

Figure 5.5: Comparison of dispersion curves for a plate in vacuum, plate in water an a cylinder in vacuum, derived through theory temporal finite element (FE) simulations and frequency finite element (FE) simulations.

Table 5.1: Mean squared error (MSE) for modal analysis derived dispersion curves compared to theoretical and temporal finite element (FE) simulated curve (A0-mode only).

Reference	Plate in vacuum	Plate in water	Cylinder in vacuum
Theory	$2.00 \cdot 10^{-4}$	$5.08 \cdot 10^{-3}$	$2.94 \cdot 10^{-4}$
Temporal FE	$5.95 \cdot 10^{-3}$	$1.42 \cdot 10^{-1}$	$1.88 \cdot 10^{-3}$

The good correspondence of the derived dispersion characteristics from modal analysis and theory shows that the proposed approach is a valid and representative alternative as fitting ground truth in phase speed analysis for SWE-based material characterization. This is confirmed by the derived dispersion characteristics of the virtual SWE measurement.

5.3.2 Accuracy of modal analysis based dispersion curve extraction

The accuracy of the calculated natural frequencies mainly depends on the chosen mesh size in the model. For this approach, it is recommended to work

with at least 20 nodes per wavelength [203]. An even finer mesh size might be necessary if highly accurate numerical results are desired. Furthermore, the amount of acquired data points in the frequency and phase velocity domain is dependent on the modeled length L of the periodic element, which is different for the simulated plate (10 data-points for A0-mode) and the cylinder (7 data-points for A0-mode), as visible in figure 5.5. If less or more data points are required, simulations with a different model length L should be considered (as demonstrated in figure 5.6 for the plate in vacuum).

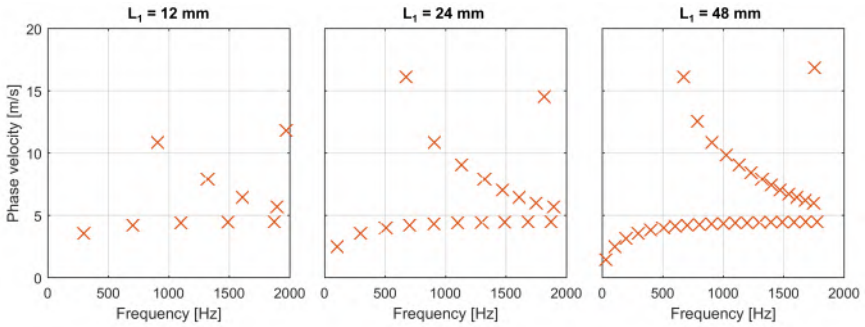

Figure 5.6: Effect of length L_1 of the plate in vacuum on the amount of extracted data points in the frequency-phase velocity domain. The A_0-mode has 5 data-points when $L_1 = 12mm$, 10 data-points when $L_1 = 24mm$ and 19 data-points when $L_1 = 48mm$. The A_1-mode has 4 data-points when $L_1 = 12mm$, 7 data-points when $L_1 = 24mm$ and 13 data-points when $L_1 = 48mm$. The A_2-mode has 1 data point in all cases for the chosen window.

Numerical modal analysis is also able to accurately represent dispersion characteristics for different geometries and boundary conditions, as can be seen in figure 5.5. Note however, that we focused on propagating modes, i.e. modes with a real wavenumber instead of a complex one. This means that we did not consider evanescent wave modes, decaying exponentially with distance (indicated with a positive imaginary part for the wavenumber). This assumption is also applied for the plate in water, as the propagating waves will only be accompanied by radiation of energy into the water if the phase velocity of these waves is higher than the sound velocity of water [123], which we did not consider. On the other hand, wave attenuation should be taken into account when modeling viscoelastic materials. *Abaqus* is able to model these rate dependent material characteristics in its modal analysis, but it assumes real valued wave numbers and complex frequencies for its solution instead of complex wave numbers and real-valued frequencies, as is usually done in the leaky wave theory. This alternative assumption indicates that waves attenuate due to energy loss in time instead of space, which is essentially a different solution to the same dispersion equations [205]. Therefore, these

dispersion curves do not necessarily match. The use of modal analysis for extracting dispersion characteristics in viscoelastic materials should thus be further investigated in future work.

5.3.3 Advantages and disadvantages

The main advantage of using the FE-method for dispersion curve extraction instead of solving the theoretical dispersion equations, is its flexibility: the FE-method gives access to several advanced material models and allows to model any geometry. Furthermore, the FE-method in the frequency domain offers the benefit of deriving dispersion characteristics purely based on geometry, material properties and boundary conditions, and thus do not require any additional knowledge about a force field, which is necessary for simulations in the time domain. Next to this, frequency domain simulations have a lower computational cost than time domain simulations (7 min on 1 CPU, 2.7 GHz, 16 GB RAM vs. 70 min on 8 CPUs, 1.6 GHz, 16GB RAM).

Another FE-based technique to obtain dispersion characteristics is the Semi-Analytical Finite Element method (SAFE), where an analytical solution is adopted for the wave propagation direction and the FE-method is applied for the cross-section. Compared to numerical modal analysis, this approach has the advantage of using exact analytical representations for one or two dimensions of the waveguide, but the disadvantage of requiring the development of new FE code with specific elements, interpolation forms and an adapted eigenvalue extraction method [123], [203].

5.3.4 Future perspectives

This chapter represents only an initial investigation of the capabilities of FEM modeling of SWE in the frequency domain. Nevertheless, it proved the feasibility of using frequency domain FEM for characterizing the dispersion characteristics in SWE, and it contributed to the general understanding of guided wave modes and their corresponding dispersion characteristics. This method has mainly been introduced in the backdrop of providing a flexible fitting ground for measured dispersion properties, however, it can also be used for simulating actual shear wave propagation. Indeed, the dynamic equations of motion dictating shear wave propagation can be solved by using direct time integration techniques (as done in chapter 4), or by using the method of modal superposition. The latter method describes the resulting response of a system as a superposition of different eigenmodes (dependent on the excited frequencies and eigenfrequencies). This method considers the general dynamic equations of motion of a system with mass-matrix $\boldsymbol{M}$, damping-matrix $\boldsymbol{C}$ and stiffness-matrix $\boldsymbol{K}$,

$$\boldsymbol{M}\ddot{U}(t) + \boldsymbol{C}\dot{U}(t) + \boldsymbol{K}U(t) = P(t) \tag{5.10}$$

with displacement $U(t)$ and loading $P(t)$, and writes the displacement as a function of eigenmodes Ψ_j and modal coordinates $x_j(t)$, i.e. $U(t) = \sum_{j=1}^{n} \Psi_j x_j(t)$, to uncouple the different differential equations. This uncoupling is based on the orthogonality-properties of the stiffness-matrix $\boldsymbol{K}$ and mass-matrix $\boldsymbol{M}$, with respect to the eigenmodes $\boldsymbol{\Psi}$: $\boldsymbol{\Psi}^T \boldsymbol{M} \boldsymbol{\Psi} = \boldsymbol{I}$ and $\boldsymbol{\Psi}^T \boldsymbol{K} \boldsymbol{\Psi} = \boldsymbol{\Lambda} = diag(\omega_j^2)$ with eigenvalues ω_j^2. Additionally, proportional damping is assumed: $\boldsymbol{\Psi}^T \boldsymbol{C} \boldsymbol{\Psi} = diag(2\xi_j \omega_j)$ with damping ratios ξ_j. This transforms the general dynamic equations of motion into the following differential equations in the modal coordinates:

$$\ddot{x}_j(t) + 2\xi_j \omega_j \dot{x}_j(t) + \omega_j^2 x_j(t) = \Psi_j^T P(t) \tag{5.11}$$

Each equation represents a single degree of freedom system, which is easily solved in the frequency domain.

Recently (2017), the wave propagation problem defined by SWE has been numerically solved in the frequency domain by using finite element simulations in a different manner than proposed above [128]. The magnitude of the ARF has been simulated in the same way as the temporal FE simulations in section 5.2.3.2, i.e. by mimicking the acoustic pressures emitted by the transducer in ultrasound simulation software. The wave equations were then evaluated in the frequency domain by considering a harmonic source of given angular frequency ω with the amplitude defined by the simulated ARF. The total response of the system in the range 10-1000 Hz was obtained by considering 100 simulations with a frequency step of 10 Hz. The result of these simulations is a displacement matrix in the frequency and space domain. Dispersion characteristics can easily be derived by taking a 1D discrete Fourier transform along the spatial dimension, converting the frequency-space domain into frequeny-wave number domain.

5.4 Conclusion

In this work, we demonstrated the feasibility of applying numerical modal analysis for dispersive media in the context of quantitative soft tissue characterization through SWE. However, further research is necessary to investigate how this method performs in 3D, for anisotropic tissues and patient-specific geometries.

III

Biomechanical factors affecting the performance of cardiac shear wave elastography

Chapters

Chapter 6

Effect of left ventricular geometry on shear wave physics and characterization:

Experiments and simulations

Shear wave elastography (SWE) applied to the heart is challenged by various technical and biomechanical factors, as mentioned in chapter 3. This chapter studies the influence of the curved and thin walled left ventricular geometry on shear wave propagation and characterization. For this purpose, the shear wave propagation excited by an acoustic radiation force (ARF) in an isotropic low-viscous representative of a child's left ventricle (LV) is analyzed by using the combined experimental and numerical approach proposed in chapter 4. Next to investigating the shear wave propagation pattern, the accuracy and robustness of two commonly used shear modulus estimation techniques, group and phase velocity analysis (see section 2.4 in chapter 2), are studied by comparing the estimated stiffness from SWE to the mechanically determined one, for various SWE acquisitions with different transducer angles with respect to the LV phantom. Furthermore, the finite element approach as proposed in chapter 4 is extended by introducing modeling features such as acoustic interface pressure and tissue surrounding, both affecting shear wave propagation and subsequent characterization.

This chapter is based on the IEEE-TUFFC paper *"Investigating Shear Wave Physics in a Generic Pediatric Left Ventricular Model via In Vitro Experiments*

and Finite Element Simulations", vol. 64, no. 2, pp. 349-361, February 2017 [20] and the IEEE-proceeding of the International Ultrasound Symposium 2015, entitled *"Myocardial Stiffness Assessment in Pediatric Cardiology using Shear Wave Imaging"* [23].

6.1 Introduction

Non-invasive myocardial stiffness assessment with ultrasound SWE is a highly promising tool for direct assessment of ventricular diastolic function. Several animal studies have demonstrated the technical feasibility to generate and track shear waves (SWs) in the myocardium of a perfused animal heart ex-vivo [16] and during open-heart surgery [15], [134], [150], [206]. Furthermore, these studies also showed that SWE-derived mechanical parameters (elasticity and viscoelasticity) varied throughout the cardiac cycle and that local ischemia [15], [206] affected shear wave speed (see also section 3.3 in chapter 3). In clinical practice, however, diastolic function is still assessed by invasively measuring filling pressures or by registering pressure-volume loops (gold standard technique) [8]. Echocardiography has been used to non-invasively evaluate diastolic function using measurements obtained from pulsed wave or tissue Doppler imaging [9]. The downside of these techniques is that they do not directly measure cardiac stiffness [11], [207]. These issues are even worse in the field of pediatric cardiology, as the first-mentioned techniques require cardiac catheterization and the second type of measurement uses adult-specific guidelines which are not readily applicable to children [10]. SWE might however be particularly useful for children with valvular disease (more specifically, aortic stenosis and repaired tetralogy of Fallot), because such direct assessment of ventricular tissue characteristics could be a major determinant of treatment timing, clinical status and outcomes [167], [170]. Besides this obvious clinical value, SWE could also contribute to our fundamental understanding of the role of ventricular remodeling and myocardial fibrosis in the disease process [169], [208].

Myocardial stiffness evaluation with transthoracic SWE however faces many technical challenges, ranging from proper excitation of the SWs to robust imaging and tracking of shear wave propagation (see also section 3.2 in chapter 3). These challenges are different for children than for adults as the imaging depth is shallower (5-10 cm for a conventional pediatric cardiac probe) and the chest wall is thinner, requiring the use of higher frequency ultrasound (US). A recent study [95] demonstrated that implementation of pulse-inversion harmonic imaging (PIHI), previously shown to improve SW motion detection in adults [152], also substantially enhanced SW signal quality in children (more information about this technique can be found in section 3.2.1 of chapter 3). Besides challenges to generate and detect SWs, the

intrinsic ventricular structure complicates the application of signal processing and tissue characterization algorithms as used in bulk tissue applications such as liver and breast tissue. Indeed, the ventricular geometry, tissue surroundings and the layered anisotropic material properties induce complex 3D guided wave propagation, complicating the relationship between shear wave characteristics and material properties [15], [181], [183].

Hence, the aim of this work is to explore the feasibility of cardiac SWE through in-vitro experiments and finite element (FE) simulations by (i) investigating the performance of current SWE techniques for mechanical characterization of the pediatric LV and (ii) pinpointing the geometrical and biomechanical factors potentially influencing SW propagation in a child's heart. More specifically, these objectives will translate into: (i) assessing and comparing the accuracy of shear modulus estimation techniques used for non-dispersive and dispersive media for various left ventricular curvatures and thicknesses, and (ii) studying the effect of the ventricular configuration (geometry, material properties, tissue surroundings) on the detected SW patterns and characteristics. Note however that we will focus on the aforementioned biomechanical challenges, and thus not take into account the technical challenges related to the excitation and imaging of the SWs at real-life imaging depths.

The first part of the objective will be realized by means of SWE-experiments on a polyvinyl alcohol (PVA) replicate of the LV-model. By changing the scanned zone and the probe orientation during these experiments, different left ventricular curvatures and thicknesses will be studied. As dispersion can be caused by the phantom's geometry and/or viscoelasticity, we will study the accuracy of two different shear modulus estimation techniques, i.e. time-of-flight method (used for non-dispersive media) versus phase velocity analysis (used for dispersive media), by quantifying the difference between their outcome and the ground truth stiffness as obtained from uniaxial mechanical testing of the PVA-material. These SWE experiments will also provide initial insights into the geometrical features influencing SW physics, which is part of our second objective. However, if we want to gain a more in-depth understanding of SW patterns and dispersion, we need a flexible testing platform at the level of the ventricular geometry, tissue surroundings, material properties and acoustic loading. Hence, we will use a previously described finite element (FE) approach [23], [149], [194] to simulate SWs in this LV-model, for which geometry, material characteristics and SWE set-up are derived from experiments (see also chapter 4). This *in vitro* based computer modeling approach has already been validated for (visco)elastic bulk media [149], [194] and plates [23] in vacuum, and will now be examined for ventricular

structures. This methodology will allow us to study in a fully controlled environment the effect of tissue surroundings, material and acoustic loading on the SW physics and propagation characteristics in the LV.

6.2 Materials and methods

6.2.1 Left ventricular geometry and phantom construction

The left ventricle was mimicked by a simplified geometrical model, i.e. a truncated prolate spheroid [160] (see upper panel of figure 6.1). In the CAD-program Siemens NX (Siemens PLM Software, Plano, US), dimensions of this model were chosen based on reported echocardiographic measures of an adolescent's (10-15 years) left ventricle [178], [209], [210]. This resulted in dimensions of 55.2 mm and 43.6 mm for the principal axes of the inner prolate spheroid, a thickness of 7.6 mm and a truncation at 27.6 mm from the base (see upper panel of figure 6.1). To create the corresponding *in vitro* phantom, molds were 3D-printed in polylactic acid (PLA, Ø 0.25mm) at the lab of Polymer Chemistry and Biomaterials of Ghent University. In order to easily remove the molds, the truncated prolate spheroid model was slightly modified by replacing the truncation at 27.6 mm from the base with a straight extrusion of 27.6mm. Next, the tissue-mimicking material was created with 10 percentage by weight PVA (molecular weight of 85000-124000 g/mol and 99+% hydrolyzed, Sigma-Aldrich, Saint Louis, US), 1 percentage by weight SiO_2-particles to enhance scattering (15-40µm, Merck, Darmstadt, Germany) and 89 percentage by weight cooling liquid (Basic Safe, Halfords, The Netherlands) [103], [211]. The use of cooling liquid instead of water guaranteed no damage to our molds during the freezing process. The final 10% PVA-solution was freeze-thawed once. Besides this left ventricular geometry, a rectangular slab was created from the same batch of PVA-solution for mechanical testing as described in section 6.2.2.2.

6.2.2 *In vitro* SWE and mechanical experiments

6.2.2.1 SWE experiments

Set-up - SW acquisitions were performed on the left ventricular phantom, completely submerged in water, using the L15-4 probe (pitch 0.2 mm, central frequency 8 MHz, 256 elements) connected to an Aixplorer system (SuperSonic Imagine, Aix-en-Provence, France). To investigate the effect of ventricular geometry on SW physics and shear modulus characterization techniques, SWs were excited in two different zones as indicated in figure 6.1a (basal and apical) using four different probe orientations (0°, 30°, 60° and 90°; 0° corresponds to the largest principal axis in figure 6.1a). We used an 8 MHz sinusoidal pulse of 250 µs, an F-number of 1.5, and an excitation voltage

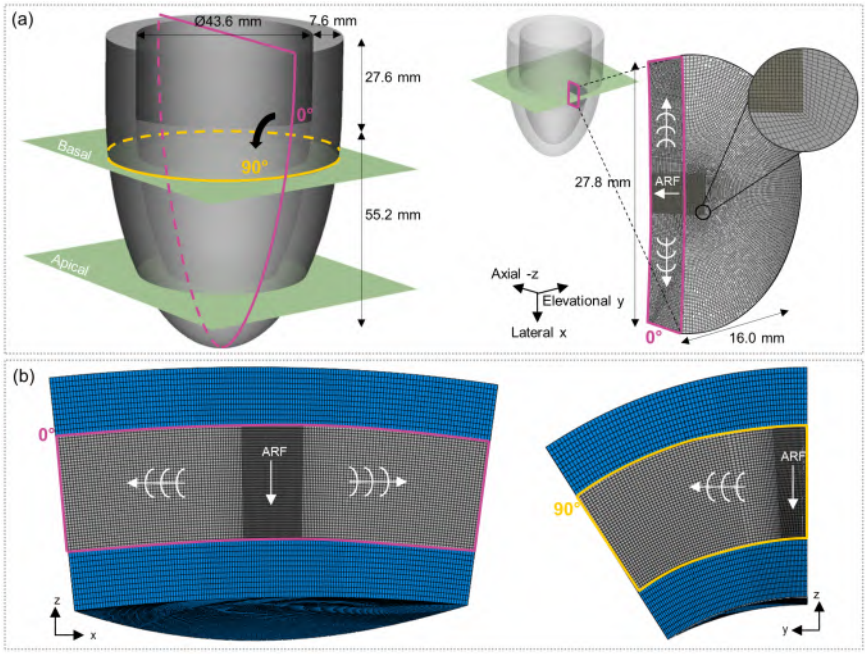

Figure 6.1: (a) Geometry of left ventricular PVA-phantom, with indication of imaging planes and angles in left panel, and illustration of location of numerical model in right panel (dimensions not to scale). (b) Geometry of 3D finite element model of basal zone for 0° (left panel) and 90° (right panel) probe orientation.

of 50 V. Then, SW propagation was imaged using all 256 probe elements and an effective pulse repetition frequency of 7 kHz.

Post-processing - The axial velocities were obtained after applying an autocorrelation algorithm [103] to the acquired In-phase Quadrature (IQ)-data. To extract material stiffness, these velocities were first averaged over 0.6 mm axial depth and then up-sampled in the slow-time domain with a factor 10. Afterwards, these datasets were subsequently processed using the following algorithms (see also section 2.2 and section 2.4 in chapter 2):

1. Time-of-flight (TOF) method [44], as applied for stiffness assessment in bulk media. This method tracks the maximal velocities to obtain the position of the shear wave front as a function of time. A linear regression curve is then fitted between the arrival time and position, of which the slope corresponds to the SW velocity. This process is repeated for multiple depths across the phantom's thickness (n = 10), discarding information from 10 central and 20 edge elements on each side in order to properly catch the starting point of the SW and to reduce noise. Note that 35 edge elements were discarded in case of the

apical zone when using a probe orientation of 60° and 90° as these elements only captured echoes from outside the LV phantom. Assuming an isotropic unbounded elastic material with density ρ (table 6.1), the shear modulus μ can be derived from this SW speed c_T as [54]:

$$\mu = \rho c_T^2 \tag{6.1}$$

2. Phase velocity analysis or c_ϕ-method [14], [125], [136], as applied for stiffness assessment in thin plates and cylindrical structures. This technique estimates stiffness by fitting a theoretical model of antisymmetric plate modes in water to the experimental dispersion curve, i.e. the phase speed versus frequency as derived from the maximally measured Fourier energy at each frequency. This procedure was repeated for multiple depths across the phantom's thickness (n = 10). The different steps in this fitting procedure were automated as follows, as shown in figure 6.2:

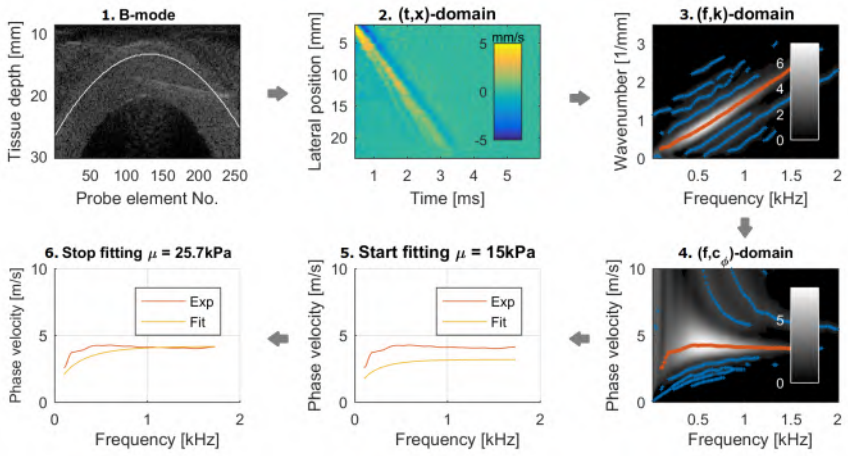

Figure 6.2: Procedure of phase velocity analysis: (1) B-mode of SWE experiment at basal zone and probe orientation 60°, where the white curve indicates the location of extracted axial velocities. (2) Extracting averaged axial velocities for left SW in mm/s. (3) Converting (time, space)-domain into (frequency, wave number)-domain by taking 2D-Fourier transform, and identifying excited modes (blue and orange curves). (4) Converting (frequency, wave number)-domain into (frequency, phase velocity)-domain. (5) Considering the excited mode with the highest energy and (6) Fitting the extracted mode to a theoretical model of the A0-mode of a plate in water.

Panel 1: The axial velocity map was extracted along the selected SW path, where the same amount of center and edge elements of the probe were discarded as for the TOF-method.

Panel 2: Resulting velocity map for left SW is shown.

Panel 3: The axial velocities in the (slow time t, space x)-domain were transformed into energies in the (frequency f, wave number k)-domain by taking the 2D Fast Fourier Transform (FFT). To reduce noise in the k-space, an amplitude mask at 10% of the maximal Fourier energy was applied [136]. Next, the main excited modes were identified in the (f, k)-domain by tracking per frequency the maximal and higher energy content, as respectively illustrated by the orange and blue curves in the (f, k)-space.

Panel 4: The phase velocity c_ϕ was derived via the formula $c_\phi = (2\pi f)/k$.

Panel 5: Only the dispersion curve with the maximal energy content was considered in the fitting procedure, as this is the main mode excited during SWE. Since there is no theoretical model describing the wave modes in a ventricle, we fitted the extracted dispersion curve to the A0-mode of a plate in water, which is the main excited mode when applying SWE to a plate [14], [125], [136]. The considered theoretical antisymmetric dispersion equation is [38], [133]:

$$\begin{aligned} 4k_\phi^3\beta cosh(k_\phi h)sinh(\beta h) - \left(k_T^2 - 2k_\phi^2\right)^2 \\ sinh(k_\phi h)cosh(\beta h) = k_T^4 cosh(k_\phi h)cosh(\beta h) \end{aligned} \tag{6.2}$$

where $k_\phi = \frac{\omega}{c_\phi}$ is the Lamb wave number, $k_T = \frac{\omega}{c_T} = \omega\sqrt{\frac{\rho}{\mu}}$ is the shear wave number, ω is the angular frequency, $\beta = \sqrt{k_\phi^2 - k_T^2}$, and h is the half-thickness of the phantom. The latter was derived from the B-mode by averaging the thickness at three locations, taking into account the actual sound speed as derived in section 6.2.2.2 below [195].

Panel 6: For an SWE experiment, all variables in equation equation (6.2) are known except for the shear wave number k_T (because of the unknown shear modulus μ). As the phase velocity varies as a function of frequency, we iteratively fit the theoretical dispersion curve for various shear moduli to the one obtained from the experiment. The fitting procedure is a least squares problem, which was solved in *Matlab R2013a* (The MathWorks Inc., Natick, MA).

6.2.2.2 *Mechanical experiments*

Uniaxial tensile testing - The PVA-material was mechanically tested on a uniaxial tensile testing machine (Instron 5944, Norwood, USA). One PVA-slab (dimensions 56.2 mm x 25.0 mm x 5.7 mm) was clamped between two grips, with one stretching the phantom at a strain rate of 0.2%/s until a threshold of 5% strain was reached. To estimate the Young's modulus, a linear trendline was fitted to the obtained stress-strain data in a least squares manner using *Matlab*. This mechanical and fitting procedure was repeated 5 times. The resulting averaged E-modulus was 73.0 ± 1.8 kPa as shown in table 6.1. The ground truth shear modulus was then derived via the relationship $\mu \approx E/3$ [54].

Density measurement - The density of the PVA-sample was measured by using the principle of Archimedes, which required to measure the mass in air and water with an analytical scale [212]. The obtained density was 1045 kg/m³ as listed in table 6.1.

Sound speed measurement - A short longitudinal pulse with center frequency of 5 MHz (contact transducer Olympus type V109-RB) was excited in the PVA-sample using a pulse echo setup. The wave signals were measured with an oscilloscope using a sampling frequency of 400 MHz. The TOF was then determined as the arrival time between subsequent pulse echoes, which allowed to determine the longitudinal sound speed as 1568 m/s (table 6.1).

Table 6.1: Material characteristics of water and PVA in the finite element model.

Material	Characteristics	Unit	Value
Measurement-based			
PVA	Density ρ	$[kg/m^3]$	1045.5
	Speed of sound c_L	$[m/s]$	1568
	Young's modulus E	$[kPa]$	73.0
	Viscoelasticity		
	g_1	$[-]$	$4.04 \cdot 10^{-3}$
	τ_1	$[s]$	$99.8 \cdot 10^{-6}$
	g_2	$[-]$	$7.04 \cdot 10^{-2}$
	τ_2	$[s]$	77.9
Literature-based			
Water	Density ρ	$[kg/m^3]$	1000
	Speed of sound c_L [213]	$[m/s]$	1480
	Bulk modulus K [213]	$[MPa]$	2200
PVA	Attenuation coefficient α [199]	$[dB/cm/MHz]$	0.4
	Coefficient of Poisson v [23]	$[-]$	0.49999

6.2.3 3D *in silico* models

6.2.3.1 *Initial model (model I)*

To investigate how SW physics are altered by viscoelastic tissue properties, the surrounding environment and the acoustic loading due to ultrasonic

reflections, we mimicked numerically one specific SWE-experiment, i.e. the basal zone imaged with a probe orientation of 0°, using a finite element (FE) approach previously validated for a (visco)elastic bulk medium [149], [194] and plate [23] in vacuum. In the first instance, we modeled the SW propagation in our PVA LV model by assuming an elastic medium in vacuum, further referred to as our initial model (model I), using the FE-software *Abaqus* (Abaqus Inc., Providence US). To decrease computational time, the modeled geometry was reduced to half an ellipsoidal shaped disk shown in figure 6.1a-b, as a circular wave propagation pattern was expected and the symmetry of the 0° imaging plane (indicated in magenta in figure 6.1b) was taken into consideration. This disk had a lateral and elevational length of 27.8 mm and 16.0 mm respectively.

The ARF was applied as a temporally and spatially varying volume force:

$$B = \frac{2\alpha I}{c_L} \tag{6.3}$$

$$I = \frac{P^2}{\rho c_L} \tag{6.4}$$

with B the volume force, α the attenuation coefficient, I the time-averaged acoustic intensity, P the time-averaged acoustic pressure, ρ the density and c_L the longitudinal wave speed. The latter two parameters were determined via mechanical testing (see section 6.2.2.2), whereas the attenuation coefficient α was derived from literature [199]. An overview of all material parameters is shown in table 6.1. Pressure P was numerically retrieved from *Field II* [185], [186] simulations, by mimicking the pushing sequence in the PVA-material (see section 9.2.1). This led to a temporally averaged acoustic intensity I which was then normalized and subsequently scaled to 1500 W/cm² [49]. For more details about this volume force, we refer to [23]. The resulting spatial distribution and magnitude of the imposed volume force is illustrated in the lower panels of figure 6.3, in the imaging and lateral-elevational plane. This force was imposed for 250 µs in a zone extending 4.0 mm in the lateral direction and 2.3 mm in the elevational direction.

The model was meshed with 8-noded brick elements with reduced integration, oriented perpendicularly to the expected direction of wave incidence (see zoomed-in region in figure 6.1a) in order to minimize any numerical errors and computational time [214]. A mesh sensitivity study was done to establish the required size and number of elements for the phantom. We evaluated the accuracy of the resulting axial velocities (i.e. numerical oscillations, but also numerical reflections and dispersion caused by sudden changes in

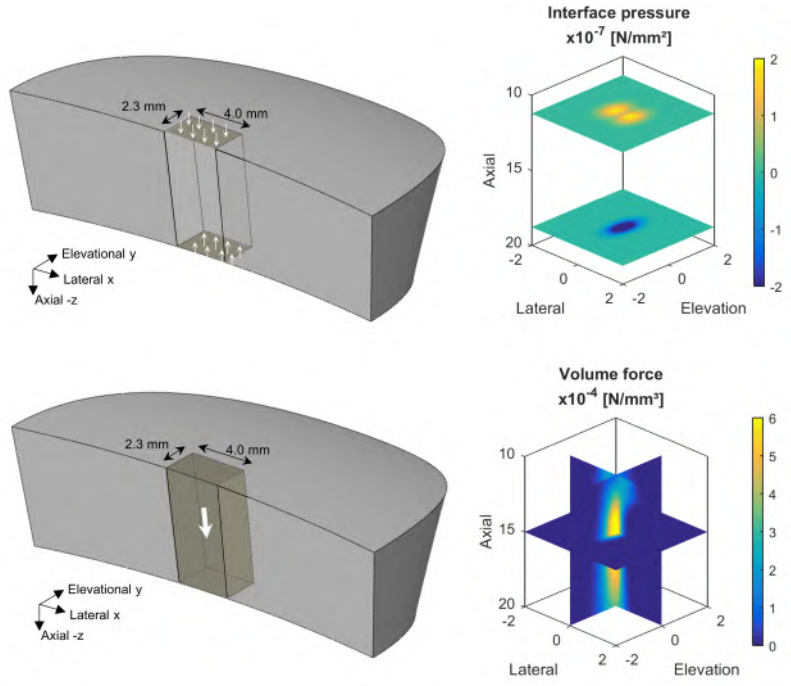

Figure 6.3: Applied loading on the volume designated in dark grey in the finite element model: the upper panels indicate the magnitude of the surface pressure on upper and lower surface and the lower panels depict a XY- and XZ-section of the volume force magnitude.

mesh density or too large mesh sizes) versus computational time, taking into account the following considerations: (i) literature suggests a criterion of 10-15 elements per wavelength [196], and (ii) a local mesh refinement in the ARF-zone (see dark grey zone in figure 6.1a-b and figure 6.3) guaranteeing accurate application of the volume force. This led to a mesh of 347 624 solid brick elements. All PVA material characteristics were derived from literature or our mechanical experiments (see section 6.2.2.2), as summarized in table 6.1.

6.2.3.2 Advanced models

Next to this initial model (model I), we considered three more models, each including additional factors potentially influencing SW propagation, as described below.

Modeling the surrounding water (model II) - We extended our initial FE model consisting of half an ellipsoidal PVA disk in vacuum to include the water surrounding the disk, further referred to as model II. The real-life PVA-phantom was indeed submerged in water during the experiment. To

mimic this in the FE model, we surrounded the ellipsoidal disk with acoustic elements (blue zones in figure 6.1b), representing an elastic medium where stress is purely hydrostatic (no shear stress) and pressure is proportional to volumetric strain. The upper and lower surface of the phantom were connected to the modeled water layers through a tie-constraint which couples mechanical displacement to acoustic pressure. The other surfaces of the modeled water were considered to be infinite, assuming that the incident wave energy is completely absorbed, which was realized with radiation boundaries and acoustic infinite elements in the model. Radiation boundary conditions were applied on the upper and lower surface of respectively the upper and lower water layer, while acoustic infinite elements were defined on the circular-shaped surfaces of both water layers.

We performed a mesh sensitivity study for the water zone, as previously done for the PVA medium in the initial model, and took into account the same considerations. The mesh density of the water region was taken the same as in the PVA-medium (outside the applied ARF-region), in order to ensure that the wave field in the vicinity of the fluid-solid interface is accurately simulated and that the tie-constraint is appropriately applied. This resulted in two meshed layers of water, each with a thickness of 3.8 mm and 78 375 acoustic brick elements. The values of the modeled bulk modulus, speed of sound and density of water are mentioned in table 6.1.

Modeling interface pressure (model III) - The ARF does not only consist of a body force, but also of an interface pressure arising at the interfaces between the phantom and water. Indeed, when the ultrasonic pushing beam encounters an interface, a local surface radiation force is created causing a displacement of the nearby medium. By assuming a plane wave with perpendicular incidence traveling from medium 1 to medium 2, the interface pressure Π can be written as a pressure acting on the interface surface [215]:

$$\Pi = \frac{I}{c_1}\left(1 + R - (1 - R)\frac{c_1}{c_2}\right) \tag{6.5}$$

With $R = \left(\frac{Z_2 - Z_1}{Z_2 + Z_1}\right)^2 = 2.61 \cdot 10^{-3}$ the energetic reflection coefficient, Z_1 and Z_2 the acoustic impedances ($Z_i = \rho_i c_i$), and c_1 and c_2 the sound speeds of media 1 and 2. The maximal absolute interface pressure is $1.82 \cdot 10^{-7} N/mm^2$ and $3.13 \cdot 10^{-7} N/mm^2$ for respectively the upper and lower surface, as depicted in the upper panels of figure 6.3. Note the opposite sign of the interface pressure at the lower surface, compared to the upper surface, reflecting the fact that this force works in the opposite direction of the acoustic radiation force. Furthermore, a two-peaked pressure zone was noticed for the upper surface corresponding to the two side lobes, present in the volume force at

an axial depth of around 12 mm (light blue zones in the lower right panel of figure 6.3). This interface pressure was applied on the surfaces of the phantom model indicated in figure 6.3 and this setup will further be referred to as model III.

Modeling viscoelasticity (model IV) - Viscoelasticity was modeled in *Abaqus* by using a Prony model, describing the time dependent behavior of the shear modulus G with n_G terms [23], [149]:

$$G(t) = G_0 \left(1 - \sum_{i=1}^{n_G} g_i \left(1 - e^{-\frac{t}{\tau_i}}\right)\right) \tag{6.6}$$

With G_0 the initial shear modulus, g_i the normalized shear coefficient, and τ_i the material time constants. These parameters were determined by performing a least-squares fit to relaxation measurements we executed on our uniaxial mechanical test bench, stretching the phantom at 5% strain for 10 s (section 6.2.2.2 describes the specifications of the mechanical testing system). This fitting procedure resulted in a Prony model with two terms and the parameters described in table 6.1, with a root mean square error of 0.11% between the fitted and measured data. We will refer to model IV when discussing results obtained from this viscoelastic case.

A summary of all modeled features in models I, II, III and IV is described in table 6.2.

Table 6.2: Overview of modeled features in FE-model I, II, III, and IV.

Modeled features	Model I	Model II	Model III	Model IV
Material PVA				
Elastic	x	x	x	
Viscoelastic				x
Surrounding				
Vacuum	x			
Water		x	x	x
Interface pressure			x	x

6.3 Results

6.3.1 *In vitro* assessment of shear modulus estimation techniques

We investigated the accuracy of the TOF-method and the phase velocity analysis, by comparing the resulting shear modulus to the mechanically determined one ($\mu_{mech} = 24.3 \pm 0.6kPa$). This was done for different zones (basal and apical) and probe orientations (0°, 30°, 60° and 90°) as shown in figure 6.1a. For each SWE-acquisition, we also studied the depth variation of the shear modulus estimations for both algorithms.

6.3.1.1 *TOF-method*

Figure 6.4 shows the boxplots for the shear modulus as estimated with the TOF-method (red) in the basal and apical zone and the four probe orientations. The ends of the whiskers indicate the minimum and maximum shear modulus assessed over 10 depths for each SWE-acquisition. These varied from 11.6 kPa to 20.8 kPa for all considered zones and probe angles, which is considerably lower than the ground truth stiffness of 24.3 kPa. Further, the acquisitions performed under probe orientations of 60° and 90 ° for both zones show larger variation in shear modulus estimation across depth than when using probe orientations of 0° and 30°. For example, in the basal zone, the shear modulus range was 3.6 kPa for a 0° probe angle, and 8.1 kPa for a 90° probe angle.

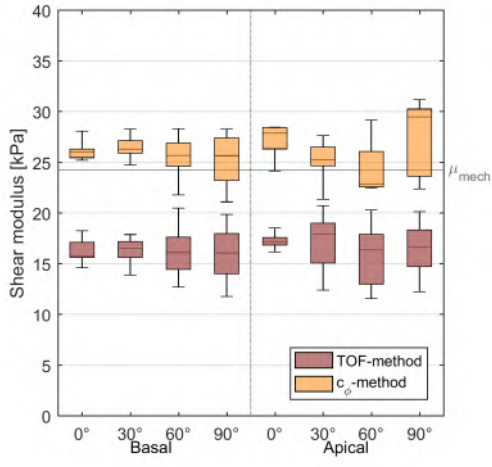

Figure 6.4: Boxplot of estimated shear modulus across depth for various zones and probe orientations with TOF-method and phase velocity analysis (c_ϕ-method), in comparison with the mechanically determined shear modulus μ_{mech}.

6.3.1.2 *Phase velocity method*

The orange boxplots in figure 6.4 show that the phase velocity analysis evaluates the phantom's shear modulus between 21.1 kPa and 31.2 kPa, assessed over 10 depths, for all studied zones and probe orientations, corresponding better to the actual stiffness of 24.3 kPa. The shear modulus estimation differs most across depth for the apical zone and an angle of 90°, corresponding to the most left ventricular curved acquisition, with an estimated range of 8.8 kPa.

Figure 6.5a zooms further in on how the shear modulus estimation depends on the analyzed depth by demonstrating the difference in axial velocity

and Fourier energy maps at three different SW paths for the representative case of the basal zone and a probe orientation of 30°. In the time domain (middle column figure 6.5a), the axial velocity map for SW path 1 shows the largest tissue velocities and a uniform SW front, whereas the maps at larger depths depict lower axial velocities and a clear split in SW front. In the frequency domain (right column figure 6.5a), all Fourier energy plots show clearly that SWE mainly excites one mode, as most of the energy is situated on one straight line from the origin. Furthermore, we observe a second high energy zone, indicating a secondary mode is excited but to a lesser extent than the first mode. When comparing these Fourier energy maps across depth, we see that the frequency content and energy amplitude of the main mode decreases when depth increases. On the other hand, for the secondary mode, the energy amplitude also decreases, whereas its frequency content shifts to higher frequencies for deeper tissue regions. These observations are representative for all acquisitions as shown in figure 6.5b, where the obtained (f, k)-dispersion characteristics are grouped over three zones across depth with all curves following the same trend in general. Here, the yellow curves correspond to the SWE-measurement on the basal zone and probe angle of 30° and the orange curves represent all the other acquisitions.

6.3.2 Effect of the ventricular configuration on shear wave characteristics

In the first section, we will demonstrate the effect of the ventricular geometry on the SW physics by comparing experimentally obtained SW patterns for different zones and probe orientations. In the second section, we will study the influence of viscoelasticity, the surrounding water and the interface pressure on the observed SW physics by means of an FE-model of one representative zone, i.e. the basal zone. The impact of each of these factors on the arising SW physics will be examined by comparing the simulated SW pattern and estimated shear moduli to the experiment.

6.3.2.1 In vitro study of the effect of ventricular geometry

Figure 6.6 compares the measured SW propagation at the apical zone for a probe orientation of 0° and 90°, respectively referring to a less and more curved tissue cross-section. For the first two time points (0.59 and 1.49 ms), the SW pattern corresponds for both probe orientations. For the last time point, at 2.45 ms, we see a clear split in SW-front for both cases. However, a small difference in SW pattern is present at the top edge of the phantom: the wave front stays split into two for the 90°-configuration, whereas these merge for the 0°-configuration (indicated with arrows in figure 6.6).

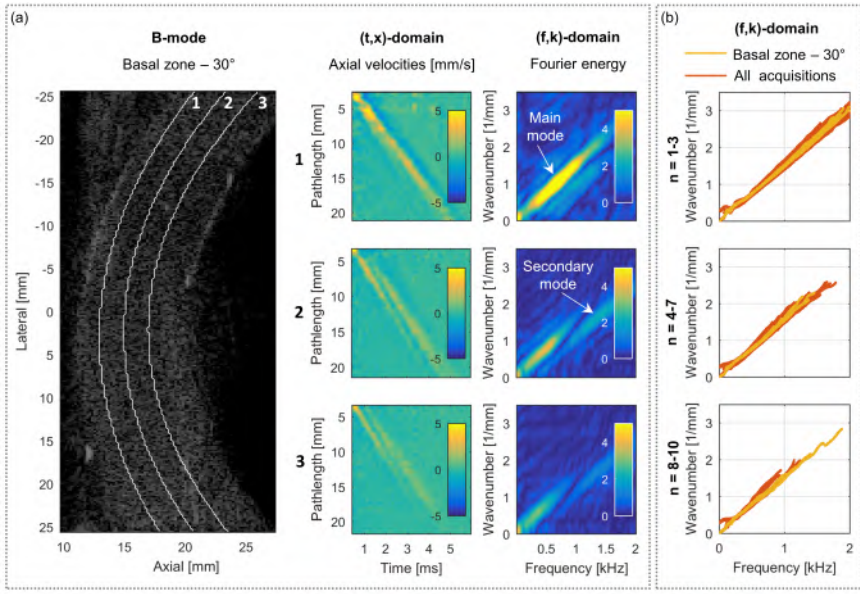

Figure 6.5: (a) Change in axial velocity and Fourier energy maps across thickness for SW paths 1, 2 and 3 (right panels), as indicated in the B-mode image of the acquisition performed on the LV basal zone with a probe orientation of 30° (left panel). (b) Obtained (f,k)-dispersion curves of all acquisitions, where the considered 10 SW paths across depth are grouped together in three zones corresponding to the ones indicated on the B-mode in (a): results for the first three SW paths (n=1-3) are indicated in the upper panel, the following four SW paths (n=4-8) in the middle panel and the last three SW paths (n=8-10) in the lower panel.

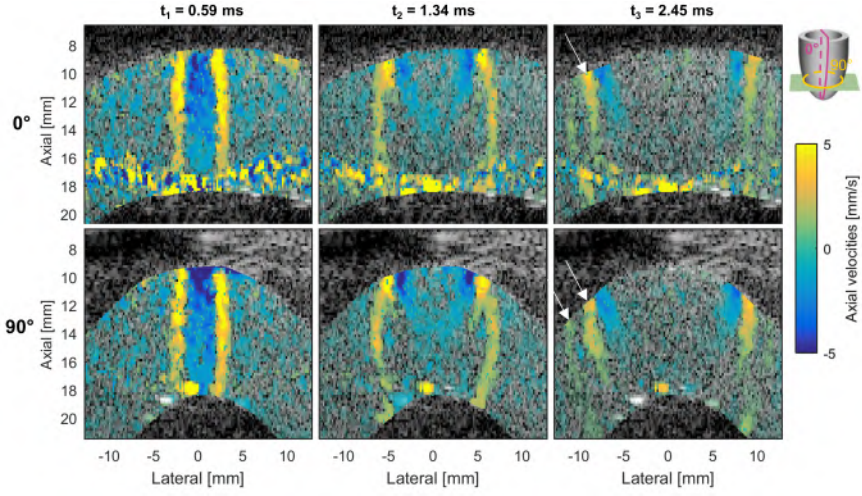

Figure 6.6: Comparison of shear wave propagation in the LV apical zone for probe orientations of 0° (upper panels) and 90° (lower panels), represented in axial velocities on top of the B-mode image at time points 0.59, 1.34 and 2.45 ms.

6.3.2.2 *In silico study of the effect of surrounding media, interface pressure and viscoelasticity*

Figure 6.7 illustrates the axial velocities plotted on top of a B-mode image of the LV basal zone for a probe orientation of 0° at three different time points t_1 = 0.59 ms, t_2 = 1.49 ms and t_3 = 2.45 ms. In order to study the effect of surrounding water and interface pressure, we will focus on two key wave features during propagation: (i) location of the main shear wave front, identified by the high downward velocities at the center of the phantom, which are indicated with black boxes in figure 6.7, and (ii) location of high velocities at the bottom or top edge of the phantom, designated with white boxes in figure 6.7.

The first row in figure 6.7 depicts the SW propagation during the experiment. The red wave front at time t_1 represents the downward push followed by a blue zone of relaxation. For the next time point, the downward velocity wave front becomes more convex (cfr. black box). Additionally, maximal absolute velocities are located at the top edge of the phantom (cfr. white box). At time point t_3, the maximal velocities remain located at the top edge (cfr. white box). The most dominant downward velocity zone is now concave (cfr. black box), lagging behind a weaker convex downward velocity front. This change in wave front shape from time point t_2 to t_3 is caused by dispersion. The black boxes in figure 6.7 thus indicate the effect of dispersion on the SW features.

The other rows in figure 6.7 illustrate the axial velocities as extracted from our corresponding 3D FE-simulations, with each row corresponding to a model with increasing complexity. SW propagation in model I (excluding both water and interface force) is demonstrated in the second row of figure 6.7. Here, we clearly observe a convex wave front for all time points (yellow), which is in disagreement with the measurements. By incorporating water in the FE model (model II in figure 6.7), similar dispersion phenomena as in the experiment are observed, with a change in shape of the yellow SW front, going from convex at time points t_1 and t_2 to concave at t_3 (see black box in figure 6.7). Model III (fourth row in figure 6.7) includes both water and interface force, revealing an even better qualitative correspondence with the experiment. Apart from a similar dispersion effect, i.e. the shift in yellow wave front shape (cfr. black box), one also observes the same location of the absolute maximum of the tissue velocities, i.e. the top edge of the phantom (cfr. white box) when including the interface force. Without the interface force (model I and II in figure 6.7), the absolute maximum remains located at the bottom edge of the phantom throughout the entire time lapse. Hence, the white boxes in figure 6.7 illustrate the effect of the interface force on the SW pattern. When including viscoelasticity in the model, i.e. model IV (last row

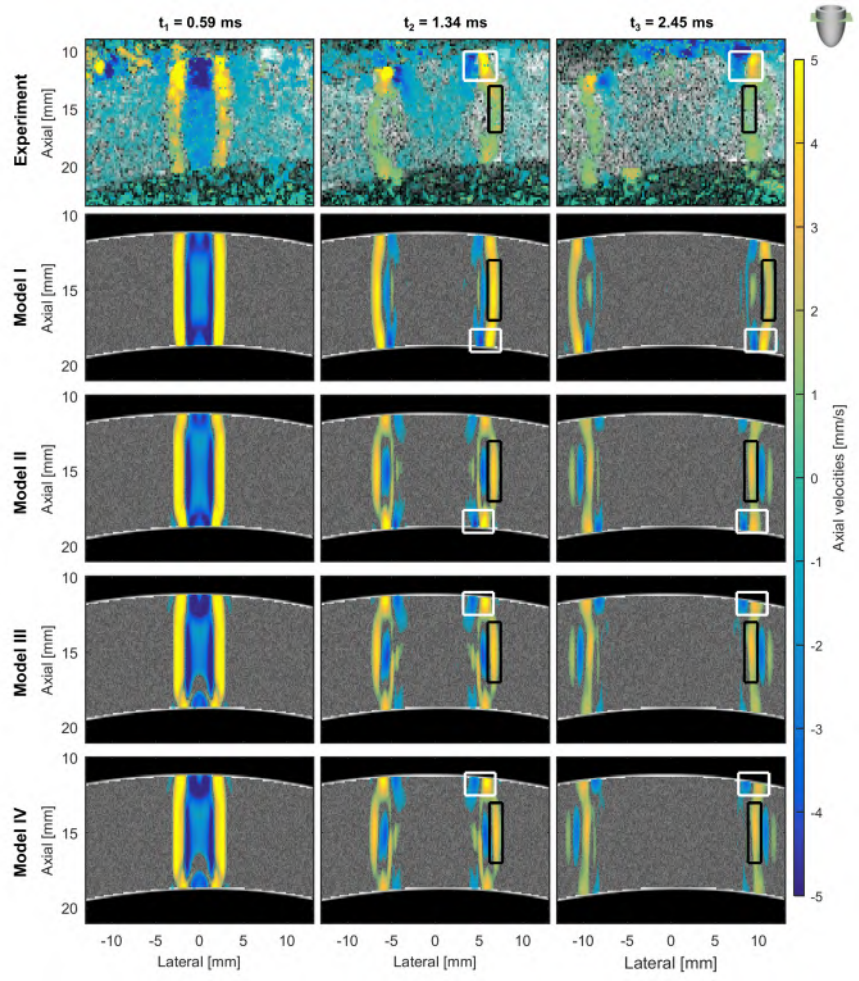

Figure 6.7: Shear wave propagation in the LV basal zone with probe orientation 0° at time points 0.6, 1.5 and 2.5 ms for experiment, model I, II, III and IV. White boxes indicate changes in SW features by including interface force, while black boxes designate SW pattern change by modeling water.

in figure 6.7), the SW patterns are very similar to those of model III. Only a small decrease in overall velocity magnitude is noticeable, together with a slight increase in propagation speed (cfr. black box).

To further analyze and validate our modeled results, both shear modulus estimation techniques are applied to all considered models and the resulting shear moduli are compared to the experimentally obtained ones in figure 6.8. The stiffness estimates of the more advanced models II, III and IV, i.e. median values of 16.6, 16.7 and 16.8 kPa (TOF-method) and 25.4, 25.1 and 25.0 kPa (c_ϕ-method), are in the same range as the experimental SWE-derived stiffness (median value of 15.8 kPa for TOF-method and 26.0 kPa for c_ϕ-method). The same shear modulus estimates also provide a quantitative assessment of the impact of all newly modeled features. Including water in the computational model (model II in figure 6.8) results in considerably lower stiffness assessments than for the original modeling approach (model I) where the assumptions of the surrounding vacuum and the absence of the interface force are valid (median value of 23.9 kPa for the TOF-method and 36.2 kPa for phase velocity analysis). Modeling the interface force (model III) or viscoelasticity (model IV) gives very similar stiffness estimates as for model II.

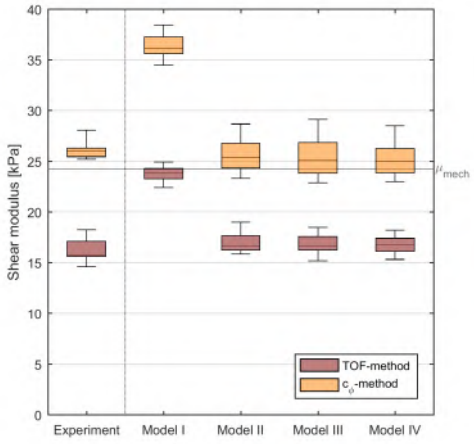

Figure 6.8: Estimated shear moduli of the simulations (model I, II, III and IV) via TOF-method and c_ϕ-method, in comparison with experimental obtained stiffness in the LV basal zone and probe orientation of 0°.

6.4 Discussion

6.4.1 *In vitro* assessment of shear moduli estimators

TOF-method is the gold standard method to use for bulk non-viscous media [44], whereas phase velocity analysis is traditionally used for bulk viscous and thin (viscous) media [125], [136]. For the left ventricular curved geometry, we assessed the performance of both stiffness characterization algorithms by comparing their outcome in an in-vitro myocardial model to a mechanically derived shear modulus. SWE experiments were performed on a left ventricular PVA-model representative of adolescents of 10-15 years old, probing different ventricular zones with varying transducer orientations to study the robustness of these algorithms for varying curvature. Our experimental results showed a clear stiffness underestimation for the TOF-method and a slight stiffness overestimation for the phase velocity analysis for all imaged ventricular areas and probe orientations, as demonstrated in figure 6.4. For the TOF-method, this underestimation of group SWS is caused by SW dispersion, visible as a spatial shift in SW front during propagation (as indicated by the black boxes in figure 6.7), leading to a longer SW travel time. On the other hand, for the phase velocity analysis, the discrepancy is probably due to the fact that the algorithm was based on the dispersion equation of an elastic plate in water, neglecting the curved, ventricular structure and viscosity. Other potential sources for discrepancies between the mechanical testing and the SWE experiment are the uncontrolled and varying environmental conditions, such as the temperature and surroundings (water vs. air). Another way to improve performance of these shear modulus estimators for such curved tissue configuration is to measure the displacement vectors in 2D in order to assess movement perpendicular to the SW path instead of only axial movement.

Next to comparing SWE-estimated shear moduli to actual stiffness, we also studied the depth-dependency of the TOF- and c_ϕ-method. For the TOF-method, figure 6.4 shows an increase in the estimated stiffness range for more curved ventricular settings: 3.6 kPa for 0° vs. 8.1 kPa for 90° in the basal zone and 2.4 kPa for 0° vs. 7.9 kPa for 90° in the apical zone. For the phase velocity analysis, the extracted velocity and Fourier energy maps differ across thickness as illustrated in figure 6.5. The amplitude of these maps decreases when axial depth increases, possibly caused by increased attenuation and the presence of an interface force, as confirmed by the simulations in figure 6.7 (indicated in white boxes). Furthermore, the shape of the axial velocity pattern varies as a function of the analyzed depth because of SW dispersion, leading to a varying energy content of the two main excited modes. However, despite their unlike energy content, the characteristics of the excited modes are similar, i.e. the location of the (f, k)-points with high energy are alike as

shown in figure 6.5b, meaning that they are converted into similar dispersion curves and thus provide a similar stiffness estimate. However, stiffness estimates based on deeper SW paths will be less reliable because (i) the extracted dispersion curves will be shorter due to their smaller energy content (less data points) and (ii) the lower amplitude of motion (lower signal-to-noise ratio) hampers the analysis.

This assessment of the accuracy of myocardial SWE across depth in different imaging regions and for varying probe orientations is highly relevant as fibrosis has been reported to be inhomogeneously distributed throughout the cardiac wall [171], [208], [216]. However, few validation studies have been published on this topic, and certainly not for children. Pislaru et al [206] performed a validation study of myocardial SWE in an open-chest pig setting for a single ventricular imaging location, without reporting any depth-variation of estimated stiffness. They showed a strong correlation between the elastic moduli obtained from phase velocity analysis and their ground truth assessment via the pressure-segment length method. Maksuti et al [14] performed a comparative validation study of the phase velocity and TOF method but in the context of arterial SWE on vessel-mimicking in-vitro phantoms. They also showed that the TOF-method severely underestimated actual stiffness, while phase velocity analysis provided a better estimate.

Besides these validation studies, several groups have demonstrated the feasibility of myocardial SWE, both in an invasive and non-invasive setting. Transthoracic application of this technique in children requires the use of a phased array transducer, for which Song et al [95] have shown an increased signal-to-noise ratio for the obtained SW signal by using pulse-inversion harmonic imaging. Other feasibility studies [15], [16], [133], [134], [150] mainly focused on invasive assessment of the dynamics of SWE-derived mechanical properties at one particular ventricular location in animals. The applied tissue characterization techniques ranged from estimating the myocardial elasticity in [15], [16], [150], to more complex material description as achieved in [133], [134] by including the viscosity. While our evaluation of the shear modulus estimators did not incorporate any complex material properties, the measured Young's modulus was in agreement with *in vivo* values reported in literature (10 to 150 kPa in the physiological regime [217]). However, future work will involve evaluation of SWE tissue characterization in more complex material conditions similar to the heart's viscoelastic and anisotropic behavior, expected to affect the outcome of current post-processing methods.

6.4.2 Effect of the ventricular configuration on shear wave characteristics

We used both SWE-experiments and SW-simulations to gain better insights into which factors influence SW patterns. Next to the *in vitro* assessment

of shear moduli estimators, the SWE-experiments also gave us a qualitative impression of the effect of the ventricular geometry on the SW physics. On the other hand, the 3D SW-simulations allowed us to fully investigate how the surroundings, interface pressure and viscoelasticity affect the SW propagation.

In all measurements, the identified main SW front split into two due to dispersion, as can be seen for the selected acquisitions in figure 6.5, figure 6.7 and figure 6.8. When comparing two SWE-acquisitions in different ventricular settings, as done in figure 6.5 for the apical 0° and 90° cases, we observed a very similar SW propagation pattern, independent of ventricular curvature/thickness, and only small differences were noticeable after the SW had traveled for 2.45 ms.

Next to these SWE-measurements, we also studied the SW physics by means of a 3D computational model mimicking the SWE experiments. Figure 6.7 and figure 6.8 illustrated that the original approach [23], [194] of modeling SWs in an elastic medium in vacuum (model I) did not suffice to correctly represent the SWE experiment at the basal zone and probe orientation 0°. However, this measurement could be correctly mimicked after introducing advanced modeling features such as the surrounding water, the interface force and the material viscoelasticity. In particular, we demonstrated that including the surrounding water (model II) introduced similar dispersion phenomena as present in the experiments, with the shape of the most dominant downward velocity wave front shifting from convex to concave during its propagation. Additionally, the shear modulus estimations via the TOF- and c_ϕ-method decreased compared to the original approach (model I) and corresponded better to the experimental observations. The qualitative match of the modeled SW patterns with the experiments could be further improved by including the interface force (model III), increasing the velocities at the top edge of the phantom but decreasing velocities at the bottom edge. However, the interface force proved not to have a significant effect on the shear modulus estimation (cfr. figure 6.8). Finally, modeling viscoelasticity (model IV) did not evoke any substantial changes in SW patterns, or shear modulus estimations.

While we could conclude that the propagation of the downward push was well represented by the final numerical model (model IV), we also noticed some discrepancies between the model and SWE-experiment. First, the simulations overestimated tissue velocity magnitudes and a higher relaxation peak was present (figure 6.7). Secondly, slightly higher stiffness estimates were derived with the c_ϕ-method, compared to SWE-measurement (figure 6.8). We hypothesize that these differences in SW physics arise due to some of the inherent assumptions behind our simulation methodology and in particular

the way we excite the SWs: (i) approximating the emitted acoustic pressures as a time-averaged volume and interface force and (ii) neglecting the actual propagation, reflection and attenuation of the US-beam. Furthermore, the magnitude and ratio of these imposed forces were determined using a normalized acoustic intensity, as well as an attenuation coefficient, speed of sound and density, either mechanically estimated or literature-based and hence potentially introducing errors (in particular for the attenuation coefficient). Another potential error source is the bias and variance associated with the autocorrelation algorithm for velocity estimation. This is in contrast to the simulations, where the temporal and spatial accuracy of the tissue velocities is not affected by any imaging factors. Hence, future work will include the imaging physics into the computational modeling approach, to investigate the contribution of this latter error source. Additionally, such multiphysics approach provides a general learning platform to study the effect of certain SW excitation and imaging settings (as the use of a phased array probe which is necessary for *in vivo* studies).

Nonetheless, the added value of these 3D-simulations is significant as they allow for a better and more in depth investigation of SW characteristics since experiments are subject to noise and other imaging artifacts. As such, FE modeling permitted to investigate the isolated effect of the surrounding water, the interface pressure and viscoelasticity on the SW propagation and dispersion characteristics, which is much less feasible during experiments. Furthermore, the simulations confirmed that the observed changes in SW pattern are caused by the ventricular setting, and not by inconsistencies in the experimental set-up (e.g. inhomogeneities in the PVA-material due to inconsistent PVA-solving during phantom preparation).

While we provided a unique advanced FE modeling approach to myocardial SW propagation, integrating features such as the surrounding water and the interface force, FE modeling in the myocardium was recently also presented by Urban et al [183]. They introduced an FE method for SW propagation in the myocardium with the aim to investigate the effect of excitation frequency on the accuracy of SW speed estimation and derived fiber direction detection, for harmonic and impulsive SW generation. For this purpose, they applied a complex material model incorporating anisotropy by modeling various transversely isotropic layers oriented at different angles, with material parameters based on literature. They showed that a higher frequency excitation led to a more accurate estimation of SWS and fiber direction. However, the SWs in their FE-model were generated by a line force instead of a spatially varying volume and interface force and they did not perform independent material testing for validation purposes.

6.5 Conclusion

In this work, we assessed the accuracy and robustness of currently available SWE-processing methods to derive myocardial stiffness based on measured axial velocities in a myocardial phantom. Phase velocity analysis provided a better stiffness estimate than the TOF-method, with respect to the mechanically determined shear modulus. Additionally, both methods showed a limited variation in stiffness estimates dependent on the extracted axial depth. We further studied the complex SW physics in pediatric myocardium by modeling SW excitation and propagation in 3D. This computational approach identified the crucial role of the interface force, surrounding water and viscoelasticity on the SW propagation pattern and the shear modulus estimation. Furthermore, as phase velocity analysis will be challenged in patient-specific geometries and complex anisotropic materials, we foresee an important role for FE-modeling in developing new material characterization methods through providing additional information on the complex relationship between stiffness and wave characteristics.

Chapter 7

Effect of myocardial anisotropy on shear wave physics and characterization: *Ex vivo* experiments on porcine hearts

The anisotropic material properties of the heart hinder application of shear wave elastography (SWE) as developed for bulk media, because it makes shear wave propagation and characterization orientation-dependent [15], [16]. In a similar way as done in chapter 6 for studying the effect of a child's left ventricular geometry on SWE, this and the next chapter investigate the anisotropy in the shear wave propagation pattern and in shear wave characterization by using experiments (this chapter) and simulations (chapter 8) on hearts. Therefore, the experimental and numerical hearts were cut open and unfolded to a planar geometry, to discard other effects on shear wave propagation, such as cardiac geometry and residual strains, and focus solely on the effect of interest, i.e. cardiac anisotropy. The 3D shear wave anisotropy complicates on one hand SWE-based material characterization, but on the other hand it can be exploited to extract myocardial fiber orientation [149]. This way of determining myocardial fiber architecture from SWE is employed and compared with results from image analysis to further validate the SWE-technique for cardiac applications. Furthermore, this chapter also examined various degrees of shear wave anisotropy by uniaxial stretching the myocardial slab.

This chapter is based on the IEEE-proceeding of the International Ultrasound Symposium 2017, entitled *"The Effect of Stretching on Transmural Shear Wave Anisotropy in Cardiac Shear Wave Elastography"* [18].

7.1 Introduction

The microstructural organization of the myocardium and its material properties play an essential role in the heart's physiology and pathophysiology. A non-invasive ultrasonic technique, i.e. Shear Wave Elastography (SWE), may allow the assessment of these intrinsic characteristics and therefore contribute to cardiac function evaluation in healthy and diseased conditions. Initial feasibility studies have shown the potential of SWE in (i) generating and tracking shear waves transthoracically in the myocardium [95], but also in (ii) representing the structural and material characteristics of the myocardium by analysis of shear wave characteristics [15], [16]. In this work, we focus on the isolated effect of the myocardial fiber architecture on shear wave characterization, complementing previous work where we studied the isolated effect of left ventricular geometry [20].

The myocardium is composed of layers of parallel myocytes (predominant fiber type) and matrix proteins such as collagen [160]. As it is known from physics that shear waves propagate faster along than across fiber orientation, the SWE-excited shear wave in the myocardium is anticipated to be anisotropic in 3D. This feature has been employed to extract fiber orientation in various anisotropic tissues, with validation in a.o. *ex vivo* pig hearts [149]. The effect of this spatial 3D anisotropy in shear wave propagation on group shear wave speed has also been studied in a freshly explanted sheep heart [15] and in *in vivo* ovine hearts at mid-systole [149]. Cardiac dynamics also affect shear wave propagation and characterization, as shown in [16] for Langendorff perfused rat hearts (studied at one axial depth across tissue thickness).

The aim of this work is to study the combined effect of the 3D myocardial fiber anisotropy and mechanical loading on shear wave propagation and characterization, which has not been studied yet. Furthermore, we wish to extend the shear wave analysis from the time domain to the time and frequency domain (group and phase speed analysis, respectively). The 2D group shear wave speed surfaces across tissue thickness are used to derive fiber orientations and the results were compared to those obtained from image analyses. The study is performed on *ex vivo* pig myocardial slabs of the left ventricle, such that complicating factors such as ventricular geometry and surrounding tissue, residual strains and stresses do not need to be accounted for.

7.2 Materials and methods

7.2.1 Myocardial tissue

Four porcine hearts were freshly obtained from a slaughterhouse, and immediately cryopreserved. One day before the SWE experiment, the hearts were thawed and subsequently dissected to harvest rectangular slabs of left ventricular tissue. Therefore, the atria and right ventricle were removed and the left ventricle was incised along the interventricular septum until the apex, as shown in the left panel of figure 7.1.

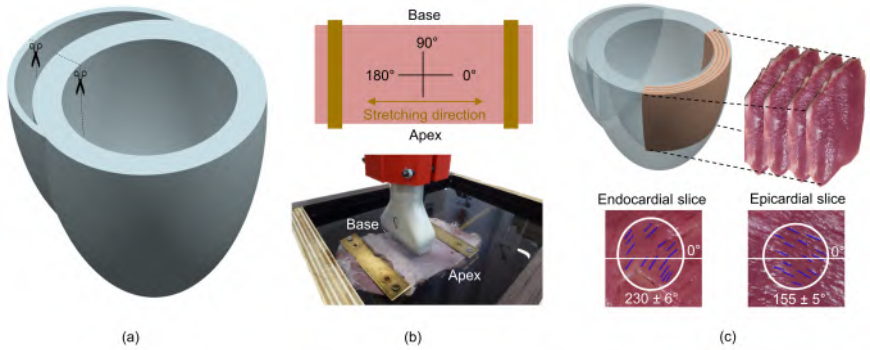

Figure 7.1: Left panel - Indication of the location of tissue excision. Middle panel - Actual and schematic representation of the experimental set-up. Right panel - Extraction of myocardial fiber orientation based on image analysis.

7.2.2 SWE-experiments

7.2.2.1 Set-up

The myocardial slabs were submerged in a warm water bath (temperature range of 36-38 °C), and uniaxially stretched at 5%, 10% and 15% with respect to the zero-stretch length along the heart's circumferential direction between the clamps, as shown in the middle panel of figure 7.1. The L15-4 probe (pitch of 0.2 mm and 256 elements) of the Aixplorer system (SuperSonic Imagine, Aix-en-Provence, France) was placed in the center of the stretched myocardial sample to image the left ventricular free wall. Shear waves were generated by an 8MHz sinusoidal pulse of 250 µs, an F-number of 1.5 and an excitation voltage of 50V while rotating the probe from 0° to 180° in steps of 10° (total of 19 angles). A probe orientation of 0° or 180° corresponded to the circumferential direction of the heart as shown in figure 7.1. The shear wave propagation was imaged using 128 probe elements with a pulse repetition frequency of 6.3 kHz.

7.2.2.2 Data analysis

Pre-processing - Axial velocities were obtained after applying an auto-correlation algorithm [103] to the In-phase Quadrature (IQ)-data. These velocities were averaged across depth every 0.6 mm and up-sampled in the slow time domain by a factor 10.

Group velocity analysis - Shear wave propagation characteristics were studied at 30 axial paths across the myocardial slab covering 17 mm of tissue thickness. Group Shear Wave Speed (SWS) was calculated by the Time To Peak (TTP) algorithm [44], a time-of-flight method fitting a linear regression curve to the shear wave's tracked position, i.e. maximal tissue velocities, in function of time. For fitting, the robustfit function in *MATLAB R2014a* (The MathWorks Inc., Natick, MA, USA) was used. Only regression curves with an R-squared value higher than 0.9 were considered for shear wave speed calculation. Left and right SWS were averaged if both fits fulfilled this criterium.

Fiber orientation analysis - Approaching the myocardium as a composite of transversely-isotropic layers [149], fiber orientation for each layer can be derived based on the direction of fastest shear wave travel. Translating this to our experimental setting, the fiber orientation can be estimated by searching for the probe orientation yielding the highest shear wave speed for a certain shear wave path. Hence, for each sample at a given stretch, group speed analysis yielded a 30x19 SWS-matrix for the considered 30 shear wave paths and 19 probe angles. As the group speed surface in a transversely isotropic material is ellipse-shaped in the plane of symmetry [117], the fiber orientation corresponds with the tilted major axis of a fitted ellipse. This ellipse fitting is performed in *Matlab* in a least squares manner [218]. Mean Squared Error (MSE) was reported as a measure of the goodness of fit.

Phase velocity analysis - The dispersive shear wave characteristics are studied in the frequency f and wave number k domain by taking the 2D Fast Fourier Transform (FFT) of the axial velocities of left/right shear wave for 5 shear wave paths across tissue thickness [136]. An amplitude mask of 10% was applied to reduce the noise in the (f, k)-space. Excited modes were identified by tracking the wavenumbers with high Fourier energies for each frequency. The main excited mode is found by selecting the mode with the highest frequency energy content. Phase velocities c_ϕ were calculated as $c_\phi = 2\pi f/k$.

Statistical analysis - We further analyzed group and phase velocity values by performing a General Linear Model (GLM) univariate analysis in the statistical software *SPSS* version 24 (IBM Corp., Armonk, NY, USA). This model included the fixed factors heart (4 different samples), depth (30 paths),

angle (0-180°) and stretch (5-15%), but also the interaction terms angle*stretch and angle*depth as fiber angle varies with depth and stretch. A factor was statistically significant when it entered the model with a P-value <0.001. Estimated marginal means were calculated for the 3 stretch ratios and the 19 investigated probe angles.

7.2.3 Image analysis

The myocardial fiber orientations can be studied optically due to the laminar structure of the myocardium [163]. Therefore, the ventricular slabs were cut into 4 slices of 5 mm thick by using an electrical meat slicer. A picture was taken of the upper and lower side of each slice (right panel of figure 7.1). On these photographs, the center of the probe was located and fibers (n = 15) were tracked in a circular region with radius of 12.8 mm (representing 128 probe elements) around this center point. This analysis was repeated for each photo, except for epi- and endocardium, leading to an average fiber angle (and standard deviation) at three different points across tissue thickness.

7.3 Results

7.3.1 Group speed analysis

All group velocity data are pooled in boxplots in the upper panel of figure 7.2. The 25th and 50th percentile do not show a clear trend with respect to stretch ratio, whereas the 75th percentile increases with stretch for all hearts. Note the SWS variability in between hearts. Median value for hearts 3 and 4 is around 4 m/s for all stretch ratios, while values are higher for heart 1 (4.7-4.8 m/s) and lower for heart 2 (3.3-3.6 m/s). The GLM univariate analysis revealed that all defined factors entered the model: heart, angle, stretch, depth, angle*stretch and depth*angle, mentioned in order of importance. The GLM also yields the marginal mean of the group speed for a given average sample and depth. The lower panel of figure 7.2 clearly shows that group speed only increased with stretch for probe orientations 0-30° and 120-180° (i.e. along the fiber direction). Additionally, the probe orientation giving the maximum of the estimated marginal mean group speed value varied depending on the applied stretch: 150° for 5%, 160° for 10% and 170° for 15%.

The spatial anisotropy in group speed becomes apparent in figure 7.3, displaying group shear wave speed as a function of probe angle and tissue thickness (data shown for heart sample 3). This figure confirms that group speed increases when stretch increases and visualizes the variation of the maximal SWS with probe orientation across tissue thickness.

7.3.2 Fiber orientation analysis

The SWE-derived fiber orientation (colored symbols in figure 7.4) varied across tissue thickness in a range from 133°-166° (heart 1), 135°-210° (heart 2), 150°-182° (heart 3) and 130°-207° (heart 4) at a stretch of 5%, where the first mentioned value represents the fiber orientation closest to the epicardium

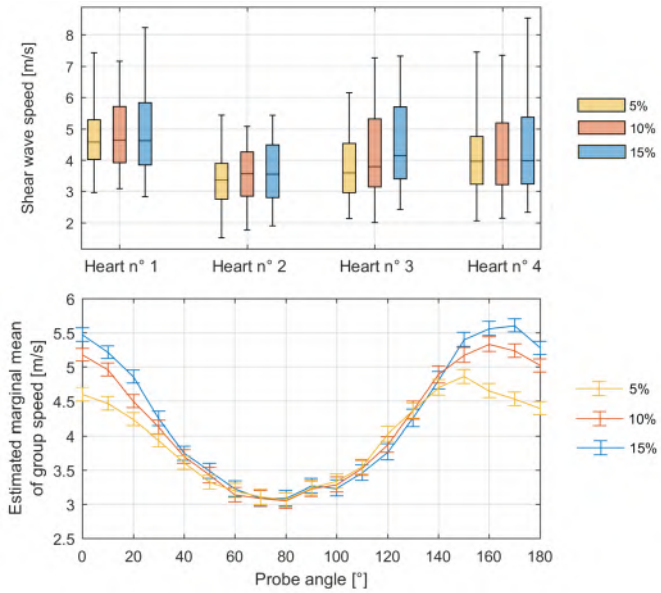

Figure 7.2: Upper panel – Effect of stretching on group speed values for all acquisitions with probe rotation from 0-180°, demonstrated in a boxplot (box represents the 3 quartiles, whiskers indicate minimum/maximum). Lower panel – Combined effect of stretching and probe orientation on estimated marginal mean of group speed values for all hearts (errorbars indicate 95% confidence interval).

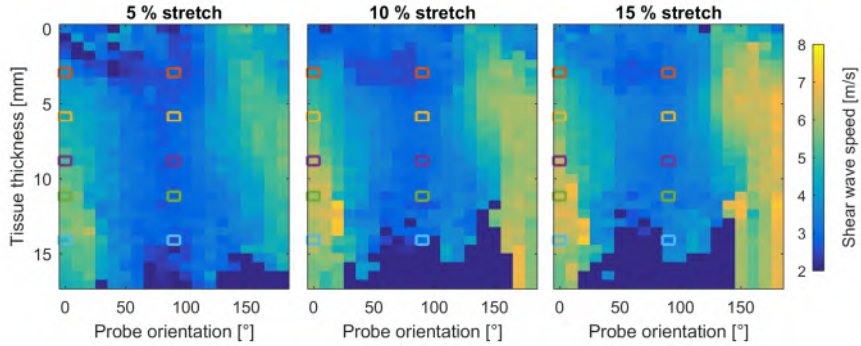

Figure 7.3: Spatial anisotropy in group shear wave speed during stretching for heart n° 3 (raw data). Colored boxes indicate extracted locations for figure 7.6 and figure 7.7.

and the last mentioned value closest to the endocardium. During stretching, the transmural variation in fiber orientation decreased for hearts 2, 3 and 4, as shown in table 7.1, and the fibers approached the stretching direction, i.e. 180°, for all hearts. The maximal MSE-value of the ellipse fitting procedure for deriving myocardial fiber orientation varied between 0.057 and 0.215 $(m/s)^2$ for all SWE-acquisitions. The SWE-derived fiber orientation corresponded reasonably well with those of the image analysis (open symbols in black) for the epi- and mid-cardiac point. Data obtained at the endocardial side differed a bit more from the SWE-based values. Note that the image analysis was performed at 0% stretch.

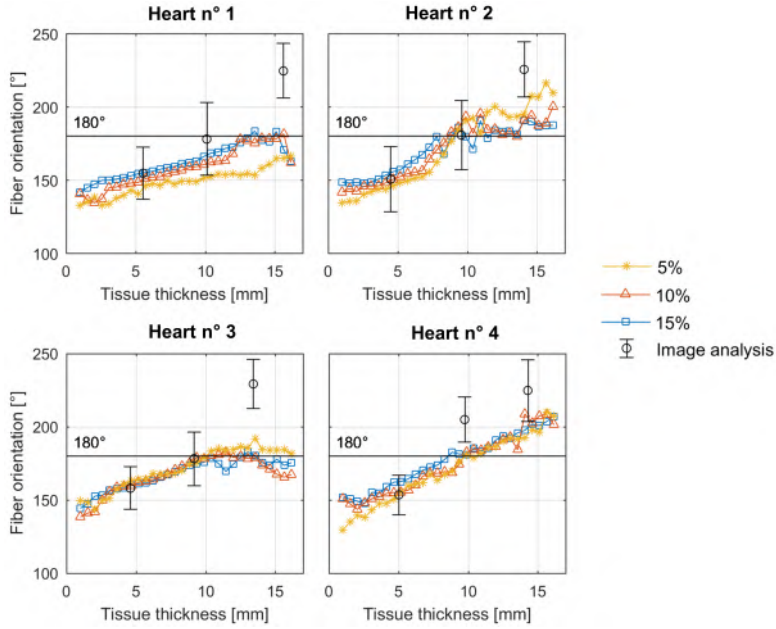

Figure 7.4: Comparison of fiber orientation derived from group speed and image analysis for all hearts. Error bar represents mean with 95% confidence interval.

Table 7.1: SWE-derived transmural fiber variation for all hearts (=max-min) [°].

Heart n°	5% stretch	10% stretch	15% stretch
1	34	47	42
2	82	59	43
3	48	44	39
4	81	65	59

7.3.3 Phase speed analysis

Phase velocity data of the dominant excited mode (i.e. phase velocity corresponding to frequency with maximal Fourier energy) in all acquisitions are

grouped in boxplots in the upper panel of figure 7.5. Median values varied between 3.5-4.0 m/s (heart 1), 2.8-3.0 m/s (heart 2), 3.2-3.5 m/s (heart 3) and 3.1-3.4 m/s (heart 4). The 75th percentile increased for all heart samples when stretch increases. The GLM analysis indicated that all factors heart, depth, angle, stretch, depth*angle and angle*stretch were statistically significant (mentioned in order of importance). The estimated marginal mean depicted a similar trend as for the group speeds: an increase of the maximally excited phase speed when stretch increases for probe angles 0-50° and 140-180°, in combination with a small spatial shift of the maximum phase speed in function of probe angle.

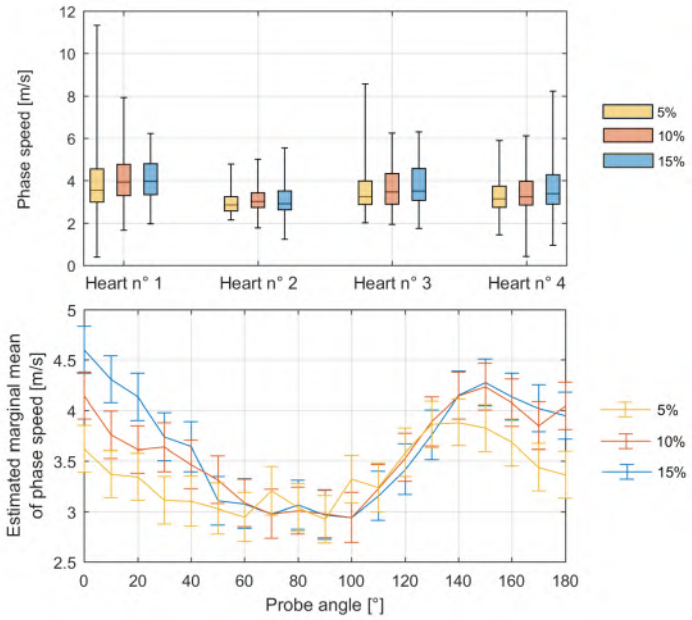

Figure 7.5: Upper panel – Effect of stretching on phase speed at maximum excited frequency (= frequency with highest Fourier energy) for all acquisitions with probe rotation from 0-180°, demonstrated in a boxplot (box represents the 3 quartiles, whiskers indicate minimum/maximum). Lower panel – Combined effect of stretching and probe orientation on estimated marginal mean of phase speed values for all hearts (errorbars indicate 95% confidence interval).

The combined effect of stretching and shear wave anisotropy on the dispersion curve of the main excited mode is demonstrated in figure 7.6 for heart sample 3. The main excited frequencies varied from 153.5 Hz to 476.0 Hz for 0° probe orientation and from 168.9 Hz to 307.1 Hz for 90° probe orientation (all in the ascending part of the dispersion curve, suggesting the occurrence of dispersion) and the depths selected in this figure are indicated

in figure 7.3. For the 0°-acquisitions, one observes an increase in the plateau-value of the dispersion curve while stretching, whereas this is less noticeable for the 90°-acquisitions. Furthermore, for a given stretch state, dispersion curves vary depending on the axial depth but there is no clear trend in this depth-dependency.

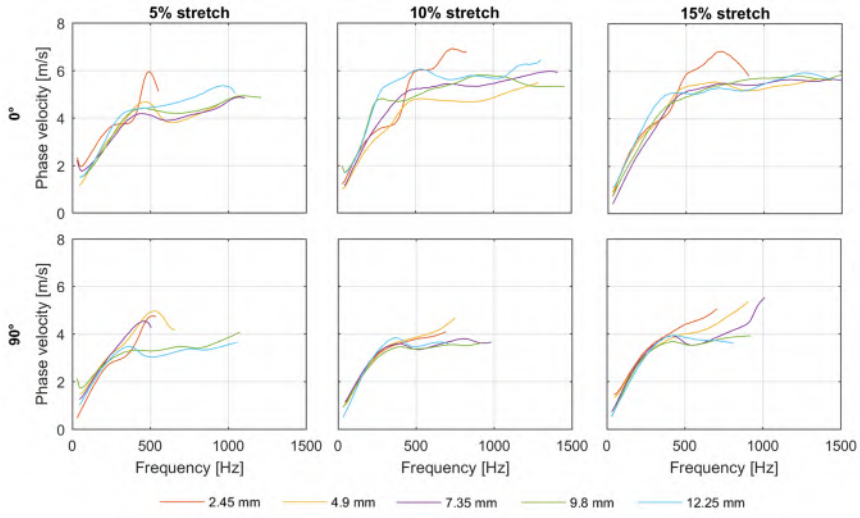

Figure 7.6: Effect of stretching on dispersion curves of left shear wave for 0°- and 90°-acquisitions for 5 different depths, as indicated in figure 7.3.

7.3.4 Group vs. phase speed analysis

The resulting group and phase speed surface at 200 and 400 Hz are compared across depth for heart 3 at a stretch state of 5% in figure 7.7. At a frequency of 200 Hz, the phase speed surface is almost circular across depth, whereas the group speed surface is ellipsoidally shaped. Furthermore, the phase and group velocity values correspond around the minor axis of the group speed ellipse for all considered depths, whereas the largest difference in phase and group velocity values is obtained for probe angles along the major axis of the group speed ellipse. At a frequency of 400 Hz, the phase speed surface becomes also ellipsoidally shaped like the group speed surface for all depths. Their velocity values are very similar for all probe angles at this frequency.

7.4 Discussion

7.4.1 Effect of stretching on shear wave characteristics

As expected, group and phase speed values for a certain heart sample at a given stretch state were depth- and probe orientation-dependent (see figure 7.3),

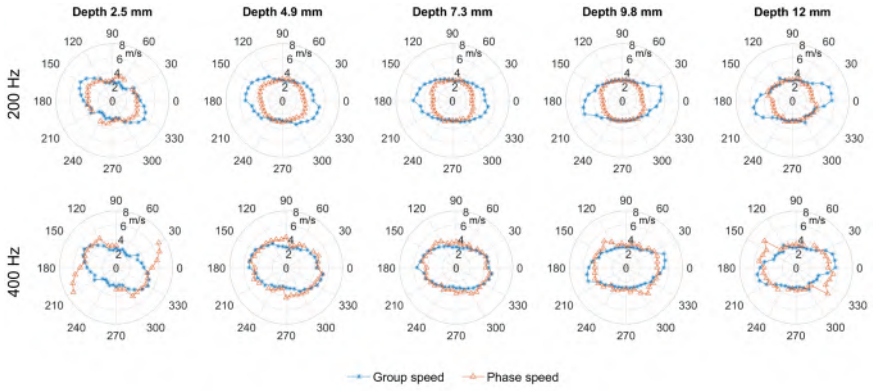

Figure 7.7: Comparison of group and phase speeds at frequencies of 200 and 400 Hz for 5 different tissue depths in heart 3 at a stretch of 5% (locations indicated in figure 7.3). R-axis depicts wave speed in m/s, whereas θ-axis represents probe orientation in °. Both group and phase speed results are averaged results of left and right shear wave.

due to the varying myocardial fiber orientation across tissue thickness. The range of the resulting group speed values of all hearts corresponded to values previously reported in literature: 2-6 m/s for *in vitro* porcine hearts at 0% stretch [149]. Uniaxial stretching the myocardial slab increased the group and maximally excited phase speed, as could be seen from the 75th percentile increase, but also from the increasing predicted marginal mean of each variable during stretching. This increase was mainly caused by an increase in wave speed for probe orientation angles oriented along the fiber direction for both cases. This trend was more convincing for group speed than for phase speed, as the GLM statistical model fit showed an adjusted R-squared value of 0.804 for group speed vs. a value of 0.415 for maximally excited phase speed (also related to the fewer data points for phase speed analysis). Furthermore, for maximally excited phase speed, tissue depth was the second most relevant factor in determining marginal mean phase speed for a mean heart at a mean depth, whereas this was the fourth relevant factor for the group speed. This is also noticed from the larger 95% confidence interval in figure 7.5 vs. figure 7.2.

Phase velocities at 200 and 400 Hz were also analyzed. Marginal means of the GLM analysis showed similar trends as for the maximally excited phase velocity but models reached a lower R-squared value (0.366 and 0.252 for 200 and 400 Hz respectively). Nevertheless, the spatial variance in the phase velocity polar plots of figure 7.7 showed that frequency mainly affected phase speed values at probe orientations close to the fiber direction. Furthermore, phase and group speed values corresponded for cross-fiber probe orientations at the two investigated frequencies.

It should be noted that the presence of trabeculae caused considerable variation in myocardial thickness, however we analyzed only the tissue depths in which shear waves are generated by SWE. Additionally, stretching altered the myocardial thickness slightly.

7.4.2 Effect of stretching on SWE-derived fiber orientation

The extracted fiber orientation from SWE altered slightly during stretching, as the fibers became more aligned to the stretching direction of 180°. SWE-derived fiber orientation of heart 1 was different than that of the other hearts, probably due to difference in imaged location or intraspecific variability in fiber architecture. Fiber organization was assessed by using an ellipse based extraction method, which was more robust than utilizing maximal group velocity as surrogate for fiber angle, as done in [149]. This is also noticeable when comparing the probe orientations with maximal velocity in the group speed maps of figure 7.3 to the extracted fiber orientation in figure 7.4 for every depth.

These SWE-derived fiber orientations corresponded well with image analysis for the first two data points, but not for the last one (closest to the endocardium). Possible causes for this discrepancy are: (i) fiber direction might locally vary as this data point of the image analysis is closely located to the trabeculae in which fibers are longitudinally oriented [219], (ii) difference in location studied with both measurements and (iii) limited accuracy in image analysis due to suboptimal light incidence and photo resolution. Studying more than three samples or using a microscopic image analysis might prevent these inaccuracies.

7.4.3 Study limitations and future work

We considered the myocardium as transversely isotropic layers parallel to the lateral-elevational plane of the ultrasound transducer, which imposes the analyzed shear wave propagation paths in these layers, and thus does not allow a full 3D study of the 3D shear wave. It is known that the myocardial fiber architecture also has a transverse angle component next to the helix angle component, which we did not consider. This transverse angle variation is smaller than that of the helix component (+9° to +34° vs. -41° and +66°) [161], but future work should include more advanced analyzes taking 3D shear wave tracking into account. Also, as we did not account for cardiac physiological loading, our findings cannot assess the *in vivo* performance of cardiac SWE. A third limitation is the reliability of the extracted dispersion curves, which is undetermined for every considered location as it is dependent on the acquisition's frame rate, but also on the quality of the SWE-acquisition.

Note that it is generally known that the myocardium is a viscoelastic tissue, as is reflected by the hysteresis effect in the stress-strain curve during

mechanical loading and unloading (see for example the work of Sommer et al [163] on biaxial testing of human myocardial tissue). Furthermore, the magnitude of the hysteresis effect varies with the orientation of the mechanical loading with respect to the intrinsic myocardial structure. Next to this, preconditioning alters as well the mechanical response of myocardial tissue. The overall cardiac mechanical response is thus dependent on various factors, which might affect the resulting group speed derived from SWE. However, its quantitative effect on group shear wave speed is unknown. Therefore, it is unsure how representative the obtained group speed values are for an actual *in vivo* cardiac SWE acquisition. Nevertheless, the mechanical response of myocardial tissue along and across the fiber is remarkably different [163], which is reflected by the anisotropy in the group speed maps of figure 7.3. Additionally, the relaxation effect between the SWE acquisition with a probe orientation of 0° (start of experiment) and 170° (end of experiment) is minimal, as demonstrated by the similar group speed values obtained for these angles (see figure 7.3). This is confirmed by Sommer et al [163], who showed that most of the myocardial relaxation behavior occurs within the first 150 s of the experiment.

In future work (chapter 8), finite element modeling will complement these experiments, in which shear wave propagation is modeled by applying a temporal and spatial varying body force, representing the acoustic radiation [20]. These simulations provide access to the ground truth fiber orientation at the exact same location where shear wave analysis will be performed. This modeling should therefore resolve most of the above-mentioned study limitations.

Chapter 8

Effect of myocardial anisotropy on shear wave physics and characterization:

Ex vivo simulations

The effect of anisotropic cardiac material properties and mechanical loading on the performance of shear wave elastography (SWE) is experimentally investigated on *ex vivo* porcine hearts in chapter 7. This chapter now represents the numerical expansion of previous chapter, in order to gain a better understanding of the interaction between myocardial anisotropy and mechanical loading on shear wave physics and subsequent characterization. As complete mechanical characterization of the tested porcine cardiac tissue was not possible, the numerical SWE acquisition was performed on a slab of porcine left ventricular tissue with its material parameters obtained from literature (cut open along the interventricular septum and stretched in its circumferential direction, similar as mentioned in chapter 7). The computer model provided access to the true fiber orientation and material properties, allowing assessment of the accuracy of two methods determining fiber orientation based on SWE and a preliminary evaluation of the impact of pathology on shear wave physics and characterization.

This chapter is based on the paper submitted to the journal of Physics and Medicine: *"An in silico framework to analyze the anisotropic shear wave mechanics in cardiac shear wave elastography"*.

8.1 Introduction

Tissue stiffness is a relevant clinical biomarker reflecting pathological changes of the involved tissue [28], [31], [43]. Using ultrasound-based SWE tissue stiffness can be derived from the propagation characteristics of internally excited shear waves in tissue. More specifically, we are interested in impulsive shear wave excitation (order of 100-500 μs), realized through a focused ultrasound beam generated by a conventional transducer, resulting in an acoustic radiation force (ARF). This technique has been widely recognized as a reliable, quantitative tool for evaluating tissue stiffness in bulky media, such as breast and liver tissue [74], [75].

Over the past few years, SWE has been applied to assess stiffness of other organs including the myocardium [15], [16], [150], [181], [182], [184]. While these initial studies on cardiac SWE yielded encouraging results, they also raised two major potential issues (as discussed in section 3.2 of chapter 3). First, all reported studies were invasive *in vivo* or *ex vivo* animal studies, as transthoracic generation and detection of shear waves seems limited by the location of the heart deep in the chest and by the limited ultrasound access between the rib spaces. Different solutions have been proposed for this problem, such as the implementation of pulse inversion harmonic imaging (PIHI) for improving the SWE image quality in closed chests [152] or the use of trans-esophageal transducers [151]. Recently, the combination of PIHI and coherent compounding has demonstrated the potential of transthoracic ultrafast imaging of the heart [177]. The second more fundamental concern raised by these feasibility studies relates to the shear wave physics excited in a non-homogeneous, non-linearly elastic and anisotropic medium, such as the cardiac wall, possibly causing anisotropy in wave propagation [15] and other more complex wave features such as wave dispersion and guided wave effects [38], [133], [134]. Consequently, the relationship between the wave propagation characteristics and tissue material properties in the cardiac setting may be more complex than for homogeneous and isotropic bulk media. Initial steps have been taken in cardiac SWE towards more advanced material characterization techniques based on the wave's phase speed instead of the conventionally analyzed group speed. In that case, the theoretical Lamb wave dispersion model for viscoelastic media [38], [133], [134] is used as fitting ground truth for the measured one, taking into account the confined geometry of the cardiac wall and its viscous material properties (see section 3.3 of chapter 3).

It is non-trivial to untangle the complex relationships between the heart's intrinsic material properties, tissue surrounding, mechanical loading and geometry on one hand; and the SWE-excited wave mechanics together with its material characterization on the other. To be able to address these complex

relationships, we developed an in silico framework using the finite element method (FEM) to mimic the biomechanics of an actual myocardial SWE acquisition. This approach was previously successfully applied to isotropic bulk and ventricular geometries [20], [194] (see chapter 6). Recently, Urban et al [183] introduced a cardiac FEM-model to study the effect of SWE excitation frequency, using impulsive and harmonic excitations, on shear wave propagation in diastole and systole. They modeled the myocardium as a composite of transversely isotropic layers with different material orientations and varied the number of layers and stiffness parameters to represent the diastolic and systolic phase.

In this work, we extend on the computational cardiac SWE simulation work by (i) implementing a more realistic cardiac material model using the orthotropic material law as proposed by Holzapfel and Ogden in 2009 [160] for myocardial tissue, and (ii) explicitly accounting for the effect of mechanical loading on shear wave characteristics in the simulations. This work focuses on SWE using impulsive ARF methods. The validity of the cardiac SWE simulations is assessed by comparing the resulting shear wave group speed features to those of our earlier *ex vivo* cardiac experiments reported in chapter 7 [18].

The developed numerical framework for cardiac SWE has the advantage over *ex vivo* or *in vivo* cardiac experiments to provide direct access to the true cardiac material properties and the ground truth fiber orientations. This advantage will be exploited in two applications of the model. First, a parameter study will be performed to examine the effect of cardiac material properties in combination with mechanical loading on shear wave propagation and characterization. Here, we take into account the shear wave variability across thickness due to the myocardial fiber architecture. Second, as Lee et al [220], [221] demonstrated the feasibility of SWE in detecting the transmural variation of the myocardial fiber orientation, we will use the numerical framework to assess the accuracy of different methods in determining cardiac fiber architecture from SWE acquisitions [117], [221].

8.2 Materials and methods

8.2.1 Geometry and set-up

The geometry of the FEM-model is the same geometry used previously in our experimental set-up in [18], i.e. a rectangular section of left ventricular tissue, obtained from the heart by first removing the right ventricle and cutting the left ventricle from base to apex, along the interventricular septum (see left panel of figure 8.1) . Next, this cardiac tissue slab is clamped at both interventricular septal ends, and uniaxially stretched along the circumferential

direction of the ventricle, as indicated in figure 8.1. The resulting dimensions of the tissue slab in between the clamps are 60.0 mm x 20.0 mm x 64.6 mm. Similar to the SWE experiments in [18], three stretch ratios, i.e. 5%, 10% and 15% with respect to the original length of the slab, were considered. These stretch values are based on recently reported biaxial tests performed on human myocardium [163], [222], where cardiac samples were stretched from 5% to 15-20% (until the tissue fails). At each stretch ratio, a virtual SWE acquisition is performed in the center of the cardiac slab using a linear probe with an axial focus of 30 mm. The lateral axis of the probe corresponds to the circumferential direction of the ventricle (0° or 180° as indicated in the right panel of figure 8.1).

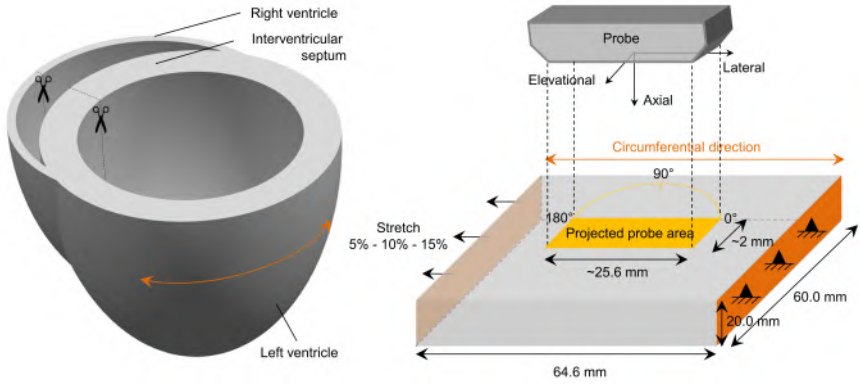

Figure 8.1: Followed protocol to obtain a quasi-rectangular slab of left ventricular tissue (left panel): the left ventricle is cut-open from base to apex along the interventricular septum. Geometry of the finite element model of the myocardial slab (right panel): orange planes indicate fixation and the yellow zone represents the probe area with dimensions indicating the active piezoelectric zone.

8.2.2 Material model

The cardiac wall is composed of two relatively thin outer (epicardium) and inner (endocardium) layers, and the thicker middle layer, the myocardium. Myocardial tissue is non-linear, viscoelastic and orthotropic in its behavior [160]. In this work, we only consider the passive mechanical behavior of the myocardium, neglecting the (relatively small) mechanical contribution of the other two layers. The ventricular myocardium is a composite of sheets of parallel myocytes (predominant muscle cells), anchored in a connective tissue network, containing mainly collagen and elastic fibers. The muscle fiber orientations follow a complex architecture which alters with depth throughout the cardiac wall. Overall, the fiber angle (relative to the circumferential direction of the left ventricle) changes from -50° to -70° in the sub-epicardial

region to nearly 0° in the mid-wall region, to +50° to +70° in sub-endocardial region [160].

A constitutive law describing the mechanical behavior of the ventricular myocardium is derived by decomposing the strain energy function ψ in a volumetric part ψ^{vol} and a deviatoric part ψ^{dev}:

$$\psi = \psi^{vol} + \psi^{dev} \tag{8.1}$$

The volumetric bulk material was described by a hyperelastic constitutive Arruda-Boyce model [204], which has the following strain energy density function:

$$\psi^{vol} = \frac{1}{D}\left(\frac{J^2-1}{2} - ln(J)\right) \tag{8.2}$$

With J the elastic volume ratio and D inversely proportional to the bulk modulus K ($D = 2/K$). The deviatoric part of the strain energy function can be further additively decomposed into the isotropic contribution ψ^{iso} of the tissue matrix, the contribution of the combined myocyte fibers ψ^{f}, the contribution of collagen struts connecting the individual myocardial sheets (cross-fiber) ψ^{s}, and the relative shear contribution ψ^{fs}, as proposed by Holzapfel-Ogden (HO) [160]:

$$\begin{aligned}\psi^{dev} &= \psi^{iso} + \psi^{f} + \psi^{s} + \psi^{fs} \\ &= \frac{a}{2b} exp[b(I_1 - 3)] + \sum_{i=f,s} \frac{a_i}{2b_i}\left\{exp[b_i(I_{4i}-1)^2 - 1]\right\} \\ &+ \frac{a_{fs}}{2b_{fs}}[exp(b_{fs}I_{8fs}^2 - 1)]\end{aligned} \tag{8.3}$$

with eight material constants a, b, a_f, b_f, a_s, b_s, a_{fs} and b_{fs}; and material invariants I_1, I_{4f}, I_{4s} and I_{8fs}. It should be noted that the terms ψ^{f} and ψ^{s} only contribute to the stored energy when the associated directions are under tension. When they are under compression ($I_{4s} < 1$ or $I_{4f} < 1$), their contribution is zero, as myocytes nor collagen fibers support compression. The material constants for the deviatoric part of the strain energy function were derived from healthy porcine myocardium as reported in [223], whereas the density ρ and parameter D were derived from our previous work [20], [24]. Parameter D is chosen to ensure (quasi)-incompressibility of the tissue. Given that D is inversely proportional to the bulk modulus and computational time, a trade-off between high enough bulk modulus values and computational

cost was made in choosing its value. An overview of all parameters is given in table 8.1. The modeled fiber orientation varied from -50° (epicardium) to +50° (endocardium) [160].

Table 8.1: Material constants in ventricular myocardial model, described by equation (8.1), equation (8.2) and equation (8.3). Values of ρ and D were derived from our previous work [20], [24]; all other values were taken from [223].

Material parameters	Value
Density ρ	1045.5 kg/m^3
a	0.236 kPa
b	10.81
a_f	20.03 kPa
b_f	14.15
a_s	3.72 kPa
b_s	5.16
a_{fs}	0.41 kPa
b_{fs}	11.3
D	0.01 MPa^{-1}

The constitutive model was implemented in the user-defined subroutine VUANISOHYPER_HYPER, available in Abaqus Explicit [204], which updates the stress state in the local material orientations based on the first and second derivative of the strain energy potential function defined in equation (8.3) for each time increment of the simulation.

8.2.3 Numerical implementation: uniaxial stretching in combination with shear wave elastography

Simulating an SWE acquisition on uniaxially stretched myocardium encompassed at least two different modeling steps, as both processes are of a different mechanical nature (static vs. dynamic), requiring different numerical solution techniques. Furthermore, static problems such as the uniaxial stretching procedure typically require a larger mesh size and temporal sampling than dynamic problems such as the SWE-induced shear wave propagation. Therefore, the uniaxial stretching problem was solved considering the complete myocardial slab as presented in figure 8.1 (the so-called *global model*), whereas the shear wave propagation problem was studied in a cylindrical subdomain of the myocardial slab, situated in the center of the model, right below the probe area (the so-called *local model*; see also figure 8.2), in order to obtain a reasonable computational time and accuracy. For the same reasons, the diameter dimension of this local domain was chosen in the same order of magnitude as the length of a conventional probe with 128 elements and a pitch of 0.2 mm. In practice, the complete numerical procedure consisted of the following steps (figure 8.2): (i) uniaxially loading the global model, (ii)

translating the stresses of the global model to stresses of the local model and (iii) performing a virtual SWE acquisition on the local model.

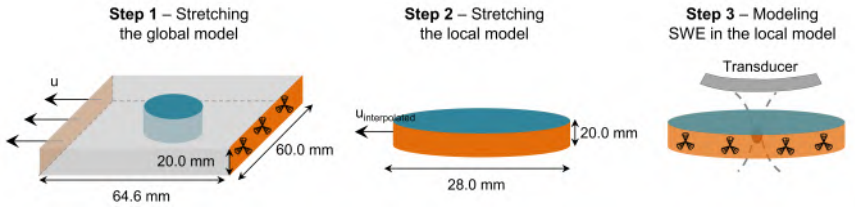

Figure 8.2: Overview of the different modeling steps: (i) uniaxially stretching the global model using a displacement-driven load u with one side fixed (orange), (ii) uniaxially stretching the local model based on the results of the first model and (ii) modeling the shear wave acquisition in the local model.

The mesh of the global model (mesh size determined from a mesh sensitivity study) consisted of 9600 hexahedral solid elements. The cylindrical geometry of the unloaded local model becomes ellipsoidal during stretching (see figure 8.2 for dimensions). A circular mesh allowed to orient the mesh perpendicular to the expected direction of wave incidence to minimize any numerical errors and computational time [214]. The mesh size is determined by the accuracy needed for the wave propagation problem in modeling step 3, requiring at least 10-15 elements per wavelength [196] and a mesh refinement zone for accurate ARF application [20]. This led to a total of 514560 hexahedral solid elements for the local model.

The uniaxial stretching procedure in modeling steps 1 and 2 is simulated as a quasi-static problem using the explicit dynamics in *Abaqus* (Abaqus Inc., Providence, RI, USA). The displacement-based loading rate of the simulation was chosen based on a trade-off between short computational time and ensuring insignificance of inertial forces [204]. This led to total simulation durations of 0.3 s for 5% stretch and 0.5 s for 10% and 15% stretch. Additionally, viscous pressure loads were applied at the boundaries of the local model to further damp out any dynamic effects, and thus to sooner reach a static equilibrium [204]. A parameter study was performed to determine the viscosity factor of this viscous pressure load, which was defined as $0.02\rho c_L = 9.15 \cdot 10^{-6} N$, leading to the largest reduction in residual axial velocities at the end of modelling step 2. To transfer the results from modeling step 1 to step 2, the node-based submodeling technique was used to interpolate the results of the global model to the boundaries of the submodel.

In the third modeling step, the acoustic radiation force (ARF) is applied, and the resulting shear wave propagation is modeled. In practice, this implies a third *Abaqus/Explicit* analysis which starts from the imported model information and results (stretched geometries and stress/strain field) from the

second modeling step (see also figure 8.2). The ARF is applied as a body force for the push duration of 250 µs in the focal region under the probe, extending 4 mm in the lateral and elevational direction. The spatially varying body force $B(x, y, z)$ was modeled as a 3D Gaussian function with the following expression [141]:

$$B(x, y, z) = B_{max} e^{-\left(\frac{(x-x_0)^2}{\sigma_x^2} + \frac{(y-y_0)^2}{\sigma_y^2} + \frac{(z-z_0)^2}{\sigma_z^2} \right)} \tag{8.4}$$

with maximal amplitude B_{max}, coordinates of the focal point (x_0, y_0, z_0), and Gaussian width in lateral, elevational and axial direction, σ_x, σ_y and σ_z respectively. The focus of the ARF was taken the same as in the experiment in [18], i.e. (0 mm, 0 mm, 30 mm), corresponding to the center of the myocardial slab (axial depth thus varied from 20 mm to 40 mm for the non-stretched myocardial slab; with stretching, the thickness of the slab decreases). For the Gaussian widths of the ARF-excitation, we assumed: $\sigma_x = \sigma_y = 0.4$ mm and $\sigma_z = 10$ mm [141]. Lastly, the maximal amplitude B_{max} is derived from the following ARF-expression [81]:

$$B_{max} = \frac{2\alpha I_{max}}{c_L} \tag{8.5}$$

With attenuation coefficient α (0.4 dB/cm/MHz), longitudinal wave speed c_L (1540 m/s), density ρ (1045.5 kg/m^3) and maximal time-averaged acoustic intensity I_{max}. For the latter parameter, a maximal intensity of 1500 W/cm^2 was assumed, which is in the range of commonly reported intensities for ARF excitations used in SWE [49].

8.2.4 Post-processing of shear wave elastography data

8.2.4.1 Data extraction and interpolation

The velocity data resulting from modeling step 3 (the virtual SWE acquisition on the local model) were extracted at a sampling rate of 25 kHz during the complete SWE-simulation of 4 ms. For visualization and post-processing purposes, subsequent interpolation of the extracted data was necessary from the mesh geometry defined in *Abaqus* to a newly defined equidistant rectangular grid with sampling 0.2 mm in all three directions and a polar grid with similar sampling in the radial and axial direction and an angular sampling of $\Delta\theta = 5°$ (two times smaller than the rotation angle of the linear probe in the experiments [18]). Interpolation was performed using *Matlab 2016b* (The MathWorks Inc., Natick, MA, USA).

8.2.4.2 Group velocity analysis

Shear wave characteristics were studied at 30 axial depths across the thickness of the modeled myocardial slab. Group velocity of the simulated shear wave is estimated at each depth by applying a time-of-flight (TOF) method, which characterizes shear wave position in function of time. This was realized by finding the location with maximal velocity in function of time using a subsample peak algorithm, provided in the open-source post-processing code of Peter Hollender, PhD from Duke university (Durham, NC, United States). As the shear wave's position varied a lot depending on the selected axial shear wave path and the applied stretch, the shear wave's positions that were taken into account for a linear regression fit were identified based on Radon sum criteria [94]. Subsequently, a linear regression curve was fitted through the selected tracked shear wave positions using *Matlab 2016b*, of which its slope corresponded to the group shear wave speed [44] (see section 2.2.2 of chapter 2). Only fits with a goodness of fit or R^2 above 0.90 were considered.

8.2.4.3 Phase velocity analysis

The phase velocity characteristics were derived by applying a 2D Fast Fourier Transform (FFT) on the temporal shear wave pattern of the left and right shear wave for a selected shear wave path [125]. This transformed the axial velocities in the time-lateral space domain into Fourier energies in the frequency-wave number domain. Consequently, phase velocity c_ϕ can be derived based on frequency f and wave number k using the following relationship:

$$c_\phi = \frac{2\pi f}{k} \tag{8.6}$$

The dispersion characteristics of the excited modes in the simulation can then be identified by tracking the maximal energies for every frequency in the frequency-phase velocity domain [125]. Further details about this procedure can be found in section 2.2.3 of chapter 2.

8.2.4.4 SWE-based fiber estimation

The anisotropy in shear wave propagation can be employed to extract the myocardial fiber orientation, as shown by Lee et al [221]. As our simulation framework provides direct access to the modeled fiber direction, we used the model to assess the accuracy of two previously reported SWE-based fiber extraction techniques. Approaching the myocardium as a composite of transversely-isotropic layers, the fiber orientation for each layer was estimated based on: (i) the direction of fastest wave travel, or highest shear wave speed [221], and (ii) the angle of the major axis of the ellipse, fitted to the shear wave speed surface [117]. For the latter method, mean squared error (MSE) was reported to assess the goodness of the ellipse fit.

8.2.5 Parameter study

The fiber orientation and material characteristics of the model were altered to investigate their influence on the shear wave propagation pattern and subsequent material characterization:

1. For the fiber orientation, two cases were considered at the 5% stretch state: a transverse isotropic material orientation (25° with respect to the LV circumferential direction for the complete myocardial thickness) using the implemented HO material law with parameters mentioned in table 8.1 and an elastic material law with Young's modulus of 1.13 kPa and a coefficient of Poisson of 0.49999 (similar mechanical properties as the isotropic term in the HO law).

2. To theoretically evaluate the impact of cardiac pathology on shear wave characteristics, we altered the material characteristics in the 5% stretch state based on values reported in literature by Wang et al [224] for myocardial fibrosis. Wang et al. quantified mechanical changes based on the collagen thickening in high resolution confocal images of a spontaneously hypertensive rat model. Cardiac pathology was associated with increasing the fiber and sheet stiffness with a factor 5, representing endomysial collagen thickening, and increasing sheet-normal stiffness with a factor 10, representing perimysial collagen thickening. The conventional Holzapfel-Ogden law, as described in equation equation (8.3), does not allow to alter solely sheet-normal stiffness. Therefore, a modified Holzapfel-Ogden law (mHO) was defined by adding a term representing the contribution along the sheet-normal axis n, defined as follows:

$$\psi^n = \frac{a_n}{2b_n}\left\{exp[b_n(I_{4n}-1)^2]-1\right\} \tag{8.7}$$

with material constants a_n and b_n; and material invariant I_{4n}. This material law is designated with the terminology '*modified Holzapfel-Ogden*' (mHO) throughout this manuscript. The mHO law uses the same parameters as tabulated in table 8.1 for the fiber and sheet contribution, and parameters as reported in [224] for the sheet-normal contribution, i.e. a_n = 6.4 kPa and b_n = 0.2. The effect of increasing fiber and sheet stiffness in the HO material law (i.e. af and as) with a factor 5 on shear wave propagation and characteristics was first separately analyzed. Then, we considered two ways to model the fibrotic myocardium: the fibrotic HO-model, increasing parameters a_f and a_s simultaneously with a factor 5; and the fibrotic mHO law,

increasing parameters a_f and a_s as well with a factor 5 and additionally augmenting the parameter a_n with a factor 10.

3. The effect of the tissue surroundings was investigated by considering water around the 5% stretched myocardial slab. Water was modeled in *Abaqus* using acoustic elements, and radiation boundary conditions were imposed at their geometrical boundaries to avoid any wave reflections (see chapter 6).

8.3 Results

8.3.1 Shear wave propagation

The resulting axial velocities in the lateral-axial and five lateral-elevational planes depicting shear wave propagation at 1.2 ms after the push are illustrated in figure 8.3 for the three considered stretch states of 5%, 10% and 15%. The conventional lateral-axial imaging plane clearly demonstrates a curved shear wave front, with the furthest wave travel around the center of the myocardial slab. The shear wave magnitude (expressed by the magnitude of the induced axial velocities) is the largest in the center region (average of -15.76 mm/s, -6.27 mm/s and -2.02 mm/s for 5%, 10% and 15% stretch respectively), and becomes smaller towards the edges of the slab (average of -6.50 mm/s, -2.44 mm/s and -0.53 mm/s for 5%, 10% and 15% stretch respectively). The axial velocity patterns in the lateral-elevational planes of figure 8.3 show that the shear wave travels faster along the fiber orientation than across, leading to an anisotropic shear wave propagation in 3D. This effect becomes more outspoken when the uniaxial stretch ratio increases. The shear wave magnitude was larger in the fiber direction than in the cross-fiber direction. For example, at an axial depth of 24 mm and for the stretch ratios of 5%, 10% and 15%, the average maximal displacement velocity was -12.64 mm/s, -6.12 mm/s and -2.04 mm/s in the fiber direction, versus -4.22 mm/s, -2.93 mm/s and -1.95 mm/s in the cross-fiber direction.

8.3.2 Group speed

The group speed results for each virtual SWE acquisition are illustrated in maps, showing the dependency on angle and axial depth (figure 8.4). Group speeds varied between 0.87-2.21 m/s, 1.13-4.22 m/s and 1.60-8.64 m/s for 5%, 10% and 15% stretch respectively. Depending on the selected axial depth, the location of maximal shear wave speed varied between -40° to +40° for 5% stretch, -20° to +40° for 10% stretch and -25° to +15° for 15% stretch.

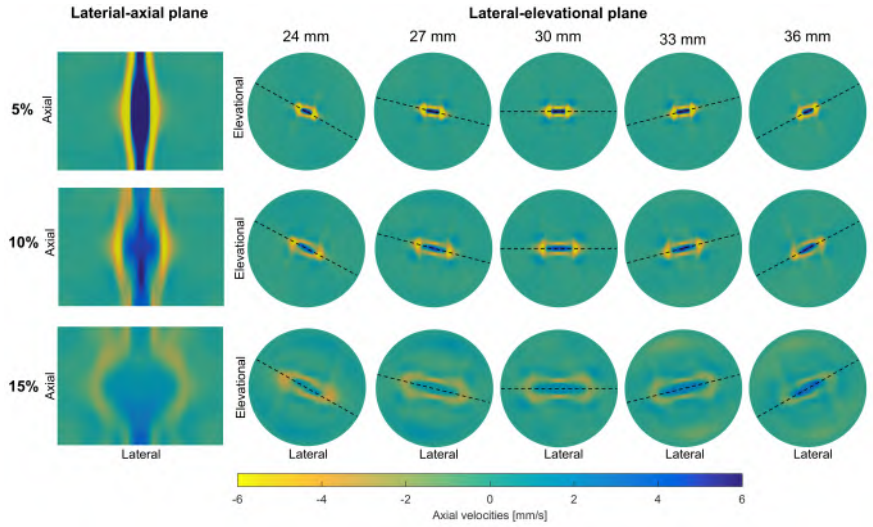

Figure 8.3: Axial velocity pattern from the *Abaqus*-model (r = 14 mm) in the lateral-axial and lateral-elevational planes representing shear wave propagation at 1.2 ms. Patterns are compared for five different axial depths across tissue thickness (an axial depth of 30 mm corresponds to the center of the myocardial slab) and the three considered stretch ratios. The dotted line represents the fiber angle orientation in the specific stretch state.

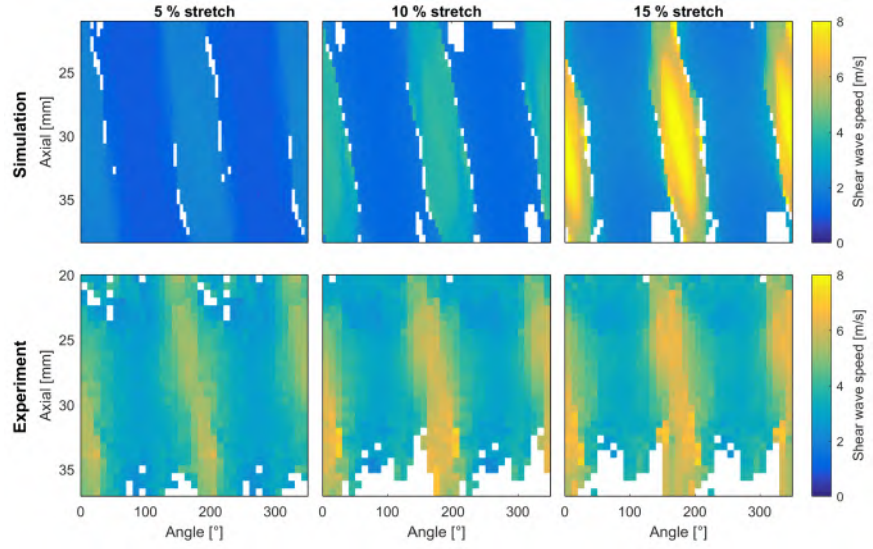

Figure 8.4: Group speed maps in function of axial depth and probe rotation angle as defined in figure 8.3. These maps are compared for simulation (upper panels) and measurement (lower panels) for all three stretch states. White values correspond with not-a-number, indicating that the goodness of fit is below 0.90.

8.3.3 Phase speed

Phase speed characteristics of the maximally excited mode in the virtual SWE acquisitions are plotted for five different depths across tissue thickness in figure 8.5, and compared for different angles (0° - 45° - 90° - 135°) and stretch states (5% - 10% - 15%). For 5% stretch (first row of panels in figure 8.5), the plateau-value of the dispersion curve of 0° and 90° corresponded to 2.11 and 1.07 m/s, respectively, for all 5 depths. Though, for the other two angles, the plateau-value of the dispersion curves varied between 1.20 m/s and 2.25 m/s, depending on the analyzed axial depth. Similar observations are made for the 10% stretch dispersion characteristics (second row of panels in figure 8.5): the curve plateau-values of 0° and 90° did not change across depth (3.90 m/s and 1.38 m/s, respectively), whereas the plateau-values for 45° and 135° varied between 1.56 m/s and 3.45 m/s. For 15% stretch (third row of panels in figure 8.5), the plateau-value of the dispersion curve for 90° remained the same across depth, i.e. 2.04 m/s. However, the dispersion characteristics for the 0° SWE acquisition were now depth-dependent, especially the dispersion curve at 30 mm axial depth increases in function of frequency, whereas the other dispersion curves slightly increased towards ±7 m/s at 1400 Hz. The plateau-value of the dispersion characteristics for angles 45° and 135° varied between 2.22 and 4.77 m/s.

8.3.4 SWE-derived fiber orientation

From the FE simulations, it was found that uniaxial stretching decreased the myocardial fiber variation from a non-stretched range of -50° (epi) to 50° (endo) to a stretched range of -46.5° (epi) to 46.5° (endo), -44.7° (epi) to 44.7° (endo) and -43.5° (epi) to 43.5° (endo) for 5%, 10% and 15% stretch, respectively. The estimated fiber orientation based on the anisotropic shear wave pattern is given in figure 8.6 for the SWS_{max}-method and the ellipse fitting method. The MSE-values for the ellipse fitting method varied between 0.10-0.32 m^2/s^2, 0.04-0.27 m^2/s^2 and 0.02-0.25 m^2/s^2 for 5%, 10% and 15% stretch, respectively.

The performance of the two methods is assessed by considering three different depth ranges of 20-25 mm (region 1), 25-35 mm (region 2) and 35-40 mm (region 3). For 5% stretch, the SWS_{max}-method deviated on average 16.8°, 4.3° and 20.9° from the modeled fiber orientation for region 1, 2 and 3, respectively. The error for the ellipse fitting method was on average 17.2°, 6.2° and 15.9° for region 1, 2 and 3, respectively. For 10% stretch, similar trends were observed: deviations of 41.5°, 10.7° and 35.4° for the SWS_{max}-method and 17.6°, 4.7° and 15.4° for the ellipse fitting method for regions 1, 2, and 3, respectively. The SWS_{max}-method for the stretch state of 15% yielded discrepancies of 21.4°, 3.6° and 21.5° compared to the ground truth

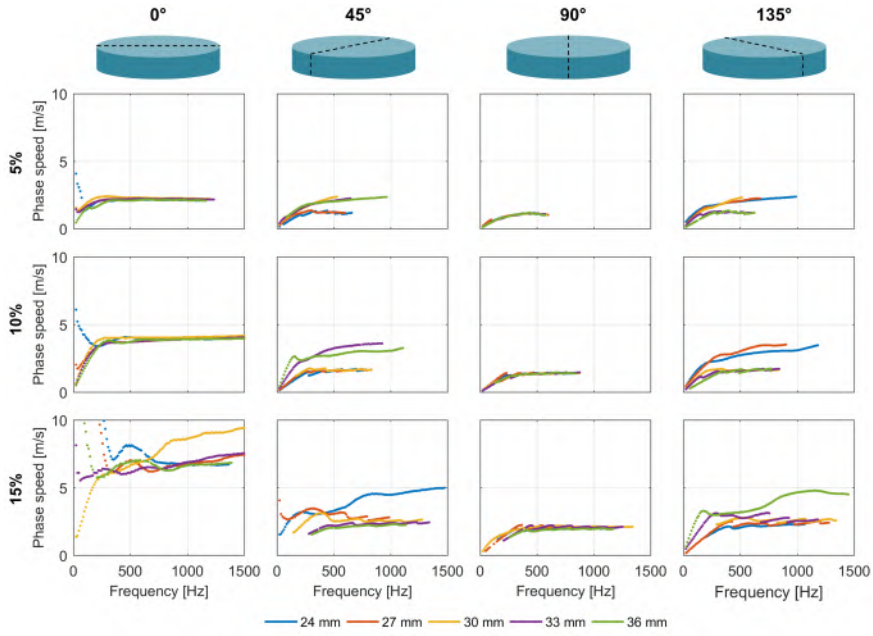

Figure 8.5: Phase speed curves for five different axial depths across tissue thickness. Phase speed characteristics are compared for probe angles 0°, 45°, 90° and 135° and stretch state 5%, 10% and 15%.

fiber orientations for regions 1, 2 and 3, respectively. The same regions at 15% stretch resulted in errors of 11.9°, 6.1° and 20.0° for the ellipse fitting method.

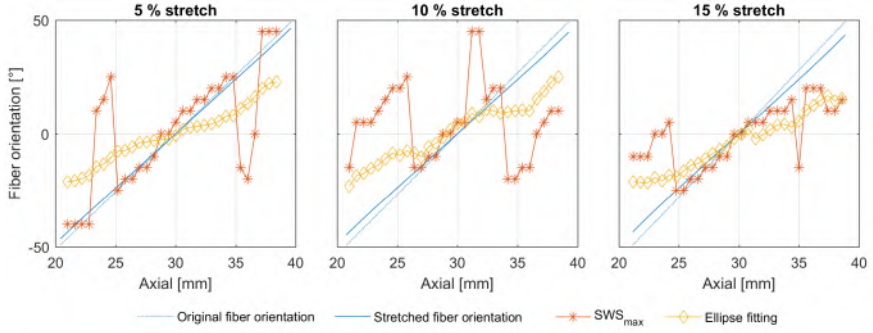

Figure 8.6: SWE-based fiber orientation: comparison of two fiber extraction methods, i.e. the SWS_{max}-method and the ellipse fitting method, to the modeled fiber orientation (stretched and non-stretched) for all three stretch states.

8.3.5 Parameter study

8.3.5.1 Fiber orientation

The shear wave propagation pattern and resulting group speed map for an elastic and transverse isotropic material are illustrated in figure 8.7. For the

elastic material, a circular wave front is visible in the lateral-elevational plane at 3.2 ms (see upper left panel of figure 8.7). The shear wave magnitude is minimally -20.19 mm/s and maximally 15.20 mm/s. The group speed map, shown in the upper right panel of figure 8.7, varied between 0.57 m/s and 0.64 m/s, and is thus more or less uniform. For the transverse isotropic material, the wave front has an elliptical shape as demonstrated in the lower left panel of figure 8.7. The axial velocities caused by the downward push varied between -1.92 mm/s (around the short axis of the ellipse) and -5.11 mm/s (around the long axis of the ellipse). The maximal relaxation velocity was 3.42 mm/s at the considered time point of 3.2 ms. The elliptical wave pattern caused a group speed map with zones of higher wave speed (range of 1.77-2.06 m/s) for angles 330°-60° and 150°-230°; and lower wave speed (range of 0.87-1.04 m/s) for angles 65°-145° and 245°-325°, of which the width did not vary across depth (see lower right panel of figure 8.7 and figure 8.4 for comparison).

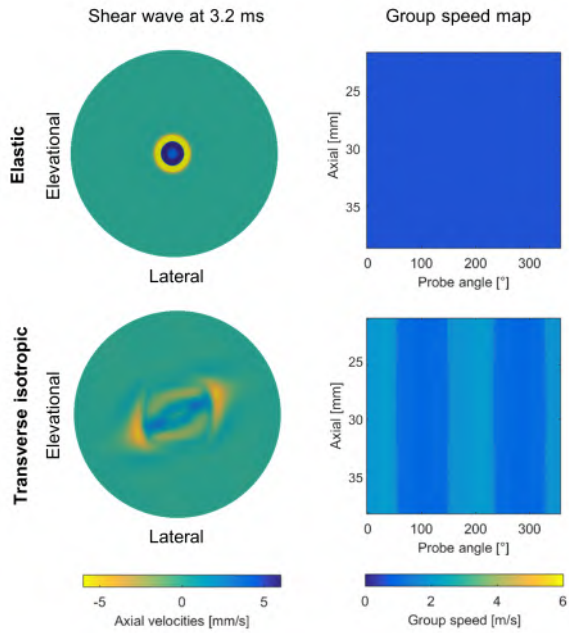

Figure 8.7: Effect of fiber orientation: comparison of shear wave propagation at time point 3.2 ms in the lateral-elevational plane and group speed maps at 5% stretch. Upper panels depict the results in an elastic material with a Young's modulus of 1.13 kPa and a coefficient of Poisson of 0.49999 from the *Abaqus*-model (r = 14 mm), whereas lower panels show the results in a transverse isotropic material (constant θ = 25° throughout depth).

8.3.5.2 Material characteristics

Individually changing the contribution of the fiber (a_f) and sheet (a_s) in the material law of equation (8.3) led to the shear wave propagation results depicted in figure 8.8 (showing also the comparison with the original group speed surface). The upper panels demonstrate the limited effect of increasing as with a factor 5. The group speed values were very similar to those for the original model (range of 0.91 – 2.22 m/s vs. 0.88 - 2.21 m/s). Moreover, the shape of the group speed surface does not significantly change with respect to the original simulation, except towards the edges of the sample. Here, the group speed surface expands along the minor axis from 0.90 m/s to 1.07 m/s at 24 mm depth.

The effect of increasing a_f with a factor 5 is shown in the lower panels of figure 8.8. Now, the observed range of group speed values is clearly larger, varying from 1.31 to 4.77 m/s. Although the largest increase is observed along the major axis of the group speed surface (from 2.21 m/s to 4.77 m/s at 30 mm depth), the speed along the minor axis is also affected by changing the fiber contribution in the HO material law (variation from 0.89 m/s to 1.44 m/s at 30 mm depth).

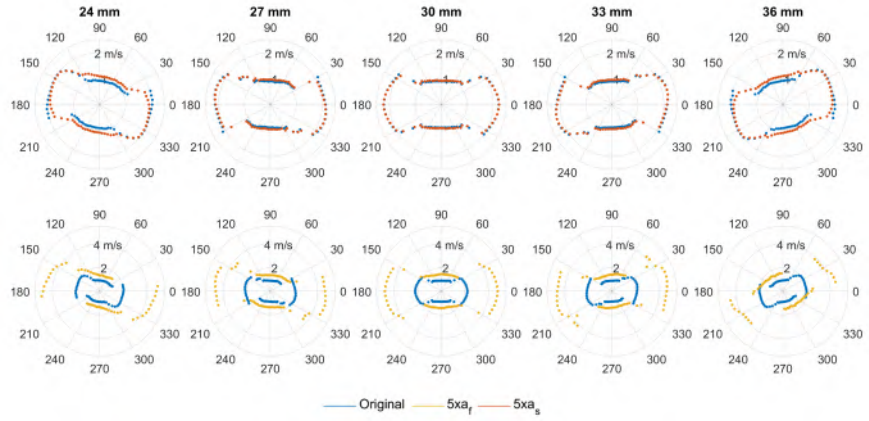

Figure 8.8: Effect of material characteristics for Holzapfel-Ogden law: group speed surfaces are compared in polar plots to the original simulations at five depths across tissue thickness. The radial coordinate represents the group speed, whereas the angular coordinate indicates probe rotation angle. Upper panels show the effect of increasing a_s with a factor 5; whereas lower panels demonstrate the effect of increasing a_f with a factor 5.

Figure 8.9 illustrates the resulting shear wave propagation patterns for both healthy and fibrotic myocardium, modeled with the HO and mHO material law. Results are presented in the lateral-axial plane, as this encompasses the sheet-normal direction. The shear wave pattern for both material models

representing the healthy myocardium appeared very similar for all probe angles. Only small differences were noticeable, e.g. the more uniform shear wave magnitude for the model with the mHO law compared to the original model (see first column of panels in figure 8.9). The range of shear wave magnitude at the depicted time point increased slightly for the mHO law: -19.37 to 13.88 mm/s vs. -16.89 to 11.63 mm/s.

For the modeled fibrotic myocardium in figure 8.9, including the a_n-term in the HO law yielded larger differences in shear wave propagation pattern, of which the most obvious is the altered location of the shear wave front for the center region of the myocardial slab for probe angles 0° and 30°. The range of shear wave magnitude for the mHO law (-7.02 to 10.92 mm/s) was slightly different compared to the axial velocity range for the HO law (-8.18 to 7.13 mm/s).

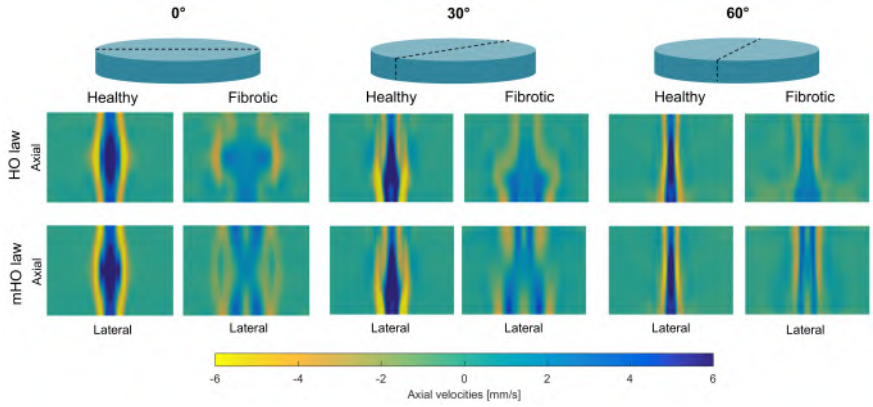

Figure 8.9: Effect of material characteristics for healthy and fibrotic myocardium modeled with Holzapfel-Ogden (HO) and modified Holzapfel-Ogden (mHO) law: axial velocity pattern at 1.6 ms for probe angles 0°, 30° and 60° for 5% uniaxial stretch.

The differences in shear wave pattern between healthy and fibrotic myocardium are further analyzed in figure 8.10 for the mHO material law and a probe angle of 0°. This figure clearly shows that the axial velocity pattern is depth-dependent, as is also noticeable from the left bottom panels in Figure 9. The wave pattern and magnitude itself, however, was similar for healthy and fibrotic tissue at 23 mm and 37 mm depth. Similar observations are made for the Fourier energy plots.

The virtual SWE acquisition in the healthy myocardium showed a 'clean' shear wave propagation, translated in the excitation of mainly one mode in the Fourier domain, independent of the analyzed depth (see figure 8.10). On the other hand, the fibrotic myocardium depicted complex shear wave propagation for all depths, i.e. a split or second wave front at 30 mm depth

and widened wave front at 23 and 37 mm depth. This resulted in altered relationships between frequency and wavenumber: the linear relationship between frequency and wavenumber became less steep and a secondary mode was excited.

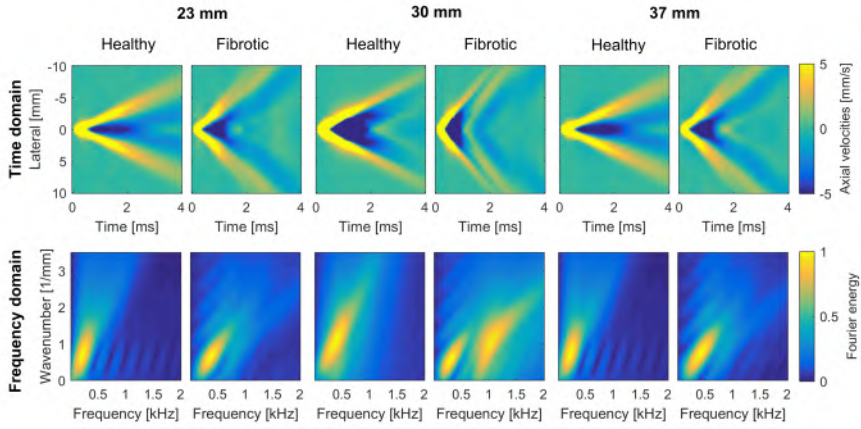

Figure 8.10: Effect of material characteristics for healthy and fibrotic myocardium modeled with modified Holzapfel-Ogden (mHO) law at 5% stretch: axial velocities and corresponding Fourier energies at the lateral-elevational planes of 23 mm, 30 mm and 37 mm depth (0° probe angle).

8.3.5.3 Tissue surrounding

The results of the simulated shear wave propagation in the lateral-axial plane of the HO-model with water is depicted in figure 8.11, in comparison with the HO-model without water. The shear wave pattern looked very similar for the FEM-model with or without water. The range of the shear wave magnitude is different for both models: 9.80 to -10.74 mm/s vs. 9.83 to -12.84 mm/s at 1.60 ms and 5.15 to -5.79 mm/s vs. 4.85 to -5.75 mm/s at 2.40 ms, for model without water vs. model with water.

8.4 Discussion

8.4.1 Combining an orthotropic material law with SWE-modeling

This study presents a FEM model of the anisotropic shear wave mechanics observed with impulsive ARF driven SWE using an orthotropic material law [160]. As the material is non-linear, we investigated the effect of uniaxial stretch on the material response and subsequent shear wave characteristics. Additionally, we used this model to (i) assess the accuracy of SWE-based myocardial fiber extraction algorithms and (ii) investigate the sensitivity and specificity of SWE to detect changes in fiber orientation and material characteristics.

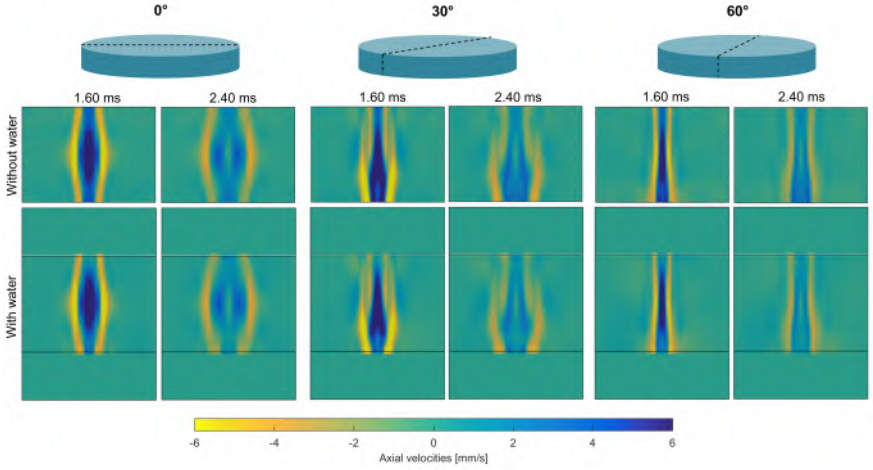

Figure 8.11: Effect of tissue surrounding for Holzapfel-Ogden (HO) model: axial velocity pattern at 1.60 ms and 2.40 ms for probe angles 0°, 30° and 60° for 5% uniaxial stretch.

FEM is an ideal method to study the performance and accuracy of SWE as it provides full flexibility at the level of the tissue setting (i.e. geometry, material characteristics, surrounding, mechanical loading) and the applied acoustic radiation force. It was originally proposed and validated by Palmeri et al [194] for bulky isotropic elastic media. This approach has later been adapted and further validated for other geometries and material models, such as an isotropic low-viscous ventricle [20] and an arterial slab [24]. To the best of our knowledge, our study is the first to study SWE in a FEM model that makes use of the orthotropic HO material law [160], in combination with mechanical loading. This material model has been previously suggested to mimic the passive orthotropic and non-linear behavior of myocardial tissue. It is based on the microstructure of the myocardium, accounting for the muscle fiber direction and the myocyte sheet structure, and has shown realistic results of representing the cardiac mechanics in various studies [223], [225], [226]. This allowed us to simulate ARF-excited shear wave propagation in a realistic model of the myocardium, leading to clear shear wave guiding along the modeled fiber direction at a specific depth, as visualized in figure 8.3 for all stretch states. The simulated shear wave propagation pattern in the imaging plane was similar to the one reported by Pernot et al [16] for Langendorff perfused rat hearts and by Couade et al [15] for *in vivo* open-chest sheep hearts (see shear wave pattern in lateral-axial plane of figure 8.3). Additionally, the anisotropy in subsequently derived group speed map for 15% stretch (figure 8.4) showed a similar pattern and magnitude as previously observed for the *in vivo* open-chest ovine myocardium at mid-systolic phase by Lee et al [221].

The effect of uniaxial stretching on the simulated group speed maps was validated by comparing the derived group speed features to the results of actual SWE experiments on *ex vivo* pig myocardial slabs, subjected to the same uniaxial stretch ratios as in chapter 7 [18] (see figure 8.4). The simulated group speed patterns were very similar to the measured ones for all stretch ratios, suggesting a realistic modeling of the myocardial fiber anisotropy. Furthermore, stretching increased the maximally observed group speeds for both model and experiment, resulting in 2.21 m/s - 4.22 m/s - 8.64 m/s and 6.15 m/s - 7.26 m/s - 7.32 m/s in order of increasing stretch, respectively. However, the values did not agree as the myocardial model in the simulations is derived from mechanical tests on pre-conditioned porcine tissue whereas experiments were performed on *ex vivo* porcine hearts. Furthermore, other relevant factors in this comparison are (i) the asymmetry in the ARF possibly affecting the excited shear wave characteristics during rotation of the probe in the experiments [141] and (ii) the bias and variance inherently related to ultrasound imaging and post-processing.

The modeled anisotropic group speed surface, as shown in figure 8.8, was comparable to the one reported by Urban et al [183] in their FEM-model, even though the simulated shear wave pattern in the imaging plane did not correspond. Discrepancies in modeled shear wave propagation might be related to differences in assumed material law (composite of transverse isotropic layers in their model vs. orthotropic material law in our model), modeled loading conditions (line force in their model vs. spatially varying body force in our model) and discretely modeled fiber orientation (20 layers in their systole-model vs. 67 layers in our model).

The two applications of the model, i.e. assessment of the performance of SWE-based fiber extraction methods and evaluation of the effect of altered stiffness and fiber orientation on shear wave characteristics, demonstrated the strengths and possibilities of the developed simulation environment. However, it should be noted that these two applications only provided initial conclusions and that both studies should be elaborated in future research.

8.4.2 Representing myocardial stiffness by shear wave characteristics

This study assessed myocardial material properties by analyzing group and phase shear wave speeds of the virtual SWE acquisition at different depths and probe rotation angles (see figure 8.4 and figure 8.5). Previous studies on cardiac SWE reported a variety of indices representative of cardiac stiffness: group speed in [15], [150], [180]–[182], [221], elasticity in [15], [16], [182], [184] or a combination of elasticity and viscosity in [38], [133], [134]. One should keep in mind that, when reporting an elastic or viscoelastic material parameter, underlying assumptions are made for a material model for the

myocardium ranging from an isotropic linear elastic to a viscoelastic material. Additionally, some studies [38], [133], [134] accounted for the cardiac wall thickness into their shear wave analysis by fitting theoretical Lamb wave dispersion characteristics to the measured ones. The large variety in reported SWE-metric(s) across different studies highlight the need of further research in cardiac SWE to standardize reported SWE-metric(s) in order to obtain a reliable representation of cardiac stiffness with high diagnostic value in clinical practice. A concerted approach as undertaken by the liver SWE community for liver fibrosis staging [227] might speed up this process.

In this study, we chose to not make any tissue material assumptions and therefore reported general shear wave characteristics such as group and phase speed. Urban et al [183] reported group speeds from their SWE simulations in the myocardium, which they could directly link to the pre-defined shear stiffness along and across the fibers in the transverse isotropic material law. However, we could not accomplish a similar comparison as the implemented orthotropic material law does not yield a direct link between shear stiffness and group shear wave speed.

The anisotropy in the myocardial material properties (becoming even more anisotropic with uniaxial stretching), were well reflected in group and phase speed characteristics, both showing a dependency on probe angle and axial depth (figure 8.4 and figure 8.5). Figure 8.5 visualized the depth-dependency in the dispersion characteristics for two probe orientations, 45° and 135°, which was also visible in the group speed map of figure 8.4 for the same angles, for all stretch states. This anisotropy in shear wave characteristics is caused by the large range in (non-stretched) myocardial fiber orientation, varying from 95° (epi) to -5° (endo) with respect to the probe orientation of 45° and from -5° (epi) to 95° (endo) with respect to the probe orientation of 135°. Furthermore, the dispersion curve at 30 mm depth was the same for both orientations, whereas the dispersion characteristics at the other depths were reversed, i.e. the dispersion curve at 24 mm depth at 45° corresponded to the dispersion curve at 36 mm depth at 135°, etc. This is due to the assumed symmetric myocardial fiber definition with respect to the center of the tissue sample. The other two probe angles, 0° and 90°, showed a more or less isotropic tissue behavior across depth for both group and phase speed characteristics, as illustrated in figure 8.4 and figure 8.5. This isotropy in shear wave characteristics is due to the small range in (non-stretched) myocardial fiber orientation, varying from -50° (epi) to 50° (endo) with respect to the probe orientation of 0° and from 40° (epi) to 140° (endo) with respect to the probe orientation of 90°. Shear wave speed values along the 0° probe orientation were larger than for 90°, as this direction corresponded to the stretching direction and the globally averaged myocardial fiber orientation.

The isotropic shear wave behavior in group and phase speed for probe angles of 0° and 90° decreased during stretching, leading to higher shear wave speeds around the center of the myocardial slab, as its myocardial fiber orientation corresponded to the stretching direction.

The group speed analysis was challenged for several SWE acquisitions as can be seen from the white pixels in figure 8.4 (signifying TOF-fit with a goodness of fit lower than 0.9). For the simulations, this was caused by complex shear wave propagation and low shear wave magnitude, especially in between the fiber and cross-fiber direction and near the edges (as also can be seen in figure 8.3). For the experiments, the TOF speed estimate was remarkably unreliable near the bottom edges of the myocardial tissue, probably due to low signal-to-noise ratio. On the other hand, it should be noted that the accuracy of the phase speed analysis is determined by the spatial observation window in the 2D FFT, as the Fourier signal is the convolution of the true signal and the observation window. This might be improved by accounting for the finite window as recently proposed in [228].

8.4.3 Accuracy of fiber extraction methods

As the proposed numerical framework provided direct access to the ground truth myocardial fiber orientation, it is an ideal environment to investigate the accuracy of SWE-based fiber extraction methods. Figure 8.6 compared the accuracy of estimating fiber orientation (i) based on the maximal shear wave speed and (ii) on the major axis of the fitted ellipse to the group speed surface. We could demonstrate that the estimated fiber direction approached the true fiber orientation well at the mid-region of the investigated sample (between 25-35 mm axial depth), which is a similar finding as reported by Urban et al for impulsive shear wave excitations using the ellipse fitting method [183]. However, the observed bias of the ellipse fitting method was found to be higher than for the SWS_{max}-method in the mid-region: 6.2° vs. 4.3° for 5% stretch, 4.7° vs. 4.0° for 10% stretch (without outliers) and 6.1° vs. 3.6° for 15% stretch. This is visible from figure 8.3, where it is observed that the direction of the major axis of the ellipsoidal shear wave surface does not necessarily correspond with the direction of furthest wave travel (i.e. direction of the fiber). This observation becomes more obvious near the edges of the myocardial tissue. Both methods underperformed significantly near the edges of the tissue sample, as demonstrated by the reported high averaged deviations of 41.5° and 21.5° (maximum) for SWS_{max} and ellipse fitting method respectively. This was also observed in [183] for the ellipse fitting method. A potential source for this discrepancy is the increased complexity in shear wave propagation pattern, potentially in combination with wave dispersion, close to the edges of the sample. Even though small differences are visible in the performance of both fiber extraction methods

across stretch states, further research is necessary to quantify the effect of stretching on the accuracy of both fiber analysis methods.

The ellipse fitting method proved to be more robust to outliers than the SWS_{max}-method in this study, as it takes shear wave directionality into account based on the group speed surface instead of one single value. The accuracy of both fiber extraction methods is dependent on the selected axial and angular sampling size of the group speed map (figure 8.4). This is especially true for the SWS_{max}-method, as a peak in group shear wave speed might be missed if the sampling size is taken too large, potentially resulting in an outlier. Another factor that plays a role in the accuracy of the SWS_{max}-method is the amount of data points taken into account during the TOF-fitting procedure, which is dependent on the local wave speed since the time-space observation window is fixed (i.e. a simulation duration of 4 ms and a lateral extent of 14 mm – half of the diameter of the local model). Nevertheless, post-processing techniques in an actual SWE acquisition will average and smooth the axial velocity pattern, decreasing the number of outliers for the SWS_{max}-method.

The main objective of presented fiber extraction study was to demonstrate one of the abilities of the developed simulation environment, but more extensive and complete studies varying fiber angle and stretch are mandatory to formulate any definite conclusions about the performance of both fiber extraction methods. Furthermore, future research should also focus on more advanced SWE-based fiber extraction methods, accounting for the out-of-plane fiber orientation. Indeed, it is generally known that the myocardial fibers have a transverse angle component (out-of-plane), next to the studied helix angle component (in-plane) in this study. This component is generally smaller than the helix angle component: variations are reported from +9° (epi) to +34° (endo), with an average of +7° for the complete wall thickness [161]. Therefore, before SWE can be used to non-invasively measure myocardial fiber orientation as valid alternative to histology or other imaging techniques (such as diffusion tensor magnetic resonance imaging [229]), it will be necessary to expand current SWE-based fiber extraction methods from 2D to 3D. The proposed computational framework might be a useful tool in this process, as it allows definition of any muscle fiber orientation field, and thus provides an easy and straightforward way to assess the accuracy of the newly defined fiber extraction algorithms.

8.4.4 Factors affecting shear wave propagation and characteristics

Several cardiac disorders implicating left ventricular dysfunction are associated with structural remodeling of the left ventricle, leading to changes in ventricular geometry and regional wall thickness and to the development

of fibrosis [224], [230]. Additionally, it is believed that disarrangement of myocardial fiber architecture appears in hearts with both congenital and acquired conditions [231]. Hence, it is relevant to investigate the sensitivity of SWE in detecting changes in myocardial material characteristics and fiber orientation as it could further improve diagnosis.

Myocardial fibrosis was modeled in the SWE simulation environment using two different material models: the HO and the mHO law. The HO law allowed to model the endomysial collagen thickening by increasing fiber and sheet stiffness, as associated with fibrotic myocardium. Increasing the fiber stiffness augmented the group wave speed globally, as demonstrated in the lower panels of figure 8.8. There were however some regional differences in group speed increases as the increase along the major axis (115.8%) was larger than along the minor axis (61.8%) of the group speed surface. On the other hand, stiffening the material response along the sheet axis affected the shear wave speed locally. Indeed, upper panels of figure 8.8 showed only an increase in group speed (18.8%) for the minor axis of the group speed surface near the edges of the tissue sample. Changing sheet and fiber stiffness simultaneously yielded group speed surfaces that were very similar to the ones where we solely increased fiber stiffness.

A more realistic shear wave pattern is obtained using the mHO law, as it allowed to model myocardial fibrosis in all 3 dimensions, by increasing fiber, sheet and sheet-normal stiffness, as quantified in diseased rat hearts in [224]. The addition of the stiffness-term along the sheet-normal axis in the material law changed the shear wave propagation pattern in fibrotic myocardium drastically compared to the HO law (see figure 8.9). Indeed, the shear wave front became split for probe angles of 0° and 30°, mainly affecting shear wave characteristics for the center region of the myocardial slab, when comparing to the fibrotic HO model. Such a split wave pattern was also observed in our previous study [20] (see chapter 6), where ventricular geometry was identified as the cause for the dispersive shear wave pattern. This might indicate that the effect of geometry and surrounding becomes more important when sheet-normal stiffness is augmented.

Shear wave propagation patterns in the simulated fibrotic myocardium (mHO material law) appeared more complex than for the healthy myocardium, as demonstrated by the split (or second) wave front at 30 mm depth and a widened wave front at 23 mm and 37 mm depth in figure 8.10. This might challenge stiffness characterization methods in the fibrotic myocardium due to the observed complex wave physics. This figure also shows that increased group and phase speeds are expected in the diseased myocardium compared to the healthy, because (i) the shear wave reaches the end of the lateral space observation window sooner and (ii) the slope of the linear

relationship between frequency and wavenumber of main excited mode is smaller. It should be noted that this study is only an initial step towards investigating the effect of myocardial fibrosis on shear wave physics and characterization, and further research is still necessary as there is no established material model yet for the fibrotic myocardium.

Next to altering the cardiac material properties, we also studied the effect of fiber organization on shear wave physics and characterization by simulating SWE in an isotropic elastic material and a transverse isotropic material, as illustrated in figure 8.7. This altered the shape of the shear wave surface (circular vs. ellipsoidal) and eliminated its depth-dependency. It is unsure whether the depicted shear wave pattern for a transverse isotropic material in figure 8.7 realistically represents shear wave propagation in an actual transverse isotropic material as the implemented material law (HO law) is specifically designed to characterize the myocardium, and thus not transverse isotropic materials. Despite this, Rouze et al [140] presented very similar simulated shear wave propagation patterns for a transverse isotropic material for a comparable ratio of transverse and longitudinal stiffness (corresponding approximately to the ratio of a_s and a_f). Nevertheless, this study showed that fiber orientation determined the spatial features in the group speed map (see figure 8.7). The pattern in the group speed map might thus be relevant to detect fiber disorganization associated with cardiac disease. As myocardial tissue experiments performed in [18] were performed with tissue embedded in water, the effect of including a water layer surrounding the myocardium was also investigated (data not shown). The presence of water, however, did not have a significant effect on the simulated shear wave propagation.

Even though our parameter study proved the feasibility of the SWE in detecting changes in material characteristics and fiber orientation, the imposed changes in fiber orientation and material properties were quite drastic. Future work could focus on elaborating this sensitivity-analysis of SWE by considering various gradations of fibrosis and degrees of fiber disorganization. Additionally, the current model did not take into account (i) the local variations of cardiac properties as fibrosis might not be homogeneously distributed throughout the cardiac wall [171], [216] and (ii) the alterations in left ventricular geometry due to the development of fibrosis.

Our work demonstrated that not only intrinsic material properties and orientations determined the resulting shear wave characteristics, but it was also affected by other biomechanical factors such as uniaxial stretching (see figure 8.4). Even though the surrounding water did not alter the observed shear wave propagation pattern in the model, it is necessary to further investigate the effect of tissue surrounding on shear wave physics in an in vivo transthoracic acquisition. Furthermore, it is known that the myocardial fiber

orientation in the left ventricle varies depending on the analyzed zone and subject [161], leading to additional factors that affect shear wave propagation and characteristics. Next to these biomechanical factors, technical settings of the SWE acquisition will additionally influence SWE-excited shear wave propagation, as shown by Urban et al [183] for ARF excitation frequency and Palmeri et al [141] for other relevant ARF-settings. This is also visible from the phase speed surfaces depicted in figure 8.5. Therefore, guidelines need to be developed to guarantee robust and reliable SWE performance in different age groups and disease states, for which the developed simulation framework could form a useful tool to test various SWE acquisitions in combination with different myocardial models.

8.4.5 Limitations of SWE simulation environment

Even though the presented numerical framework yielded realistic shear wave propagation results, one should be careful with the assumptions that are inherently present in the proposed modeling methodology. The model did not account for the myocardium's viscoelastic behavior. Given that viscosity is known to act as a low pass filter [65], this might affect the excited frequencies during the SWE acquisitions. Future work could assess this effect by implementing a viscoelastic orthotropic material law for the heart, as recently proposed by Cansiz et al [232], where distinct relaxation mechanisms for each fiber orientation are considered. Furthermore, a true validation step of the numerical SWE methodology is lacking because multiaxial mechanical tests, e.g. a combination of planar biaxial extension and triaxial shear tests [222], are necessary to adequately capture the orthotropic material behavior of the myocardium. Additionally, to allow a one-to-one comparison between simulation and experimental SWE results, it will be necessary to include modeling of the imaging physics into the numerical framework, as was done in [19], [148]. Furthermore, we only considered passive myocardium, reflecting the properties of the heart in late diastole. To model an actual SWE acquisition in an *in vivo* beating heart, the proposed numerical framework needs to be extended to include more advanced modeling features such as a realistic ventricular geometry, tissue surrounding, a viscoelastic orthotropic material law [232], active contraction and representative cardiac loading.

8.5 Conclusion

This study described a numerical SWE simulation environment using an orthotropic material law representing the passive myocardium to mimic the anisotropic shear wave propagation of an actual cardiac SWE acquisition. Its realism was assessed by comparing the resulting shear wave characteristics for various uniaxial stretches to those previously reported in *ex vivo* pig slabs.

Compared to conventional 2D SWE-experiments, the model offered the advantages of providing direct access to generated 3D displacements/velocities in the 3D spatial domain and allowing us to independently study the relationship between myocardial material characteristics such as fiber orientation and stiffness along fiber and sheet direction, and shear wave characteristics. This allowed us to (i) address the accuracy of two SWE-based fiber extraction techniques, and (ii) evaluate the impact of altered myocardial stiffness and fiber orientation on shear wave characteristics. The model provided valuable insights into the relationship between material anisotropy and non-linearity on one hand, and SWE-derived shear wave group and phase speed characteristics on the other hand. The framework forms an elegant and versatile tool to assess the accuracy of current post-processing techniques for cardiac SWE, and assists in the development of new material characterization algorithms.

SWE is thus capable in detecting changes in fiber, sheet and sheet-normal stiffness, which can be related to the presence of myocardial fibrosis. Furthermore, large changes in fiber stiffness are reflected in globally altered shear wave characteristics, whereas alterations in sheet and sheet-normal stiffness led to regional differences in shear wave features.

IV

Ultrafast imaging settings affecting the performance of shear wave elastography

Chapters

Chapter 9

Effect of ultrafast imaging on shear wave visualization and characterization:

Experiments and simulations

Previous chapters studied the effect of biomechanical factors on shear wave propagation in shear wave elastography (SWE), taking not into account the effects of imaging on shear wave visualization. Indeed, the shear wave features depicted in a cardiac SWE image are affected by the characteristics of the acoustic radiation force and the medium's biomechanical properties such as geometry and cardiac anisotropy, but also by the selected ultrafast imaging settings. Therefore, this chapter explores the effects of ultrafast imaging on shear wave physics and characteristics, and tries to quantify these effects by means of group and phase speed. For this purpose, we used again the combined *in vitro* and numerical approach as proposed in chapter 4, chapter 6 and chapter 8, and extended the modeling methodology to incorporate the ultrafast imaging physics. This extended model then allowed to quantify the effect of ultrafast imaging settings on the visualized shear wave physics by comparing the visualized shear wave features to the true biomechanics. We applied this framework on the generic pediatric left ventricle of chapter 6, a setting shown to evoke complex shear wave propagation.

This chapter is based on the paper published in the special issue *Ultrafast imaging* of the Applied Sciences journal: *"Effect of ultrafast imaging on shear*

wave visualization and characterization: An experimental and computational study in a pediatric ventricular model", vol. 7, no. 8, August 2017 [19].

9.1 Introduction

Ultrafast ultrasound imaging uses plane-wave transmissions instead of the conventional line-by-line focused beam transmissions, increasing the frame rate by at least a factor of 100 (typically >1000 frames per second) [91], [97]. This ultrafast imaging technology was an essential breakthrough for the field of Shear Wave Elastography (SWE), as it allowed real-time imaging of shear waves in soft tissues with a high temporal resolution [54], [99], [233]. Because of this, the technique was almost instantaneously applied and therefore less sensitive to respiratory and/or cardiac motion. This allowed local quantitative estimates of wave speed and therefore of tissue stiffness [34]. Initially, shear waves were generated with a transient vibration originating from an external mechanical vibrator [99], [233]. However, as these vibrators were challenging to integrate in daily clinical practice, the excitation source was changed into a remote palpation induced by a radiation force of focused ultrasonic beam(s), unifying the shear wave excitation source and ultrafast imaging modality together in the ultrasound transducer [43], [54], [81], [234]. At the beginning, the ultrafast frame rates came at the cost of reduced image contrast and resolution compared to conventional transmissions as the transmit focusing step is skipped in the ultrafast imaging modality. However, this limitation was overcome by introducing coherent plane wave compounding [98], [99], which consists of sending out multiple tilted and non-tilted plane waves into the medium and coherently summing the backscattered echoes to compute the full image. In this manner, the image quality is improved compared to single plane wave imaging while still maintaining sufficiently high frame rates [98]. The concept of compounding has been applied to different ultrasound modalities [100], [235]–[237], and has become a key feature of ultrafast ultrasound imaging. An overview of the commonly used imaging techniques in SWE can be found in section 1.2.2.3 of chapter 1.

Ultrafast imaging in SWE to assess tissue stiffness has been clinically applied in several areas such as breast cancer diagnosis [238] and liver fibrosis staging [191]. The ability of ultrafast imaging—with or without plane wave compounding—in displaying and characterizing the true biomechanical shear wave propagation has not been well studied yet, to the best of our knowledge. We are particularly interested in the performance of ultrafast imaging in tissues with thin and layered geometries and other intricate anisotropic material properties, as complex shear wave propagation phenomena such as wave guiding, mode conversions and dispersion are expected to arise [125], [193]. These wave features will complicate shear wave visualization,

characterization and interpretation, eventually affecting SWE-based stiffness estimation, as explained in chapter 2. This may be especially true when plane wave compounding is applied, as the compounded image fuses temporal characteristics of the propagating shear wave at different time points. Indeed, a recent study in *ex vivo* thoracic aorta [239] has experimentally shown that certain SWE settings, such as pushing length and number of compounding angles, influenced the technique's accuracy to estimate phase velocity-based tissue stiffness.

Therefore, the objective of this work was to establish a flexible framework that allows us to investigate the performance of ultrafast imaging in SWE in accurately displaying and characterizing the true biomechanical shear wave propagation. As actual SWE experiments do not provide access to a ground truth for imaged shear wave propagation, a multiphysics modeling approach combining computational solid mechanics (CSM) of the shear wave propagation [23], [149], [194] (as proposed in chapter 4) with ultrasound (US) modeling of ultrafast imaging was used for this purpose. The resulting wave mechanics from CSM provided the true mechanical shear wave propagation whereas the virtual images represented the imaged shear wave propagation. The multiphysics model was employed in combination with SWE experiments, for validation purposes. This combined approach was applied on an idealized left ventricular phantom model with pediatric dimensions, as this has been demonstrated to evoke dispersive guided wave propagation patterns due to left ventricular geometry [20] (see chapter 6). The proposed multiphysics model in this work thus adds an extra modeling layer to the previously presented SWE biomechanics model in chapter 6 [20], expanding our scope from studying the effect of *biomechanical* factors on shear wave physics to investigating the effect of *imaging* factors on shear wave physics. Our objective can be translated into two main study questions: (i) study the effect of compounding through comparison of single and compounded plane wave acquisitions from SWE experiments, for which more in-depth insights are realized by modeling both acquisitions using the multiphysics methodology, and (ii) study the effect of ultrafast imaging by analyzing the mechanical versus imaged shear wave acquisitions in the simulations. The study of each effect consisted of examining the shear wave propagation patterns in the time and frequency domain, and inspecting the accuracy of two different shear modulus estimation techniques, based on group and phase velocity, through comparison with the mechanically determined shear modulus.

9.2 Materials and methods

9.2.1 SWE experiments

SWE acquisitions were performed on an ultrasound phantom (10% polyvinylalcohol (PVA), freeze-thawed once) of the mimicking pediatric left ventricular geometry as illustrated in figure 9.1. Further details on this phantom can be found in chapter 6. Shear waves were generated and imaged by a SL15-4 linear transducer with 256 elements, a pitch of 200 µm and an elevation focus of ~30 mm, connected to the Aixplorer system (SuperSonic Imagine, Aix-en-Provence, France). We considered two SWE acquisitions, one with single plane wave emissions (0°) and the second with coherent plane wave compounding (−2°, 0°, 2°) [98], in which the single plane waves are emitted at a pulse repetition frequency (PRF) of 6.9 kHz for both acquisitions. All other pushing and imaging parameters for both SWE acquisitions are listed in table 9.1. The Aixplorer system provided us beamformed in-phase and quadrature-demodulated (IQ) signals with a fast time sampling rate of 32 MHz.

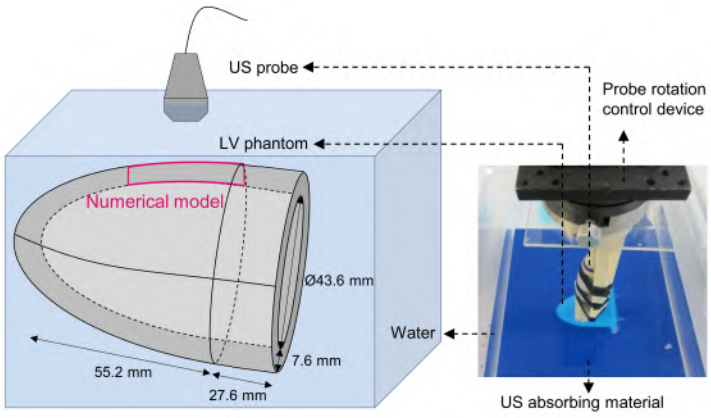

Figure 9.1: Experimental set-up (dimensions are not to scale in schematic diagram).

9.2.2 SWE multiphysics model

Concordant with an actual SWE measurement, the SWE model also splits the SWE acquisition into a pushing and an imaging sequence. This multiphysics platform contains three modeling parts, i.e., modeling of the acoustic radiation force (ARF), the shear wave propagation and the ultrafast imaging acquisition. The first two modeling parts compose the pushing sequence, whereas the third modeling part represents the imaging sequence (see figure 9.2). These models need to be run consecutively as the output of the first model is used as input for the second model and likewise for the second

Table 9.1: *In vitro* SWE pushing and imaging parameters.

	Parameters	Values
Pushing sequence	Push frequency f_0	8 MHz
	F-number	2.5
	Apodization	-
	Push duration	250 µs
Imaging sequence	Number of cycles	2
	Emission frequency	8 MHz
	Pulse repetition frequency (PRF)	6.9 kHz
	Imaging depth	40 mm
	F-number on transmit	-
	Transmit apodization	-
	F-number on receive	1.2
	Receive apodization	Hanning
	Receive bandwidth	60%

and third model, as indicated by the arrows in figure 9.2. The first and the third part of the multiphysics platform model the ultrasound physics through *Field II* [185], [186], whereas the second modeling part simulates the wave mechanics in the finite element software *Abaqus* (Abaqus Inc., Providence, USA). The modeling methodology for the pushing and imaging sequence is concisely described below. The reader is referred to chapter 6 for further details about the pushing sequence, comprising the first two modeling parts.

9.2.2.1 Pushing sequence

The pushing sequence in the numerical model consists of two steps: ARF generation and mechanical wave propagation (figure 9.2). For the first step, the ARF applied on the PVA phantom is numerically mimicked by a volume force in combination with an interface pressure. Both types of loading act on the PVA phantom in the focal zone of the probe, extending ~2 mm from the probe's center point in the lateral and elevation direction. The volume force acts throughout the complete thickness of the PVA phantom in this focal region, whereas the interface pressure is only active on the interfaces between phantom and water. Volume force B and interface pressure Π are calculated based on the time-averaged acoustic intensity I, of which its spatial distribution is derived by simulating acoustic probe pressures mimicking the push sequence (see table 9.1) with *Field II* and its magnitude is scaled to 1500 W/cm² [49], as follows [194], [215]:

$$B = \frac{2\alpha I}{c_L} \tag{9.1}$$

$$\Pi = \frac{I}{c_1}\left(1 + R - (1 - R)\frac{c_1}{c_2}\right) \tag{9.2}$$

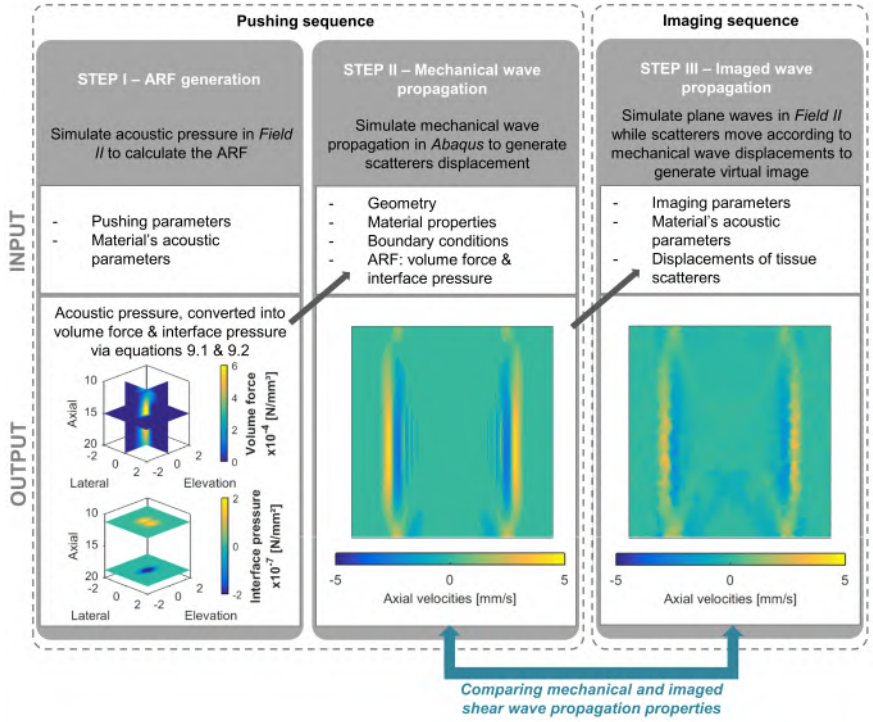

Figure 9.2: Workflow of the multiphysics platform.

with α the attenuation coefficient [dB/cm/MHz], ρ the density of PVA [kg/m^3], c_L the longitudinal wave speed of PVA [m/s], $R = \left(\frac{Z_2 - Z_1}{Z_2 + Z_1}\right)^2$ the energetic reflection coefficient [-], Z_1 and Z_2 the acoustic impedances ($Z_i = \rho_i c_i$) [Pa · s/m^3], and c_1 and c_2 the speeds of sound in media 1 and 2 [m/s]. Material characteristics of the modeled water and PVA can be found in table 9.2. The PVA's Young's modulus and viscoelastic behavior were mechanically determined on a uniaxial tensile testing machine (Instron 5944, Norwood, MA, USA), whereas its density and speed of sound were measured using the principle of Archimedes [240] and an oscilloscope respectively (for more details on all measurements, we refer to section 6.2.2 in chapter 6). The resulting spatial distribution of the volume force in the axial-lateral plane is shown in the bottom-left panel of figure 9.2. Both loads are imposed for 250 µs in the numerical model.

For the actual mechanical wave simulation (step II in figure 9.2), the PVA phantom was modeled as one half of an ellipsoidal-shaped disk with a lateral and elevational length of 27.8 mm and 16.0 mm respectively, taking the symmetry of the imaging plane into account. For reasons of computational efficiency, we considered only half the width of the transducer in the model,

Table 9.2: Material characteristics of water and polyvinylalcohol (PVA).

	Characteristics	Values
Water	Density ρ	1000 kg/m^3
	Speed of sound c_L [213]	1480 m/s
	Bulk modulus K [213]	2200 MPa
PVA	Density ρ	1045.5 kg/m^3
	Speed of sound c_L	1568 m/s
	Young's modulus E	73.0 kPa
	Attenuation coefficient α [199]	0.4 dB/cm/MHz
	Coefficient of Poisson ν [23]	0.49999
	Normalized shear modulus g_1	$4.04 \cdot 10^{-3}$
	Relaxation time τ_1	$99.8 \cdot 10^{-6}$ s
	Normalized shear modulus g_2	$7.04 \cdot 10^{-2}$
	Relaxation time τ_2	77.9 s

and modeled structural infinite elements at the edges of the defined domain. This PVA model was meshed with 8-noded brick elements with reduced integration, leading to 355,680 elements in total. The water below and above the phantom is represented by two layers of 8-noded hexahedral acoustic elements, each with a thickness of 3.8 mm and 79,684 elements. Mechanical displacements of the PVA phantom were coupled to acoustic pressures in the water layer through a tie-constraint. The other surfaces of the modeled water were modeled to be infinite. The PVA was modeled as a viscoelastic material by assuming a 2-term Prony series model with normalized shear moduli g_i and relaxation times τ_i as mentioned in table 9.2, which are derived from a uniaxial mechanical relaxation test stretching the PVA material at 5% strain for 10 s [20]. It should be noted that the modeled viscoelasticity has a negligible influence on shear wave propagation characteristics, indicating that the actual and modeled PVA phantom have very low viscosity [20]. The water was defined as an acoustic medium in the model with bulk modulus K and density ρ as tabulated in table 9.2. More details about mesh geometry, boundary conditions, material characteristics and loading can be found in section 6.2.3 of chapter 6.

The dynamic equations of motion of this numerical problem were solved by the *Abaqus/explicit* solver and the particle velocities were extracted at a sampling rate of 40 kHz for further analysis. The wave propagation resulting from these simulations is called *'mechanical shear wave propagation'* throughout this work (see figure 9.2).

9.2.2.2 Imaging sequence

The imaging sequence simulation in the multiphysics approach is illustrated in step 3 of figure 9.2. The basis of the ultrasound simulation is *Field II*, in which tissue is represented by a collection of random point scatterers reflecting

the ultrasonic waves emitted by the modeled probe. For each emitted beam, the scatterer's position is updated based on the CSM extracted displacement fields, utilizing first a temporal interpolation from the CSM timescale to US timescale and subsequently spatial interpolation from CSM mesh grid to US scatterer grid. In order to obtain a proper random distribution of point scatterers within our numerical phantom, we used an algorithm based on the open-source software Visualization ToolKit (VTK) [241]. This algorithm first generates randomly distributed scatterers in a box surrounding the phantom's geometry and then removes the abundant scatterers outside the actual geometry based on geometric criteria of the scatterers relative to the phantom's surface [242]. Approximately 10 scatterers per resolution cell (with its size calculated based on receive F-number, transmit frequency and pulse length) were considered to ensure a Gaussian-distributed RF signal [243].

To mimic our SWE experiments (see section 9.2.1), two ultrafast imaging settings were simulated, one with and one without coherent plane wave compounding, using the same probe parameters as mentioned in table 9.1. However, the virtual transducer's size was reduced to 128 piezoelectric elements to decrease computational time. For the same reason, the number of simulated frames was limited to 27 and 9 for the single and compounded Plane Wave Imaging (PWI) acquisition, respectively. For the estimation of the scatterer displacement during these simulations, the displacement information of the same CSM simulation was used since the pushing parameters or location did not change throughout the experiments (see table 9.1). In our simulation setup, each transducer element was divided into four rectangular mathematical elements in the elevational direction to ensure a far-field approximation of the spatial impulse response. Channel data were acquired at a fast time sampling rate of 100 MHz, IQ-demodulated to 32 MHz and subsequently delay-and-sum beamformed with parameters mentioned in table 9.1 using an in-house developed code from the Norwegian University of Science and Technology (NTNU). The obtained wave propagation from these simulations is termed *'virtual imaged shear wave propagation'* throughout this work (see figure 9.2).

9.2.3 Post-processing

The data acquired from the SWE experiments and the SWE multiphysics model were both processed as described below to obtain the axial particle velocities as a function of time and space and the shear modulus estimate.

9.2.3.1 *Axial velocity estimation*

Axial velocities $\widehat{v}_z$ were obtained by applying the autocorrelation technique on the IQ-data as follows [103], [244]:

$$\widehat{v}_z = \frac{c_L \left(\frac{PRF}{n_T} \right)}{4\pi f_0} \angle \widehat{R}_x(1) \tag{9.3}$$

where $\angle \widehat{R}_x(1)$ represents the phase angle of the autocorrelation function of lag one which is estimated from the received signal sequence, and n_T the number of transmit beams to obtain one image. The axial velocity estimate was further improved by spatial averaging the autocorrelation estimate over an area of approximately 0.6 × 0.6 mm both in simulations and *in vitro*.

Note that this post-processing step is not applied on the mechanical shear wave simulations, as these immediately provide access to all components of the particle velocities in the 3D spatial domain. Additionally, the mechanical wave simulations have a slow time sampling rate of 40 kHz, whereas the sampling rate of the real and virtual SWE imaging measurements depends on the acquisition, i.e., 6.9 kHz for single plane wave emissions and 2.3 kHz for plane wave compounding.

9.2.3.2 *Shear modulus estimation*

As chapter 6 has shown that dispersive shear wave propagation patterns arose in the studied setting due to geometry, two different shear modulus estimation techniques were applied on the mechanical and (real and virtual) imaged wave propagation, i.e., a time-of-flight (TOF) method—implemented in commercial SWE systems and used for non-dispersive media—and a phase velocity analysis—used for dispersive media. The real and virtual imaging acquisitions were pre-processed by averaging the axial velocities over 0.6 mm axial depth and temporally up-sampling the slow time domain by a factor 10.

For the TOF method, the shear wave's position was tracked by searching the maximal axial velocity for every lateral spatial location as a function of time and fitting a linear model to estimate the shear wave velocity (goodness of fit should be equal to or larger than 0.95) [20], [44]. In general, to make the most complete use of the measured data and to increase the reliability of the fit, axial velocity data acquired from all probe elements should be taken into account during this linear fitting procedure. This is true for large isotropic homogeneous elastic media, but usually data from the probe's edge elements is discarded due to low signal-to-noise ratio and/or high attenuation of the propagating shear wave in the measurement. Even though the studied PVA setting is isotropic, homogeneous and low viscous, the left ventricular

geometry induces dispersive shear wave features in the SWE-acquisitions which affect the tracked shear wave's position as a function of time. To investigate the effect of this observation on the results of the TOF method, we altered the number of data points taken into account during the TOF fitting procedure: the shear wave speed was estimated by rejecting 5 and 20 data points from the probe's edge elements for each shear wave. The shear modulus μ can then be derived from this wave speed c_T by assuming an isotropic bulky elastic material with density ρ and applying the following formula:

$$\mu = \rho c_T^2 \tag{9.4}$$

For the phase velocity analysis, measured or simulated dispersion characteristics were derived by taking the 2D Fast Fourier Transform (FFT) of the axial velocity wave propagation pattern as a function of lateral space and slow time at a specific depth [136]. Subsequently, the wavenumber k with the maximal Fourier energy is tracked at each frequency f in order to identify the main excited mode. Phase velocity c_ϕ as a function of frequency f is found through $c_\phi = (2\pi f)/k$. The shear modulus is then estimated by fitting a theoretical model in a least squares manner to the obtained dispersion curve. Neglecting the ventricular curvature [133] and PVA's viscoelasticity, and assuming that the main excited mode is the first antisymmetric mode (A0) [125], we minimized the difference between the theoretical A0 dispersion curve of a plate in water and the extracted dispersion characteristics over a frequency range spanning from 0.2 kHz up to maximally 2 kHz, dependent on the considered acquisition [38], [136]. Only fits giving a standard deviation less than 0.6 kPa for the shear modulus estimate were considered.

Both procedures were repeated for multiple depths across the phantom's thickness (n = 10). For further details on both shear modulus estimation techniques, we refer to section 2.2.2.2 in chapter 2 for the TOF-method and to section 2.2.3.2 in chapter 2 for the phase velocity analysis.

9.3 Results

9.3.1 Analyzing the shear wave's characteristics in the time domain

To study the shear wave's temporal characteristics, we examined its magnitude and shape throughout time by visualizing the axial velocities at three different time points. The resulting shear wave propagation of the experimentally measured SWE acquisitions with and without compounding are compared in figure 9.3. Immediately, we observe a different shear wave propagation pattern: the shear wave front, represented by the downward axial velocities,

is split into two for the single plane wave images whereas one uniform wave front is present for the compounded images. Furthermore, the wave front is also broader along the lateral direction when including compounding. Next to these differences in shear wave shape, we also observe a lower shear wave magnitude (maximal axial velocity amplitude at a certain time point can be up to 3 mm/s smaller) for the compounded images.

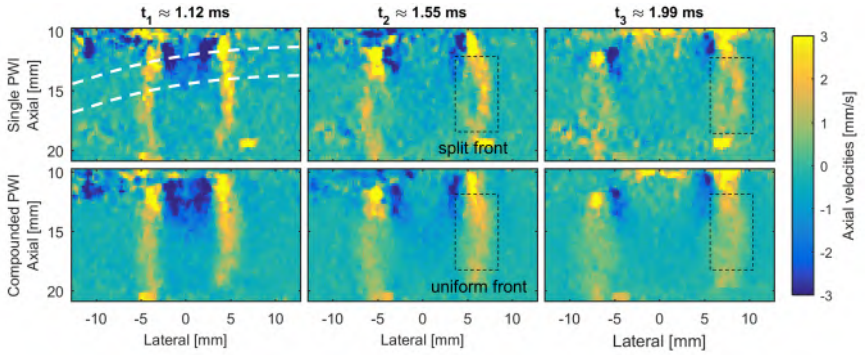

Figure 9.3: Experimental axial velocities depicting shear wave propagation in the ventricular phantom: comparison of shear wave propagation pattern at time points 1.12 ms, 1.55 ms and 1.99 ms (assuming t_o = 0 s corresponds with the start of the pushing sequence and an ultrasound system's electronic dead time of 0 s) for single and compounded Plane Wave Imaging (PWI). The white dotted lines represent shear wave propagation paths at 15% and 40% tissue depth with respect to the ventricular thickness.

The imaged and biomechanical shear wave propagation for the simulations are depicted in figure 9.4. For the biomechanical simulation (first row in figure 9.4), we observe again a split in shear wave front during wave propagation, which is well captured in the virtual single plane wave images (second row in figure 9.4), but less visible in the virtual compounded images (third row in figure 9.4). Furthermore, the shear wave front is apparently broader in the imaging simulations compared to the biomechanical simulation. Additionally, the simulated axial velocity patterns of the virtual images show a clear decrease in tissue velocity magnitude (~23.0% for single PWI and ~69.4% for compounded PWI at the top of the phantom compared to the biomechanics simulation).

9.3.2 Analyzing the shear wave's characteristics in the frequency domain

The shear wave's frequency features were studied by taking the 2D FFT of the axial velocity map in time and lateral space (see section 9.2.3.2) at 15% and 40% tissue thickness, representing two different shear wave propagation paths as indicated by the white dotted lines in figure 9.3 and figure 9.4. The Fourier

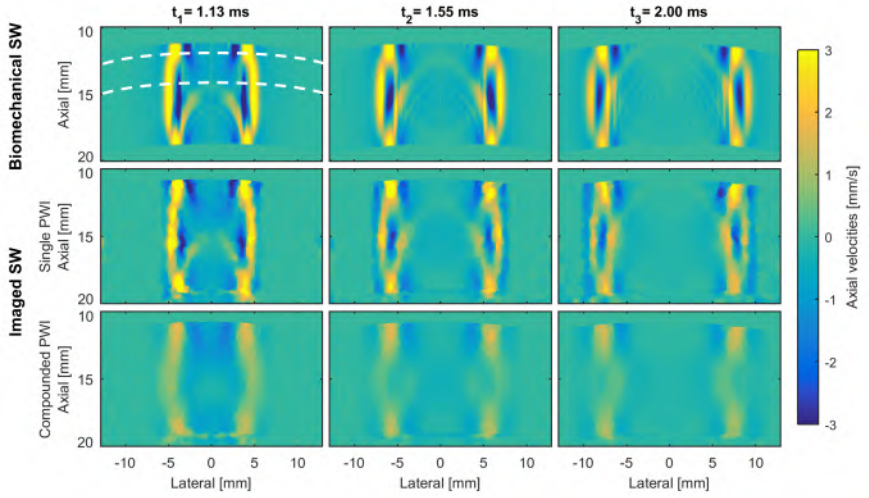

Figure 9.4: Simulated axial velocities depicting shear wave propagation in the ventricular phantom: comparison of the biomechanical shear wave propagation (upper panels) and the virtually imaged shear wave propagation without and with compounding (middle and lower panels respectively) at time points 1.13 ms, 1.55 ms and 2.00 ms (assuming t_0 = 0 s corresponds with the start of the pushing sequence). The white dotted lines represent shear wave propagation paths at 15% and 40% tissue depth with respect to the ventricular thickness.

energy magnitudes of both simulations and measurements are mentioned in table 9.3. Observations concerning mode(s) excitation, Fourier energy magnitude and frequency content in the Fourier spectra are consecutively discussed below.

9.3.2.1 Mode(s) excitation

For experimental single PWI (first column of figure 9.5), we observed that mainly one mode was excited at the shallow tissue depth, whereas two modes were excited for deeper tissue regions. The mode excited on lower frequencies is designated with the term 'primary mode', whereas the other mode is defined as 'secondary mode'. This primary mode is the one that will be tracked and fitted to the theoretical A0-mode in the phase velocity analysis to estimate shear stiffness. Applying compounding in the experiment led to one visible excited mode in the spectra of both tissue depths, as can be seen in the second column of figure 9.5. For the simulations (third, fourth and fifth columns of figure 9.5), we see one excited mode for 15% tissue thickness, and two excited modes for 40% tissue thickness, independent of the application of the compounding technique.

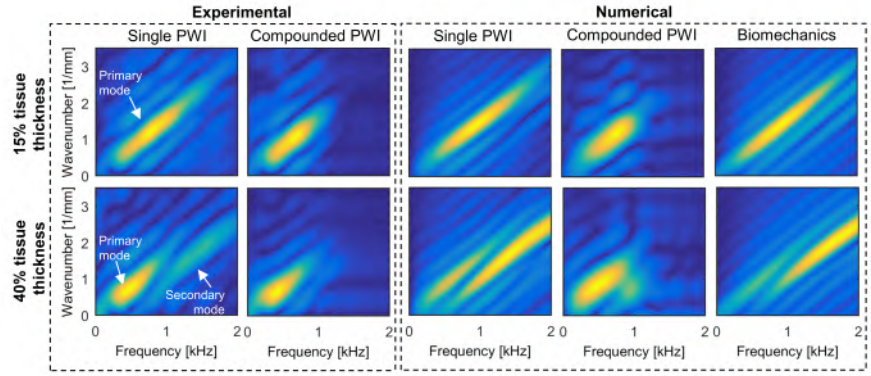

Figure 9.5: Fourier energy maps at two paths across the phantom's thickness—15% and 40%—for the right shear wave in the experimental (single and compounded PWI) and numerical (single PWI, compounded PWI and biomechanics) shear wave acquisitions. Location of the two shear wave paths is indicated in figure 9.3 and figure 9.4 for experiment and simulation respectively. The primary mode is defined as the mode excited on lower frequencies and the secondary mode is the mode excited on higher frequencies, as indicated in the biomechanics column. Each Fourier energy map was normalized to its maximal energy (displayed in red); amplitudes are given in table 9.3. The measured temporal shear wave data for one specific shear wave path across axial depth were cropped in lateral space (12.8 mm) and time (4 ms) such that its spatial and temporal resolution corresponded to the simulated ones.

9.3.2.2 Fourier energy magnitude

For the applied experiments, coherent compounding decreased the maximal Fourier energy magnitude with a factor of 3.9 for 15% tissue depth and 2.7 for 40% tissue thickness (see table 9.3). A similar observation was made for the simulations: compounding reduced the maximal Fourier energy magnitude by factors of 8.0 and 10.5 for 15% and 40% tissue thickness respectively. Furthermore, when comparing the virtual single PWI to the biomechanics simulation, an additional decrease by factors of 6.5 and 9.2 was noticed for the two considered tissue depths. Next to these dissimilarities in maximal Fourier energy magnitude, the relative energy magnitude of secondary to primary mode for the deeper tissue region also differed (see figure 9.5). This proportion was 0.5 for the experimental single PWI. For the simulations, this ratio shifted from 1.7 for the virtual biomechanics to 1.3 for single PWI and 0.6 for compounded PWI.

9.3.2.3 Frequency content

The bandwidth of the Fourier spectra was about 2.0 kHz for the experimental single PWI and 1.0 kHz for the compounded acquisition (see figure 9.5),

Table 9.3: Tabulation of the magnitude of the maximal Fourier energy amplitude in figure 9.5 [mm/s/Hz].

Acquisitions	15% tissue thickness	40% tissue thickness
Experimental		
Single PWI	6.52	3.42
Coumpounded PWI	1.68	1.26
Numerical		
Single PWI	5.13	3.45
Coumpounded PWI	0.64	0.33
Biomechanics	33.37	31.91

at both tissue depths. On the other hand, the bandwidth of the simulated Fourier spectra of the single PWI acquisition was around 2.0 kHz for 15% tissue thickness, and 3.0 kHz for 40% tissue thickness. When compounding was applied in the simulations, the maximal excited frequency was reduced to nearly 1.0 kHz for both tissue depths. However, the bandwidth of the biomechanical Fourier spectra of both virtual imaging acquisitions was about 2.0 kHz and 3.5 kHz for 15% and 40% tissue thickness, respectively.

The frequency content of the detected signal was further changed when compounding was used: the frequency with maximal Fourier energy content shifted from 0.69 kHz to 0.79 kHz for 15% tissue thickness and from 0.42 kHz to 0.47 kHz for 40% tissue thickness. For the virtual single PWI, the maximal Fourier energy was reached at 0.98 kHz for 15% tissue thickness and 1.4 kHz for 40% tissue thickness. Coherent compounding in the simulations downshifted these frequencies to about 0.50 kHz for both tissue regions. The frequencies with highest Fourier energy content in the biomechanics simulation were 0.93 kHz and 1.70 kHz for 15% and 40% tissue thickness, respectively.

9.3.3 Shear wave speed analysis

The quantitative analysis of shear wave observations consisted of shear modulus estimation based on group and phase velocity analysis for real and virtual SWE acquisitions, as visualized in figure 9.6. For the measurements, the group velocity analysis provided median shear stiffness values of 14.6 kPa and 17.1 kPa for single and compounded PWI respectively, when discarding data of 5 edge elements for each shear wave during shear modulus estimation. These estimations increased to 23.8 kPa and 18.8 kPa when 15 more data points were not considered during the fitting procedure for each shear wave. Phase velocity analysis gave median values of 24.7 kPa and 27.3 kPa for the measurements. For single PWI, the stiffness range of TOF-estimations when taking less data points into account during fitting (15.9 kPa) was remarkably higher than for other stiffness estimation methods (5.0 kPa and 4.6 kPa for group and phase speed analysis respectively). Actual PVA stiffness was mechanically determined at 24.3 ± 0.6 kPa.

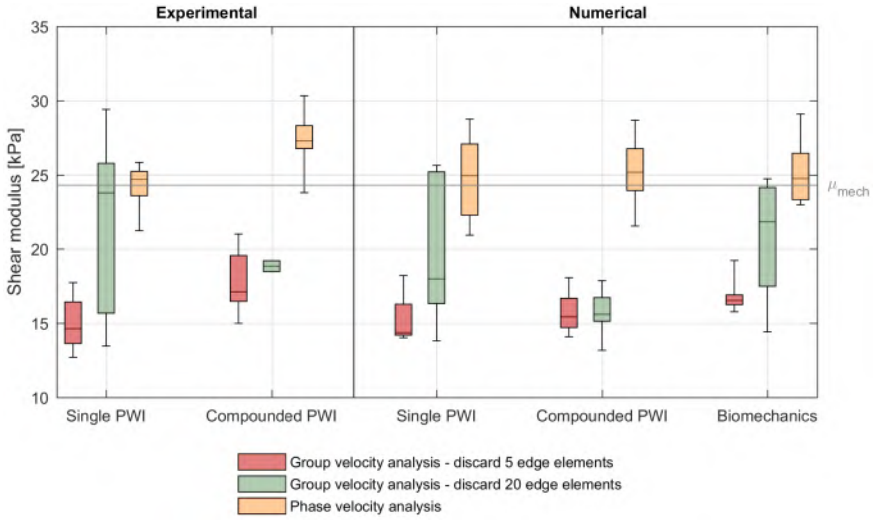

Figure 9.6: SWE-derived shear moduli: comparison of estimated shear modulus via material characterization methods based on group and phase velocity for the numerical (biomechanics and ultrasound simulations with single and compounded plane wave imaging (PWI)) and experimental shear wave acquisitions (single and compounded PWI). The mechanically determined shear modulus μ_{mech} of 24.3 kPa is also indicated in this figure, corresponding to the modeled stiffness. The boxplot represents the variation in shear modulus estimation throughout depth (n = 10), where the box displays first, second (median) and third quartiles and the whiskers indicate minima and maxima.

For the virtual imaging acquisitions, the group velocity-based method estimated median stiffness at 14.4 kPa and 15.4 kPa for single and compounded PWI, respectively. When discarding data from 20 edge probe elements, TOF stiffness estimations increased to 18.0 kPa and 15.6 kPa. Phase velocity analysis provided, for both imaging simulations, higher estimates of median shear stiffness, i.e., 24.9 kPa and 25.2 kPa for single and compounded PWI, respectively. As for the experiments, the largest spread in stiffness estimation across depth (11.8 kPa) was obtained for single PWI when applying the group velocity analysis and discarding data from 20 probe elements. For the biomechanics simulations, median shear stiffness measurements of 16.5 kPa, 21.8 kPa and 24.7 kPa were obtained for group velocity (discarding 5 data points), group velocity (discarding 20 data points) and phase velocity analysis respectively. Again, the depth-dependency of stiffness estimations was the largest for the group speed method taking less data points into account during fitting (10.3 kPa).

9.4 Discussion

9.4.1 Multiphysics modeling

In this work, a SWE multiphysics modeling approach incorporating the biomechanics and imaging physics of the shear wave propagation problem was presented, providing valuable insights into how the ultrafast US sequence and signal processing affects the true shear wave's characteristics in the time and frequency domain, and the subsequent shear modulus characterization. Furthermore, a modeling approach offers the benefits of full flexibility at the level of the tissue mechanics (tissue geometry, material properties and tissue surrounding) and ultrasound physics (ARF configuration, imaging settings and processing techniques). This approach was applied to a low-viscous pediatric ventricular phantom model, displaying clear shear wave dispersion as can be seen from the frequency-dependent phase velocity in the Fourier spectra and the split shear wave front in the temporal shear wave pattern for both experiment and biomechanics model (see chapter 6). The ventricular geometry was mainly the cause of the observed dispersion, as incorporating the measured viscoelastic material properties in the model did not significantly alter the shear wave characteristics (see section 6.3.2.2 in chapter 6 for details). A similar multiphysics approach has already been used by Palmeri et al [148] to study jitter errors and displacement underestimation in unbounded media, also in combination with experiments. Another study [245] used these same tools to investigate how parameters related to shear wave excitation and tracking affected the quality of shear wave speed images. However, both studies mimicked a different elastography technique, called Acoustic Radiation Force Imaging (ARFI), which employs conventional line-by-line scanning instead of plane wave imaging to visualize the shear wave propagation.

In general, the multiphysics model was capable of reproducing the experimental results (see figure 9.3, figure 9.4 and figure 9.5), indicating that the simulated biomechanical ground truth is a good representation of the actual shear wave physics occurring in the PVA phantom. However, there were also some discrepancies in shear wave visualization and characterization. For the shear wave's characteristics in the time and frequency domain, we firstly noticed a different axial velocity magnitude (see figure 9.3 and figure 9.4) and Fourier energy amplitude (see table 9.3) as a result of scaling the time-averaged acoustic intensity to 1500 W/cm^2 when calculating the numerical ARF. For the virtual compounded acquisition, there was the additional effect of large shear wave travel in between ultrasound frames in combination with the presence of high relaxation velocities (blue in figure 9.4) in the biomechanical simulation, indicating that compounding in the simulation reduces the downward velocities (red in figure 9.4) more than in the experiment.

Secondly, there were also differences in the temporal axial velocity pattern (e.g., larger relaxation peak at the center of the phantom for the simulations) and frequency spectra (e.g., more secondary mode excitation at 40% tissue thickness in the simulations). This can potentially be attributed to: (i) the manner of shear wave excitation in the model, i.e., applying a time-averaged body force and interface pressure instead of modeling the longitudinal wave propagation in the focused US beam, including reflection and attenuation, (ii) the difference in location of the actual and virtual SWE acquisitions, and (iii) the unknown experimental dead time between the pushing and imaging sequence. It should also be kept in mind that the beamforming process for experiment and simulation was performed with different infrastructure, i.e., the Aixplorer system and the NTNU in-house developed beamformer, respectively. Next to these dissimilarities in shear wave pattern in time and frequency, there were also inconsistencies in shear modulus estimation (see figure 9.6). These discrepancies are partly due to the same factors, as explained above, influencing shear wave propagation patterns and thus also stiffness characterization. Additionally, the simulations are noise-free, allowing more reliable shear stiffness estimates for every shear wave propagation path across depth compared to the experiments. Another potential cause explaining the stiffness discrepancy between experiment and simulation is a wrongly modeled material stiffness (based on uniaxial mechanical testing), as the mechanical properties of the PVA phantom could alter in the time difference between mechanical testing and SWE experiment.

9.4.2 Effect of ultrafast imaging on SWE in the studied left ventricular model

We studied the effect of ultrafast imaging on SWE by comparing shear wave visualization and characterization obtained from US and CSM simulations of our left ventricular phantom model. When analyzing the temporal shear wave patterns of all simulations in figure 9.4, a clear broadening of the shear wave front and underestimation of axial velocities is noticeable for both imaging acquisitions. A similar negative velocity bias was also recently reported when using coherent plane wave compounding for Doppler imaging [246]. Furthermore, the plane wave compounded images revealed a shear wave pattern different than the single plane wave images: the split shear wave front, clearly visible in the single plane wave acquisition, was less observable in the compounded images (see figure 9.4). Furthermore, the experimental compounded images in figure 9.3 showed a completely merged wave front instead of the split wave front as observed in the single plane wave images. Even though this observation was less clearly noticeable in the simulations (due to the presence of a larger relaxation peak in between the split wave front compared to the measurements, as mentioned in section 9.4.1), the

multiphysics model still demonstrated that these observed differences in temporal characteristics of the shear wave are mainly attributed to the chosen imaging parameters, as both virtual imaging acquisitions were derived from the same true mechanical wave propagation (see figure 9.4). We also investigated the subsequent changes in the shear wave's frequency characteristics, which showed that the detected excited frequencies, amplitudes and modes did not necessarily correspond to the ones excited in the biomechanical model. Indeed, the biomechanical frequency spectra are solely dependent on the model characteristics and the ARF properties [141], whereas the imaged spectra are also affected by plane wave imaging, acting as a low-pass filter, and by image processing techniques such as pixel averaging and slow time up-sampling.

Next to this qualitative investigation, we also quantitatively studied the effect of ultrafast imaging on the performance of SWE by comparing the SWE-derived shear modulus for both US and CSM simulations (see figure 9.6). This study showed that ultrafast imaging had mainly an effect on stiffness characterization through the group speed method: single and compounded PWI simulations led to median stiffness underestimations of −2.2 kPa (−4.0 kPa when discarding 20 data points) and −1.1 kPa (−6.2 kPa when discarding 20 data points) respectively, compared to the SWE-derived stiffness estimates from the biomechanical simulations. Additionally, the results of the TOF method when discarding 20 edge elements were very depth-dependent for the single PWI simulation. This was also observed for the experiments in figure 9.6. This large dissimilarity in depth-dependency of the stiffness estimates is due to a difference in meaning of the fitted linear relationship in the TOF method when discarding more or less data points for the single PWI acquisition. When 20 data points are discarded during the fitting procedure, the fitted linear relationship represents the true non-shifted shear wave position throughout time which varies a lot across depth, whereas it depicts an averaged shear wave position in time when only 5 data points are discarded (see figure 9.7). The latter is closer to the TOF shear wave characterization with compounded PWI (as can be seen in figure 9.6 and figure 9.7), as the compounded images already visualize the averaged shear wave behavior. Nevertheless, the shear modulus estimates are depth-dependent for all applied material characterization methods, as can be seen in the spread of the boxplots in figure 9.6. For the group velocity analysis (discarding 5 data points), this is mainly due to the difference in the shear wave propagation pattern at the upper and lower boundaries of the phantom (±0–25% and ±75–100% depth) compared to the middle segment of the phantom (±25–75% depth), as visible in figure 9.7. This group speed-derived stiffness difference between the boundaries and center of a tissue-mimicking medium was experimentally studied by Mercado et al. [247], in which they identified the presence

of Scholte surface waves at the fluid–solid interface as the primary reason for this discrepancy. For the phase velocity analysis, the cause of the depth-dependency of the stiffness estimates is less straightforward, as the extracted frequency characteristics of the primary mode across depth were very similar (see figure 9.5). However, as also shown in chapter 6, characterizing deeper shear waves via the phase velocity analysis is more challenging as their 2D FFT energy content is smaller (fewer data points to fit) and their velocity amplitude is lower (lower signal-to-noise ratio), leading to less reliable shear modulus estimates.

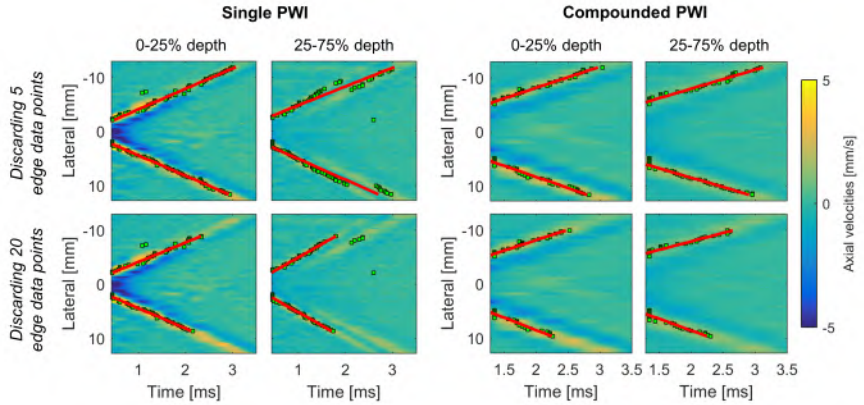

Figure 9.7: Illustration of the effect of discarding 5 or 20 data points at the edges of each shear wave during the fitting procedure in the time-of-flight (TOF) method: a comparison between different depths and imaging acquisitions. The green dots represent tracked maximal axial velocity, whereas the red line represent the linear TOF fit.

Phase velocity analysis provided a more robust and correct estimate for both the biomechanics and imaging simulations, as spectral characteristics of the tracked primary mode (fitted to the theoretical A0-mode) for all acquisitions are very similar, as shown in figure 9.5. Furthermore, for both experiment and simulation, the true tissue stiffness was underestimated by the TOF method, independent of the number of considered data points, whereas phase velocity analysis provided a better estimate of the mechanically determined stiffness. This is in accordance with our previous findings of experimental work on the same ventricular model in which we only applied single PWI (see chapter 6). Nevertheless, if the stiffness estimation technique is chosen based on observed shear wave physics (i.e., TOF method for compounded images visualizing almost no dispersion and phase velocity analysis for single plane wave images depicting dispersion), differences of minimally 5.9 kPa and 9.3 kPa are obtained for measurements and simulations, respectively. This is about 25% of the value of the actual shear modulus,

and non-negligible. Therefore, when studying low viscous settings evoking guided wave dispersion due to geometry, one should be cautious when selecting a tissue characterization method based on the observed shear wave pattern as this might be affected by the applied imaging set-up. In these cases, it might be relevant to also study phase velocity next to group velocity.

It should be noted that the primary objective of this work was not to compare the performance of single and compounded PWI, as this requires (i) the study of multiple configurations and material models, (ii) the use of more complex SWE-based material characterization and (iii) the inclusion of noise in the numerical models. However, this work shows the potential of computational modeling in identifying potential pitfalls in shear wave visualization and characterization with SWE, demonstrated through a case study of an idealized SWE setting with little amount of noise (as shown by the good correspondence between experiment and simulation). Future research should focus on applying the current modeling technique to different settings to further study the performance of single and compounded PWI.

9.4.3 Recommendations and impact for other applications

The dispersive shear wave propagation pattern studied here is inherently linked to the considered setting, i.e., a left ventricular low viscous phantom with pediatric geometry. We focused on the isolated effect of guided wave dispersion due to geometry, and therefore, the formulated conclusions cannot simply be extrapolated to actual tissue settings as dispersion in tissues can be caused by a combination of varying factors such as geometry, viscosity and non-homogeneous (potentially anisotropic) material characteristics. This is among other things noticeable in the excited frequency range of the studied shear wave (up to 2 kHz), which is much larger than the conventional 1 kHz shear wave frequency spectra reported in real tissue settings due to tissue's high shear viscosity [125]. Additionally, the observed shear wave fronts were quite isotropic in all directions of the shear wave paths in 2D, whereas these will become guided along the fiber orientation in anisotropic tissue [15], [149]. These true tissue characteristics demand more advanced tissue characterization algorithms as now (i) an isotropic bulky elastic material is assumed in the group speed analysis in order to apply equation (9.4), and (ii) a theoretical dispersion curve of an isotropic homogeneous elastic plate in water is used as fitting ground truth in the phase speed analysis. Therefore, complementary research is necessary to investigate how the formulated conclusions concerning shear wave visualization and characterization are translated to actual tissue settings *in vivo*, particularly when assessing the effect of compounding.

Despite these dissimilarities between shear wave physics in the phantom-model and actual tissue, the multiphysics model of the presented case study

allowed the assessment of the effect of ultrafast imaging on shear wave visualization and characterization from a mechanical point of view, as described in the previous section. Furthermore, this study showed that the number of compounding angles (i.e., the factor with which the frame rate is reduced) should be chosen taking the maximal reachable PRF (linked to imaged depth and technical capabilities of the ultrasound system), the wave propagation speed of the investigated material (related to its mechanical properties) and the bandwidth of the imaged phenomenon (related to different absorption mechanisms such as viscosity) into account. The resulting compounded frame rate should be sufficiently high to obtain an accurate representation of the mechanical shear wave physics, which was not the case for the studied left ventricular phantom model. Additionally, a high frame rate is also desirable from the shear wave characterization point of view, as this means a high Nyquist cut-off frequency, providing a more extensive Fourier spectrum, and thus a more reliable stiffness estimate via the phase velocity analysis.

Similar recommendations were recently published by Widman et al [239], who studied the optimal ARF and imaging settings to maximize bandwidth for phase velocity analysis in SWE on *ex vivo* arterial settings. In their study on arterial stiffness estimation, they claimed that a high PRF with poorer image quality is more desirable than a lower PRF with better image quality.

9.5 Conclusions

In this work, we assessed the effect of ultrafast imaging on dispersive shear wave visualization and subsequent shear stiffness characterization by means of SWE experiments in combination with a multiphysics model of a LV phantom model with pediatric geometry. This model offers the advantage of giving access to the true biomechanical wave propagation, which is unknown in the SWE measurements. The multiphysics model of the idealized LV phantom revealed that the detected shear wave features in the time and frequency domain by ultrafast imaging do not necessarily depict the ARF-excited characteristics of the biomechanical model. Furthermore, application of the compounding technique in ultrafast imaging even altered the dispersion features in the temporal shear wave pattern for both experiments and simulations, leading to a stiffness underestimation of minimally 25% when choosing a group velocity-based algorithm instead of a phase velocity one. Additionally, the applied group speed material characterization method was very sensitive to the applied algorithm settings (such as the number of tracked data points) and the selected axial depth, as ultrafast imaging can alter the shear wave front location in the shear wave visualization. Therefore, it is important to keep a high frame rate during compounding in order to obtain an accurate representation of shear wave physics and the subsequently derived

material stiffness. Future research should focus on investigating additional configurations with more advanced SWE-based material characterization to further generalize these conclusions. Nevertheless, this work presents a versatile and powerful simulation environment to evaluate the performance of ultrafast imaging in shear wave visualization and characterization with SWE, and to identify potential pitfalls in accurately capturing shear wave propagation.

Conclusion

A multiphysics model for cardiac shear wave elastography

SWE distinguishes itself from conventional imaging techniques by its ability to provide information about the tissue mechanical properties non-invasively. Therefore, it has the potential to improve diagnosis, monitoring and therapeutic decision making in the clinical world in a number of clinical domains. In that context, this dissertation explored the feasibility of SWE in assessing myocardial stiffness, for its potential application in children with cardiac disorders.

The first feasibility study of cardiac SWE was performed by Kanai et al [38] in 2005, in which they were able to link the vibrations measured in the cardiac wall due to aortic valve closure, to shear elasticity and viscosity. Then, four years later, Bouchard et al [150] explored the possibility to use an external instead of an internal excitation method to excite shear waves inside the cardiac wall, which was realized by employing an acoustic radiation force (ARF). Since then, many others have studied the performance of ARF driven cardiac SWE [15], [16], [133], [134], [149], [183]. All studies investigated different SWE metrics and showed variability in the reported metrics depending on the analyzed depth, location, moment in the cardiac cycle, etc. Furthermore, some acquisitions demonstrated complex shear wave propagation phenomena in the myocardium such as wave dispersion and guiding due to its geometry and intrinsic material properties.

Hence, in order to gain a better understanding in how the ARF-generated shear wave interacts with geometry, mechanical features and tissue surrounding, and how this affects SWE-based material characterization techniques, a flexible testing environment is needed. We developed a modeling framework, which was most suited for this purpose, as it allowed to (i) separately investigate the effect of each relevant factor in-to-depth in a controlled environment, (ii) inspect the accuracy of different SWE-based material characterization techniques in reconstructing mechanical properties by comparing its results with the modeled ground truth material properties and (iii) assess the performance of imaging techniques to correctly visualize the underlying shear

wave mechanics, as modeling provides access to the shear wave mechanics behind a SWE image.

We developed an *in vitro* based multiphysics simulation environment for ARF driven cardiac SWE in children, combining advanced structural modeling of cardiac wall mechanics with numerical modeling of ultrasound imaging (see chapter 4). Ultrasound modeling was used for two purposes: modeling of the ARF and modeling of the ultrafast imaging acquisition. The latter was only included in the numerical framework to investigate the effect of imaging factors on shear wave physics and characterization (see chapter 9). Now, in order to increase our understanding of shear wave physics in cardiac SWE, we applied this numerical framework on settings with gradually increasing complexity concerning geometry and material characteristics, i.e. from viscoelastic plate to viscoelastic left ventricle, to *ex vivo* myocardial tissue. We also created an experimental variant for each model such that the realism and accuracy of the model could be assessed. These SWE-experiments allowed optimization of the numerical framework such as the inclusion of the acoustic interface pressure during numerical ARF application (see chapter 6). Furthermore, the numerical settings of our framework were also theoretically validated by simulating Lamb wave propagation and comparing the results to the theoretical solution.

Simulated shear wave propagation and characterization corresponded well with the SWE experiments for the viscoelastic plate (chapter 4) and ventricle model (chapter 6 and chapter 9). One-to-one comparison of the shear wave results for simulations and measurements on the *ex vivo* cardiac tissue was not possible due to lack of complete 3D mechanical characterization of the myocardium (chapter 7 and chapter 8). Nevertheless, their simulated and measured group speed features showed similar trends across depth for varying probe angles. Even though our multiphysics computer models showed realistic results, one has to be aware of the inherent assumptions and limitations related to the modeling approach. Indeed, the SWE modeling methodology imposed the calculated ARF as a time-averaged body force in the FEM model, instead of modeling the actual travel of the emitted acoustic pressures from probe to the modeled tissue of interest. Furthermore, the formulas used for ARF calculation consider tissue as viscous fluids at ultrasonic frequencies and assume plane wave conditions. Additionally, the accuracy of the numerical shear wave propagation is affected by (i) mesh size, selected based on a trade-off between modeled shear wave length and computational cost (mesh should also be able to represent the spatial variation of the ARF distribution), (ii) mesh orientation, which should be ideally oriented perpendicular to the direction of wave incidence in order to minimize numerical errors and dispersion, and (iii) temporal sampling rate, chosen

in function of the material properties of the media and the amount of data generated.

Cardiac shear wave elastography in pediatric models of the heart

In this work, we used the SWE multiphysics model of chapter 4 in combination with *in vitro* SWE-experiments to perform a sensitivity analysis of the biomechanical factors affecting the performance of SWE. More specifically, we investigated the effect of pediatric left ventricular geometry in chapter 6 and the effect of myocardial anisotropy in chapter 7 and chapter 8 on cardiac SWE. At last, the SWE multiphysics model was extended to include the effect of *ultrafast* imaging on visualized shear wave physics and characteristics (see chapter 9).

Performing SWE on the left ventricular homogeneous phantom model gave rise to complex shear wave propagation with visible dispersion, as the shear wave front shifted spatially for shear wave paths between 25%-75% phantom thickness. Here, the multiphysics model identified the relevance of modeling features such as tissue surrounding (water) and the acoustic interface pressure to mimic the shear wave propagation as observed in the SWE-experiment. Additionally, modeling water also affected SWE-derived stiffness based on group and phase speed, whereas the acoustic interface pressure did not. We also investigated the effect of modeling viscoelasticity, but this did not have a significant effect on either. Both experiment and model showed that phase speed analysis provided a better estimate of mechanical (and modeled) stiffness than group speed analysis. The same was true for other analyzed ventricular zones and probe angles in the experiment. Both SWE algorithms showed a limited variation in function of analyzed shear wave path across depth. However, it should be noted that the spatially shifted shear wave front challenged the performance of group speed analysis, which becomes dependent on the number of data-points taken into account during the analysis.

The complex anisotropic myofiber architecture of myocardial tissue causes 3D anisotropic shear wave propagation in cardiac SWE, as the myocardial fiber orientation varies throughout tissue thickness. This part of the dissertation focused on assessing the combined effect of myocardial anisotropy in combination with mechanical loading, which, according to the best of our knowledge, has not been evaluated yet. As complete mechanical characterization of myocardial tissue was not feasible, the SWE-modeling methodology was applied to a literature-based material model of the porcine myocardium. Nevertheless, SWE model and experiment were constructed in a similar fashion, i.e. a left ventricular slab subjected to three uniaxial

stretch states, to allow partly validation of the model. From the experiment, it was clear that uniaxial stretching increased the group and dominant phase speed, especially along the fiber direction. Furthermore, their maximal value spatially shifted during stretching, indicating an alignment of the fibers to the stretch direction.

The SWE multiphysics model of the left ventricular slab is the first model to combine the SWE modeling steps with a realistic orthotropic material law of the myocardium and mechanical loading. This model provided access to the true fiber orientation and material characteristics, making the developed framework ideal for (i) assessing the accuracy of fiber orientation extraction methods based on SWE, and (ii) theoretically evaluating the effect of pathology on shear wave physics and characterization. For the first application, we analyzed the performance of two fiber orientation extraction methods, one based on maximal shear wave speed (SWS_{max}-method) and one based on ellipse fitting (ellipse fitting method). Both methods gave a better estimate for actual fiber orientation for the center region of the cardiac wall than towards the edges. The accuracy of the SWS_{max}-method was higher than the ellipse fitting method, but it was less robust to outliers. The second application of the multiphysics model demonstrated clearly altered shear wave patterns for fibrotic myocardium, compared to healthy myocardium, which forms an initial but promising outcome of this modeling study.

Next to these biomechanical factors that affect shear wave propagation, the observed shear wave patterns might also be influenced by the imaging settings. This was investigated using an extended version of the developed multiphysics environment through inclusion of *ultrafast* imaging in the model. We applied this extended modeling approach on the left ventricular phantom model, a setting depicting dispersive shear wave propagation. We showed that *ultrafast* imaging broadened the shear wave front, and decreased the tissue velocity estimates. Furthermore, improving image resolution with the *compounding* technique, altered the visual appearance of dispersion. Similar observations were made in the experiments. This indicates that the resulting compounding frame rate was not high enough to obtain an accurate representation of the mechanical shear wave physics. Indeed, the number of compounding angles should be chosen based on a trade-off between maximal reachable PRF, wave propagation speed of the investigated material and bandwidth of the imaged phenomenon. For SWE-based stiffness estimation, both model and experiment demonstrated again that phase velocity analysis provided a more accurate and robust stiffness estimate than group velocity analysis. The presented multiphysics model was the first one to combine computational mechanics of shear wave propagation with ultrasound modeling of the *ultrafast* imaging technique.

Is myocardial stiffness assessment feasible with shear wave elastography?

The crucial question that we ultimately aimed to answer, is whether shear wave elastography is able to assess myocardial stiffness. However, as often in research, the answer is not straightforward. First of all, which SWE-metric(s) represent(s) cardiac stiffness? Multiple SWE-metrics have been reported in the past for myocardial stiffness, ranging from shear wave characteristics such as group and phase speed to mechanical parameters such as shear modulus and viscosity. It is generally known from soft tissue mechanics that the mechanical behavior of cardiac tissue is to be characterized with more than one parameter. In that context, it is relevant to explore more advanced material models of the cardiac wall.

Phase speed analysis proved to be superior in estimating myocardial stiffness compared to group speed analysis for pediatric ventricular phantoms, as shown in chapter 6. However, estimating stiffness based on phase speed analysis for the *ex vivo* porcine myocardial tissue considered in chapter 7 and chapter 8 is not that simple, since no theoretical model is available. Nevertheless, the theoretical dispersion relationships could be replaced by semi-analytical dispersion relationships obtained from our developed multiphysics simulation environment, yielding more flexibility in geometry and material models. Or even further, the experimentally measured phase speed characteristics might be fitted to the resulting dispersion properties of the frequency domain simulations presented in chapter 5, which are computationally less expensive than the simulations in the time domain. For both cases, the phase velocity based stiffness estimation yields an optimization problem that needs to be solved for a multi-parameter material model. These additional metrics of the material model may create new clinical opportunities in further differentiating diseases states. To apply phase velocity analysis to *in vivo* SWE data, it remains to be investigated whether it is feasible to accurately extract dispersion characteristics from noisy SWE data.

Another hurdle in *in vivo* cardiac SWE is obtaining values of relevant SWE-metric(s) in a standardized way. Indeed, SWE-metric(s) are known to vary depending on the chosen ARF-settings, shear wave imaging settings, the chosen location of the imaged tissue, etc. Furthermore, the available acoustic windows for application of transthoracic cardiac SWE are limited, as the ARF pushing beam needs to be quasi-orthogonally oriented with respect to the cardiac wall and the ventricular wall might not be located too deep to avoid substantial ultrasound attenuation. Therefore, guidelines regarding optimal probe orientation, excitation settings and so on should be developed to guarantee robust and reliable SWE performance. In general, efforts are currently ongoing to standardize SWE measurements in other application

domains. For example, the Quantitative Imaging Biomarker Alliance (QIBA) was created by the Radiological Society of North America (RSNA) to set-up protocols to use shear wave speed as biomarker for liver fibrosis staging [227]. In this regard, finite element simulations are used to develop elastic and viscoelastic digital calibration phantoms for commercial systems. The developed cardiac SWE models in this thesis might thus contribute in a similar way to move forward standardization in pediatric cardiac SWE.

Future perspectives

Although the original research of this dissertation is mainly fundamental, future research may focus on optimizing and extending the developed multiphysics models to actual patient-specific models for healthy and diseased conditions. Until now, our experiments and simulations have focused on the individual factors affecting shear wave physics and characterization in *in vitro* and *ex vivo* cardiac settings. The next logical step is thus combining all studied factors into one computer model and checking whether the previously studied shear wave propagation and subsequent formulated conclusions are still valid for this newly defined model. Next, the computer model can be further refined by implementing anatomically realistic patient models, child-specific material models or numerically mimicking curved array probes instead of conventionally linear array probes. Cardiac disease models such as myocardial fibrosis should also be included to investigate their effect on shear wave physics and characterization. As there is no established material model for fibrotic myocardium yet, such a model should first be validated with an animal model. These advanced patient-specific models in healthy and diseased conditions can then be used for two purposes: (i) establishment of reference values for SWE-metric(s) and (ii) optimization of the excitation and imaging settings of SWE acquisitions.

Reference SWE-metric(s) should be set-up based on the multiphysics model of healthy and diseased myocardium for different demographics (e.g. age, gender, weight) in a standardized way. Additionally, the reference SWE-metric(s) for diseased cardiac tissue should depend on the degree and type of cardiac pathology. These reference metrics can assist medical doctors in their diagnosis and clinical decision making. The studied model is however an ideal setting, thus *in vivo* evaluation of SWE-metric(s) will be crucial in order to investigate the inter-subject variability. Here, it is important to perform SWE in a standardized way such that the influence of non-disease factors affecting shear wave propagation is rendered minimal.

Another future application of the most advanced computer model for cardiac SWE in children is to optimize SWE acquisitions by designing an appropriate pediatric probe, scan acquisition and signal processing algorithms

based on the multiphysics approach. Complementarily, this model disposes of a large flexibility both at the level of the cardiac tissue properties, shear wave excitation and imaging processing, and thus can be used as virtual learning platform for medical doctors. Clinicians (and researchers) can use this platform to qualitatively and quantitatively see the effect of certain choices concerning excitation/imaging settings and probe orientations.

It should be noted that we could also deploy our framework to study myocardial stiffness variation throughout the cardiac cycle. Application of transthoracic cardiac SWE in systole is however currently challenged due to the rapid motion of the heart and the significantly stiffer cardiac wall (requiring a very high frame rate).

Non-invasive stiffness assessment of cardiac intrinsic properties in diastole is also highly relevant for the field of adult cardiology. It is especially interesting for diagnosing patients with heart failure (HF), as almost half of the patients with HF cannot be diagnosed with the standard echocardiographic evaluation of ejection fraction (volumetric fraction of blood pumped out of a ventricle with each heartbeat). This way, SWE could allow identification of HF patients with preserved ejection fraction, in which abnormalities in cardiac relaxation and stiffness are key pathophysiological mechanisms. Furthermore, if technical challenges are overcome to transthoracically measure systolic stiffness, SWE is able to provide a true measure of cardiac contractility. Myocardial stiffness assessment in systole allows to increase our understanding in the contraction physiology of the heart, potentially altered by disease, but also to assess changes in contractility after administration of therapies.

Bibliography

[1] L. I. Bezold and J. T. Bricker, 'Advances in acquired pediatric heart disease', *Current opinion in cardiology*, vol. 10, no. 1, pp. 78–86, 1995.

[2] D. T. Hsu and G. D. Pearson, 'Heart failure in children: Part i: History, etiology, and pathophysiology', *Circ Heart Fail*, vol. 2, no. 1, pp. 63–70, 2009.

[3] A. Frazier, E. A. Hunt and K. Holmes, 'Pediatric cardiac emergencies: Children are not small adults', *Journal of Emergencies, Trauma and Shock*, vol. 4, no. 1, p. 89, 2011.

[4] N. Jayaprasad, 'Heart failure in children', *Heart views: the official journal of the Gulf Heart Association*, vol. 17, no. 3, p. 92, 2016.

[5] A. Dragulescu and L. L. Mertens, 'Developments in echocardiographic techniques for the evaluation of ventricular function in children', *Arch Cardiovasc Dis*, vol. 103, no. 11-12, pp. 603–14, 2010.

[6] J. W. Rossano, A. I. Dipchand, T. M. Hoffman, T. Singh and J. L. Jefferies, 'Advances in pediatric heart failure and treatments', *Progress in Pediatric Cardiology*, vol. 39, no. 1, pp. 33–36, 2015.

[7] L. Mertens and P. Khairy, 'Right ventricular diastolic function in congenital heart disease', *Can J Cardiol*, vol. 29, no. 7, pp. 755–6, 2013.

[8] D. Burkhoff, I. Mirsky and H. Suga, 'Assessment of systolic and diastolic ventricular properties via pressure-volume analysis: A guide for clinical, translational, and basic researchers', *Am J Physiol Heart Circ Physiol*, vol. 289, no. 2, H501–12, 2005.

[9] C. B. Chapman, S. M. Ewer, A. F. Kelly, K. M. Jacobson, M. A. Leal and P. S. Rahko, 'Classification of left ventricular diastolic function using american society of echocardiography guidelines: Agreement among echocardiographers', *Echocardiography*, vol. 30, no. 9, pp. 1022–31, 2013.

[10] A. Dragulescu, L. Mertens and M. K. Friedberg, 'Interpretation of left ventricular diastolic dysfunction in children with cardiomyopathy by echocardiography: Problems and limitations', *Circ Cardiovasc Imaging*, vol. 6, no. 2, pp. 254–61, 2013.

[11] T. Elgeti, M. Laule, N. Kaufels, J. Schnorr, B. Hamm, A. Samani, J. Braun and I. Sack, 'Cardiac mr elastography: Comparison with left ventricular pressure measurement', *J Cardiovasc Magn Reson*, vol. 11, p. 44, 2009.

[12] W. A. Berg, D. O. Cosgrove, C. J. Doré, F. K. Schäfer, W. E. Svensson, R. J. Hooley, R. Ohlinger, E. B. Mendelson, C. Balu-Maestro and M. Locatelli, 'Shear-wave elastography improves the specificity of breast us: The be1 multinational study of 939 masses', *Radiology*, vol. 262, no. 2, pp. 435–449, 2012.

[13] E. Bavu, J. L. Gennisson, M. Couade, J. Bercoff, V. Mallet, M. Fink, A. Badel, A. Vallet-Pichard, B. Nalpas, M. Tanter and S. Pol, 'Noninvasive in vivo liver fibrosis evaluation using supersonic shear imaging: A clinical study on 113 hepatitis c virus patients', *Ultrasound Med Biol*, vol. 37, no. 9, pp. 1361–73, 2011.

[14] E. Maksuti, E. Widman, D. Larsson, M. W. Urban, M. Larsson and A. Bjallmark, 'Arterial stiffness estimation by shear wave elastography: Validation in phantoms with mechanical testing', *Ultrasound Med Biol*, vol. 42, no. 1, pp. 308–21, 2016.

[15] M. Couade, M. Pernot, E. Messas, A. Bel, M. Ba, A. Hagege, M. Fink and M. Tanter, 'In vivo quantitative mapping of myocardial stiffening and transmural anisotropy during the cardiac cycle', *IEEE Trans Med Imaging*, vol. 30, no. 2, pp. 295–305, 2011.

[16] M. Pernot, M. Couade, P. Mateo, B. Crozatier, R. Fischmeister and M. Tanter, 'Real-time assessment of myocardial contractility using shear wave imaging', *J Am Coll Cardiol*, vol. 58, no. 1, pp. 65–72, 2011.

[17] A. Swillens, 'A multiphysics model for improving the ultrasonic assessment of large arteries', Thesis, 2010.

[18] A. Caenen, A. Thabit, M. Pernot, D. A. Shcherbakova, L. Mertens, A. Swillens and P. Segers, 'The effect of stretching on transmural shear wave anisotropy in cardiac shear wave elastography', in *IEEE International Ultrasonics Symposium (IUS) 2017*, IEEE TUFFC.

[19] A. Caenen, M. Pernot, I. Kinn Ekroll, D. Shcherbakova, L. Mertens, A. Swillens and P. Segers, 'Effect of ultrafast imaging on shear wave visualization and characterization: An experimental and computational study in a pediatric ventricular model', *Applied Sciences*, vol. 7, no. 8, 2017.

[20] A. Caenen, M. Pernot, D. A. Shcherbakova, L. Mertens, M. Kersemans, P. Segers and A. Swillens, 'Investigating shear wave physics in a generic pediatric left ventricular model via in vitro experiments and finite element simulations', *IEEE Trans Ultrason Ferroelectr Freq Control*, vol. 64, no. 2, pp. 349–361, 2017.

[21] A. Caenen, P. Segers and A. Swillens, 'Finite element simulations to support the measurement and analysis of shear wave dispersion', in *IEEE International Ultrasonics Symposium (IUS) 2016*, IEEE, pp. 1–4.

[22] A. Caenen, M. Pernot, C. Papadacci, D. Shcherbakova, L. Mertens, P. Segers and A. Swillens, 'Myocardial stiffness assessment in pediatric cardiology using shear wave imaging', in *IEEE International Ultrasonics Symposium (IUS) 2015*, IEEE, pp. 1–4.

[23] A. Caenen, D. Shcherbakova, B. Verhegghe, C. Papadacci, M. Pernot, P. Segers and A. Swillens, 'A versatile and experimentally validated finite element model to assess the accuracy of shear wave elastography in a bounded viscoelastic medium', *IEEE Trans Ultrason Ferroelectr Freq Control*, vol. 62, no. 3, pp. 439–450, 2015.

[24] D. A. Shcherbakova, N. Debusschere, A. Caenen, F. Iannaccone, M. Pernot, A. Swillens and P. Segers, 'A finite element model to study the effect of tissue anisotropy on ex vivo arterial shear wave elastography measurements', *Phys Med Biol*, vol. 62, no. 13, pp. 5245–5275, 2017.

[25] D. Shcherbakova, A. Caenen, A. Swillens, P. Segers, S. Chatelin, C. Papadacci and M. Pernot, 'Experimental study on the effect of the cylindrical vessel geometry on arterial shear wave elastography', in *IEEE International Ultrasonics Symposium (IUS) 2015*, IEEE, pp. 1–4.

[26] D. A. Shcherbakova, C. Papadacci, A. Swillens, A. Caenen, S. De Bock, V. Saey, K. Chiers, M. Tanter, S. E. Greenwald, M. Pernot and P. Segers, 'Supersonic shear wave imaging to assess arterial nonlinear behavior and anisotropy: Proof of principle via ex vivo testing of the horse aorta', *Advances in Mechanical Engineering*, vol. 6, pp. 1–12, 2014.

[27] D. Shcherbakova, A. Swillens, A. Caenen, S. De Bock, P. Segers, C. Papadacci, M. Tanter, M. Pernot, V. Saey and K. Chiers, 'Supersonic shear wave imaging to assess arterial anisotropy: Ex-vivo testing of the horse aorta', in *IEEE International Ultrasonics Symposium (IUS) 2013*, IEEE, pp. 1545–1548.

[28] J. Ophir, S. Alam, B. Garra, F. Kallel, E. Konofagou, T. Krouskop and R. Varghese, 'Elastography: Ultrasonic estimation and imaging of the elastic properties of tissues', *Journal of Engineering in Medicine*, vol. 213, pp. 203–233, 1999.

[29] M. M. Doyley and K. J. Parker, 'Elastography: General principles and clincial applications', *Ultrasound Clin*, vol. 9, no. 1, pp. 1–11, 2014.

[30] R. M. Lerner, K. J. Parker, J. Holen, R. Gramiak and R. C. Waag, 'Sono-elasticity: Medical elasticity images derived from ultrasound signals in mechanically vibrated targets', in *Acoust Imaging*, K. L. W., Ed. 1991, vol. 16.

[31] L. Gao, K. J. Parker, R. Lerner and S. Levinson, 'Imaging of the elastic properties of tissue - a review', *Ultrasound Med Biol*, vol. 22, no. 8, pp. 959–977, 1996.

[32] J. Ophir, I. Céspedes, H. Ponnekanti, Y. Yazdi and X. Li, 'Elastography: A quantitative method for imaging the elasticity of biological tissues', *Ultrason Imaging*, vol. 13, pp. 111–134, 1991.

[33] B. Garra, 'Tissue elasticity imaging using ultrasound', *Applied Radiology*, pp. 24–30, 2011.

[34] J. L. Gennisson, T. Deffieux, M. Fink and M. Tanter, 'Ultrasound elastography: Principles and techniques', *Diagn Interv Imaging*, vol. 94, no. 5, pp. 487–95, 2013.

[35] J. F. Greenleaf, M. Fatemi and M. Insana, 'Selected methods for imaging elastic properties of biological tissues', *Annu Rev Biomed Eng*, vol. 5, pp. 57–78, 2003.

[36] Y. K. Mariappan, K. J. Glaser and R. L. Ehman, 'Magnetic resonance elastography: A review', *Clin Anat*, vol. 23, no. 5, pp. 497–511, 2010.

[37] U. Bae, D. Manjiri, T. Dubinsky, S. Minoshima, S. V. and Y. Kim, 'Ultrasound thyroid elastography using carotid artery pulsation', *J Ultrasound Med*, vol. 26, pp. 797–805, 2007.

[38] H. Kanai, 'Propagation of spontaneously actuated pulsive vibration in human heart wall and in vivo viscoelasticity estimation.' *IEEE Trans Ultrason Ferroelectr Freq Control*, vol. 52, no. 11, pp. 1931–42, 2005.

[39] J. Mai and M. Insana, 'Strain imaging of internal deformation', *J Ultrasound Med*, vol. 28, no. 11/12, pp. 1475–1484, 2002.

[40] T. L. Szabo, 'Diagnostic Ultrasound Imaging: Inside Out'. Elsevier Academic Press, 2004.

[41] S. Cournane, A. J. Fagan and J. E. Browne, 'Review of ultrasound elastography quality control and training test phantoms', *Ultrasound*, vol. 20, no. 1-2, 2012.

[42] O. V. Rudenko, A. P. Sarvazyan and S. Y. Emelianov, 'Acoustic radiation force and streaming induced by focused nonlinear ultrasound in a dissipative medium', *J Acoust Soc Am*, vol. 99, no. 5, pp. 2791–2798, 1995.

[43] A. P. Sarvazyan, O. V. Rudenko, S. D. Swanson, J. B. Fowlkes and S. Y. Emelianov, 'Shear wave elasticity imaging: A new ultrasonics technology of medical diagnostics', *Ultrasound Med Biol*, vol. 24, no. 9, pp. 1419–1435, 1998.

[44] M. L. Palmeri, M. H. Wang, J. J. Dahl, K. D. Frinkley and K. R. Nightingale, 'Quantifying hepatic shear modulus in vivo using acoustic radiation force', *Ultrasound Med Biol*, vol. 34, no. 4, pp. 546–58, 2008.

[45] R. J. Dickinson and C. R. Hill, 'Measurement of soft tissue motion using correlation between a-scans', *Ultrasound Med Biol*, vol. 8, no. 3, pp. 263–271, 1982.

[46] A. Tang, G. Cloutier, N. M. Szeverenyi and C. B. Sirlin, 'Ultrasound elastography and mr elastography for assessing liver fibrosis: Part 1, principles and techniques', *AJR Am J Roentgenol*, vol. 205, no. 1, pp. 22–32, 2015.

[47] C. L. De Korte, E. I. Cespedes, A. F. Van der Steen, G. Pasterkamp and N. Bom, 'Intravascular ultrasound elastography: Assessment and imaging of elastic properties of diseased arteries and vulnerable plaque', *European Journal Of Ultrasound*, vol. 4, pp. 219–224, 1998.

[48] J. D'Hooge, B. Bijnens, J. Thoen, F. Van de Werf, G. R. Sutherland and P. Suetens, 'Echocardiographic strain and strain-rate imaging: A new tool to study regional myocardial function', *IEEE Trans Med Imaging*, vol. 21, no. 9, pp. 1022–30, 2002.

[49] K. Nightingale, 'Acoustic radiation force impulse (arfi) imaging: A review', *Curr Med Imaging Rev*, vol. 7, no. 4, pp. 328–339, 2011.

[50] E. E. Konofagou, C. Maleke and J. Vappou, 'Harmonic motion imaging (hmi) for tumor imaging and treatment monitoring', *Curr Med Imaging Rev*, vol. 8, no. 1, pp. 16–26, 2012.

[51] W. F. Walker, F. J. Fernandez and L. A. Negron, 'Method of imaging viscoelastic parameters with acoustic radiation force', *Phys Med Biol*, vol. 45, pp. 1437–1447, 2000.

[52] M. W. Urban, S. Chen and M. Fatemi, 'A review of shearwave dispersion ultrasound vibrometry (sduv) and its applications', *Curr Med Imaging Rev*, vol. 8, no. 1, pp. 27–36, 2012.

[53] Q. Wang, Y.-C. Ahn, C. Kim, L. Yu, W. Jia, B. Rao, Z. Chen and H. K. Chiang, 'Thermoelastic optical dopler tomography of biological tissues', *Proceeding SPIE*, 2008.

[54] J. Bercoff, M. Tanter and M. Fink, 'Supersonic shear imaging: A new technique for soft tissue elasticity mapping', *IEEE Trans Ultrason Ferroelectr Freq Control*, vol. 51, no. 4, pp. 396–409, 2004.

[55] X. Liang, M. Orescanin, K. S. Toohey, M. F. Insana and S. A. Boppart, 'Acoustomotive optical coherence elastography for measuring material mechanical properties', *Optics Letter*, vol. 34, no. 19, pp. 2894–2896, 2009.

[56] R. Muthupillai, P. J. Rossman, D. J. Lomas, J. F. Greenleaf, S. J. Riederer and R. L. Ehman, 'Magnetic resonance imaging of transverse acoustic strain waves', *Magn Reson Med*, vol. 36, no. 2, pp. 266–274, 1995.

[57] L. Sandrin, B. Fourquet, J.-M. Hasquenoph, S. Yon, C. Fournier, F. Mal, C. Christidis, M. Ziol, B. Poulet, F. Kazemi, M. Beaugrand and R. Palau, 'Transient elastography: A new noninvasive method for assessment of hepatic fibrosis', *Ultrasound Med Biol*, vol. 29, no. 12, pp. 1705–1713, 2003.

[58] L. Gao, K. J. Parker and S. Alam, 'Sonoelasticity imaging: Theory and experimental verification', *J Acoust Soc Am*, vol. 97, no. 6, pp. 3875–86, 1995.

[59] S. K. Venkatesh and R. L. Ehman, 'Magnetic Resonance Elastography'. New York: Springer, 2014.

[60] S. A. Kruse, G. H. Rose, K. J. Glaser, A. Manduca, J. P. Felmlee, C. R. Jack Jr. and R. L. Ehman, 'Magnetic resonance elastography of the brain', *Neuroimage*, vol. 39, p. 1, 2008.

[61] P. N. Wells and H. D. Liang, 'Medical ultrasound: Imaging of soft tissue strain and elasticity', *J R Soc Interface*, vol. 8, no. 64, pp. 1521–49, 2011.

[62] B. F. Kennedy, P. Wijesinghe and D. D. Sampson, 'The emergence of optical elastography in biomedicine', *Nature Photonics*, vol. 11, no. 4, pp. 215–221, 2017.

[63] S. Wang and K. V. Larin, 'Optical coherence elastography for tissue characterization: A review', *J Biophotonics*, vol. 8, no. 4, pp. 279–302, 2015.

[64] J. Ophir, B. Garra, F. Kallel, E. Konofagou, T. Krouskop, R. Righetti and R. Varghese, 'Elastographic imaging', *Ultrasound Med Biol*, vol. 26, no. Supplement 1, S23–S29, 2000.

[65] J. Bercoff, M. Tanter, M. Muller and M. Fink, 'The role of viscosity in the impulse diffraction field of elastic waves induced by the acoustic radiation force', *IEEE Trans Ultrason Ferroelectr Freq Control*, vol. 51, no. 11, pp. 1523–1536, 2004.

[66] R. Sinkus, M. Tanter, S. Catheline, J. Lorenzen, C. Kuhl, E. Sondermann and M. Fink, 'Imaging anisotropic and viscous properties of breast tissue by magnetic resonance-elastography', *Magn Reson Med*, vol. 53, no. 2, pp. 372–87, 2005.

[67] S. Chen, W. Sanchez, M. R. Callstrom, B. Gorman, J. T. Lewis, S. O. Sanderson, J. F. Greenleaf, H. Xie, M. Shi Y. Pashley, M. Shamdasani, M. Lachman and S. Metz, 'Assessment of liver viscoelasticity by using shear waves induced by ultrasound radiation force', *Radiology*, vol. 266, no. 3, pp. 964–970, 2013.

[68] O. A. Smiseth, H. Torp, A. Opdahl, K. H. Haugaa and S. Urheim, 'Myocardial strain imaging: How useful is it in clinical decision making?', *Eur Heart J*, vol. 37, no. 15, pp. 1196–207, 2016.

[69] Y. Li and J. G. Snedeker, 'Elastography: Modality-specific approaches, clinical applications, and research horizons', *Skeletal Radiol*, vol. 40, no. 4, pp. 389–97, 2011.

[70] A. P. Sarvazyan, T. J. Hall, M. W. Urban, M. Fatemi, S. R. Aglyamov and B. Garra, 'An overview of elastography - an emerging branch of medical imaging', *Curr Med Imaging Rev*, vol. 7, pp. 255–282, 2011.

[71] R. M. S. Sigrist, J. Liau, A. E. Kaffas, M. C. Chammas and J. K. Willmann, 'Ultrasound elastography: Review of techniques and clinical applications', *Theranostics*, vol. 7, no. 5, pp. 1303–1329, 2017.

[72] D. Cosgrove, R. Barr, J. Bojunga, V. Cantisani, M. C. Chammas, M. Dighe, S. Vinayak, J. M. Xu and C. F. Dietrich, 'Wfumb guidelines and recommendations on the clinical use of ultrasound elastography: Part 4. thyroid', *Ultrasound Med Biol*, vol. 43, no. 1, pp. 4–26, 2017.

[73] R. G. Barr, D. Cosgrove, M. Brock, V. Cantisani, J. M. Correas, A. W. Postema, G. Salomon, M. Tsutsumi, H. X. Xu and C. F. Dietrich, 'Wfumb guidelines and recommendations on the clinical use of ultrasound elastography: Part 5. prostate', *Ultrasound Med Biol*, vol. 43, no. 1, pp. 27–48, 2017.

[74] G. Ferraioli, C. Filice, L. Castera, B. I. Choi, I. Sporea, S. R. Wilson, D. Cosgrove, C. F. Dietrich, D. Amy, J. C. Bamber, R. Barr, Y. H. Chou, H. Ding, A. Farrokh, M. Friedrich-Rust, T. J. Hall, K. Nakashima, K. R. Nightingale, M. L. Palmeri, F. Schafer, T. Shiina, S. Suzuki and M. Kudo, 'Wfumb guidelines and recommendations for clinical use of ultrasound elastography: Part 3: Liver', *Ultrasound Med Biol*, vol. 41, no. 5, pp. 1161–79, 2015.

[75] R. G. Barr, K. Nakashima, D. Amy, D. Cosgrove, A. Farrokh, F. Schafer, J. C. Bamber, L. Castera, B. I. Choi, Y. H. Chou, C. F. Dietrich, H. Ding, G. Ferraioli, C. Filice, M. Friedrich-Rust, T. J. Hall, K. R. Nightingale, M. L. Palmeri, T. Shiina, S. Suzuki, I. Sporea, S. Wilson and M. Kudo, 'Wfumb guidelines and recommendations for clinical use of ultrasound elastography: Part 2: Breast', *Ultrasound Med Biol*, vol. 41, no. 5, pp. 1148–60, 2015.

[76] U. Zaleska-Dorobisz, K. Kaczorowski, A. Pawlus, A. Puchalska and M. Inglot, 'Ultrasound elastography - review of techniques and its clinical applications', *Adv Clin Exp Med*, vol. 23, no. 4, pp. 645–655, 2014.

[77] A. Huber, L. Ebner, J. T. Heverhagen and A. Christe, 'State-of-the-art imaging of liver fibrosis and cirrhosis: A comprehensive review of current applications and future perspectives', *Eur J Radiol Open*, vol. 2, pp. 90–100, 2015.

[78] P. Ricci, E. Maggini, E. Mancuso, P. Lodise, V. Cantisani and C. Catalano, 'Clinical application of breast elastography: State of the art', *Eur J Radiol*, vol. 83, no. 3, pp. 429–37, 2014.

[79] H. M. Wang, 'Shear wave imaging using acoustic radiation force', Thesis, 2013.

[80] J. R. Doherty, D. M. Dumont, G. E. Trahey and M. L. Palmeri, 'Acoustic radiation force impulse imaging of vulnerable plaques: A finite element method parametric analysis', *J Biomech*, vol. 46, no. 1, pp. 83–90, 2013.

[81] K. Nightingale, M. S. Soo, R. Nightingale and G. Trahey, 'Acoustic radiation force impulse imaging: In vivo demonstration of clinical feasibility', *Ultrasound Med Biol*, vol. 28, no. 2, pp. 227–235, 2002.

[82] S. A. McAleavey, M. G. Menon and J. Orszulak, 'Shear-modulus estimation by application of spatially-modulated impulsive acoustic radiation force', *Ultrason Imaging*, vol. 29, pp. 87–104, 2007.

[83] P. Song, H. Zhao, A. Manduca, M. W. Urban, J. F. Greenleaf and S. Chen, 'Comb-push ultrasound shear elastography (cuse): A novel method for two-dimensional shear elasticity imaging of soft tissues', *IEEE Trans Med Imaging*, vol. 31, no. 9, pp. 1821–32, 2012.

[84] S. Chen, M. W. Urban, C. Pislaru, R. R. Kinnick, Y. Zheng, A. Yao and J. F. Greenleaf, 'Shearwave dispersion ultrasound vibrometry (sduv) for measuring tissue elasticity and viscosity', *IEEE Trans Ultrason Ferroelectr Freq Control*, vol. 56, no. 1, pp. 55–62, 2009.

[85] Z. Hah, C. Hazard, Y. Cho, D. Rubens and K. J. Parker, 'Crawling waves from radiation force excitation', *Ultrason Imaging*, vol. 32, pp. 177–189, 2010.

[86] R. S. C. Cobbold, 'Foundations of Biomedical Ultrasound'. Oxford University Press, 2002.

[87] A. P. Sarvazyan, O. V. Rudenko and W. L. Nyborg, 'Biomedical applications of radiation force of ultrasound: Historical roots and physical basis', *Ultrasound Med Biol*, vol. 36, no. 9, pp. 1379–94, 2010.

[88] M. L. Palmeri and K. R. Nightingale, 'Acoustic radiation force-based elasticity imaging methods', *Interface Focus*, vol. 1, no. 4, pp. 553–64, 2011.

[89] R. Mortimer, 'Physical Chemistry - 2nd Edition'. San Diego, CA: Academic Press, 2000.

[90] K. Nightingale and M. Palmeri, *Elasticity imaging - methods and applications*, Personal Communication, 2014.

[91] M. Tanter and M. Fink, 'Ultrafast imaging in biomedical ultrasound', *IEEE Trans Ultrason Ferroelectr Freq Control*, vol. 61, no. 1, pp. 102–119, 2014.

[92] K. Nightingale, S. A. McAleavey and G. Trahey, 'Shear wave generation using acoustic radiation force - in vivo and ex vivo results', *Ultrasound Med Biol*, vol. 29, no. 12, pp. 1715–1723, 2003.

[93] J. J. Dahl, G. F. Pinton, M. Palmeri, V. Agrawal, K. Nightingale and G. Trahey, 'A parallel tracking method for acoustic radiation force impulse imaging', *IEEE Trans Ultrason Ferroelectr Freq Control*, vol. 54, no. 2, pp. 301–312, 2007.

[94] N. Rouze, H. M. Wang, M. Palmeri and K. Nightingale, 'Robust estimation of time of flight shear wave speed using a radon sum transformation', *IEEE Trans Ultrason Ferroelectr Freq Control*, vol. 57, no. 12, pp. 2662–2670, 2010.

[95] P. Song, M. C. Macdonald, R. H. Behler, J. D. Lanning, H. M. Wang, M. W. Urban, A. Manduca, H. Zhao, M. R. Callstrom, A. Alizad, J. F. Greenleaf and S. Chen, 'Two-dimensional shear wave elastography on conventional ultrasound scanners with time aligned sequential tracking (tast) and comb-push ultrasound shear elastography', *IEEE Trans Ultrason Ferroelectr Freq Control*, vol. 62, no. 2, pp. 290–302, 2015.

[96] P. Song, 'Innovations in ultrasound shear wave elastography', Thesis, 2014.

[97] J. Bercoff, 'Ultrafast Ultrasound Imaging', ser. Ultrasound Imaging - Medical Applications. Intech, 2011.

[98] G. Montaldo, M. Tanter, J. Bercoff, N. Benech and M. Fink, 'Coherent plane-wave compounding for very high frame rate ultrasonography and transient elastography', *IEEE Trans Ultrason Ferroelectr Freq Control*, vol. 56, no. 3, pp. 489–506, 2009.

[99] L. Sandrin, M. Tanter, S. Catheline and M. Fink, 'Shear modulus imaging with 2-d transient elastography', *IEEE Trans Ultrason Ferroelectr Freq Control*, vol. 49, no. 4, pp. 426–435, 2002.

[100] C. Papadacci, M. Pernot, M. Couade, M. Fink and M. Tanter, 'High contrast ultrafast imaging of the human heart', *IEEE Trans Ultrason Ferroelectr Freq Control*, vol. 61, no. 2, pp. 288–301, 2014.

[101] M. Cikes, L. Tong, G. R. Sutherland and J. D'Hooge, 'Ultrafast cardiac ultrasound imaging: Technical principles, applications, and clinical benefits', *JACC Cardiovasc Imaging*, vol. 7, no. 8, pp. 812–23, 2014.

[102] Y. Deng, N. C. Rouze, M. L. Palmeri and K. R. Nightingale, 'Ultrasonic shear wave elasticity imaging (swei) sequencing and data processing using a verasonics research scanner', *IEEE Trans Ultrason Ferroelectr Freq Control*, pp. 1–1, 2017.

[103] C. Kasai, K. Namekawa, A. Koyano and R. Omoto, 'Real-time two-dimensional blood flow imaging using an autocorrelation technique', *IEEE Trans Sonics Ultrasonics*, vol. SU-32, no. 3, pp. 458–464, 1985.

[104] T. Loupas, J. T. Powers and R. W. Gill, 'An axial velocity estimator for ultrasound blood flow imaging based on full evaluation of the doppler equation by means of a 2d autocorrelation approach', *IEEE Trans Ultrason Ferroelectr Freq Control*, vol. 42, no. 4, pp. 672–688, 1995.

[105] T. A. Krouskop, D. R. Dougherty and F. S. Vinson, 'A pulsed doppler ultrasonic system for making noninvasive measurements of the mechanical properties of soft tissue', *Journal of Rehabilitation Research and Development*, vol. 24, no. 2, pp. 1–8, 1987.

[106] G. F. Pinton, J. J. Dahl and G. Trahey, 'Rapid tracking of small displacements with ultrasound', *IEEE Trans Ultrason Ferroelectr Freq Control*, vol. 53, no. 6, pp. 1103–1117, 2006.

[107] F. A. Duck, 'Medical and non-medical protection standards for ultrasound and infrasound', *Prog Biophys Mol Biol*, vol. 93, no. 1-3, pp. 176–91, 2007.

[108] M. Palmeri, K. D. Frinkley and K. Nightingale, 'Experimental studies of the thermal effects associated with radiation force imaging of soft tissue', *Ultrason Imaging*, vol. 26, pp. 100–114, 2004.

[109] FDA, *Information for manufacturers seeking marketing clearance of diagnostic ultrasound systems and transducers*, Government Document, 2008.

[110] M. G. Menon, 'Resolution estimation and bias reduction in acoustic radiation force impulse imaging', Thesis, 2010.

[111] C. C. Church, C. Labuda and K. Nightingale, 'Should the mechanical index be revised for arfi imaging?', *IEEE Int Ultrason Symp*, vol. 2012, pp. 17–20, 2012.

[112] M. L. Palmeri and K. R. Nightingale, 'What challenges must be overcome before ultrasound elasticity imaging is ready for the clinic?', *Imaging Med*, vol. 3, no. 4, pp. 433–444, 2011.

[113] S. Dokos, 'Modeling Organs, Tissues, Cells and Devices'. Springer, 2017.

[114] J. Ophir, S. Alam, B. Garra, F. Kallel, E. Konofagou, T. Krouskop, C. R. B. Merritt, R. Righetti, R. Souchon, S. Srinivasan and T. Varghese, 'Elastography: Imaging the elastic properties of soft tissues with ultrasound', *J Med Ultrasonics*, vol. 29, pp. 155–171, 2002.

[115] A. Sarvazyan, 'Elastic properties of soft tissues', *Handbook of elastic properties of solids, liquids and gases*, vol. 3, pp. 107–127, 2001.

[116] R. J. van Sloun, R. R. Wildeboer, H. Wijkstra and M. Mischi, 'Viscoelasticity mapping by identification of local shear wave dynamics', *IEEE Trans Ultrason Ferroelectr Freq Control*, 2017.

[117] M. Wang, B. Byram, M. Palmeri, N. Rouze and K. Nightingale, 'Imaging transverse isotropic properties of muscle by monitoring acoustic radiation force induced shear waves using a 2-d matrix ultrasound array', *IEEE Trans Med Imaging*, vol. 32, no. 9, pp. 1671–84, 2013.

[118] B. Qiang, J. C. Brigham, S. Aristizabal, J. F. Greenleaf, X. Zhang and M. W. Urban, 'Modeling transversely isotropic, viscoelastic, incompressible tissue-like materials with application in ultrasound shear wave elastography', *Phys Med Biol*, vol. 60, no. 3, pp. 1289–306, 2015.

[119] J. Brum, M. Bernal, J. Gennisson and M. Tanter, 'In vivo evaluation of the elastic anisotropy of the human achilles tendon using shear wave dispersion analysis', *Phys Med Biol*, vol. 59, no. 3, p. 505, 2014.

[120] J. McLaughlin and D. Renzi, 'Shear wave speed recovery in transient elastography and supersonic imaging using propagating fronts', *Inverse Problems*, vol. 22, no. 2, pp. 681–706, 2006.

[121] K. Hoyt, K. J. Parker and D. J. Rubens, 'Real-time shear velocity imaging using sonoelastographic techniques', *Ultrasound Med Biol*, vol. 33, no. 7, pp. 1086–1097, 2007.

[122] M. H. Wang, M. L. Palmeri, V. M. Rotemberg, N. C. Rouze and K. R. Nightingale, 'Improving the robustness of time-of-flight based shear wave speed reconstruction methods using ransac in human liver in vivo', *Ultrasound Med Biol*, vol. 36, no. 5, pp. 802–13, 2010.

[123] J. L. Rose, 'Ultrasonic guided waves in solid media'. New York: Cambridge University Press, 2014.

[124] T. Deffieux, G. Montaldo, M. Tanter and M. Fink, 'Shear wave spectroscopy for in vivo quantification of human soft tissues visco-elasticity', *IEEE Trans Med Imaging*, vol. 28, no. 3, pp. 313–22, 2009.

[125] M. Couade, M. Pernot, C. Prada, E. Messas, J. Emmerich, P. Bruneval, A. Criton, M. Fink and M. Tanter, 'Quantitative assessment of arterial wall biomechanical properties using shear wave imaging', *Ultrasound Med Biol*, vol. 36, no. 10, pp. 1662–76, 2010.

[126] S. L. Lipman, N. C. Rouze, M. L. Palmeri and K. R. Nightingale, 'Impact of acoustic radiation force excitation geometry on shear wave dispersion and attenuation estimates', *Ultrasound Med Biol*, 2018.

[127] E. Budelli, J. Brum, M. Bernal, T. Deffieux, M. Tanter, P. Lema, C. Negreira and J.-L. Gennisson, 'A diffraction correction for storage and loss moduli imaging using radiation force based elastography', *Phys Med Biol*, vol. 62, no. 1, p. 91, 2017.

[128] E. Maksuti, F. Bini, S. Fiorentini, G. Blasi, M. W. Urban, F. Marinozzi and M. Larsson, 'Influence of wall thickness and diameter on arterial shear wave elastography: A phantom and finite element study', *Phys Med Biol*, vol. 62, no. 7, pp. 2694–2718, 2017.

[129] I. Nenadic, M. W. Urban, B. Qiang, S. Chen and J. Greenleaf, 'Model-free quantification of shear wave velocity and attenuation in tissues and its in vivo application', *J Acoust Soc Am*, vol. 134, no. 5, pp. 4011–4011, 2013.

[130] I. Z. Nenadic, B. Qiang, M. W. Urban, H. Zhao, W. Sanchez, J. F. Greenleaf and S. Chen, 'Attenuation measuring ultrasound shearwave elastography and in vivo application in post-transplant liver patients', *Phys Med Biol*, vol. 62, no. 2, pp. 484–500, 2017.

[131] N. C. Rouze, M. L. Palmeri and K. R. Nightingale, 'An analytic, fourier domain description of shear wave propagation in a viscoelastic medium using asymmetric gaussian sources', *J Acoust Soc Am*, vol. 138, no. 2, pp. 1012–1022, 2015.

[132] E. Widman, E. Maksuti, D. Larsson, M. W. Urban, A. Bjallmark and M. Larsson, 'Shear wave elastography plaque characterization with mechanical testing validation: A phantom study', *Phys Med Biol*, vol. 60, no. 8, pp. 3151–74, 2015.

[133] I. Z. Nenadic, M. W. Urban, S. A. Mitchell and J. F. Greenleaf, 'Lamb wave dispersion ultrasound vibrometry (lduv) method for quantifying mechanical properties of viscoelastic solids', *Phys Med Biol*, vol. 56, no. 7, pp. 2245–64, 2011.

[134] M. W. Urban, C. Pislaru, I. Z. Nenadic, R. R. Kinnick and J. F. Greenleaf, 'Measurement of viscoelastic properties of in vivo swine myocardium using lamb wave dispersion ultrasound vibrometry (lduv)', *IEEE Trans Med Imaging*, vol. 32, no. 2, pp. 247–61, 2013.

[135] R. Marks, A. Clarke, C. Featherston, C. Paget and R. Pullin, 'Lamb wave interaction with adhesively bonded stiffeners and disbonds using 3d vibrometry', *Applied Sciences*, vol. 6, no. 1, p. 12, 2016.

[136] M. Bernal, I. Nenadic, M. W. Urban and J. F. Greenleeaf, 'Material property estimation for tubes and arteries using ultrasound radiation force and analysis of propagating modes', *J Acoust Soc Am*, vol. 129, no. 3, pp. 1344–1354, 2011.

[137] M. Balda, *Lmfnlsq - solution of non-linear least squares*, Online Multimedia, 2012.

[138] B. Pavlakovic, M. Lowe, D. Alleyne and P. Cawley, 'Disperse: A general purpose program for creating dispersion curves', in *Review of progress in quantitative nondestructive evaluation*. Springer, 1997, pp. 185–192.

[139] M. Doyley, 'Model-based elastography: A survey of approaches to the inverse elasticity problem', *Phys Med Biol*, vol. 57, no. 3, R35, 2012.

[140] N. C. Rouze, M. H. Wang, M. L. Palmeri and K. R. Nightingale, 'Finite element modeling of impulsive excitation and shear wave propagation in an incompressible, transversely isotropic medium', *J Biomech*, vol. 46, no. 16, pp. 2761–8, 2013.

[141] M. Palmeri, Y. Deng, N. Rouze and K. Nightingale, 'Dependence of shear wave spectral content on acoustic radiation force excitation duration and spatial beamwidth', *IEEE Trans Ultrason Ferroelectr Freq Control*, 2014.

[142] K. R. Nightingale, N. C. Rouze, S. J. Rosenzweig, M. H. Wang, M. F. Abdelmalek, C. D. Guy and M. L. Palmeri, 'Derivation and analysis of viscoelastic properties in human liver: Impact of frequency on fibrosis and steatosis staging', *IEEE Trans Ultrason Ferroelectr Freq Control*, vol. 62, no. 1, pp. 165–75, 2015.

[143] M. W. Urban, I. Z. Nenadic, S. Chen and J. F. Greenleaf, 'Discrepancies in reporting tissue material properties', *J Ultrasound Med*, vol. 32, no. 5, pp. 886–888, 2013.

[144] I. Z. Nenadic, B. Qiang, M. W. Urban, L. H. de Araujo Vasconcelo, A. Nabavizadeh, A. Alizad, J. F. Greenleaf and M. Fatemi, 'Ultrasound bladder vibrometry method for measuring viscoelasticity of the bladder wall', *Phys Med Biol*, vol. 58, no. 8, pp. 2675–95, 2013.

[145] N. C. Rouze, Y. Deng, M. L. Palmeri and K. R. Nightingale, 'Robust characterization of viscoelastic materials from measurements of group shear wave speeds', in *IEEE International Ultrasonics Symposium (IUS) 2016*, IEEE, pp. 1–4.

[146] L. Sandrin, D. Cassereau and M. Fink, 'The role of the coupling term in transient elastography', *J Acoust Soc Am*, vol. 115, no. 1, pp. 73–83, 2004.

[147] S. Chatelin, J. L. Gennisson, M. Bernal, M. Tanter and M. Pernot, 'Modelling the impulse diffraction field of shear waves in transverse isotropic viscoelastic medium', *Phys Med Biol*, vol. 60, no. 9, pp. 3639–54, 2015.

[148] M. Palmeri, S. A. McAleavey, G. Trahey and K. Nightingale, 'Ultrasonic tracking of acoustic radiation force-induced displacements in homogeneous media', *IEEE Trans Ultrason Ferroelectr Freq Control*, vol. 53, no. 7, pp. 1300–1313, 2006.

[149] Y. Lee, W. Y. Lee, C. E. Lim, J. H. Chang, T. K. Song and Y. Yoo, 'Compounded direct pixel beamforming for medical ultrasound imaging', *IEEE Trans Ultrason Ferroelectr Freq Control*, vol. 59, no. 3, pp. 573–82, 2012.

[150] R. R. Bouchard, D. T. Hsu, P. D. Wolf and G. Trahey, 'In vivo cardiac, acoustic-radiation-force-driven, shear wave velocimetry', *Ultrason Imaging*, vol. 31, no. 3, pp. 201–213, 2009.

[151] W. Kwiecinski, F. Bessiere, E. C. Colas, W. A. N'Djin, M. Tanter, C. Lafon and M. Pernot, 'Cardiac shear-wave elastography using a transesophageal transducer: Application to the mapping of thermal lesions in ultrasound transesophageal cardiac ablation', *Phys Med Biol*, vol. 60, no. 20, pp. 7829–46, 2015.

[152] P. Song, H. Zhao, M. W. Urban, A. Manduca, S. V. Pislaru, R. R. Kinnick, C. Pislaru and S. Chen, 'Improved shear wave motion detection using pulse-inversion harmonic imaging with phased array transducer', *IEEE Trans Med Imaging*, vol. 32, no. 12, pp. 2299–2310, 2013.

[153] S. J. Hsu, R. R. Bouchard, D. M. Dumont, P. D. Wolf and G. Trahey, 'In vivo assessment of myocardial stiffness with acoustic radiation force impulse imaging', *Ultrasound Med Biol*, vol. 33, no. 11, pp. 1706–1716, 2007.

[154] E. N. Marieb and K. Hoehn, 'Anatomy and physiology', 4th. San Francisco, USA: Pearson Education, 2011.

[155] R. M. Lang, M. Bierig, R. B. Devereux, F. A. Flachskampf, E. Foster, P. A. Pellikka, M. H. Picard, M. J. Roman, J. Seward and J. Shanewise, 'Recommendations for chamber quantification', *European journal of echocardiography*, vol. 7, no. 2, pp. 79–108, 2006.

[156] L. G. Rudski, W. W. Lai, J. Afilalo, L. Hua, M. D. Handschumacher, K. Chandrasekaran, S. D. Solomon, E. K. Louie and N. B. Schiller, 'Guidelines for the echocardiographic assessment of the right heart in adults: A report from the american society of echocardiography', *J Am Soc Echocardiogr*, vol. 23, no. 7, pp. 685–713, 2010.

[157] T. Traill, D. Gibson and D. Brown, 'Study of left ventricular wall thickness and dimension changes using echocardiography', *British heart journal*, vol. 40, no. 2, p. 162, 1978.

[158] R. Prakash, 'Determination of right ventricular wall thickness in systole and diastole. echocardiographic and necropsy correlation in 32 patients', *Heart*, vol. 40, no. 11, pp. 1257–1261, 1978.

[159] L. Overbeek, L. Kapusta, P. Peer, C. De Korte, J. Thijssen and O. Daniels, 'New reference values for echocardiographic dimensions of healthy dutch children', *European Journal of Echocardiography*, vol. 7, no. 2, pp. 113–121, 2006.

[160] G. A. Holzapfel and R. W. Ogden, 'Constitutive modelling of passive myocardium: A structurally based framework for material characterization', *Philos Trans A Math Phys Eng Sci*, vol. 367, no. 1902, pp. 3445–75, 2009.

[161] H. Lombaert, J. M. Peyrat, P. Croisille, S. Rapacchi, L. Fanton, F. Cheriet, P. Clarysse, I. Magnin, H. Delingette and N. Ayache, 'Human atlas of the cardiac fiber architecture: Study on a healthy population', *IEEE Trans Med Imaging*, vol. 31, no. 7, pp. 1436–47, 2012.

[162] P. F. Ferreira, P. J. Kilner, L.-A. McGill, S. Nielles-Vallespin, A. D. Scott, S. Y. Ho, K. P. McCarthy, M. M. Haba, T. F. Ismail and P. D. Gatehouse, 'In vivo cardiovascular magnetic resonance diffusion tensor imaging shows evidence of abnormal myocardial laminar orientations and mobility in hypertrophic cardiomyopathy', *Journal of Cardiovascular Magnetic Resonance*, vol. 16, no. 1, p. 87, 2014.

[163] G. Sommer, A. J. Schriefl, M. Andra, M. Sacherer, C. Viertler, H. Wolinski and G. A. Holzapfel, 'Biomechanical properties and microstructure of human ventricular myocardium', *Acta Biomater*, vol. 24, pp. 172–92, 2015.

[164] F. Bailliard and R. H. Anderson, 'Tetralogy of fallot', *Orphanet Journal of Rare Diseases*, vol. 4, no. 1, p. 2, 2009.

[165] G. S. Van Arsdell, G. S. Maharaj, J. Tom, V. K. Rao, J. G. Coles, R. M. Freedom, W. G. Williams and B. W. McCrindle, 'What is the optimal age for repair of tetralogy of fallot?', *Circulation*, vol. 102, no. Supplement 3, pp. III-123-III-129, 2000.

[166] G. Van Arsdell and T. J. Yun, 'An apology for primary repair of tetralogy of fallot', *Semin Thorac Cardiovasc Surg Pediatr Card Surg Annu*, pp. 128–31, 2005.

[167] T. Geva, 'Indications and timing of pulmonary valve replacement after tetralogy of fallot repair', *Semin Thorac Cardiovasc Surg Pediatr Card Surg Annu*, pp. 11–22, 2006.

[168] S. V. Babu-Narayan, P. J. Kilner, W. Li, J. C. Moon, O. Goktekin, P. A. Davlouros, M. Khan, S. Y. Ho, D. J. Pennell and M. A. Gatzoulis, 'Ventricular fibrosis suggested by cardiovascular magnetic resonance in adults with repaired tetralogy of fallot and its relationship to adverse markers of clinical outcome', *Circulation*, vol. 113, no. 3, pp. 405–13, 2006.

[169] P. Munkhammar, M. Carlsson, H. Arheden and E. Pesonen, 'Restrictive right ventricular physiology after tetralogy of fallot repair is associated with fibrosis of the right ventricular outflow tract visualized on cardiac magnetic resonance imaging', *Eur Heart J Cardiovasc Imaging*, vol. 14, no. 10, pp. 978–85, 2013.

[170] K. G. Friedman, D. B. McElhinney, J. Rhodes, A. J. Powell, S. D. Colan, J. E. Lock and D. W. Brown, 'Left ventricular diastolic function in children and young adults with congenital aortic valve disease', *Am J Cardiol*, vol. 111, no. 2, pp. 243–9, 2013.

[171] M. D. Cheitlin, M. Robinowitz, H. McAllister, J. I. Hoffman, S. Bharati and M. Lev, 'The distribution of fibrosis in the left ventricle in congenital aortic stenosis and coarctation of the aorta', *Circulation*, vol. 62, no. 4, pp. 823–830, 1980.

[172] S. Ghonim, I. Voges, P. D. Gatehouse, J. Keegan, M. A. Gatzoulis, P. J. Kilner and S. V. Babu-Narayan, 'Myocardial architecture, mechanics, and fibrosis in congenital heart disease', *Frontiers in Cardiovascular Medicine*, vol. 4, 2017.

[173] J. Powers and F. Kremkau, 'Medical ultrasound systems', *Interface Focus*, vol. 1, no. 4, pp. 477–89, 2011.

[174] G. Seidel and K. Meyer, 'Harmonic imaging - a new method for the sonographic assessment of cerebral perfusion', *European Journal Of Ultrasound*, vol. 14, no. 2-3, pp. 103–113, 2001.

[175] P. Song, X. Bi, D. C. Mellema, A. Manduca, M. W. Urban, S. Chen and J. F. Greenleaf, 'Implementation of shear wave elastography on pediatric cardiac transducers with pulse-inversion harmonic imaging and time-aligned sequential tracking', in *IEEE International Ultrasonics Symposium (IUS) 2015*, IEEE, pp. 1–4.

[176] P. Song, X. Bi, D. C. Mellema, A. Manduca, M. W. Urban, P. A. Pellikka, S. Chen and J. F. Greenleaf, 'Pediatric cardiac shear wave elastography for quantitative assessment of myocardial stiffness: A pilot study in healthy controls', *Ultrasound Med Biol*, vol. 42, no. 8, pp. 1719–29, 2016.

[177] M. Correia, J. Provost, S. Chatelin, O. Villemain, M. Tanter and M. Pernot, 'Ultrafast harmonic coherent compound imaging for high frame rate echocardiography and shear wave elastography', *IEEE Trans Ultrason Ferroelectr Freq Control*, vol. 63, no. 3, pp. 420–431, 2016.

[178] G. L. Burke, R. A. Arcilla, W. S. Culpepper, L. S. Webber, Y. K. Chiang and G. S. Berenson, 'Blood pressure and echocardiographic measures in children: The bogalusa heart study', *Circulation*, vol. 75, no. 1, pp. 106–114, 1987.

[179] J. L. Gennisson, T. Deffieux, E. Mace, G. Montaldo, M. Fink and M. Tanter, 'Viscoelastic and anisotropic mechanical properties of in vivo muscle tissue assessed by supersonic shear imaging', *Ultrasound Med Biol*, vol. 36, no. 5, pp. 789–801, 2010.

[180] H. J. Vos, B. M. van Dalen, I. Heinonen, J. G. Bosch, O. Sorop, D. J. Duncker, A. F. van der Steen and N. de Jong, 'Cardiac shear wave velocity detection in the porcine heart', *Ultrasound Med Biol*, vol. 43, no. 4, pp. 753–764, 2017.

[181] M. Vejdani-Jahromi, M. Nagle, G. E. Trahey and P. D. Wolf, 'Ultrasound shear wave elasticity imaging quantifies coronary perfusion pressure effect on cardiac compliance', *IEEE Trans Med Imaging*, vol. 34, no. 2, pp. 465–73, 2015.

[182] M. Vejdani-Jahromi, J. Freedman, M. Nagle, Y.-J. Kim, G. E. Trahey and P. D. Wolf, 'Quantifying myocardial contractility changes using ultrasound-based shear wave elastography', *J Am Soc Echocardiogr*, vol. 30, no. 1, pp. 90–96, 2017.

[183] M. W. Urban, B. Qiang, P. Song, I. Z. Nenadic, S. Chen and J. F. Greenleaf, 'Investigation of the effects of myocardial anisotropy for shear wave elastography using impulsive force and harmonic vibration', *Phys Med Biol*, vol. 61, no. 1, pp. 365–82, 2016.

[184] M. Pernot, W.-N. Lee, A. Bel, P. Mateo, M. Couade, M. Tanter, B. Crozatier and E. Messas, 'Shear wave imaging of passive diastolic myocardial stiffness: Stunned versus infarcted myocardium', *JACC Cardiovasc Imaging*, vol. 9, no. 9, pp. 1023–1030, 2016.

[185] J. A. Jensen and N. B. Svensen, 'Calculation of pressure fields from arbitrarily shaped, apodized, and excited ultrasound transducers', *IEEE Trans Ultrason Ferroelectr Freq Control*, vol. 39, no. 2, pp. 262–267, 1992.

[186] J. A. Jensen, *Field: A program for simulating ultrasound systems*, Conference Paper, 1996.

[187] M. Fatemi, 'Ultrasound-stimulated vibro-acoustic spectrography', *Science*, vol. 280, no. 5360, pp. 82–85, 1998.

[188] L. Sandrin, S. Catheline, M. Tanter and M. Fink, '2d transient elastography', in *Acoustical Imaging*. Springer, 2002, pp. 485–492.

[189] A. Athanasiou, A. Tardivon, M. Tanter, B. Sigal-Zafrani, J. Bercoff, T. Deffieux, J.-L. Gennisson, M. Fink and S. Neuenschwander, 'Breast lesions: Quantitative elastography with supersonic shear imaging—preliminary results 1', *Radiology*, vol. 256, no. 1, pp. 297–303, 2010.

[190] M. Tozaki, S. Isobe and E. Fukuma, 'Preliminary study of ultrasonographic tissue quantification of the breast using the acoustic radiation force impulse (arfi) technology', *Eur J Radiol*, vol. 80, no. 2, e182–7, 2011.

[191] G. Ferraioli, P. Parekh, A. B. Levitov and C. Filice, 'Shear wave elastography for evaluation of liver fibrosis', *J Ultrasound Med*, vol. 33, no. 2, pp. 197–203, 2014.

[192] M. Tanter, D. Touboul, J. L. Gennisson, J. Bercoff and M. Fink, 'High-resolution quantitative imaging of cornea elasticity using supersonic shear imaging', *IEEE Trans Med Imaging*, vol. 28, no. 12, pp. 1881–93, 2009.

[193] T.-M. Nguyen, M. Couade, J. Bercoff and M. Tanter, 'Assessment of viscous and elastic properties of sub-wavelength layered soft tissues using shear wave spectroscopy: Theoretical framework and in vitro experimental validation', *IEEE Trans Ultrason Ferroelectr Freq Control*, vol. 58, no. 11, pp. 2305–2315, 2011.

[194] M. Palmeri, A. C. Sharma, R. R. Bouchard, R. Nightingale and K. Nightingale, 'A finite-element method model of soft tissue response to impulsive acoustic radiation force', *IEEE Trans Ultrason Ferroelectr Freq Control*, vol. 52, no. 10, 2005.

[195] H. H. Hansen, R. G. Lopata and C. L. de Korte, 'Noninvasive carotid strain imaging using angular compounding at large beam steered angles: Validation in vessel phantoms', *IEEE Trans Med Imaging*, vol. 28, no. 6, pp. 872–80, 2009.

[196] J. Kocbach, 'Finite element modeling of ultrasonic piezoelectric transducers', Thesis, 2000.

[197] H. Cherukuri, 'Dispersion analysis of numerical approximations to plane wave motions in an isotropic elastic solid', *Computational Mechanics*, vol. 25, no. 4, pp. 317–328, 2000.

[198] M. L. Palmeri, 'Imaging the mechanical properties of tissue with ultrasound: An investigation of the response of soft tissue to acoustic radiation force', Thesis, 2005.

[199] P. Dendy and B. Heaton, 'Physics for Diagnostic Radiology'. CRC press, 2012.

[200] C. V. Nielsen, W. Zhang, L. Alves, N. Bay and N. Bay, 'Modeling of thermo-electro-mechanical manufacturing processes: applications in metal forming and resistance welding'. Springer Science and Business Media, 2012.

[201] M. Fathi, A. Holland, F. Ansari and C. Weber, 'Integrated Systems, Design and Technology 2010: Knowledge Transfer in New Technologies'. Springer, 2011.

[202] C. De Korte, E. Cespedes, A. Van der Steen, B. Norder and K. Te Nijenhuis, 'Elastic and acoustic properties of vessel mimicking material for elasticity imaging', *Ultrason Imaging*, vol. 19, no. 2, pp. 112–126, 1997.

[203] S. Sorohan, N. Constantin, M. Gavan and V. Anghel, 'Extraction of dispersion curves for waves propagating in free complex waveguides by standard finite element codes', *Ultrasonics*, vol. 51, no. 4, pp. 503–15, 2011.

[204] D. S. Simulia Corporation, 'Abaqus documentation - version 6.14'. Providence, RI, 2014.

[205] A. Bernard, M. Lowe and M. Deschamps, 'Calculation of dispersion curves in bonded joints using either complex frequency or complex slowness and comparison of the results with the minima of the plane wave reflection coefficients', 1998.

[206] C. Pislaru, M. W. Urban, S. V. Pislaru, R. R. Kinnick and J. F. Greenleaf, 'Viscoelastic properties of normal and infarcted myocardium measured by a multifrequency shear wave method: Comparison with pressure-segment length method', *Ultrasound Med Biol*, vol. 40, no. 8, pp. 1785–95, 2014.

[207] P. Song, A. Manduca, H. Zhao, M. W. Urban, J. F. Greenleaf and S. Chen, 'Fast shear compounding using robust 2-d shear wave speed calculation and multi-directional filtering', *Ultrasound Med Biol*, vol. 40, no. 6, pp. 1343–55, 2014.

[208] S. M. Dusenbery, M. Jerosch-Herold, C. Rickers, S. D. Colan, T. Geva, J. W. Newburger and A. J. Powell, 'Myocardial extracellular remodeling is associated with ventricular diastolic dysfunction in children and young adults with congenital aortic stenosis', *J Am Coll Cardiol*, vol. 63, no. 17, pp. 1778–85, 2014.

[209] D. M. Regen, T. P. Graham, R. K. Wyse, J. Deanfield and R. C. Franklin, 'Left-ventricular cavity dimensions in children with normal and dilated hearts', *Pediatric cardiology*, vol. 9, no. 1, pp. 17–24, 1988.

[210] D. G. Scholz, D. W. Kitzman, P. T. Hagen, D. M. Ilstrup and W. D. Edwards, 'Age-related changes in normal human hearts during the first 10 decades of life. part i (growth): A quantitative anatomic study of 200 specimens from subjects from birth to 19 years old', in *Mayo Clinic Proceedings*, vol. 63, Elsevier, pp. 126–136.

[211] H. H. Hansen, A. E. Saris, N. R. Vaka, M. M. Nillesen and C. L. de Korte, 'Ultrafast vascular strain compounding using plane wave transmission', *J Biomech*, vol. 47, no. 4, pp. 815–23, 2014.

[212] A. C. D.-2. o. P. S. D. 70.01, 'Standard test methods for density and specific gravity (relative density) of plastics by displacement', American Society for Testing and Materials.

[213] D. C. Kamopp, D. L. Margolis and R. C. Rosenberg, 'Appendix: Typical material property values useful in modeling mechanical, acoustic and hydraulic elements', ser. System dynamics: Modeling, Simulation and Control of Mechatronic Systems. John Wiley and Sons, Inc., 2012.

[214] M. B. Drozdz, 'Efficient finite element modelling of ultrasound waves in elastic media', Thesis, 2008.

[215] V. Shutilov, 'Fundamental Physics of Ultrasound'. CRC press, 1988.

[216] M. C. K. Farah, C. R. P. d. Castro, V. M. Moreira, A. d. A. Riso, A. A. B. Lopes and V. D. Aiello, 'The myocardium in tetralogy of fallot: A histological and morphometric study', *Arquivos brasileiros de cardiologia*, vol. 92, no. 3, pp. 169–177, 2009.

[217] C. N. Grover, R. E. Cameron and S. M. Best, 'Investigating the morphological, mechanical and degradation properties of scaffolds comprising collagen, gelatin and elastin for use in soft tissue engineering', *Journal of the mechanical behavior of biomedical materials*, vol. 10, pp. 62–74, 2012.

[218] O. Gal, *Ellipse fitting in matlab*, Online Multimedia, 2003.

[219] R. Greenbaum, Y. H. Siew, D. G. Gibson, A. E. Becker and R. H. Anderson, 'Left ventricular fiber architecture in man', *Br Heart J*, vol. 45, pp. 248–263, 1981.

[220] W. N. Lee, B. Larrat, M. Pernot and M. Tanter, 'Ultrasound elastic tensor imaging: Comparison with mr diffusion tensor imaging in the myocardium', *Phys Med Biol*, vol. 57, no. 16, pp. 5075–95, 2012.

[221] W. N. Lee, M. Pernot, M. Couade, E. Messas, P. Bruneval, A. Bel, A. A. Hagege, M. Fink and M. Tanter, 'Mapping myocardial fiber orientation using echocardiography-based shear wave imaging', *IEEE Trans Med Imaging*, vol. 31, no. 3, pp. 554–62, 2012.

[222] G. Sommer, D. Haspinger, M. Andra, M. Sacherer, C. Viertler, P. Regitnig and G. A. Holzapfel, 'Quantification of shear deformations and corresponding stresses in the biaxially tested human myocardium', *Ann Biomed Eng*, vol. 43, no. 10, pp. 2334–48, 2015.

[223] H. Gao, W. Li, L. Cai, C. Berry and X. Luo, 'Parameter estimation in a holzapfel–ogden law for healthy myocardium', *Journal of engineering mathematics*, vol. 95, no. 1, pp. 231–248, 2015.

[224] V. Y. Wang, J. A. Niestrawska, A. J. Wilson, G. B. Sands, A. A. Young, I. J. LeGrice and M. P. Nash, 'Image-driven constitutive modeling of myocardial fibrosis', *International Journal for Computational Methods in Engineering Science and Mechanics*, vol. 17, no. 3, pp. 211–221, 2016.

[225] H. Gao, D. Carrick, C. Berry, B. E. Griffith and X. Luo, 'Dynamic finite-strain modelling of the human left ventricle in health and disease using an immersed boundary-finite element method', *IMA J Appl Math*, vol. 79, no. 5, pp. 978–1010, 2014.

[226] H. M. Wang, X. Y. Luo, H. Gao, R. W. Ogden, B. E. Griffith, C. Berry and T. J. Wang, 'A modified holzapfel-ogden law for a residually stressed finite strain model of the human left ventricle in diastole', *Biomech Model Mechanobiol*, vol. 13, no. 1, pp. 99–113, 2014.

[227] T. J. Hall, A. Milkowski, B. Garra, P. Carson, M. Palmeri, K. Nightingale, T. Lynch, A. Alturki, M. Andre and S. Audiere, 'Rsna/qiba: Shear wave speed as a biomarker for liver fibrosis staging', in *IEEE International Ultrasonics Symposium (IUS) 2013*, IEEE, pp. 397–400.

[228] N. C. Rouze, Y. Deng, M. L. Palmeri and K. R. Nightingale, 'Accounting for the spatial observation window in the 2-d fourier transform analysis of shear wave attenuation', *Ultrasound Med Biol*, vol. 43, no. 10, pp. 2500–2506, 2017.

[229] E. Hsu, A. Muzikant, S. Matulevicius, R. Penland and C. Henriquez, 'Magnetic resonance myocardial fiber-orientation mapping with direct histological correlation', *American Journal of Physiology-Heart and Circulatory Physiology*, vol. 274, no. 5, H1627–H1634, 1998.

[230] D. L. Mann and M. R. Bristow, 'Mechanisms and models in heart failure', *Circulation*, vol. 111, no. 21, pp. 2837–2849, 2005.

[231] A. Becker and G. Caruso, 'Myocardial disarray. a critical review', *Heart*, vol. 47, no. 6, pp. 527–538, 1982.

[232] F. B. C. Cansiz, H. Dal and M. Kaliske, 'An orthotropic viscoelastic material model for passive myocardium: Theory and algorithmic treatment', *Computer Methods in Biomechanics and Biomedical Engineering*, vol. 18, no. 11, pp. 1160–1172, 2015.

[233] M. Tanter, C. Berry, L. Sandrin and M. Fink, 'Ultrafast compound imaging for 2-d motion vector estimation: Application to transient elastography', *IEEE Trans Ultrason Ferroelectr Freq Control*, vol. 49, no. 10, pp. 1363–1374, 2002.

[234] J. R. Doherty, G. E. Trahey, K. R. Nightingale and M. L. Palmeri, 'Acoustic radiation force elasticity imaging in diagnostic ultrasound', *IEEE Trans Ultrason Ferroelectr Freq Control*, vol. 60, no. 4, pp. 685–701, 2013.

[235] J. Bercoff, G. Montaldo, T. Loupas, D. Savery, F. Meziere, M. Fink and M. Tanter, 'Ultrafast compound doppler imaging: Providing full blood flow characterization', *IEEE Trans Ultrason Ferroelectr Freq Control*, vol. 58, no. 1, pp. 134–147, 2011.

[236] O. Couture, S. Bannouf, G. Montaldo, J. F. Aubry, M. Fink and M. Tanter, 'Ultrafast imaging of ultrasound contrast agents', *Ultrasound Med Biol*, vol. 35, no. 11, pp. 1908–16, 2009.

[237] E. Mace, G. Montaldo, B. F. Osmanski, I. Cohen, M. Fink and M. Tanter, 'Functional ultrasound imaging of the brain: Theory and basic principles', *IEEE Trans Ultrason Ferroelectr Freq Control*, vol. 60, no. 3, pp. 492–506, 2013.

[238] M. Tanter, J. Bercoff, A. Athanasiou, T. Deffieux, J. L. Gennisson, G. Montaldo, M. Muller, A. Tardivon and M. Fink, 'Quantitative assessment of breast lesion viscoelasticity: Initial clinical results using supersonic shear imaging', *Ultrasound Med Biol*, vol. 34, no. 9, pp. 1373–86, 2008.

[239] E. Widman, E. Maksuti, C. Amador, M. W. Urban, K. Caidahl and M. Larsson, 'Shear wave elastography quantifies stiffness in ex vivo porcine artery with stiffened arterial region', *Ultrasound Med Biol*, vol. 42, no. 10, pp. 2423–35, 2016.

[240] ASTM, *Standard test methods for density and specific gravity (relative density) of plastics by displacement*, Standard, 2008.

[241] W. Schroeder, K. Martin and B. Lorensen, *The visualization toolkit (4th edition)*, Computer Program, 2006.

[242] D. Shcherbakova, 'A multiphysics model of the mouse aorta for the mice optimization of high-frequency ultrasonic imaging in', Thesis, 2012.

[243] I. K. Ekroll, A. Swillens, P. Segers, T. Dahl, H. Torp and L. Lovstakken, 'Simultaneous quantification of flow and tissue velocities based on multi-angle plane wave imaging', *IEEE Trans Ultrason Ferroelectr Freq Control*, vol. 60, no. 4, pp. 727–38, 2013.

[244] L. Lovstakken, 'Signal processing in diagnostic ultrasound: Algorithms for real-time estimation and visualization of blood flow velocity', Thesis, 2007.

[245] N. C. Rouze, M. H. Wang, M. L. Palmeri and K. R. Nightingale, 'Parameters affecting the resolution and accuracy of 2-d quantitative shear wave images', *IEEE Trans Ultrason Ferroelectr Freq Control*, vol. 59, no. 8, pp. 1729–40, 2012.

[246] I. K. Ekroll, M. M. Voormolen, O. K. Standal, J. M. Rau and L. Lovstakken, 'Coherent compounding in doppler imaging', *IEEE Trans Ultrason Ferroelectr Freq Control*, vol. 62, no. 9, pp. 1634–43, 2015.

[247] K. P. Mercado, J. Langdon, M. Helguera, S. A. McAleavey, D. C. Hocking and D. Dalecki, 'Scholte wave generation during single tracking location shear wave elasticity imaging of engineered tissues', *J Acoust Soc Am*, vol. 138, no. 2, EL138–44, 2015.